Aerospace Engineering Sciences Graduate Theses & Dissertations

Aerospace Engineering Sciences

Spring 1-1-2011

One-Dimensional Spacecraft Formation Flight Testbed for Terrestrial Charged Relative Motion Experiments

Carl Seubert
University of Colorado at Boulder, carl.seubert@colorado.edu

Follow this and additional works at: https://scholar.colorado.edu/asen_gradetds

Part of the Aerospace Engineering Commons

One-Dimensional Spacecraft Formation Flight Testbed for Terrestrial Charged Relative Motion Experiments

by

Carl R. Seubert

B.E., Aeronautical (Space) Engineering with Honours,

University of Sydney, Australia, 2004

M.S., Aerospace Engineering, University of Missouri - Rolla, USA 2007

A thesis submitted to the

Faculty of the Graduate School of the

University of Colorado in partial fulfillment

of the requirements for the degree of

Doctor of Philosophy

Department of Aerospace Engineering Sciences

2011

This thesis entitled:
One-Dimensional Spacecraft Formation Flight Testbed for Terrestrial Charged Relative Motion
Experiments

written by Carl R. Seubert
has been approved for the Department of Aerospace Engineering Sciences

_____
Dr. Hanspeter Schaub

_____
Dr. Penina Axelrad

_____
Dr. Daniel Moorer

_____
Dr. Zoltan Sternovsky

Date _____

The final copy of this thesis has been examined by the signatories, and we find that both the
content and the form meet acceptable presentation standards of scholarly work in the above
mentioned discipline.

Seubert, Carl R. (Ph.D., Aerospace Engineering)

One-Dimensional Spacecraft Formation Flight Testbed for Terrestrial Charged Relative Motion
   Experiments

Thesis directed by Dr. Hanspeter Schaub

Spacecraft operating in a desired formation offers an abundance of attractive mission ca-
pabilities. One proposed method of controlling a close formation of spacecraft is with Coulomb
(electrostatic) forces. The Coulomb formation flight idea utilizes charge emission to drive the
spacecraft to kilovolt-level potentials and generate adjustable, micronewton- to millinewton-level
Coulomb forces for relative position control.

In order to advance the prospects of the Coulomb formation flight concept, this dissertation
presents the design and implementation of a unique one-dimensional testbed. The disturbances of
the testbed are identified and reduced below 1 mN. This noise level offers a near-frictionless platform
that is used to perform relative motion actuation with electrostatics in a terrestrial atmospheric
environment. Potentials up to 30 kV are used to actuate a cart over a translational range of motion
of 40 cm.

A challenge to both theoretical and hardware implemented electrostatic actuation develop-
ments is correctly modeling the forces between finite charged bodies, outside a vacuum. To remedy
this, studies of Earth orbit plasmas and Coulomb force theory is used to derive and propose a
model of the Coulomb force between finite spheres in close proximity, in a plasma. This plasma
force model is then used as a basis for a candidate terrestrial force model. The plasma-like pa-
rameters of this terrestrial model are estimated using charged motion data from fixed-potential,
single-direction experiments on the testbed.

The testbed is advanced to the level of autonomous feedback position control using solely
Coulomb force actuation. This allows relative motion repositioning on a flat and level track as

well as an inclined track that mimics the dynamics of two charged spacecraft that are aligned with the principal orbit axis. This controlled motion is accurately predicted with simulations using the terrestrial force model. This demonstrates similarities between the partial charge shielding of space-based plasmas to the electrostatic screening in the laboratory atmosphere.

Dedication

To Jill Seubert,

because you read this out of love, not learning.

Acknowledgements

This research and dissertation would not have been possible without my advisor Dr. Hanspeter Schaub. Your technical prowess and Swiss efficiency are inspirational to me. You facilitated the development of my work as well as my character as a student and as a person. I thank you for your influence, time, guidance, and continued support throughout all the endeavors of my research. I would also like to thank the members of my committee; Dr. Penina Axelrad, Dr. Webster Cash, Dr. Daniel Moorer, and Dr. Zoltan Sternovsky.

Thanks is also deserved of some notable figures in the Aerospace Engineering Sciences Department. Firstly, Joe Tanner, the great astronaut who has walked in space and now walks next to me in the hallway. You are an idol and I thank you for your truthful words and fun times. Ann Brookover, the 'mother' of the graduate student body, we are in gratitude for your hard work, supporting the students and Department. I also thank the graduate students at CU who make the Department so vibrant, fun and intelligent.

I personally thank Seebass, whether on the singletrack or the porch we both got through it together, thanks mate. I thank all my friends, both in boulder and abroad, for riding the roller coaster of life's thrills with me. My parents, Reiner and Julianne Seubert deserve a thanks as large as the ocean physically between us. Your unequivocal support has motivated me to reach for the stars without apprehension, and I am grateful.

Finally, I thank my wife, Jill. You are by my side without question and illuminate my life with an unparalleled joy and passion. I am so fortunate to have you during these times and forever more.

Contents

Chapter

Tables

Table

Figures

Figure

Chapter 1

Introduction

"We choose to go to the moon in this decade and do the other things, not because they are easy, but because they are hard, because that goal will serve to organize and measure the best of our energies and skills... space is there, and we're going to climb it... the most hazardous and dangerous and greatest adventure on which man has ever embarked." Almost 50 years after this famous speech was given by President John F. Kennedy on September 12 1962, space still remains the formidable frontier for human utilization.

Space is an attractive location for scientific, surveillance or exploratory missions of Earth and beyond. Whether it is for monitoring the Earth's climate or geological features, communications, solar power extraction or the search for Earth-like planets about other stars, there is an abundance of possible remote sensing, radiometric, and telescopic operations that benefit from a space-based platform. As declared by President Kennedy in the 60's and still holding true today, it is necessary to expand spacecraft technology and capabilities to continue growth in the areas of space research. As an example, sensor baselines of tens to hundreds of meters are sought to increase observation power and sensor resolution. For imaging, such as space-based telescopes, large physical sizes are desired as it increases the baseline of the collector (or aperture) and consequently improves the angular resolution. While not an easy feat, these sensor platforms can be achieved with a dedicated space structure, deployable components, or of particular interest here, with a formation of spacecraft.

Large space structures offer a rigid configuration producing a precise sensor array or plat-

form for highly accurate observations. In contrast, inflatable and deployable systems offer a low mass, high mechanical packaging efficiency and potentially low cost solution. Large structures and gossamer inflatables are sought for their use as space-based antennas, telescopes, for solar array deployment or isolating sensing equipment such as Langmuir probes [19; 37; 148]. An ongoing area of research is the development and testing of deployable components and material membranes for large space structures [31] as well as the inflation of Gossamer structures using electrostatic forces [146]. The National Aeronautics and Space Administration (NASA) has developed a number of key technologies to support the prospects of inflatable search radar, parabolic reflectors, sun shades as well as the spherical, 100 foot diameter, Echo balloon intended as a space-based communications reflector [36]. The search for terrestrial exoplanets is one application that features prominently in astrophysics and benefits from a large-baseline receptor that would allow spatial resolutions 2 to 3 orders of magnitude higher than planned spaced-based telescopes [38].

However, there are challenges to overcome prior to large space structures becoming standard operating systems; including significant mass, volume and cost constraints, the need for on-orbit construction and the complexities and reliability of deployable components. The International Space Station (ISS), shown in Figure 1.1, is an example of an orbiting structure that has taken 15 countries of 5 space agencies,[1] ten years and contributions of tens of billions of dollars to complete.[2] Also shown in Figure 1.1 is the successful space deployment of the 14×14 m solar sail of the Interplanetary Kite-craft Accelerated by Radiation Of the Sun (IKAROS) mission by the Japanese Aerospace Exploration Agency (JAXA) [157].

1.1   Spacecraft formation flight

An alternate method of achieving space-based sensing and providing the same characteristics of a large-baseline structure is to operate a free-flying formation of spacecraft. The use of spacecraft

---

[1]   NASA International Space Station: International Partners and Participants, http://www.nasa.gov/mission_pages/station/structure/elements/partners.html, 10/11/11

[2] ESA International Space Station: How much does it cost, http://www.esa.int/esaHS/ESAQHA0VMOC_iss_0.html, 10/11/11
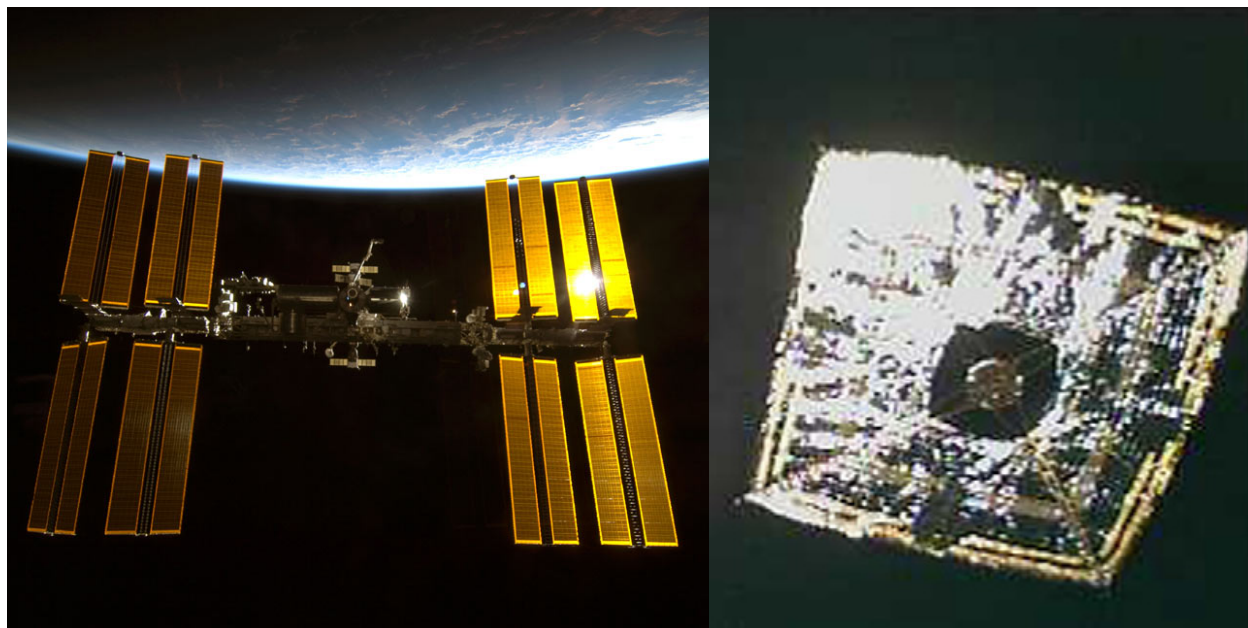
Figure 1.1: International space station and IKAROS solar sail [157]

formations is a growing area of research offering advantages that include the use of smaller, lighter, redundant, and ultimately cheaper spacecraft with lower risks. In addition, free-flying formations can provide variable baselines and can distribute payloads for fractionated and responsive architectures [9]. The technical and logistical challenges of formation flight are being overcome with several successful missions to date and numerous concepts in planning as will be introduced here [10; 82].

The proposed NASA Goddard Stellar Imager [11] and the NASA Jet Propulsion Laboratory (JPL) study on the proposed Terrestrial Planet Finder [8] are two missions that intend to operate a formation of spacecraft to create a sensor baseline in the kilometer range. An artist's impression of a potential Terrestrial Planet Finder design is shown in Figure 1.2. In this concept an array of craft are used to reflect the signals to a centrally located collector craft.

A promising future planet finder is the New Worlds Observer concept being researched by Cash [15; 16]. This large formation mission proposes to operate a 30 m to 50 m diameter occulter at a separation of approximately 40,000 km from a telescope craft. Figure 1.2 shows an illustration of the occulter, which is flower-shaped to control diffraction, shading the distant star allowing the
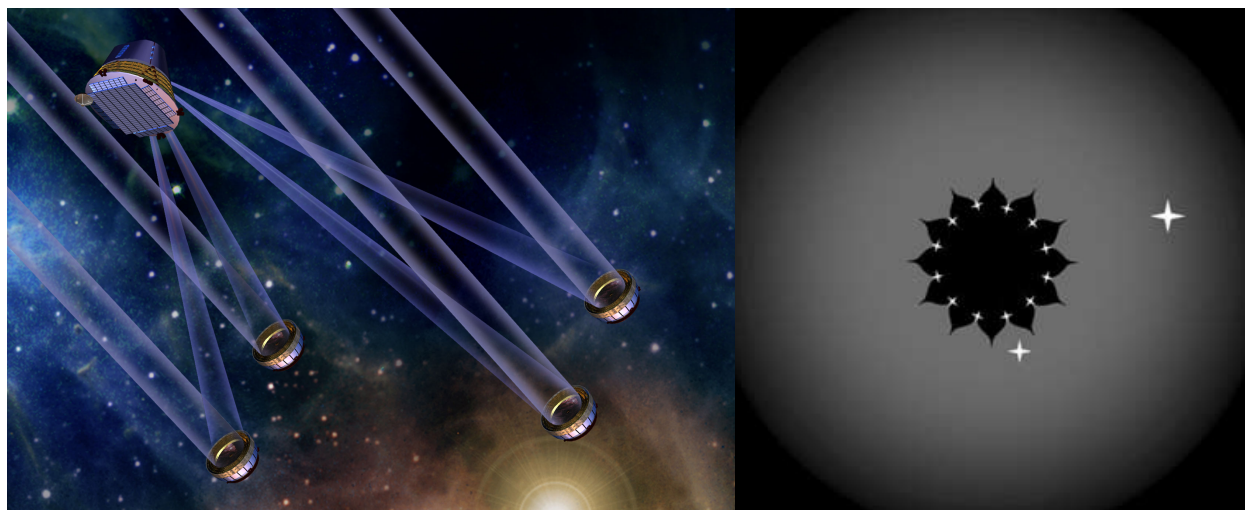
Figure 1.2: Illustrations of the NASA Terrestrial Planet Finder formation [nasa.gov] and the New Worlds Observer occulter shading a distant star to reveal orbiting planets [15]

telescope to view and study orbiting planets.

One of the leading applications for large-baseline space interferometry is observations from Geosynchronous Earth Orbit (GEO). A study by Wertz of a GEO-based free-flying formation indicates that an Earth surface resolution as low as 0.5-2 m is achievable with a viewable range of almost 50% of the planet from that altitude [167]. Similarly, the Eyeglass concept is another investigation into a GEO-based very large aperture diffractive telescope, 25-100 m two-craft formation, proposed for Earth surveillance. The Eyeglass diffractive lens is designed with a folded sequence, similar to an origami layout, that is deployed on-orbit [60; 61]. These proposed missions give an indication of the growing trend toward spacecraft formation use and capabilities.

Another application of formation flight is to enhance situational awareness capabilities. Local inspection can be an invaluable feature when diagnosing spacecraft performance or monitoring spacecraft surroundings and/or debris. An example is shown in Figure 1.1, where the JAXA IKAROS mission ejected a free-flying camera to obtain final images and confirmation of its solar sail deployment [157]. While providing amazing images, this ejection method only offers limited formation flight capabilities as the one-time use camera did not feature any active control nor

continued inspection. This would be advantageous for long term dynamical studies and stability and monitoring sail deterioration. In addition, this ejection method is not practical for Low Earth Orbit (LEO) and GEO because it only adds to the growing space debris problem.

The Prototype Research Instruments and Space Mission technology Advancement (PRISMA) mission currently demonstrates advanced autonomous formation flying techniques [46]. Intended to expand technology and knowledge of close proximity operations, the mission is developed and operated by the European Space Agency (ESA). The spacecraft use Global Positioning System (GPS) and vision-based sensors to perform proximity operations down to 3 m separations [22]. The "washing machine" size spacecraft is shown in Figure 1.3 along with another ESA formation mission, Cluster which operates at separations of 100 to 1000's of km [30].
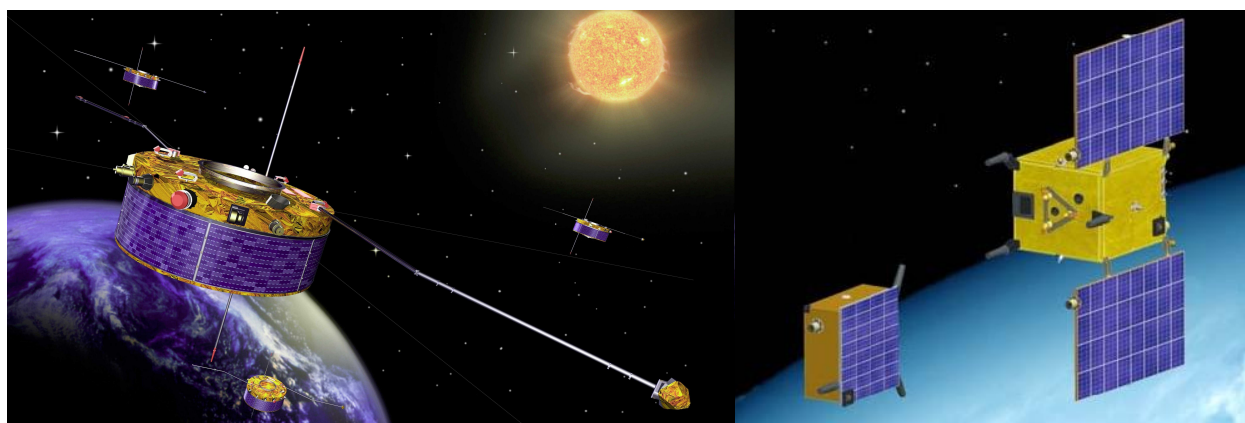
Figure 1.3: The large formation of the ESA Cluster mission [esa.int] and the close proximity operations of the ESA PRISMA formation mission [eoportal.org]

As PRISMA demonstrates, close formations flight is an important area of research. Specifically, rendezvous and docking is the essence of close proximity formation flight. Rendezvous has been a regular component of manned spacecraft missions since the Apollo era and research on supporting technology and techniques continues to grow. Of significant importance here is the expansion and utilization of autonomous rendezvous and docking such as demonstrated with the ISS and the ESA automated transfer vehicle and the JAXA H-2 transfer vehicle [174]. However, conducting close proximity operations is problematic and requires significant research and development

as demonstrated in the next section.

1.2   The challenges of formation flight

There are technological, implementation and operational challenges that must be overcome prior to spacecraft formation flight becoming routine. Safety is of utmost importance when operating numerous spacecraft remotely and autonomously, particularly in close proximities. Detailed here are some of the specific challenges of spacecraft formation flight.

A concern for formation flight operations is successful deployment of spacecraft that are launched in a docked configuration. This particular aspect of formation flight is under investigation by a joint effort between the Canadian Space Agency and JAXA. Their proposed, two nanosatellite JC2Sat mission, aims to use differential drag to autonomously assist with spacecraft separation and formation maintenance [80]. The mission plans to vary the attitude of the craft with respect to the LEO velocity profile and use fixed drag panels to manipulate the resulting differential drag. This separation technique is intended to alleviate the need for pyrotechnic devices on small spacecraft.

Challenges with free-flying craft are the complex dynamics, relative motion sensing and navigation requirements. These challenges include the associated control strategies which can often require high propellant usage to maintain accurate formations and consequently shortened missions lifetimes. Close spacecraft formations, separated by less than 100 m, present particular mission challenges. The complex relative dynamics require both very accurate relative position sensing and frequent micro-Newton-level relative motion control maneuvers to maintain formation and ensure collision avoidance. If conventional inertial thrusters such as chemical or electric propulsion systems are used, care must be taken at these separation distances to ensure exhaust plumes do not impinge on other craft and contaminate sensors and structural components. Additionally, the use of chemical thrusters with a finite propellant supply can significantly limit the operational life of the formation.

Over the past decade, several novel, essentially propellantless relative motion control concepts have been presented. These include the use of electromagnetic and flux-pinning formation flying [71;

44; 91] as well as formations maintained with Lorentz forces [109]. Electromagnetic applications intend to use electrical currents to induce magnetic fields about superconducting coils on each spacecraft. Interactions of the magnetic fields is used to control relative attitudes and separations, as well as absolute positioning utilizing the Earth's magnetic field. The research for these proposed techniques is being pursued, however the limitations to these concepts are the high power and mass requirements. This dissertation research looks at an alternative formation flight control technique using electrostatic (Coulomb) forces.

1.3   Coulomb formation flight

One attractive method of performing relative position control of close spacecraft formations is with Coulomb forces. John Cover proposed the use of Coulomb forces in space in the 1960's as a means to inflate large-scale parabolic antennas [20]. Images of the proposed concept from the 1966 Patent are shown in Figure 1.4. As shown in the figure, a charging source is used to inflate the electrically conductive surfaces with a repulsive or attractive Coulomb force. By holding a charge the reflector maintains its position relative to the radio frequency feed. It was proposed that a 30-40 foot diameter reflector at GEO requires potentials on the order of one to several tens of kilovolts and watt to kilowatt levels of power depending on the environment [20].

In 2001, King and Parker proposed the use of Coulomb forces to control a free-flying formation of spacecraft to develop a 20-30 m size array for interferometry from GEO [69]. Using an active charge emission device the charge of each craft is controlled to manipulate the Coulomb forces to desired levels. Their study concludes that it is feasible to operate a Coulomb controlled formation mission and the concept warrants further analysis. Saaj performed a study for ESA based on the utilization of electrostatics to navigate and reconfigure swarms of spacecraft [124]. Supporting work included autonomous assembly of large space structures with Coulomb forces by Izzo and Pettazzi [63], as well as the hybrid application of electrostatics with conventional thrusters to control formations by Saaj and Lappas [122].

This dissertation research builds upon this prior work and further examines the use of elec-
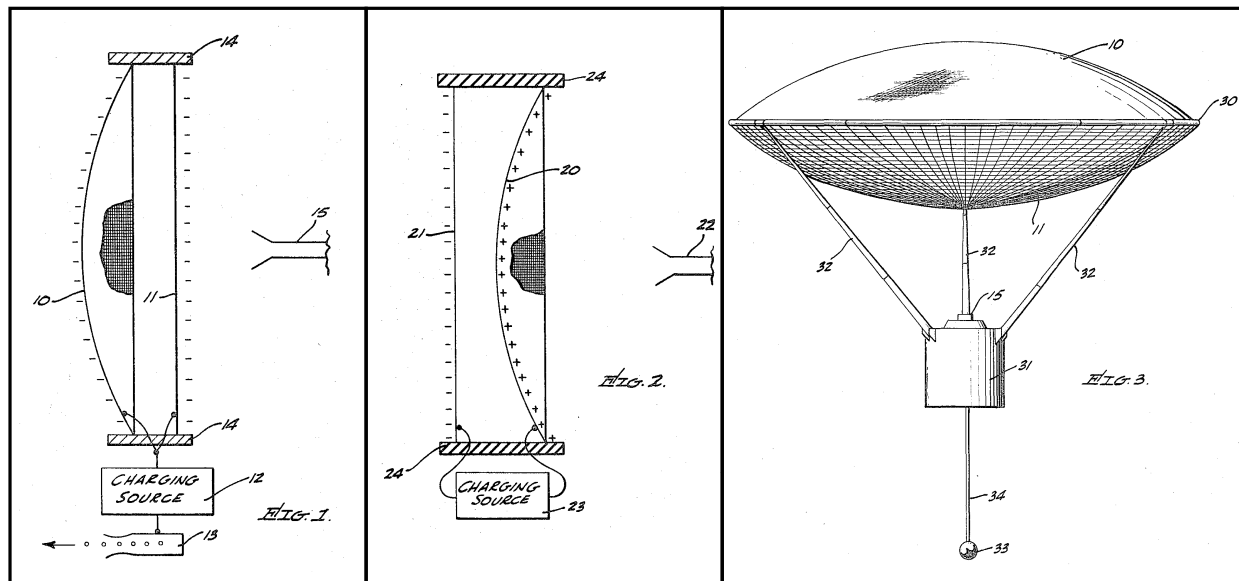
Figure 1.4: Illustrations of space antenna concepts utilizing electrostatic inflation from a 1966 Patent by John Cover [20]

trostatic actuation for spacecraft relative motion control. An illustration of a simple two-spacecraft formation using Coulomb forces for separation distance control is shown in Figure 1.5. In this concept, the potential of each craft is controlled to produce an attractive or repulsive Coulomb force between each craft, depending on the relative polarities. A charge emission device is used for active charge control, with examples given in Chapter 2. The details of Coulomb force generation are presented in Chapter 3.

Coulomb Formation Flying (CFF) is an emerging concept that addresses free-flying challenges [130]. It offers adjustable forces to control the complex relative dynamics [69; 70]. The inter-spacecraft forces are created by manipulating the spacecraft potential with continuous current emission from a charge control device. The resulting Coulomb thrust with its micronewton to millinewton force levels is generated virtually propellantless. Additionally, the charge control devices require only watt-levels of power and are space-proven [69; 70; 137]. The CFF technique also avoids close proximity plume impingement concerns (the contamination of sensors and systems from propellant). Conventional thrusters for larger and non-line-of-sight corrections and inertial
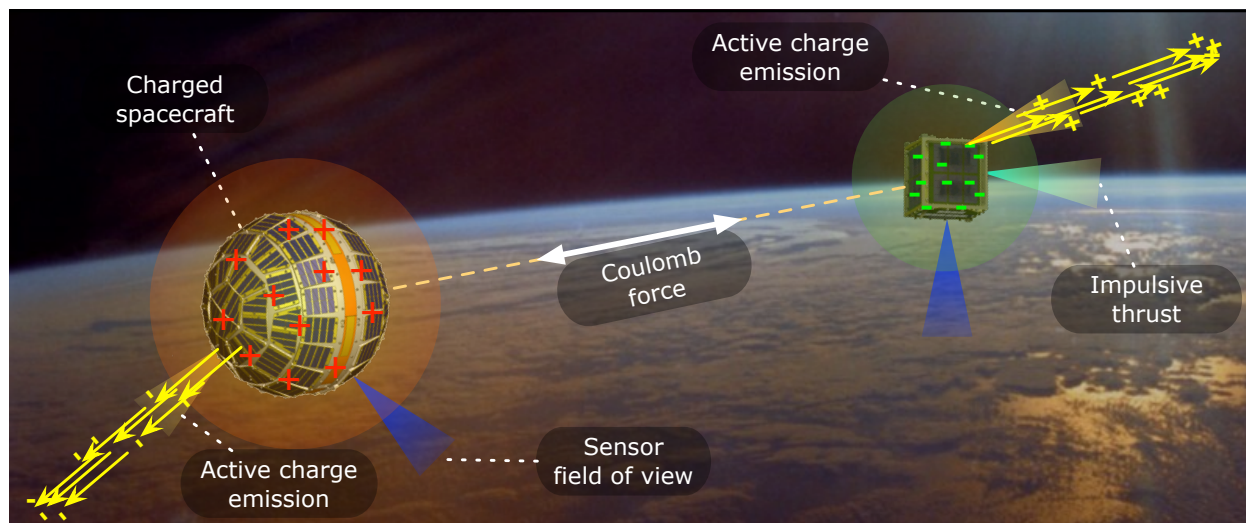
Figure 1.5: Two-craft Coulomb formation flight concept; active charge emission is used to charge craft to kilovolt-level potentials to control the separation distance with Coulomb forces[3]

maneuvers may still be used.

While the CFF craft manipulate charge with hardware devices, spacecraft will also naturally charge due to the interaction with the local plasma environment. Orbital missions such as Spacecraft Charging AT High Altitudes (SCATHA) and the Applications Technology Spacecraft (ATS-6) were designed and launched specifically to characterize and quantify the extent of natural spacecraft charging [89; 95; 169]. On-orbit studies such as these have established that a GEO spacecraft can naturally charge to kilovolt-level potentials [32; 96]. Natural spacecraft charging is an ongoing extensive study as it can lead to undesired operational consequences [55; 117]. As an example, a review by the Aerospace Corporation indicates that 161 out of 198 documented environment-related anomalies are a consequence of spacecraft charging [32; 72].

Even when operating in a variable plasma environment, spacecraft charging can be safely handled, prevented and rectified allowing on-going space operations. This has been demonstrated on-orbit with missions such as Equator-S [43; 155], the formation Cluster [154] and Space Power Experiment Aboard Rockets (SPEAR 1) [66; 67; 105]. The ESA Cluster spacecraft that are

---

[3] Model of DANDE spacecraft courtesy of Colorado Space Grant Consortium

investigating the Earth's magnetosphere and solar wind interaction require very precise potentials down to the volt-level to not bias scientific measurements [154]. The CFF concept would ultimately employ flight heritage charge control technology such as this. Furthermore, it is the absolute potential of the craft that produces the Coulomb force, so natural charge levels can be utilized and then modified as necessary to perform operational maneuvers.

One limitation of a Coulomb spacecraft formation is the natural charge shielding that occurs from the plasma environment. A charged craft will interact with the free-flying particles of the local plasma and the effective force between the craft is reduced. For this reason, it is most favorable to use Coulomb control at altitudes of GEO or above and with formation separation distances less than 100 m [69]. At GEO altitude (approximately 35,786 km), the plasma is sufficiently hot and sparse with minimal shielding to enable Coulomb thrusting when operating with spacecraft separations of dozens of meters and kilovolt level potentials. The LEO plasma is colder and more dense causing higher shielding and making the use of Coulomb thrust challenging for free-flying charged objects [69; 113]. Further details of the GEO plasma conditions and shielding properties are given in Chapter 2.

A concept that evolved from the Coulomb formation flight principles is the Tethered Coulomb Structure (TCS). Structures are generated by connecting spacecraft nodes with fine, low-mass tethers and inflating the system with repulsive Coulomb forces. This creates a semi-rigid structures by charging the craft to kilovolt-level potentials. The structure can be launched and deployed in a compact configuration and dimensions modified by varying the tether lengths. Like the CFF concept, this is to be implemented at GEO altitudes and above with separations of dozens of meters between nodes. It is envisioned that large structures of hundreds of meters are developed with a network of tethered and charged nodes. The stiffness capabilities, disturbance rejections, and power and propellant requirements are analyzed in Chapter 7.

1.4   Motivation of research

Spacecraft formation flight is a fundamental element of space utilization and will continue to grow with future science, communication and energy pursuits. Integral to these efforts are the practical applications that require flying in close proximities such as rendezvous, docking and situational awareness. To address these future needs, Coulomb formation flight is a promising concept however; it requires further investigation and development.

An essential step to maturate the CFF concept is the ability to apply the concept to hardware and perform relative motion experiments. Developing and implementing a testbed dedicated to electrostatic actuated motion studies provides abundant knowledge that is not obtainable with purely numeric or theoretical studies. A testbed offers a platform to explore the intricacies of generating and utilizing Coulomb thrust, appreciating charging characteristics and their limitations and directly studying the application of closed-loop charge control algorithms.

Potential applications and technical aspects that benefit from a Coulomb formation flight testbed include:

- Further development of terrestrial charging hardware and actuation

- Verification of Coulomb formation flight control algorithms

- Verification of electrostatic rendezvous, docking and collision avoidance maneuvering

- Further development of isolated and embedded on-board vehicle electronics

- Further development of inter-vehicle communications and information distribution

- Further development of absolute and relative motion sensing and navigation

- Verification of charged relative motion estimation techniques and capabilities

- Increased understanding of charged tethered spacecraft studies

- Increased understanding of shape and attitude dependent electrostatic forces

• Increased understanding of membrane and structural inflation with Coulomb forces

Fundamentally, a terrestrial testbed for Coulomb controlled relative motion studies is sought.

1.5   Goals of research

This dissertation research focuses on the goal of developing a dedicated one-dimensional (1-D) testbed and implementing Coulomb relative motion control. The primary outcomes to be achieved throughout this research endeavor are:

I. Develop an experimental apparatus and perform relative motion actuation with Coulomb forces in a terrestrial atmospheric environment

II. Identify, quantify and mitigate external disturbances to 1 millinewton allowing Coulomb forces to dominate

III. Produce a model of the testbed terrestrial Coulomb force and compare experimental atmospheric interactions to expected space-based Coulomb force shielding

IV. Perform autonomous feedback position control experiments with Coulomb forces

1.6   Related work

A detailed description of the literature related to the objectives of this research is presented here. This is divided into the theoretical and numerical studies focused on the advancement of CFF as well as existing testbeds that are currently used for spacecraft formation flight research.

1.6.1   Theoretical and numerical studies

Analytic studies in support of Coulomb formation flight is a growing area of research. Berryman and Schaub investigated the use of Coulomb control to create static equilibrium configurations in orbit [6; 7]. This includes analytic two- and three-craft charged relative equilibria in a rotating Hill frame [7]. This was later expanded to three dimensions with four-craft relative equilibria by

Vasavada [158]. Further work on the charge solutions for invariant shape, three-craft formations is developed by Hogan [56; 57]. While relative equilibrium solutions for Coulomb spacecraft clusters have been developed these open-loop equilibria are naturally unstable and so far only marginally stable behavior has been found for a three-craft Coulomb formation under specific conditions [57].

To implement a two-craft Coulomb formation it is essential to introduce feedback control. Natarajan in Reference [100] develops a control strategy that stabilizes the motion of two craft about an orbit radial alignment while maintaining a fixed separation distance. The details of a restricted 1-D Lyapunov-based Coulomb control regime developed for three craft operating in a linear configuration are shown by Wang [164]. Similarly, he analyzes the feasible regions of the 1-D constrained control operation that can be implemented and ensures that the spacecraft charge levels remain realistic and do not saturate in Reference [162], important considerations for hardware implementation. In Reference [161], he specifically develops a 1-D collinear position control that could be directly implemented on the 1-D Coulomb testbed. To date, none of these 1-D control techniques have been verified or tested experimentally.

Further applications such as control of a three-craft, triangular formation is problematic as it does not have an equilibrium charge solution. Wang addresses this triangular configuration with a switched control strategy that is applied by updating the worst of the two triangular sides and is shown to have global stability [163]. He then takes the Coulomb control strategies a step further in Reference [165] by implementing a stable, two-craft spinning configuration in a GEO environment rather than deep space. This control law is developed with both full-state feedback and a more realistic partial-state feedback law that is shown to be stable under fast spinning conditions. In addition, a control law for two-craft in an orbit-radial configuration about circular orbits and libration points is implemented with both Coulomb and electric propulsion thrusting and differential solar radiation perturbations by Inampudi [62].

There is also a number of research efforts supporting the control of swarms of spacecraft. Pettazzi et al. propose the use of a hybrid propulsive system that utilizes both conventional thrusters and Coulomb forces to control spacecraft formations [111]. Izzo and Pettazzi apply the hybrid

propulsion system to autonomous, self-assembly of structures and demonstrate the fuel savings of implementing electrostatic forces. A feedback control law is developed that autonomously positions a swarm of N spacecraft, however it does require the hybrid system as this cannot be done with purely electrostatics [63]. Collision-free path planning with an artificial potential field and implemented with a sliding mode control strategy is demonstrated with the hybrid propulsion system by Saaj [122]. A preliminary investigation into spacecraft and plasma interactions is provided along with a set of requirements on the charge emission system necessary to perform formation control in Reference [112].

Coulomb application studies have also expanded to large debris removal at GEO. Schaub and Moorer present a concept that uses CFF to tug and re-orbit a debris body without needing inter-spacecraft contact [129]. In a similar Coulomb tractor application, Murdoch and Izzo present the use of an electrostatic tug to deflect 100 m size, near Earth objects [97]. A number of these CFF theoretical studies would benefit from having a dedicated testbed allowing technology advancement.

A requirement of all theoretical studies is a model of the Coulomb force between finite bodies in a plasma. The interaction between charged bodies and a plasma and the resulting Coulomb forces are complex even for simple spherical shapes. For detailed modeling finite element, electrostatic solvers are typically used, however, while accurate they only provide a static force solution. For simplicity in theoretical developments the analytic vacuum Coulomb force point charge model is used [112; 161] and has validity in certain applications, albeit over estimates the force in a plasma. It is unknown what analytic force model was used by Cover in his patent for antenna inflation, but it may have been a point charge approximation that included plasma shielding [20]. Common practice is to use the conservative Debye-Hückel force model, as it is an analytic representation that accounts for the partial shielding of a plasma between point charges, as used by King, Izzo, Saaj, Lappas, Peck, and Schaub [69; 63; 123; 81; 131]. These studies use point charges and do not consider the capacitance changes of having finite bodies in close proximity in a plasma. To more accurately capture the true force between charged objects in a plasma, Murdoch presents the use of an effective Debye length in Reference [97] to use in a Debye-Hückel force model. Ultimately there

are further developments to be made with analytic modeling of Coulomb forces between bodies, particularly in non-vacuum environments. This is one direct application that can be investigated with a testbed.

1.6.2   Existing formation flight testbeds

Schwartz provides a comprehensive overview of the history of air-bearing testbeds for uses such as spacecraft attitude and motion experiments [134]. There are also existing terrestrial testing platforms dedicated to spacecraft formation flight concepts. These include the NASA JPL formation control testbed [127] and Marshall Space Flight Center flat floor testbed [17]. These testbeds provide flat, near frictionless operating surfaces that allow terrestrial relative motion and attitude experiments using air-bearing support. These testbeds are designed for large spacecraft systems with well-known dynamics and relative motion actuation devices with Newton-level and greater thrusting. One limitation to using these testing laboratories for CFF is the associated high costs and impracticality of using a Government-based facility for a University-level research project.

On a smaller scale, Peck has developed the FloatCube testbed at Cornell University to support the development of the flux pinning formation flight concept [171]. It features air levitated platforms that provide two translational and one rotational degree of freedom. The Massachusetts Institute of Technology (MIT) Synchronize Position Hold Engage and Reorient Experimental Satellite (SPHERES) formation flight program features a low-friction flatbed [17; 90]. The 4 kg SPHERES spacecraft have thrusters that operate at the low millinewton level to as great as 110 mN [87]. Terrestrial testing however was only marginally successful as the thrust "had difficulty overcoming the stiction, friction and slope irregularities of the table" [87]. Subsequent to these early experiments, the SPHERES craft are successfully operating in the zero-gravity environment within the ISS [18]. MIT also developed a flat surface testbed with large superconducting coils, cooled to 77 K, to support the electromagnetic formation flight development [126]. The force magnitudes are not published; however given the vehicles have a 36 kg mass and operate within separations of meters, the forces are likely to be in the Newton-level range [73].

The University of Illinois at Urbana-Champaign performs vacuum testing on the deployment of film for a proposed solar sail system [173]. The concept uses a formation of craft to reel out polyimide films that are stowed in a central craft. The testbed is used to study the forces on release as well as investigate different film materials [173]. In another spacecraft mechanism testbed, Stanford University uses a flat surface for testing future space manipulators and link-arms for construction purposes [133].

Stanford University also has a 9 × 12 foot granite table with three vehicles that is used as a formation flight testbed [1; 5]. The group is also performing terrestrial 3-D formation flight experiments using blimps [5]. In an equally novel approach the University of Southern California uses small model helicopters as a platform to verify spacecraft formation flight algorithms [98]. The University of Southampton, UK, also features a flat floor and has developed spacecraft mockup frames dedicated to formation flight experiments [159]. Again, all these testbeds operate with force actuators in the Newton range and with well-modeled dynamics.

1.7   Testbed challenges

The development and effective use of a relative motion testbed is not a trivial task. The specific challenges to implementing electrostatic actuation for relative motion control are highlighted in this section.

For the terrestrial Coulomb testbed, the electrostatic forces are on the order of tens of millinewtons. At these magnitudes a significant challenge is obtaining a sufficiently high actuation signal to noise ratio, where the terrestrial Coulomb forces can overcome numerous external interferences. Due to these relatively low Coulomb force magnitudes, there is a need to have an extremely low disturbance environment to perform charged relative motion experiments. Further information on the disturbance forces acting on the testbed and techniques used for mitigation are provided in Chapter 5.

In addition, models of the forces between charged bodies are limited. Analytic Coulomb force models between charged bodies in a vacuum are derived and presented in Chapter 3. However,

operation in a plasma or a terrestrial atmospheric environment increases complexity. In a plasma the Coulomb force can be computed by solving the full Poisson's equations with numerical solvers and finite element analysis. This is not efficient or even practical for computing the force values between dynamically moving bodies with varying charge levels and changing environments even if they are just spheres and not complex spacecraft. Analytic approximations for the plasma environment are available and implemented here. To model the terrestrial testbed forces the feasibility of applying the plasma model to experimental results is demonstrated in this dissertation.

In order to perform Coulomb actuation on a terrestrial testbed some of the critical challenges that need to be addressed include:

- Operation in standard laboratory atmospheric environments

- Mechanical disturbance force magnitudes below the minimum Coulomb forces (< 1 mN)

- External electrostatic interferences either removed or characterized

- Limited to the use of non-conducting and electrostatic-inert materials

- Limited models of terrestrial charged forces in an atmospheric environment

- Low mass vehicles (< 1 kg) to allow reasonable acceleration magnitudes

- Safe control and operation of electrostatic potential sources (10's kV)

- Low-cost development, test and operation

Existing and commercial testbeds are quickly dismissed as options for CFF development as they do not meet many of the above challenges. Disturbance and friction levels are typically significantly higher magnitude than the actuation Coulomb forces. In addition, they often feature metallic components and/or high mass vehicles with auxiliary air support systems.

To implement Coulomb actuated relative motion studies it is paramount to design and develop a unique testbed, dedicated to the purpose of meeting these challenges. The testbed at the University of Colorado at Boulder provides a platform to investigate charge implementation and

actuation, and environmental interactions in a low disturbance environment. These are aspects of the CFF concept that require meticulous examination prior to space-based implementation and cannot be isolated on existing formation flight testbeds.

The design, construction and implementation of a one-dimensional (1-D) Coulomb testbed is the focus of this dissertation research. Autonomous feedback control repositioning of a vehicle on the testbed using electrostatic actuation is demonstrated. Using experimental results and sensing equipment, disturbances acting on the testbed are quantified and mitigated and the causes of electrostatic interference are identified. This leads to the development of a new model of the Coulomb forces in the laboratory atmosphere based on the space-based plasma force model. This allows direct comparison between the partial force shielding of the terrestrial forces to the space plasma force.

1.8   Overview of research

The development of a dedicated Coulomb testbed provides a wealth of knowledge on electrostatic formation flight actuation and ultimately advances the overall prospects of the CFF concept. The testbed provides a platform to explore the complexities of autonomous charged motion control, which is an expansive scope of study. This entails analysis of electrostatic force generation, partial charge shielding, electrostatic field interactions, material and shape studies, surface charge distribution, and arcing. This can also be extended to testing applications such as charge feedback control strategies, development of embedded electronics, and inter-craft communication with vehicles that can accommodate variable ground levels.

In order to achieve the four main goals presented in Section 1.5 a number of tasks require completion. In this section the goals are further expanded along with details of the specific tasks that are investigated with this dissertation research.

1.8.1   Perform terrestrial electrostatic relative motion experiments

It is demonstrated that there is a need for a dedicated testbed for Coulomb actuation experiments. In this dissertation, a testing platform is implemented with surfaces that hold an electrostatic charge and generate Coulomb forces between them. The details of the design and construction of a frictionless 1-D track is given. Featuring a moveable cart, accurate position sensing, and electrostatic power supplies, the testbed is used as a platform to successfully perform relative motion control with Coulomb forces.

1.8.2   Quantify and mitigate external disturbances

With only tens of millinewtons of actuation force, it is essential that external disturbances are mitigated or reduced. Primary mechanical disturbance forces are quantified and where possible, these perturbations are mitigated. Similarly, the electrostatic interferences need to be identified and removed or reduced. Disturbance mitigation is required to increase the actuation signal to noise ratio and allow the Coulomb forces to dominate during experiments. External perturbations are reduced to a consistent 1 millinewton noise level along the entire length of track.

1.8.3   Model terrestrial Coulomb forces and compare atmospheric interactions to shielding from a space plasma

Minimizing the disturbance environment allows advanced analysis of experimental response and model fitting. A prerequisite to Coulomb force modeling in a plasma or terrestrial environment is to understand Earth orbit plasmas and interactions with charged spacecraft. This is conducted along with an overview of the models used for computing the Coulomb force between spheres, in close proximity, in these different environments. To quantify and compare the plasma and atmospheric force models, space-like plasma parameters are fitted to the terrestrial, fixed-potential, one-way, experimental data. This identifies to what degree the atmospheric interactions and resulting charge shielding compares to the expected space-based, Debye charge shielding.

1.8.4   Perform autonomous feedback position control experiments

With Coulomb actuation demonstrated on the testbed, an advancement is to implement position control. Through position sensing feedback, the charged surfaces are autonomously controlled to specific potential levels, manipulating the Coulomb force on the cart. For autonomous position control it is crucial that the hardware and driving software can promptly switch potential polarities on the testbed. Prompt polarity switching provides controllable repulsive and attractive forces. The performance of these position control experiments are directly compared to predicted performance that is simulated using the terrestrial Coulomb force model.

1.9   Thesis overview

The dissertation is organized as follows. Chapter 2 details measurements of Earth orbit plasmas collected by spacecraft, and introduces modeling of these plasmas. Plasma interactions with spacecraft, such as natural charging, are quantified and a review of active charge control in space is performed. Starting with the Coulomb force between spheres in close proximity in a vacuum, a proposed analytic representation of the force between spheres in a plasma is derived in Chapter 3. This plasma force model forms the basis of the terrestrial Coulomb force model. Utilizing the relative motion of charged craft in space, Chapter 4 analyzes the effectiveness of estimating plasma environment and charge parameters using the plasma force model. Chapter 5 presents the design and development of the Coulomb testbed apparatus and identification and mitigation of disturbances. The results of charged relative motion experiments are documented in Chapter 6, including an application of the testbed that mimics the relative dynamics of constrained 1-D orbital motion. In this chapter, the fitting of parameters of the terrestrial force model to one-way charged experiments is conducted. A simulation using this force model is then compared to autonomous position control experiments. To encapsulate the developments of this dissertation, a theoretical application of the CFF concept known as the Tethered Coulomb Structure is presented in Chapter 7. Finally, concluding remarks and potential follow-on work is given in Chapter 8.

Chapter 2

Earth orbit plasmas and spacecraft interactions

There are multiple theoretical and implementation facets to be explored and developed in order for the Coulomb formation flight concept to be demonstrated in orbit. Supporting this conceptual development, this dissertation explores the utilization of Coulomb forces for relative motion actuation in a terrestrial environment. Preceding hardware implementation, knowledge of the concept is essential. To study the applications of Coulomb forces in space it is necessary to understand the environmental plasmas of Earth orbit. This allows investigation into the interaction of energetic particles (plasma) with spacecraft materials and the resulting natural spacecraft charging as well as computation of the partial force shielding. These topics of spacecraft Earth orbit plasmas and natural and artificial charging are investigated in this chapter.

2.1   Earth plasma environment

An overview of the Earth's plasma constituents is given to provide insight to spacecraft interaction. A plasma is a medium made up of ionized and neutral particles. The Earth's immediate neutral environment of the lower atmosphere becomes an ionosphere at around 50 km with electrons e^- and primarily NO^+ and O_2^+ ions and peaks in density around 300 km to 350 km with primarily NO^+, O_2^+, and O^+ ions [113]. At this altitude the peak density is approximately 10^{11} m^{-3} and the thermal energies are typically in the range 0.1 eV to 1 eV [115]. Altitudes above this, the densities decrease and temperatures increase and the ion population is primarily N^+, O^+, and H^+. With increasing altitude the ionosphere then transitions into the plasmasphere and by GEO altitudes

the plasma is made up predominantly of singly charged protons (H^+) and free electrons [54; 113], with plasma density and temperature properties provided in detail later in this chapter. At GEO the ratio of O^+/H^+ is typically less than 0.25, however this can increase toward parity during high solar activity [28].

2.1.1   Plasma Debye lengths

The composition and properties of an Earth orbit plasma determines the extent of interactions with a spacecraft. One method of quantitatively comparing plasmas is with the Debye length (λ_D). It is a dimensional scale computed from the temperature and density of the local plasma [113].

The sphere of influence of a charged body is defined by the Debye sphere that a radius of one Debye length. This plasma sphere of influence is illustrated in Figure 2.1. Inside the Debye sphere the free-flying plasma particles are influenced by the charged body electric fields (E-fields) and screen the potential field so that outside the Debye sphere the charge is effectively shielded.
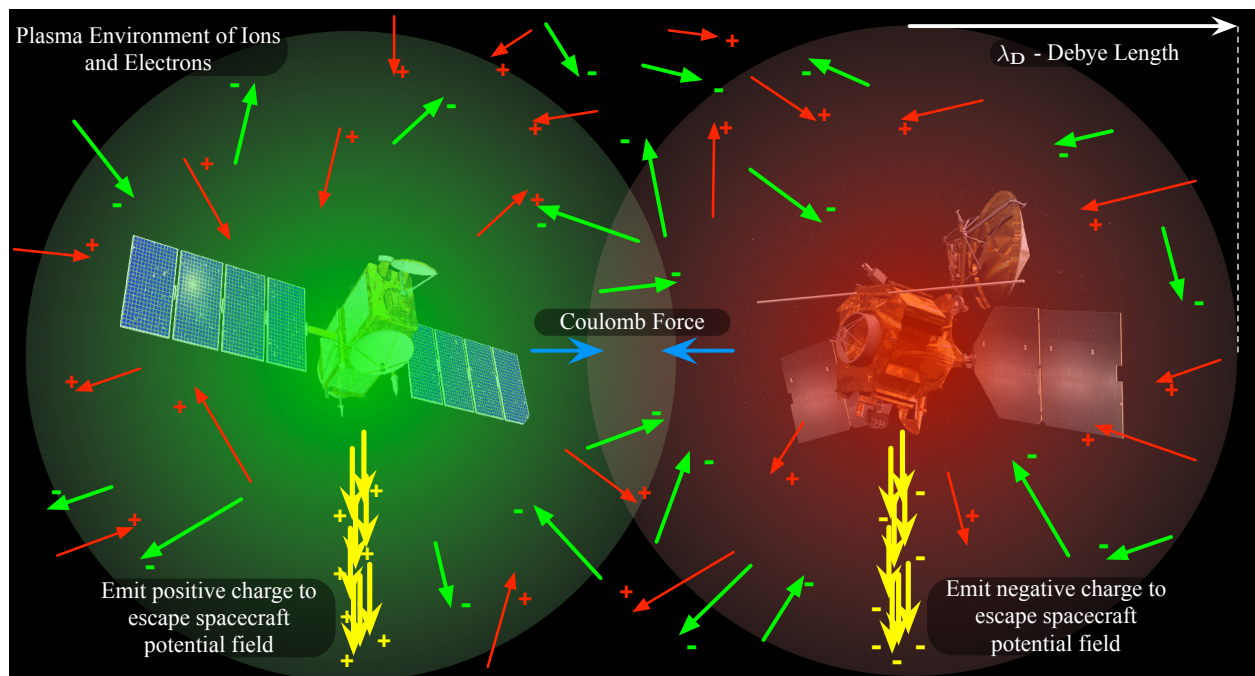
Figure 2.1: Illustration of actively charging spacecraft in a plasma

The plasma Debye sheath is the region beyond which charged bodies have minimal influence on the plasma [97]. Outside the sheath, which can be multiple Debye Lengths, the plasma is at its unperturbed equilibrium state. The plasma Debye length is important in this dissertation and in Coulomb formation flight studies as it parameterizes the screening of the E-fields of a charged body in a plasma. The Debye length indicates the limits of spacecraft separations for relative motion with Coulomb forces.

The Debye length is calculated with the densities of the plasma electrons and singly ionized species, n_e & n_i in m^{-3}, as well as their respective temperatures T_e & T_i in Kelvin, using the general expression [113]:

$$\lambda_D = \sqrt{\frac{\epsilon_0 \kappa / e_c^2}{\frac{n_e}{T_e} + \sum_i \frac{n_i}{T_i}}} \tag{2.1}$$

where $\epsilon_0 = 8.854 \times 10^{-12}$ C^{2}N^{-1}m^{-2} is the permittivity of vacuum, $\kappa = 1.381 \times 10^{-23}$ JK^{-1} is the Boltzmann constant, and $e_c = 1.602 \times 10^{-19}$ C is the elementary charge. The focus of this research is on the GEO plasma environment, which is primarily composed of H$^+$ ions so the Debye length equation reduces to:

$$\lambda_D = \sqrt{\frac{\epsilon_0 \kappa / e_c^2}{\frac{n_e}{T_e} + \frac{n_{H+}}{T_{H+}}}} \tag{2.2}$$

If the plasma energies of electrons and ions are equivalent ($T_e = T_i$) then the accelerations of the ions are significantly less in the presence of a charged object, due to their larger mass (ion mass $m_i = 1.672 \times 10^{-27}$ kg, electron mass $m_e = 9.110 \times 10^{-31}$ kg). For this reason it is often common to neglect the influence of ion species altogether and have a Debye length that is purely a function of the local plasma electrons. This is suitable when the timescales of the process are short relative to the mobility of the ions [59]:

$$\lambda_D = \sqrt{\frac{\epsilon_0 \kappa T_e}{n e_c^2}} \tag{2.3}$$

At GEO the plasma has Debye lengths ranging from 4 m to 1000 m with a nominal value of approximately 200 m [69; 137]. Debye lengths of this scale allow the use of Coulomb repulsion when operating with spacecraft separations of dozens of meters at GEO. The Low Earth Orbit (LEO) Debye lengths are typically at the cm level and the interplanetary medium is typically

at the meter level [74; 97; 113]. This chapter further explores the characteristics of Earth orbit plasmas and the models used to describe them. When describing the thermal characteristics of a plasma, the thermal energy in electronvolts (eV) is a common designation. In this dissertation, the thermal energy of the plasma is assigned the variables $\mathcal{T}$ with units of eV and can be converted to temperature, in Kelvin, with the Boltzmann constant and an electron charge using the expression:

$$\mathcal{T}_e = \frac{\kappa}{e_c}\, T_e$$

2.1.2   On-orbit plasma measurements

There have been a number of spacecraft that have studied the plasmas of Earth orbit. This section details the representations of the GEO plasma parameters (densities and temperatures) and the corresponding Debye lengths based on these space measurements. Detailed plasma measurements with dedicated spacecraft and instruments date back to the 1970-80's with the Spacecraft Charging AT High Altitudes (SCATHA) and the Applications Technology Spacecraft (ATS-5 and ATS-6) missions. Interpretation of this data comes from Purvis [117], Tribble [156], and Pisacane [113]. Data obtained from the Magnetospheric Plasma Analyzer (MPA) instruments onboard the Los Alamos National Laboratory (LANL) spacecraft are also used. These LANL spacecraft currently operate at a range of longitudinal locations around the GEO belt. An example of the electron and ion distributions measured by the ATS-5 spacecraft on 9/30/1969 is shown in Figure 2.2.

A single Maxwellian distribution that uses a nominal density and velocity value to represent the GEO plasma environment is common. This model can be limiting however, as the plasma conditions vary greatly and are comprised of a broad range of particle energies [26]. The GEO plasma environment can rapidly fluctuate and can be flooded with high energy particles, with mean values as high as a few tens of keV. The local plasma conditions are heavily dependent on the local time as well as the geomagnetic activity which is driven by solar interactions [54]. Denton in Reference [28] demonstrates with LANL MPA measurements that during solar minimum the expanding plasmasphere can cause average electron densities to grow a factor of two or more.
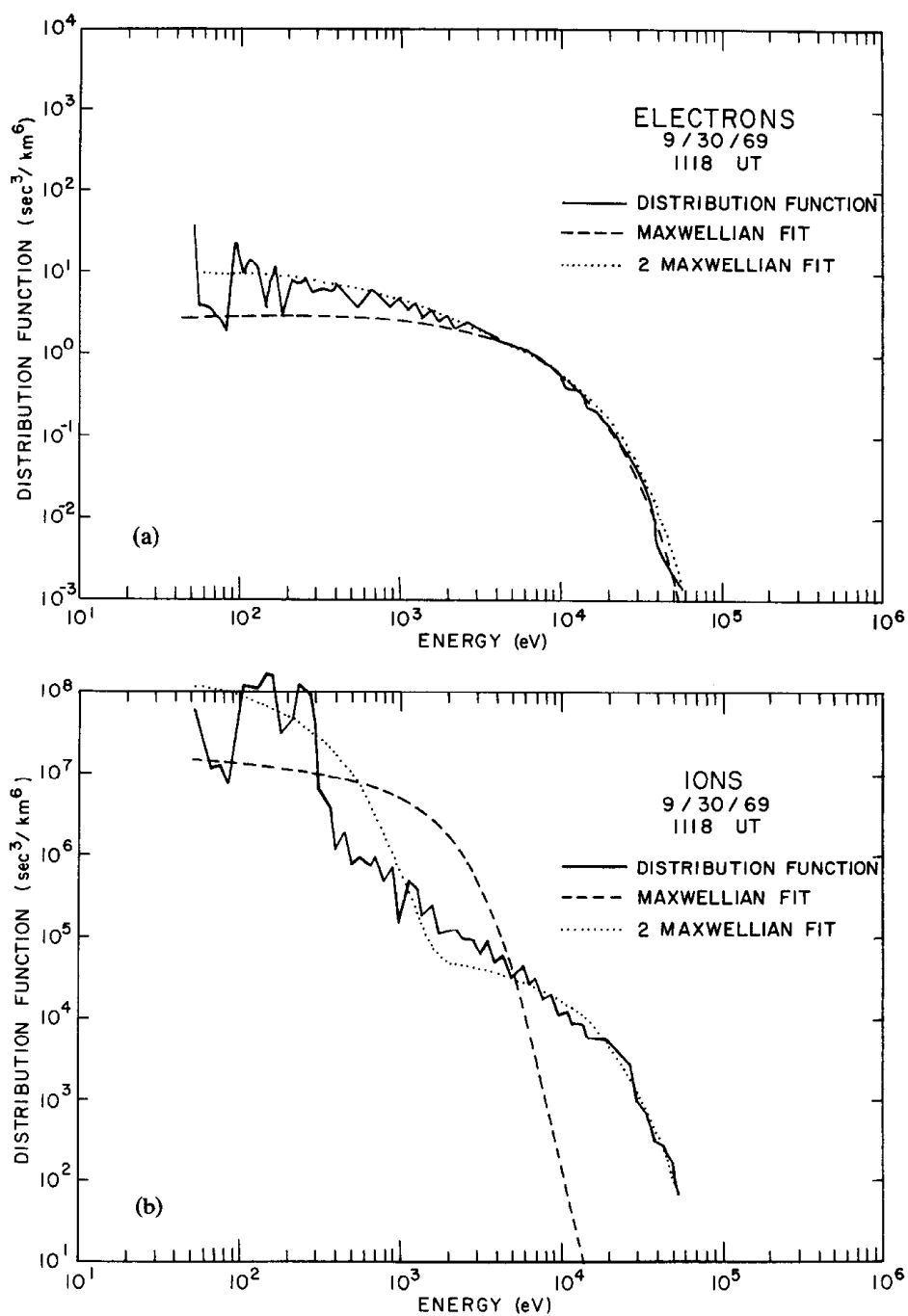
FIG. 1.(a) ELECTRON DISTRIBUTION FUNCTION OBSERVED BY ATS-5.
Also shown are a Maxwellian and two Maxwellian fit.
(b) ION DISTRIBUTION FUNCTION OBSERVED BY ATS-5.
Also shown are a Maxwellian and two Maxwellian fit.

Figure 2.2: GEO Electron and ion energy distributions measured by ATS-5 on 9/30/1969, with single and double Maxwellian fits (From: Garrett [42])

Solar storms can occur at anytime and can cause very abrupt changes in the plasma environment. These storms can lead to significant spacecraft charging and anomalies, as well as abrupt Debye length variations. Similarly, high speed solar winds can drive higher temperature (and consequently larger Debye lengths) into the magnetosphere, particularly in the declining solar cycle phase. However, for the purposes of the dissertation research a single Maxwellian distribution describing the local GEO plasma environment is suitable and is used. A single Maxwellian fit for electron and ion distributions is shown in Figure 2.2.

A GEO spacecraft will not only encounter variations in its local plasma environment, but it also will travel through different regions of Earth's magnetosphere. All of these regions are comprised of different plasma conditions and the Debye lengths can be substantially different. As an example, Figure 2.3 highlights the magnetospheric regions a spacecraft at GEO could encounter over the course of one day. This figure shows the distribution of samples an MPA instrument on a LANL spacecraft made as a function of time. An average value of the Debye length for each of these magnetospheric regions is also shown in the legend to illustrate the variability in the plasma properties [115]. This is a representative plot from one of the spacecraft,[1] averaged from a sample of days in 1992 which covers the maximum intensity of solar cycle 22. So, while this does not directly resemble a nominal GEO, it indicates that conditions can vary greatly at GEO [58; 166].

In order to capture the influence of all these GEO plasma conditions, three representative GEO plasma conditions are used for this analysis (quiet, nominal, and disturbed). Although single Maxwellian distributions are used, these three plasma conditions define the extreme bounds and nominal operating environments a GEO spacecraft will encounter on-orbit. Nominal conditions cover the typical environment at GEO, while disturbed conditions resemble large Debye lengths due to high temperature plasma injections. The quiet conditions cover times when the lower altitude plasmasphere pushes up to the GEO region [29]. While rare, during these conditions the lower energy, higher-density plasma that enters GEO results in shorter Debye lengths.

The very quiet conditions are considered the "worst-case" for the Coulomb formation flight

---

[1] MPA Data, Los Alamos National Laboratories, http://www.mpa.lanl.gov/data.shtml, 10/05/09
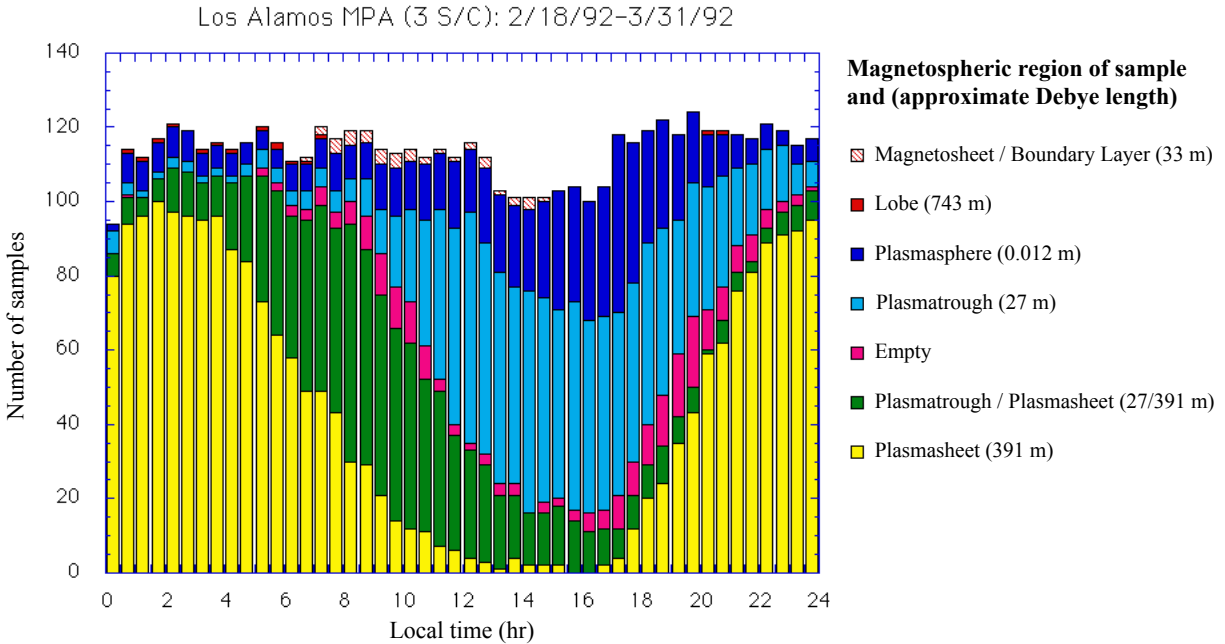
Figure 2.3: Distribution of samples from each magnetospheric region (with corresponding average Debye length) made by a LANL MPA instrument at GEO as a function of local time (Adapted from: McComas [88])

concept as they lead to significant shielding and reduced force magnitudes as well as higher power requirements. In the literature the term "worst-case" has different connotations depending on the operating scenarios. For GEO spacecraft operators that are concerned with charging the nominal higher energy, lower density plasma (large Debye lengths) is most detrimental as it leads to natural spacecraft charging and associated issues that are investigated in Section 2.2.

2.1.2.1   Nominal GEO plasma parameters

Table 2.1 gives the plasma conditions and resulting Debye lengths from a range of sources and different spacecraft instruments. The Debye lengths given in Table 2.1 are calculated using Equation 2.3 and are shown in graphical form in Figure 2.4. For representative plasma conditions where no ion data is available it is assumed that the plasma is in a net neutral state and ions have the same values as the electrons.

Table 2.1: Nominal and disturbed GEO plasma parameters and Debye lengths

Source	$\mathcal{T}_e$ (eV)	n_e (cm^{-3})	$\mathcal{T}_i$ (eV)	n_i (cm^{-3})	λ_D (m)
A-Purvis [117]	12	1.12	29.5	0.236	738
B-Tribble [156]	10	1.7	14	1.85	427
C-LANL MPA solar min	1.45	0.45	10	0.6	386
D-Tribble [156]	2.4	1	10	1	327
E-Garrett [42]	0.67	1.6	0.55	1.82	277
F-Pisacane [113]	0.86	10	0.86	10	49
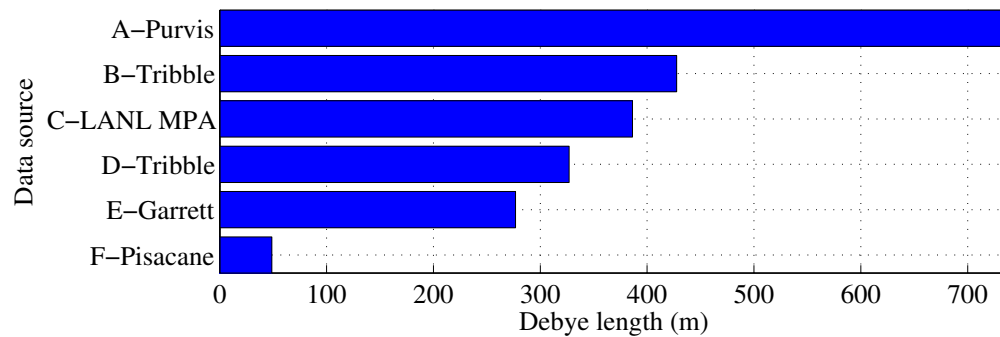
Figure 2.4: Debye lengths in nominal and disturbed GEO plasmas based on space measurements

These plasma representations come from interpretations of the SCATHA, ATS-5, and ATS-6 data from Purvis [117], Tribble [156], Garrett [42], and Pisacane [113] during disturbed and nominal GEO plasma conditions. Data set A is based on an analysis by Purvis and covers the disturbed GEO conditions. Similarly, data set B by Tribble is also based on an injection of high temperature plasma from a solar substorm. The LANL MPA data of set C is obtained from averaging the total data from multiple spacecraft. This is computed for a six month period during 1996 (solar minimum) for the low energy particle measurements and is only representative. These values correlate with the more detailed analysis of LANL MPA measurements by Thomsen and Denton that cover full solar cycles [28; 150]. Data sets D, E and F represent an average of the nominal GEO plasma conditions.

2.1.2.2 Quiet GEO plasma parameters

The nominal plasma Debye lengths that are tens to hundreds of meters are ideal for CFF operations. However, the GEO plasma can experience times of low activity where the densities increase and the temperatures are lower. These quiet times are the worst-case operating conditions for a CFF system as the highest levels of partial force shielding are encountered. Representative GEO plasma parameters for these quiet times is obtained from data measurements on ATS, SCATHA and LANL spacecraft and shown in Table 2.2 and graphically in Figure 2.5.

Table 2.2: Quiet GEO plasma parameters and Debye lengths

Source	$\mathcal{T}_e$ (eV)	n_e (cm^{-3})	$\mathcal{T}_i$ (eV)	n_i (cm^{-3})	λ_D (m)
G-LANL MPA high density	0.7	70	0.7	100	15
H-Davis [23]	2.7	0.6	5.6	2.4	9
I-Lennartsson [83]	4	5	4	5	5
J-Davis [24]	0.1	100	0.1	100	0.2
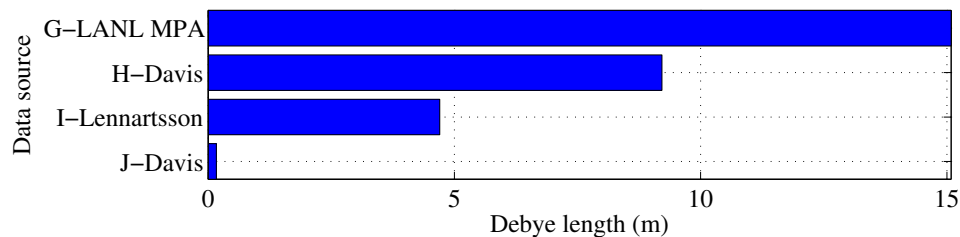
Figure 2.5: Debye lengths in quiet GEO plasmas based on space measurements

Data set G is data from MPA instruments on the LANL spacecraft. This is a storm spike condition, which is computed based upon a particular solar geomagnetic storm that occurred on April 7, 2000. This was an influx of energetic particles that resulted in a short-term (minutes) spike in the local GEO plasma densities, significantly reducing the Debye length. The remainder of the quiet plasma data is interpreted from Davis [23] and from the extensive "Spacecraft Surface Charging Handbook" [24] as well as Lennartsson [83]. Data set J from Davis is from a very specific eclipse event in 2001.

2.1.3   Representative plasma parameters for this research

Taking into account the data from each of the spacecraft measurements at GEO and the interpreted single Maxwellian representations, an approximate average is used in this research study for simplification. Table 2.3 lists the plasma temperature and densities and corresponding Debye lengths for the nominal plasma as well as the two extreme bounds (quiet, disturbed) that bound the plasma operating regime experienced at GEO. Also included in this table is a representation of the average conditions for a LEO nominal plasma environment [113]. The International Reference Ionosphere (IRI-86) indicates that LEO has a minimum Debye length of 0.12-0.17 cm [33]. With this significantly shorter Debye length the enhanced charge shielding makes it challenging to use Coulomb forces for free flying formations at LEO.

Table 2.3: Representative GEO and LEO plasma parameters and Debye lengths

Conditions	$\mathcal{T}_e$ (eV)	n_e (cm^{-3})	$\mathcal{T}_i$ (eV)	n_i (cm^{-3})	λ_D (m)
GEO Quiet	3	10	3	10	**4**
GEO Nominal	900	1.25	900	1.25	**200**
GEO Disturbed	1e4	1	1e4	1	**743**
LEO Nominal	0.2	1×10^5	0.2	1×10^5	**0.01**

These representative Earth orbit plasma conditions are used for all computations in this dissertation. Understanding the Earth plasma is important for the CFF concept as it directly alters the operating conditions and performance achievable. As demonstrated in the next section it also leads to natural spacecraft charging and consequently drives the operational power requirements to maintain desired charge levels.

2.2   Spacecraft plasma interactions

A spacecraft in a plasma is bombarded by free-flying charges as illustrated in Figure 2.1. This results in a net current flow from these free-flying particles that can be impregnated into conductive and dielectric materials and cause natural charging. In a geosynchronous orbit the spacecraft is

traveling in resonance with Earth and its plasma so that the natural current flow from these free flying charged particles can be assumed isotropic, with no ram currents[35].

The plasma at GEO is neutral, with equivalent densities of ions and electrons. However, the spacecraft is typically hit with more electrons due to their higher thermal speed as a result of their significantly lighter mass. This will cause natural spacecraft charging that can reach kilovolt-level potentials and is strongly dependent on the abundance of high energy electrons relative to the ambient ions as well as photoelectron emission from solar ultraviolet (UV) radiation [74].

2.2.1   Natural charging on GEO spacecraft missions

A number of missions have been launched to specifically study spacecraft charging at GEO. The Martian viking spacecraft utilized a number of engineering practices to mitigate charge related anomalies, specifically arcing [84]. NASA conducted charging measurements and experiments on ATS-5 that launched in 1969 as well as the follow on ATS-6 that launched in 1974 [103; 94].

ATS-5 was the first spacecraft that observed large negative potentials of hundreds of volts during eclipse [103]. The ATS-6 spacecraft measured natural charging as low as -19 kV during eclipse on October 1975 [142]. The extent of high spacecraft charging during eclipse is due to the bombardment of electrons (particularly on insulative surfaces) in combination with the absence of emitted photoelectrons from solar photon impacts. Through analysis of ATS-5 and ATS-6 data the existence of an electrostatic barrier around the charged craft was postulated. This is typically a result of differential charging as great as thousands of volts on the insulative surfaces, of which, ATS-5 featured a large external antenna and outer surfaces constructed primarily of electrical insulators. [103].

2.2.2   Natural charging at LEO altitudes

Spacecraft charging in lower altitudes is typically only to the volt level as the significantly denser plasma quickly neutralizes any charged surfaces. Measurements on board US defense meteorological satellite program spacecraft, that operate in a 840 km altitude polar orbit achieved

numerous charging occurrences down to as low as -1430 Volts [40]. Analysis of this data indicates that more severe charging occurs at solar minimum due to at least an order of magnitude decrease in the ambient plasma densities at LEO. A finding of this study is that for significant charging, greater than 100 V in magnitude, it is necessary to have a plasma density less than 10^4 cm^{-3} [40].

A LEO mission that suffered detrimental effects from charging was the NASA Tethered Satellite System Reflight (TSS-1R) mission, flown in February 1996. This tether research mission was implemented on space shuttle mission STS-75. The 20 km tether unfortunately failed due to electrostatic discharge. The tether obtained a charge as high as 3500 V, that lead to gas leakage in its enclosure, increasing the neutral pressure that ultimately led to Paschen discharge and failure [33].

2.2.3   Spacecraft charging concerns

Natural spacecraft charging from plasma and solar UV can lead to catastrophic circumstances. This is an important aspect requiring attention not only during a spacecraft's design and manufacturing phases but also for on-orbit operations. A study by the Aerospace Corporation indicated that 161 out of 198 documented environment related anomalies were a direct result of spacecraft charging [32; 72].

Environment induced hardware failures, extend beyond just spacecraft surface charging and includes dielectric charging, internal discharging, single-event effects (SEE), radiation damage, sensor contamination, and solar array degradation [107]. The source of these operational risks include solar energetic particles and associated plasma enhancement as well as cosmic galactic rays. Spacecraft weather and charging leading to internal discharges have been correlated to anomalies on the Voyager 1, GPS and SCATHA craft [120].

A NOAA report indicates that a spacecraft insurance company estimated there was over $500 million in insurance claims, between 1994-1999, as a result of on-orbit failures related to space weather.[2]   For a spacecraft designer and operator it is a requisite to have knowledge and

---

[2]   NOAA, Space Weather Prediction Center Topic Paper: Satellites and Space Weather, http://www.swpc.noaa.gov/info/Satellites.html, 10/05/11

models of the local environment and understand the interaction of the spacecraft with this plasma. Particularly for the implementation of CFF spacecraft that intend to utilize kilovolt-levels of charge. Designing spacecraft to prevent SEE from high energetic particle impacts, requires interpretation of plasma models to provide sufficient shielding, without adding excess weight [106].

What is important to note is that natural spacecraft charging is both measurable and preventable. With dedicated hardware practices naturally charging can be safely handled in the design of spacecraft. With background knowledge of the Earth orbit plasma environments it is of particular interest to this study to model both natural and artificial charging.

2.2.4   Artificial spacecraft charging

One common method of reducing natural spacecraft charging is with the use of an artificially produced current. This methodology is illustrated in Figure 2.1 where a charge control device emits a stream of charged particles with significant energy to leave the craft's charge field. The emission can be either electrons or positively charged particles to obtain both positive or negative potentials. The net result is that artificial charging is used to overcome high potentials or in the case of the CFF concept used to safely drive the craft to high kilovolt-level potentials. Charge control devices and their capabilities are explored in detail in Section 2.6.

2.3   Spacecraft plasma currents

A spacecraft interacts with its local space plasma environment with a flow of charged particles resulting in a net current as shown in Figure 2.6. The resulting currents drive the spacecraft to a charge equilibrium with the local plasma resulting in a net current of zero, which as shown with on-orbit measurements, can occur at kilovolt-level potentials. For a CFF craft, an active charge control device is implemented to neutralize, enhance or offset this natural equilibrium with an artificially produced current. This charge device can drive the craft to desired charge levels regardless of the local plasma conditions. This section further expands upon the knowledge of the interaction between a spacecraft and the plasma. Models of the natural plasma currents to a charged body are

developed (based on single Maxwellian distributions) to determine the extent of natural spacecraft charging and resulting equilibrium potentials in each plasma.
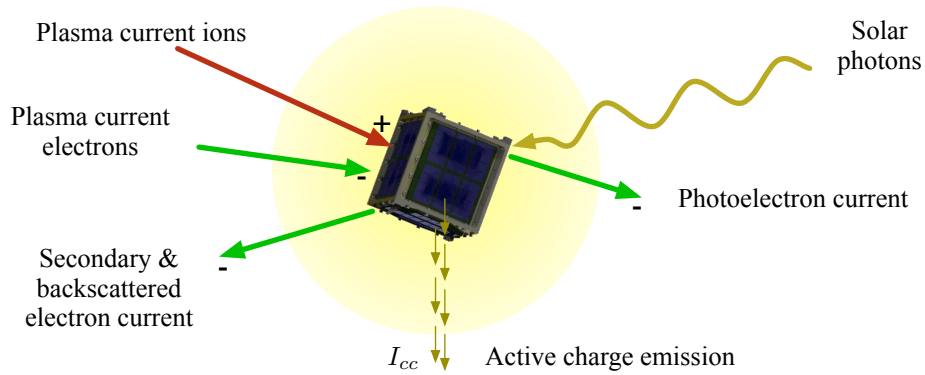
Figure 2.6: Illustration of plasma, Solar radiation and active charge emission currents to spacecraft

2.3.1   Charging currents

Considering bodies of finite dimensions but with a general surface area in contact with the plasma, a common modeling practice is to use the current density J with units of Am^{-2}. Assuming a spherical spacecraft in a plasma with an isotropic velocity distribution, the charging current is modeled with the net equation:

$$I_{\text{net}} = \frac{J_e - J_i - [J_{Se} + J_{Si} + J_{BSe}]}{A_{tot}} - \frac{J_{Pe}}{A_{sun}} \pm I_{cc} \tag{2.4}$$

where

J_e = incident electrons

J_i = incident ions

J_{Pe} = photoelectrons

J_{Se} = secondary emitted electrons due to J_e

J_{Si} = secondary emitted electrons due to J_i

J_{BSe} = backscattered electrons due to J_e

I_{cc} = active charge emission current (electrons or ions)

A_{tot} = total surface area of sphere

A_{sun} = surface area of disk impacted by Solar UV

The terminology defines all currents to the spacecraft as negative. The details of all these contributing currents is given in this section. To compute the photoelectron current the surface area is that of a disk, not the full sphere.

2.3.2   Primary electron and ion current density

It is assumed that the plasma is comprised of two populations (electrons, protons) that are modeled with single Maxwellian distributions. Also, the equations developed here assume the plasma represents a thick-sheath limit (i.e. $\lambda_D \gg \rho$, where ρ is the spacecraft spherical radius) [54]. This assumption holds when considering the nominal plasma Debye length of 200 m and craft of 1-2 m representative radii. As in earlier equations, the charging currents are developed using particle thermal energies with units of Kelvin.

For a spacecraft operating in eclipse without any backscattering or secondary electron emission the electron current density is represented with a Boltzmann factor, exponential repulsion current and Mott-Smith and Langmuir attraction current [79; 119]:

$$J_e(V < 0) = J_{0e} \ \text{Exp} \left[\frac{-e_c|V|}{\kappa T_e} \right] \tag{2.5a}$$

$$J_e(V > 0) = J_{0e} \left(1 + \frac{e_c V}{\kappa T_e} \right) \tag{2.5b}$$

where V is the spacecraft potential and J_{0e} is the electron saturation current:

$$J_{0e} = e_c n_e \sqrt{\frac{T_e}{2\pi m_e}} \tag{2.6}$$

The ion current density to the spacecraft during these conditions is modeled with:

$$J_i(V < 0) = -J_{0i} \left(1 + \frac{e_c|V|}{\kappa T_i} \right) \tag{2.7a}$$

$$J_i(V > 0) = -J_{0i} \, \text{Exp} \left[\frac{-e_c V}{\kappa T_i} \right] \tag{2.7b}$$

where J_{0i} is the ion saturation current:

$$J_{0i} = e_c n_i \sqrt{\frac{T_i}{2\pi m_i}} \tag{2.8}$$

Combining the electron and ion currents of Equations 2.5 and 2.7, the resulting net current density to the craft is:

$$J_{\text{net}}(V < 0) = J_{0e} \, \text{Exp} \left[\frac{-e_c |V|}{\kappa T_e} \right] - J_{0i} \left(1 + \frac{e_c |V|}{\kappa T_i} \right) \tag{2.9a}$$

$$J_{\text{net}}(V > 0) = J_{0e} \left(1 + \frac{e_c V}{\kappa T_e} \right) - J_{0i} \, \text{Exp} \left[\frac{-e_c V}{\kappa T_i} \right] \tag{2.9b}$$

A spacecraft will reach current equilibrium with the plasma when $J_{\text{net}} = 0$. Depending on the plasma conditions this solution exists for a specified spacecraft potential. As demonstrated on-orbit during eclipse, with only ion and electron currents acting the equilibrium occurs at a negative potential computed with the solution:

$$V_{eq} = -\frac{\kappa T_e}{e_c} \ln \left[\sqrt{\frac{T_i}{T_e} \frac{m_i}{m_e}} \left(1 - \frac{e_c V}{\kappa T_i} \right) \right] \tag{2.10}$$

which for equivalent ion and electron temperatures can be reduced to an approximate value of [54]:

$$V_{eq} \approx -2.5 \frac{\kappa T_e}{e_c} \tag{2.11}$$

2.3.3   Photoelectron current

In sunlight a spacecraft is hit with solar radiation that leads to a net outflow of photoelectrons. This occurs during sun-lit conditions when the photons impacting the spacecraft surfaces cause an electron to be emitted from the surface material via the photoelectric effect. This is an important contributor to the net current flow for a GEO spacecraft that spends the majority of its on-orbit conditions in sunlight and the magnitude of the current can be relatively high. The photoelectron current is modeled using [54]:

$$J_{Pe}(V < 0) = -J_{0pe} \tag{2.12a}$$

$$J_{Pe}(V > 0) = -J_{0pe} \, \mathrm{Exp} \left[\frac{-e_c V}{\kappa T_{Pe}} \right] \left(1 + \frac{e_c V_{sc}}{\kappa T_{Pe}} \right) \tag{2.12b}$$

where T_{Pe} in K, is the mean energy of the photoelectrons leaving the spacecraft surface and J_{0pe} in Am^{-2}, is the constant photoelectron current density for a spacecraft at zero potential. The photoelectron current is dependent on the surface materials of the spacecraft. Emitted photoelectrons leave the spacecraft surface isotropically with a near-Maxwellian energy distribution that has a mean energy T_{Pe} [51]. This mean energy value is computed both with space and laboratory experiments and is constant regardless of the incoming photon spectrum [54]. Table 2.4 lists a range of representative photoelectron currents (J_{0pe}) as well as the mean energy, $\mathcal{T}_{Pe}$, of emitted photoelectrons.

Table 2.4: Example photoelectron current and energy values

Source	J_{0pe} ($\mu\mathrm{Am}^{-2}$)	$\mathcal{T}_{Pe}$ (eV)
Grard [50; 51]	4-42	1.2-1.5
Whipple [170]	7.2-48	1-2
King [69]	10	4.5
Nakagawa [99]	85	2.1
DeForest [25]	8.2	-
Samir [125]	30	-

The photoelectron current is computed at a distance of 1 AU and with a impact trajectory that is normal to the surface. Grard in References [50] & [51] uses laboratory experimental data on a number of materials to compute the photoelectron currents. The resulting kinetic energy of the emitted electrons is measured to be approximately 1.5 eV. During positive charging these low energy electrons will be attracted back to the craft with no net current. Whipple in Reference [170] gives photoelectron current values for experiments simulating space conditions for a number of materialsl based on work originally performed by Feuerbacher and Fitton. DeForest in Reference [25] analyzes ATS-5 data to determine the maximum photoelectron current density. Torkar in Reference [152] presents the use of an active charge control device emitting a current of 10-50 μA to overcome the photoelectron current of the TC-1 spacecraft. Samir in Reference [125] demonstrates that the

photoelectron current on the Ariel 1 satellite was as high as 300 μAm^{-2} but reduced as a result of changing surface conditions such as outgassing.

For this study a photoelectron current of $J_{0pe} = 20$ μAm^{-2} will be used along with a mean energy $\mathcal{T}_{Pe} = 2$ eV. The photoelectron currents of Equations 2.12 can then be added to the spacecraft net current density Equation 2.9 to give:

$$J_{\text{net}}(V < 0) = J_{0e} \, \text{Exp} \left[\frac{-e_c|V|}{\kappa T_e} \right] - J_{0i} \left(1 + \frac{e_c|V|}{\kappa T_i} \right) - J_{0pe} \tag{2.13a}$$

$$J_{\text{net}}(V > 0) = J_{0e} \left(1 + \frac{e_c V}{\kappa T_e} \right) - J_{0i} \, \text{Exp} \left[\frac{-e_c V}{\kappa T_i} \right] - J_{0pe} \, \text{Exp} \left[\frac{-e_c V}{\kappa T_{Pe}} \right] \left(1 + \frac{e_c V_{sc}}{\kappa T_{Pe}} \right) \tag{2.13b}$$

With photoelectrons included, there is a equilibrium solution to this net current density equation that occurs at a slightly positive potential. The root to this equation is approximated using [54]:

$$V_{eq} \approx \frac{\kappa T_{Pe}}{e_c} \ln \left[\frac{J_{0pe}}{J_{0e}} \left(1 + \frac{e_c V_{sc}}{\kappa T_{Pe}} \right) \right] \tag{2.14}$$

and it is typical that $T_{Pe} \ll T_e$ so that the floating potential approximation can be further reduced to the value $V_{eq} \approx \kappa T_{Pe}/e_c$. With the example photoelectron energy values given in Table 2.4, this indicates that a craft in sunlight has a equilibrium potential of a few volts positive.

2.3.4 Secondary electrons and backscattered emission currents

Additional current sources of outgoing electrons are from secondary emissions and backscattering [168]. An impacting electron or ion can use its energy to induce a secondary electron to be ejected from the material, generating an outgoing electron current. The outgoing secondary electron yield, $\bar{\delta}$, can even be higher than the incoming flux [78]. An example of the yield as a function of the energy of the primary electrons striking a solar-cell coverslip material (assuming isotropic incidence and uncharged material) is shown in Figure 2.7 from Reference [68]. This secondary electron energy spectrum is approximately independent of the incoming particle energy, but will scale with the potential of the craft [35]. The secondary yield $\bar{\delta}$ is also a function of the surface material.
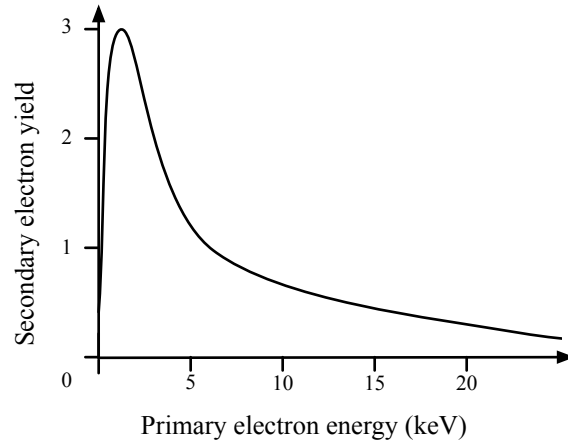
Figure 2.7: Secondary electron yield for electrons impacting solar-cell coverslip material, assuming isotropic incidence and uncharged material (Adapted from: Katz [68])

2.3.4.1   Secondary electrons

There are a number of models used to compute the curve of the secondary electron yield, such as the one shown in Figure 2.7. Sternglass developed a model that is commonly used [54; 114]:

$$\bar{\delta}(\mathcal{T},\theta) = \bar{\delta}_{\max}\frac{\mathcal{T}_e}{\mathcal{T}_{\text{eMax}}}\text{Exp}\left[2 - 2\sqrt{\frac{\mathcal{T}_e}{\mathcal{T}_{\text{eMax}}}}\right]\text{Exp}\left[2(1 - \cos\theta)\right] \tag{2.15}$$

where $\bar{\delta}_{\max}$ is the maximum yield value that occurs at an incoming electron energy of $\mathcal{T}_{\text{eMax}}$. The yield is also a function of the incoming electron angle, θ, from the surface normal. In order to compute the resulting current density the yield equation is integrated over the range of plasma electron energies. Using a Maxwellian distribution with normal incidence, Equation 2.15 can be approximated with the generic model [54]:

$$\bar{\delta}(\chi) = 7.4\bar{\delta}_{\max}\left\{\chi^3 + \frac{9}{2}\chi^2 + 2\chi - \chi^{3/2}\text{Exp}[\chi]\left(\chi^2 + 5\chi + \frac{15}{4}\right)\sqrt{\pi}\left[1 - \text{erf}\left(\sqrt{\chi}\right)\right]\right\} \tag{2.16}$$

where $\chi = \mathcal{T}_e/\mathcal{T}_{\text{eMax}}$.

A representation of typical maximum yields and the corresponding primary particle energy for spacecraft materials is given in Table 2.5 from Reference [54]. The mean energy of the secondary electron leaving the surface is typically very low, $\mathcal{T}_{\text{Se}} \approx$ 2-3 eV [35; 54; 114] and will return to a positively charged craft. The secondary electron yield from ion impacts is only larger than unity

for high primary energies (> 10 keV) [54]. Therefore modeling the secondary emissions from ions is not typically performed.

Table 2.5: Secondary electron yields and primary particle maximum energy (From: Hastings [54])

Material	$\delta_{\max}$	$\mathcal{T}_{\text{eMax}}$ (eV)
Aluminum	0.97	300
Aluminum Oxide	1.5-1.9	350-1300
Magnesium Oxide	4	400
Silicon Dioxide	2.4	400
Teflon	3	300
Kapton	2.1	150
Magnesium	0.92	250

Incorporating the yield model of Equation 2.16 to account for secondary electron emission from electron strikes the resulting net current density is:

$$J_{Se}(V < 0) = -J_{0e} \, \text{Exp} \left[\frac{-e_c|V|}{\kappa T_{\text{Se}}} \right] \bar{\delta}(\chi) \tag{2.17a}$$

$$J_{Se}(V > 0) = -J_{0e} \, \text{Exp} \left[\frac{-e_c V}{\kappa T_{\text{Se}}} \right] \left(1 + \frac{e_c V}{\kappa T_{\text{Se}}} \right) \bar{\delta}(\chi) \tag{2.17b}$$

Alternatively, a simple linear model of secondary electron currents from both ion and electron impacts suitable for GEO is given by Francis in Reference [35; 114]:

$$J_{Se}(V < 0) = -aJ_e - b|J_i| \tag{2.18a}$$

$$J_{Se}(V > 0) = 0 \tag{2.18b}$$

where $a \approx 0.4$ and $b \approx 3$ are computed from a study of ATS-5 and ATS-6 data [35]. For positive spacecraft potentials it is assumed that there is no net current influence from the emitted low energy secondary electrons that will return to the craft.

2.3.4.2 Backscattered emission

A backscattered emission occurs when an impacting particle reverses direction and leaves the surface. The backscattering of ions is very low and is omitted in this study [25; 54]. The

backscatter current is dependent on the incoming particle energy as well as the material properties. The backscatter current is typically much lower than the secondary electron yield [78] and modeling is typically performed by applying a reduction in the incoming electron current. A linear backscattering current model is:

$$J_{BSe}(V_{sc} < 0) = -cJ_e \tag{2.19a}$$

$$J_{BSe}(V_{sc} > 0) = 0 \tag{2.19b}$$

where $c \approx 0.2$ is computed from a study of ATS-5 and ATS-6 data [35]. Again, during positive charging these electrons that backscatter with lower energies are attracted back to the craft.

2.3.5   Net plasma current density

Combining all these currents produces the Hastings [54] net current density model for a spacecraft in sunlight:

$$J_{\text{net}}(V_{sc} < 0) = J_{0e} \, \text{Exp}\left[\frac{-e_c|V_{sc}|}{\kappa T_e}\right]\left\{1 - \bar{\delta}(\chi) - c\right\} - J_{0i}\left(1 + \frac{e_c|V_{sc}|}{\kappa T_i}\right) - J_{0pe} \tag{2.20a}$$

$$J_{\text{net}}(V_{sc} > 0) = J_{0e}\left(1 + \frac{e_cV_{sc}}{\kappa T_e}\right) - J_{0i}\,\text{Exp}\left[\frac{-e_cV_{sc}}{\kappa T_i}\right] - J_{0pe}\,\text{Exp}\left[\frac{-e_cV_{sc}}{\kappa T_{Pe}}\right]\left(1 + \frac{e_cV_{sc}}{\kappa T_{Pe}}\right)$$
$$- J_{0e}\,\text{Exp}\left[\frac{-e_cV_{sc}}{\kappa T_{\text{Se}}}\right]\left(1 + \frac{e_cV_{sc}}{\kappa T_{\text{Se}}}\right)\bar{\delta}(\chi) \tag{2.20b}$$

This natural plasma current model is used in this research. To compute the net current for a spacecraft in eclipse the photoelectron current is simply removed from the above expression. An alternate net current model for sunlight that uses the linear secondary currents is from Francis [35]:

$$J_{\text{net}}(V_{sc} < 0) = J_{0e}\,\text{Exp}\left[\frac{-e_c|V_{sc}|}{\kappa T_e}\right]\left\{1 - a - c\right\} - J_{0i}\left(1 + \frac{e_c|V_{sc}|}{\kappa T_i}\right)\left\{1 + b\right\} - J_{0pe} \tag{2.21a}$$

$$J_{\text{net}}(V_{sc} > 0) = J_{0e}\left(1 + \frac{e_cV_{sc}}{\kappa T_e}\right) - J_{0i}\,\text{Exp}\left[\frac{-e_cV_{sc}}{\kappa T_i}\right] - J_{0pe}\,\text{Exp}\left[\frac{-e_cV_{sc}}{\kappa T_{Pe}}\right]\left(1 + \frac{e_cV_{sc}}{\kappa T_{Pe}}\right) \tag{2.21b}$$

The spacecraft will reach a natural potential equilibrium in each of these sunlit and eclipse conditions. As there is not an easily computed analytic solution to these equations to obtain the resulting floating potential, this is demonstrated numerically in Section 2.5.3.

2.4 Double Maxwellian plasma representations and current density

While a single Maxwellian fit gives a compact approximation to the GEO plasma conditions improved modeling accuracy of the GEO plasma can be obtained with a double Maxwellian distribution [76]. As demonstrated in Figure 2.2, this fit can capture the high energy tail of the plasma [23; 42; 53]. For this reason the use of a double Maxwellian distribution is used to compute the net plasma currents and compared to the single Maxwellian representation. The summation of Maxwellian distributions can also be used to account for other plasma species populations such as Oxygen ions. The Coulomb study by King in Reference [69] uses the GEO plasma double Maxwellian fit from Hastings in Reference [53]. There are additional representations available as shown in Table 2.6. This also shows the value of the Debye length for each of the double Maxwellian plasmas, calculated using Equation 2.1.

Table 2.6: Double Maxwellian plasma parameters and Debye lengths

Source and Conditions	$\mathcal{T}_1$ (eV)	n_1 (cm^{-3})	$\mathcal{T}_2$ (eV)	n_2 (cm^{-3})	λ_D (m)
K-Hastings [53] (ATS-5 Nominal)					
electrons	277	0.578	7040	0.215	124
ions	300	0.437	14000	0.355	
L-Hastings [53] (SCATHA Nominal)					
electrons	550	0.78	8680	0.31	170
ions	800	0.36	15800	0.73	
M-Hastings [53] (SCATHA Storm)					
electrons	600	1.8	25500	3.3	80
ions	350	1.92	25100	3.17	
N-Garrett [42] (ATS-5 Storm)					
electrons	250	2	20000	0.04	59

Data set M represents a storm spike, where the GEO environment experiences a high density injection of highly energetic particles. This is a particular concern for spacecraft charging, however is of minimal concern to the CFF concept. Similarly, data set N is a representation developed by Garrett based on ATS-5 measurements to capture variations from injection events also. The Debye length for the data set N is computed using the electron only formula of Equation 2.3.

Another advantage of using a double Maxwellian representation is that it allows for analysis of high energy charging affects and the presence of multiple equilibrium roots to the net current equation [23]. Charging conditions in a single Maxwellian are independent of electron density, however are captured with the double Maxwellian fit [76]. The net current to the node, including photoelectrons, secondary and backscattering models is:

$$J_{\text{net}}(V_{sc} < 0) = \sum_{k=1}^{2} \left\{ \left| J_{0e_k} \ \text{Exp} \left[\frac{-e_c|V_{sc}|}{\kappa T_{e_k}} \right] \left[1 - \bar{\delta}(\chi) - c \right] - J_{0i_k} \left(1 + \frac{e_c|V_{sc}|}{\kappa T_{i_k}} \right) \right| \right\}$$
$$- J_{0pe} \quad (2.22\text{a})$$

$$J_{\text{net}}(V_{sc} > 0) =$$
$$\sum_{k=1}^{2} \left\{ J_{0e_k} \left(1 + \frac{e_c V_{sc}}{\kappa T_{e_k}} - \text{Exp} \left[\frac{-e_c V_{sc}}{\kappa T_{\text{Se}}} \right] \left[1 + \frac{e_c V_{sc}}{\kappa T_{\text{Se}}} \right] \bar{\delta}(\chi) \right) - J_{0i_k} \ \text{Exp} \left[\frac{-e_c V_{sc}}{\kappa T_i} \right] \right\}$$
$$- J_{0pe} \ \text{Exp} \left[\frac{-e_c V_{sc}}{\kappa T_{Pe}} \right] \left(1 + \frac{e_c V_{sc}}{\kappa T_{Pe}} \right) \quad (2.22\text{b})$$

The net current model developed here is for a double Maxwellian, however it is can be applied to a summation of any number of Maxwellian distributions of varying species making it suitable for LEO studies also.

2.5 Numerically computing plasma currents

The current density equations developed in this chapter are used to evaluate the net current to a charged spacecraft. This is numerically computed for each of the GEO plasmas given in Table 2.3. The LEO plasma currents are not computed in this research, however the same analysis techniques apply, with some additions. A spacecraft in LEO is traveling faster than the ambient plasma and consequently bombards charged particles inducing an additional current source. There are also differential charging and wake effects that require inclusion in the model. In both a GEO or LEO analysis it is also beneficial to model the finite shape, materials and attitude of the craft

as this will effect the plasma interaction. For the purposes of this research these effects are not necessary and omitted.

2.5.1   Dominant charging currents

The primary plasma currents to a spacecraft operating at a given potential in each of the GEO environments is computed. The range of spacecraft potentials used in this analysis is -30 kV to 30 kV. This is a reasonable potential range that is anticipated for CFF operations at GEO, can be achieved with current technology and has been demonstrated on-orbit [69]. The currents impacting the spacecraft during the quiet plasma conditions ($\lambda_D = 4$ m) are shown in Figure 2.8.
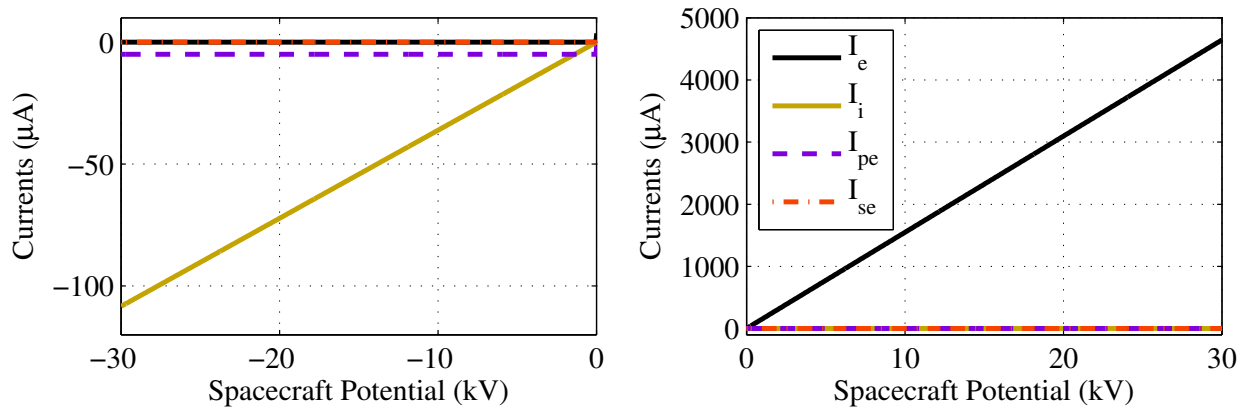
Figure 2.8: Current flows to 1 m^2 spacecraft during quiet plasma conditions, $\lambda_D = 4$ m (worst-case)

The currents are shown for a single spherical craft of 0.282 m radius. This is a reasonable size for a small formation flight spacecraft. Also, with a resulting surface area of 1 m^2 the current density and net current to craft are the same for all but the photoelectrons. This size craft is chosen as it allows easy linear scaling to craft of different sizes or when considering more than one craft. In this cold and dense plasma a negatively charged spacecraft will attract a current of ions. During positive charging electrons will be attracted to the craft and the relative ion current is zero.

The plasma currents for nominal conditions ($\lambda_D = 200$ m) is shown in Figure 2.9. In this plasma, the dominant current for a negatively charged spacecraft are the escaping photoelectrons, $I_{Pe} \approx 4$ μA. For a positively charged spacecraft the electron current bombardment dominates both

the ion current and the low energy photoelectrons that are attracted back to the craft.
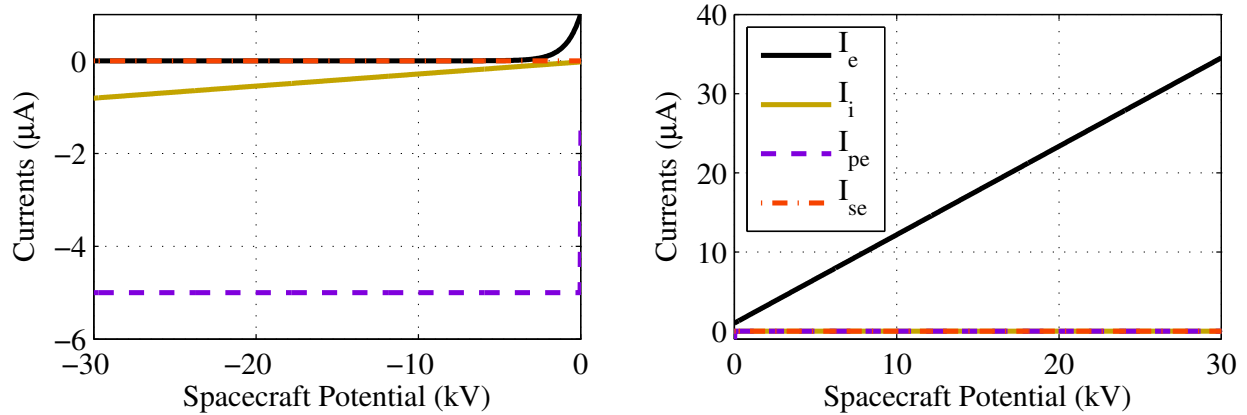
Figure 2.9: Current flows to 1 m^2 spacecraft during nominal plasma conditions, $\lambda_D = 200$ m

The plasma currents for the hotter and sparser disturbed plasma conditions ($\lambda_D = 743$ m) is shown in Figure 2.10. The dominant current for negative charge is the escaping photoelectrons while a positive charge has a dominant electron current bombardment.
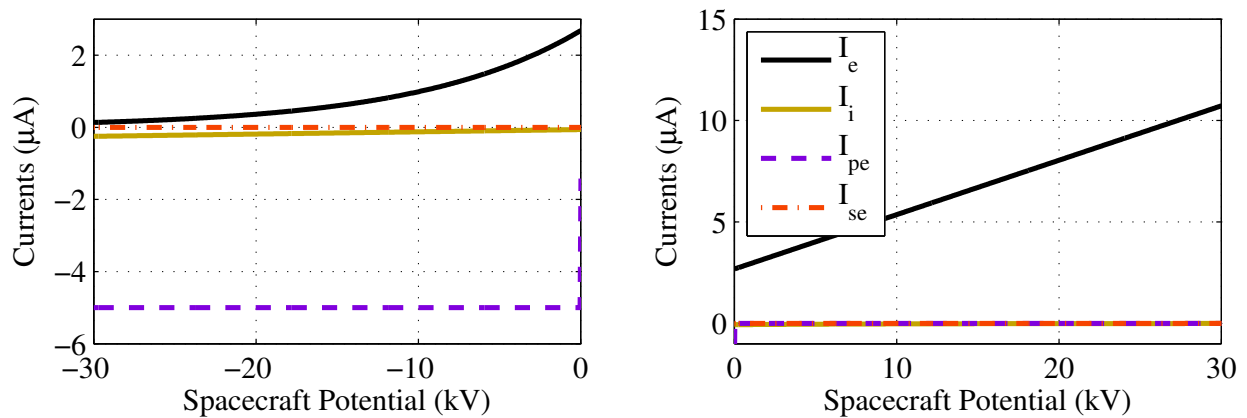
Figure 2.10: Current flows to 1 m^2 spacecraft during disturbed plasma conditions, $\lambda_D = 743$ m

The consequence of these resulting charging schemes in all environments is that to maintain a negative spacecraft potential it is necessary to emit ions to compensate for either the ion impacts and/or escaping photoelectrons. Alternatively, to maintain a positive spacecraft potential electrons are emitted to compensate for the impacting electrons from the plasma. It is also found that in all

operating plasmas the secondary and backscattered electrons have much lower current magnitudes than the dominant primary currents.

2.5.2   Net plasma current

Each contributing plasma current is summated to compute the net plasma current to a craft that holds a fixed potential. This resulting current profile indicates the equilibrium potential each craft will reach in each plasma environment. The net current flow to a spacecraft that is in eclipse (no photoelectrons) is shown in Figure 2.11 for each of the plasma conditions. The maximum net current occurs in a quiet plasma for a positively charged spacecraft.
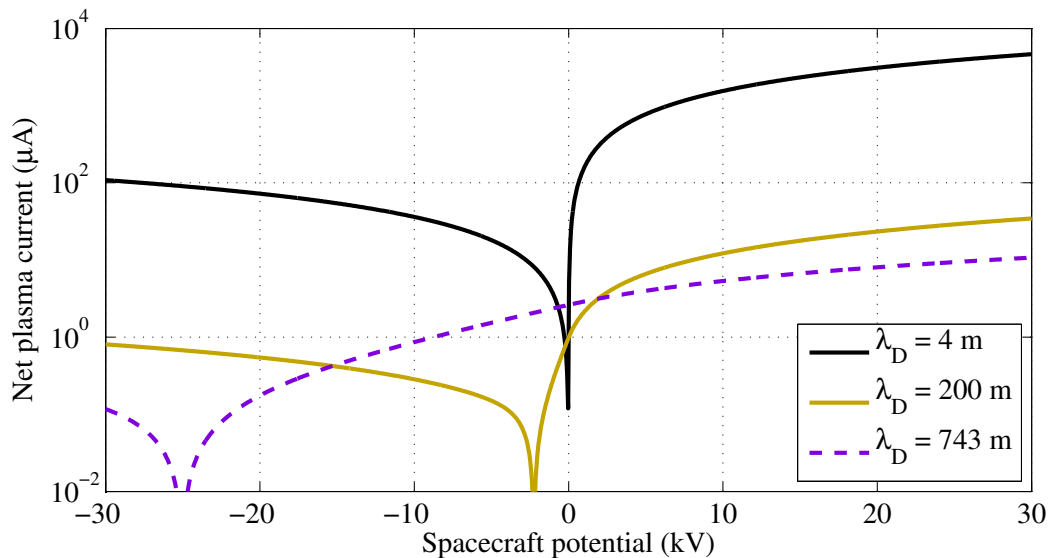
Figure 2.11: Net current flow to 1 m^2 spacecraft in eclipse for each plasma

The net current flow to a spacecraft that is in sunlight (includes photoelectron current) is shown in Figure 2.12, for each of the plasma conditions. The addition of the photoelectron current has minimal affect on the quiet plasma ($\lambda_D = 4$ m) however does contribute to a negatively charged craft in the nominal and disturbed plasmas as shown in Figures 2.9 & 2.10.

The net current flow for each of the double Maxwellian models (Table 2.6) is computed and compared to the single Maxwellian distribution for nominal conditions ($\lambda_D = 200$ m) and shown in Figure 2.13. As demonstrated the double Maxwellian distributions have similar net currents as the
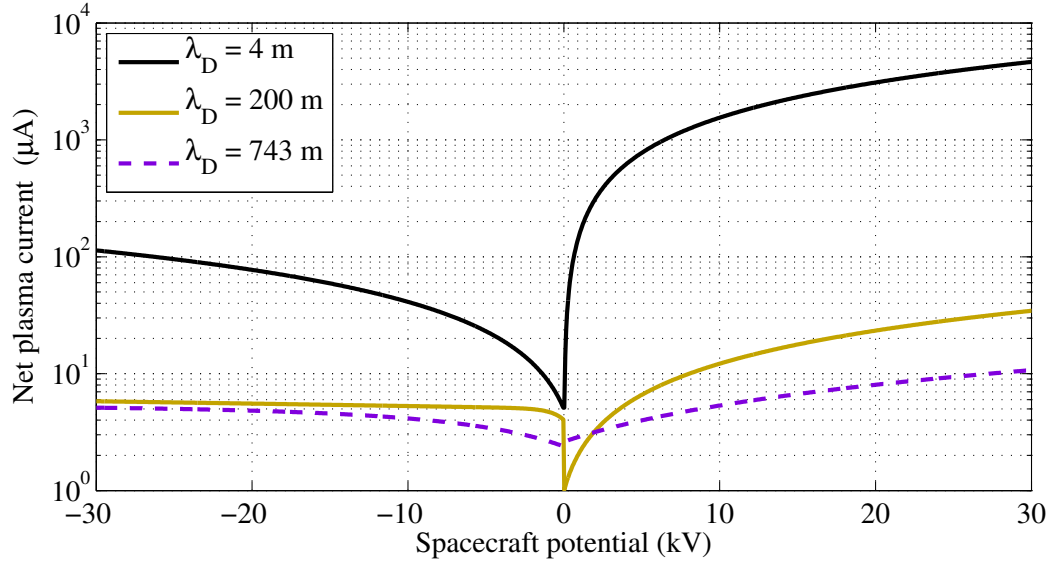
Figure 2.12: Net current flow to 1 m^2 spacecraft in sun light for each plasma

single Maxwellian distribution. One notable difference is the location of the zero current condition (equilibrium potential). The high density and temperature storm spike of data set M increases the net current by approximately a half order of magnitude. However, this magnitude is still below the predicted plasma current of the quiet plasma ($\lambda_D = 4$ m), which is modeled to be the absolute worst case GEO conditions for CFF and bound all feasible operating regimes such as this storm spike. During sunlit conditions the primary currents are near identical, and therefore not shown, as the dominant current during negative charging is the photoelectrons.

2.5.3   Plasma equilibrium currents and floating potentials

The low magnitude dips in the net current flow (Figures 2.11, 2.12 and 2.13) correspond to natural equilibrium conditions where $I_{\text{net}} = 0$. The location of this root occurs at the spacecraft floating potential. These potentials are computed assuming there is no effect from magnetic fields or dielectric barrier fields restricting the escaping photoelectrons [54]. This is a good assumption for a proposed CFF craft given that the outer surface will be conductive to distribute charge removing any differential charging effects that are seen with dielectrics [54].
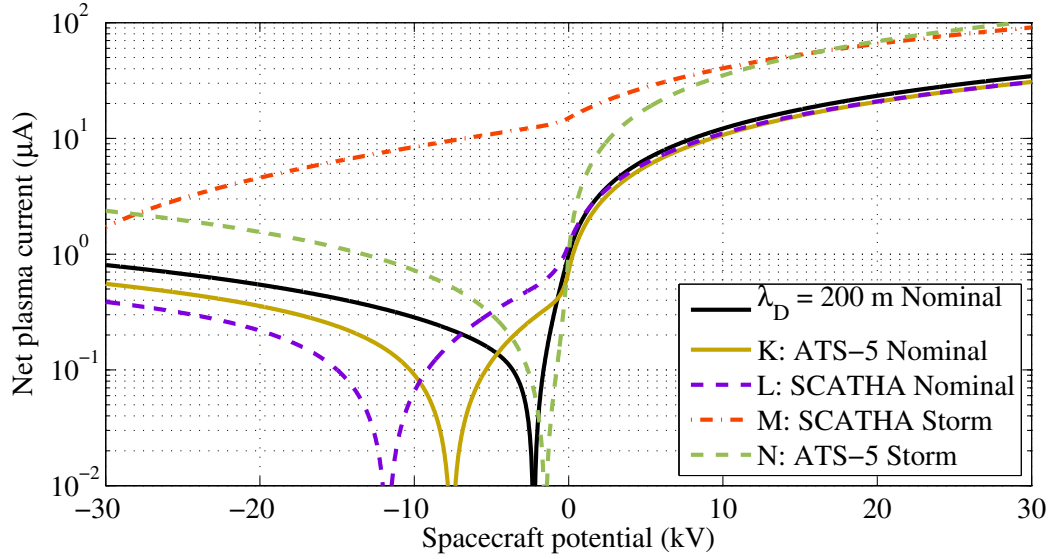
Figure 2.13: Net current flow to spacecraft during eclipse for single and double Maxwellian

For a single Maxwellian plasma there is a single root to the net current equation and consequently a sole equilibrium condition. At GEO this solution will typically produce a spacecraft floating potential that is slightly negative for sun-lit conditions and can go highly negative during eclipse. The single Maxwellian floating potentials are shown in Table 2.7 for each of the plasma environment conditions studied here. These equilibria are advantageous to the CFF concept that can utilize these naturally occurring spacecraft potentials for force production. The double Maxwellian floating potentials for these plasmas and ranges of potentials studied are also shown in Table 2.7.

Table 2.7: Spacecraft equilibrium floating potentials for each plasma condition

Conditions	Eclipse (V)	Sun-lit (V)
Quiet ($\lambda_D = 4$ m)	-8	5.3
Nominal ($\lambda_D = 200$ m)	-2250	6.0
Disturbed ($\lambda_D = 743$ m)	-25000	3.2
K-Hastings [53] (ATS-5 Nominal)	-7500	6.9
L-Hastings [53] (SCATHA Nominal)	-11700	5.5
M-Hastings [53] (SCATHA Storm Spike)	-37600	-18500
N-Garrett [42] (ATS-5 Storm)	-1500	14

It is also possible to have multiple roots (and floating potential solutions) with the inclusion of additional plasma currents. Using a single Maxwellian plasma that includes secondary electron currents produces two roots that are a function of the plasma electron temperature and the material properties. The low temperature plasma root is typically not experienced at GEO [54]. As the plasma temperature increases to the second root (critical temperature) the spacecraft will go from slight positive charge to high negative potentials [41; 54]. This occurs in eclipse with no photoelectrons and is a potentially hazardous scenario for a CFF application as the nodes could abruptly change charge polarity and magnitude losing required control forces.

A double Maxwellian is also more accurate in representing a GEO spacecrafts floating potential characteristics as it allows for multiple equilibrium roots to the net current equation. With a double Maxwellian plasma it is possible to have one, two or three roots depending on the plasma conditions. The low energy plasma determines the number of roots and the respective spacecraft charge [54]. For a double Maxwellian representation, the domains of the plasma conditions that lead to multiple equilibrium roots are developed by Lai in Reference [77] and shown in Figure 2.14.

This is a concern for spacecraft operators as the plasma conditions are always changing and consequently the potential equilibrium root varies also. A changing plasma represented as a single Maxwellian results in the spacecraft floating potential to change continuously and smoothly. With the presence of a triple root represented with a double Maxwellian it is possible that the spacecraft potential can abruptly jump between roots [76; 77]. Olsen in Reference [104] correlates abrupt on-orbit charging characteristics of the highly elliptic International Sun Earth Explorer spacecraft in 1978 to this triple root phenomena.

2.6   Active charge control in space

The fundamentals of natural spacecraft charging are presented. To bring the developments of Coulomb formation flight closer to implementation on a space bound mission, an understanding of active spacecraft charging is imperative. Natural spacecraft charging can be regulated or enhanced with a charge emission device. There are numerous missions past and present that have utilized
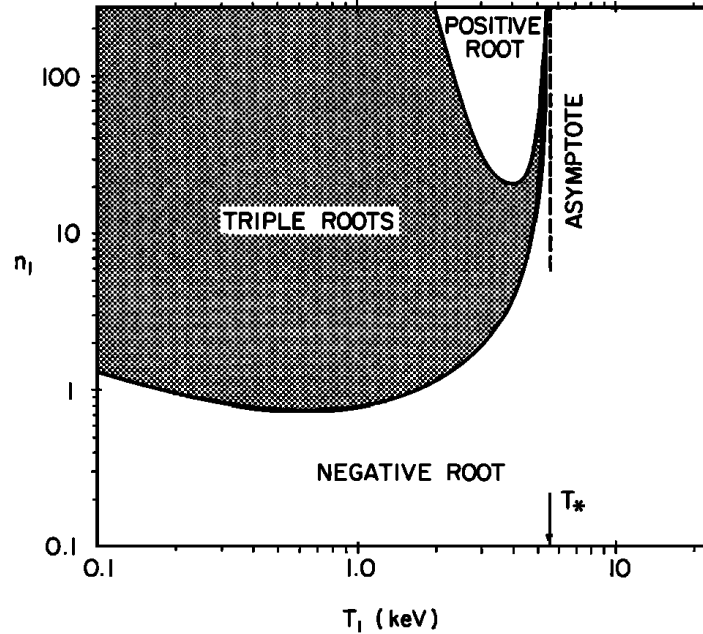
Fig. 4. Parametric domains for copper-beryllium. Incoming electrons are assumed isotropic.

Figure 2.14: Plasma conditions represented with double Maxwellian distributions and the resulting spacecraft potential equilibrium roots (From Lai in Reference [77])

hardware for active charge control in both LEO and GEO. In this Chapter a review of existing and planned spacecraft featuring charge control devices are presented. Charge control hardware technologies for both positive and negative charging are given with detailed descriptions of the capabilities including currents, mass flow rates, and system mass, size, and power needs.

2.6.1 LEO charging missions

The dense plasma of the LEO environment typically prevents naturally spacecraft charging but this also places limits on the capabilities of onboard electrical systems. Ferguson in Reference [33] provides design guidelines for the operation of high-voltage (>55 V) space power systems at LEO. The ISS operates at a potential difference across its solar arrays of 160 V. The primary driver for voltage buses as high as this is to reduce cable thickness and ultimately mass for equivalent power losses. Another advantage is when high voltage is required for a particular instrument

bias or a electric propulsion system. Having a direct high voltage (that can come from varying the solar arrays in series/parallel format) reduces the need for high mass power conversion systems.

There is a heightened concern for arcing at LEO. It is possible to arc from a voltage as low as -50 V to either an adjacent conductor or to the plasma itself [33]. Negative charging in LEO also leads to ion bombardment, sputtering and potentially chemical attack due to the presence of atomic oxygen. Negative grounding is commonly done and results in negative charging with respect to the plasma. The ISS naturally 'floats' to around -140 V, which is beyond the dielectric strength of anodized coatings. It is therefore necessary to use an artificial charging current to adjust the floating potential relative to the plasma. The ISS uses the Plasma Contactor Unit (PCU), charge control device, for this purpose.

The ISS PCU emits a current that generates a local Xenon plasma plume. The plume can have a radius as large as 8 m before its density is less than the ambient plasma. The PCU essentially uses this plasma cloud to ground the ISS to the local plasma. Electron currents as large as 10 A are possible with this device [33].

A miniaturized current collection device that operated on a CubeSat project is an alternate method of performing charge control. The Naval Research Laboratory miniaturized electrodynamic experiment is flying on the Calpoly CP-6 spacecraft to measure the collection of electrons from the LEO plasma. At the end of a 1.1 m insulated tape is a tungsten wire that is heated through electric resistance and used to emit electrons. Two collector tapes are then uncoiled and used to collect electrons from the plasma [2].

Through intended design and with the use of a charge emission devices charging at LEO can be safely managed and controlled. Although suffering technical issues, the SPEAR-I mission demonstrated that charging beyond 40 kV is possible in the dense plasma of LEO [66; 121].

2.6.2   GEO charging missions

Charge control devices have been proven in space and are commonly used on GEO spacecraft. The devices typically use one of two technologies, being either the emission of noble gas ions with

hollow cathodes or the field emission technique using metal ions. The proposed CFF spacecraft would use these charge emission devices. An overview of these technologies and their space missions is given here.

The emission of electrons can be used to drive the spacecraft to positive potentials. Electron guns are used on GEO spacecraft for charge control [12]. This technique does however suffer from the space-charge limit when neutralizing a charged craft. Particularly on spacecraft with insulative surfaces the combination of ion and electron emission is most effective as it creates a plume to ground the craft [12; 103].

The ATS-5 spacecraft used a hot wire filament for electron emission [94]. Purvis, demonstrates that the on-orbit use of ATS-5 electron emission reduced spacecraft potential magnitudes, but ground levels were not reached [116]. The ATS-6 mission reduced equilibrium potentials of hundred of volts negative to near zero as well as reduce insulator potentials with the use of a plasma emitter of ions and electrons with a plasma bridge neutralizer. During eclipse this experiment was shown to discharge kilovolt level potentials [94; 101].

2.6.3 Charge control hardware

Previously, Figures 2.11 and 2.12 demonstrate that from a power perspective it is more advantageous to charge to negative potentials. Natural negative equilibrium potentials can be utilized, requiring less current and power to reach kilovolt-level potential magnitudes. Another consideration is the technology required for charge control. The technology for electron emission (positive charging) is less complex and electrons can be obtained from solar energy. For negative charging, the use of hollow cathodes or field emission technology is envisioned and an overview of these devices and their requirements and capabilities is given here.

2.6.3.1 Hollow cathode emission

Hollow cathode emission uses an electric field to bombard a noble gas with electrons, causing ion generation. The ions are consequently accelerated away from the spacecraft, generating a

charging current. Typical gases are Argon, Krypton or Xenon that are typically stored in tanks up to 1000 psi [27]. Table 2.8 gives a summary of hollow cathode technologies used on space missions or currently available.

Table 2.8: Examples of hollow cathode space technology

Mission and reference	Technology description
SCATHA [75]	Electron gun and Xenon ion beam for positive and negative charging.
ISS [86; 149]	Features a plasma contactor to prevent large structure charging in LEO. It features an electron emitter based on FEEP neutralizer technology. ISS unit mass is 21 kg and uses an idle power of 80 W, peak 180 W. A similar unit with 5 kg mass and 5 W idle, 10 W peak also developed.
ProSEDS [3]	Was intended to be launched in 2003 to test an electrodynamic tether.[3] Stores 245 g of Xenon gas at 8-10 MPa in 0.3 L volume. Emission currents of 0-10 A. At 10 A gas consumed at 0.2 mgs^{-1}. The system is 20x30x13 cm in size and weighs 6 kg with a 30 W operating power. A smaller version <1 A max output weighs 5.6 kg and operates on 5 W.
POLAR [152]	Emits Xenon plasma to obtain operating potentials as low as 1.8 V relative to plasma.
-	In 2000, a "state of the art" system was considered a 8 W system with Xenon emitted at 100 mA at a rate of 0.1 mgs^{-1} [85].

2.6.3.2   Field emission

Field emission with metal ions is an alternate technique to generate a charging current in space. Field emission devices emit ions from a needle apex that are extracted from a liquid source using field evaporation. Table 2.9 gives a summary of field emission technologies used on space missions.

2.7   Summary

The interaction between a spacecraft and its local plasma environment is explored in this chapter. Spacecraft charging is a natural occurrence that does not pose a concern to suitably designed craft and for the CFF concept these potentials can be exploited. Models of the GEO plasma environment, developed from on-orbit measurements, are utilized to compute net currents

Table 2.9: Examples of field emission space technology

Mission and reference	Technology description
ATS - 6 [27; 94; 101; 142]	Uses Xenon neutralizing current >1 mA at energies < 50 eV. Total instrument mass with plasma measurement devices is 19 kg. Total power of 28 W, storing Xenon gas at 800 psi in a 2 L tank. Also featured two Caesium attitude thrusters that were shown to neutralize charging. Ions accelerated under the magnetoelectrostatic concept with an emission current of 0.115 A at 550 eV.
ATS - 5 [94; 102]	Caesium ion engine capable of 1 mA of singly charged ions also provides neutralizing electrons from a hot filament source
Cluster [119; 154]	Indium ion emitter with feedback control to maintain zero potential relative to the environment. Emission currents of 10-15 μA at energies of 5-8 keV. Liquid indium is kept at 520 K (247 °C) with an instrument mass of 1.85 kg and total power < 2.7 W. Only a ion emission source is used as spacecraft is always in sunlight.
Geotail [132; 153; 155]	Two instruments each containing 4 Indium ion emitters, with a mass of 1.8 kg, measuring 19 x 16 x 17 cm. Ion current of $\approx$ 15 μA at $\approx$ 6 keV with a beam divergence less than 30 degrees. Electrodes operate at $\approx$ 6 kV with a heater power of 0.55 W.
Equator-S [153; 155]	Indium ion emitter inherited from Geotail and Cluster and designed as test for Cluster-II. Instrument mass of 2.7 kg and max power of 2.7 W, with max potential of 8.3 kV. Heaters take 15 mins to heat Indium from 200 mg reservoir to operating liquid temperatures.
Double Star (TC-1) [151; 152]	Improved version of Cluster Indium ion instrument. A potential of 4-9 kV emits ions between 10-50 μA. Instrument mass is 2.54 kg, max power is 2.9 W and operational life is extended to 16000 hr.

and spacecraft floating potentials. This is important to the CFF research as it defines the operating plasma environments and their effects on Coulomb forces as investigated in the following chapter. These net charging currents are also useful for computing power requirements for CFF applications such as the tethered Coulomb structure.

Given the natural charge levels that arise at GEO, an active charge control device is a common and often necessary component. The hardware for fast and accurate potential control,

both positive and negative, is space proven technology. In addition, the capabilities of systems meet the requirements for implementation on a Coulomb controlled formation.

Chapter 3

Coulomb force modeling

This dissertation research is reliant on the modeling of Coulomb forces. The Coulomb force model, both space-based and terrestrial, is pivotal for realistic simulations of spacecraft dynamics and predicting electrostatic actuation on the testbed. In this chapter analytic models for computing Coulomb force between charged spheres are developed. It begins with the force between two point charges in a vacuum and culminates with a proposed approximate model of finite spheres in close proximity in a plasma, including contributions from position dependent combined system capacitance and uneven charge distribution.

3.1   Coulomb force modeling in a vacuum

The fundamentals of Coulomb force production between charged bodies is investigated in the isolation of a vacuum. This is advantageous as it isolates the force to be purely between the charged bodies allowing analytic expression to be used. These vacuum representations provide the foundation for modeling in more complex and realistic environments such as terrestrial and plasma.

3.1.1   Force between point charges

Consider a infinitesimally small point charge $q = 1.602 \times 10^{-19}$ C. In a vacuum and in isolation the electrostatic field $\boldsymbol{E}$, that surrounds this charge is given by

$$\boldsymbol{E}(r) = k_c \frac{q}{r^2} \hat{r} \tag{3.1}$$

where $k_c = 8.99 \times 10^9 \text{ Nm}^2\text{C}^{-2}$ is the vacuum Coulomb constant, and $\boldsymbol{r}$ is the relative position vector from the point charge. In non-charged air (absence of charged particles) the Coulomb constant k_c is scaled, accounting for the relative permittivity of air. However this is a small adjustment as the relativity permittivity of air to vacuum is 1.00054. The E-field strength for this isolated point charge is isotropic and computed with

$$E(r) = k_c \frac{q}{r^2} \tag{3.2}$$

If a second, infinitesimal point charge is placed in this unperturbed E-field then the resulting Coulomb force magnitude is

$$F = E \cdot q \tag{3.3}$$

If the second charge q_B is placed at a distance d in the E-field of charge q_A, the resulting electrostatic force magnitude is the well known Coulomb's Law:

$$F = k_c \frac{q_A q_B}{d^2} \tag{3.4}$$

This Coulomb force is an equal and opposite force acting on each charge always along the charge center line-of-sight.

3.1.2 Force between sphere and point charge

Consider now that charge A is on a finite sphere of radius R_A. In a vacuum and in isolation the potential on the surface of this sphere is represented by the equation:

$$V_A = k_c \frac{q_A}{R_A} \tag{3.5}$$

At a radial distance from the center of the sphere ($r \geq R$), the potential field strength from this isolated charge is:

$$\Phi(r) = k_c \frac{q_A}{r} = \frac{V_A R_A}{r} \tag{3.6}$$

The E-field strength of this charge is then:

$$E(r) = -\nabla_r \Phi(r) = \frac{\Phi(r)}{r} = k_c \frac{q_A}{r^2} = \frac{V_A R_A}{r^2} \tag{3.7}$$

If an infinitesimally small point charge, q_B is placed in this E-field at a distance d, the Coulomb force magnitude felt by both the point charge and the sphere is:

$$F = E(r = d) \cdot q_B = k_c \frac{q_A q_B}{d^2} = \frac{V_A R_A}{d^2} q_B \tag{3.8}$$

Here the charge q_B is infinitesimally small so that it has no radius and hence no potential. Given this, the charge has no effect on the overall charge on the sphere q_A, except that a force is exerted.

For the Coulomb formation flight concept development, the potential of the bodies is fixed rather than the charge. From an application standpoint this is advantageous. A body with an entire conductive outer material will be equipotential and therefore more readily measurable than computing the entire charge on the body.

3.1.3 Force between finite spheres

Consider now two charged bodies with finite dimensions (spheres) in close proximity. It is essential to consider the overlapping potential fields and model the consequent effects on the combined system capacitance as well as any uneven charge distribution that occurs on the surface of the conducting spheres that are held at a fixed potentials. Both of these charge effects are described and modeled for the vacuum implementation in this section.

3.1.3.1 Position dependent, combined system capacitance

The overlapping potential fields will raise or lower the effective potential of each body and consequently the Coulomb force between them. This is demonstrated graphically in Figure 3.1 for both the repulsive and attractive force case. The resulting change in capacitance and consequently force can be significant at kilovolt level potentials when the centre-to-centre separation is comparable to the sphere radii (separations less than approximately 10 sphere radii, $r < 10R$). For fixed charge magnitudes, the total potential at the location of sphere A is computed by combining the potential due to its own charge Equation 3.5 as well as the potential field from the charge of sphere
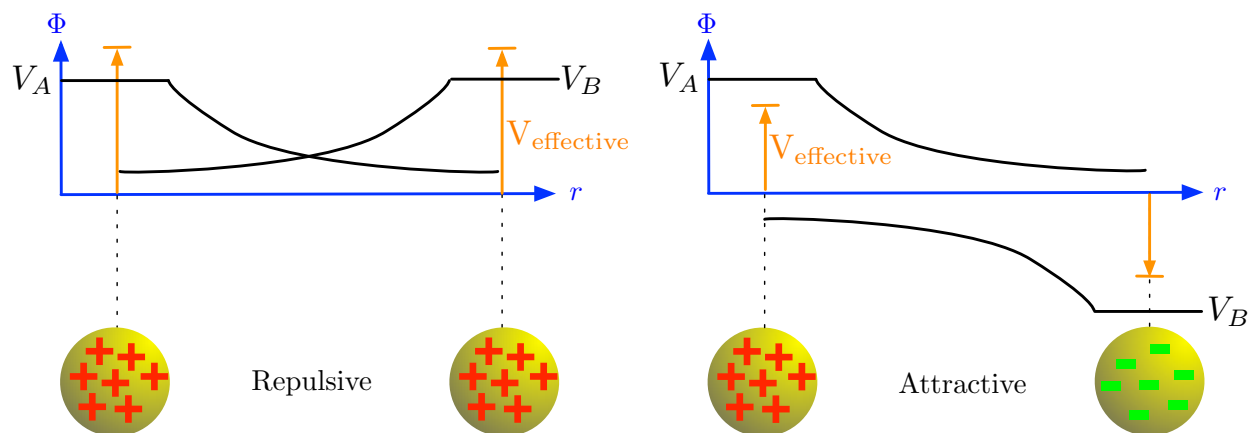
Figure 3.1: Potential fields for two charged spheres in close proximity

B in Equation 3.6 to give:

$$V_A = k_c \frac{q_A}{R_A} + k_c \frac{q_B}{d} \tag{3.9}$$

where d is the is the center to center separation of the bodies. This does assume the potential field of sphere B about the center of sphere A is reasonably flat (i.e. linear in radial distance). This potential is similarly computed for Sphere B to produce a set of equations represented in matrix form:

$$\begin{bmatrix} V_A \\ V_B \end{bmatrix} = k_c \begin{bmatrix} 1/R_A & 1/d \\ 1/d & 1/R_B \end{bmatrix} \begin{bmatrix} q_A \\ q_B \end{bmatrix} \tag{3.10}$$

For the studies conducted here and implementation on the testbed the potentials of the bodies are constrained to (V_A & V_B) and consequently the effective charge is adjusted. This is calculated by inverting the equation to the form:

$$\begin{bmatrix} \hat{q}_A \\ \hat{q}_B \end{bmatrix} = \underbrace{\frac{d}{k_c(d^2 - R_A R_B)} \begin{bmatrix} dR_A & -R_A R_B \\ -R_A R_B & dR_B \end{bmatrix}}_{C_V} \begin{bmatrix} V_A \\ V_B \end{bmatrix} \tag{3.11}$$

where C_V is the capacitance of the combined charged system in a vacuum. This set of equations is expandable to N number of charged bodies of both positive and negative potentials. This leads to

solving the effective charge solutions $\hat{q}_i$:

$$\hat{q}_A = \frac{dR_A(dV_A - R_BV_B)}{k_c(d^2 - R_AR_B)} \tag{3.12}$$

$$\hat{q}_B = \frac{dR_B(dV_B - R_AV_A)}{k_c(d^2 - R_AR_B)} \tag{3.13}$$

The effective charge solution $\hat{q}_i$ is then substituted into Equation 3.4 to compute the Coulomb force between the spheres with surface potentials V_A & V_B:

$$F = k_c\frac{\hat{q}_A\hat{q}_B}{d^2} \tag{3.14}$$

In order to compute the Coulomb force using Equation 3.4 the potential fields assuming no effect from the second sphere are used. However, the presence of the second charge is accounted for with the position dependent system capacitance and the net effect on the charges used to compute the force.

Note that if the signs of V_A and V_B differ, then the amount of charge that is stored on each sphere is actually increased by the presence of a 2nd charged sphere and the attractive force is enhanced. If the potential sign is the same, then the amount of charge and the repulsive force is reduced.

3.1.3.2   Uneven charge distribution

Another physical electrostatic parameter that occurs during close proximities is uneven charge distribution, also known as induced charge effects. With spheres fixed at desired potentials the charges will distribute on the surface to obtain this potential. In very close proximities, separations less than approximately five sphere radii, $(d < 5R)$, the Coulomb forces between individual charges can cause uneven distribution on the conductive surface [145]. This is graphically demonstrated in exaggerated form in Figure 3.2.

Given that the testbed spheres operate in close proximities these effects are included in the Coulomb force model. Under these induced circumstances the summation of charges to a point at the sphere center with a separation of d no longer provides an accurate calculation of force using Equation 3.4. Two methods for computing induced charge affects are investigated and compared.

Figure 3.2: Graphical interpretation of uneven charge distribution on spheres in close proximity

Electrostatic method of images. One method of accounting for close sphere induced effects is by representing the spheres charge with an infinite series of charges computed using the method of images [145; 21; 118; 144; 143]. This method is based on the principle of mirroring charge across a conducting plane. Figure 3.3 is an example that highlights the principles of electrostatic method of images. Separately, spheres A and B have a known potential that can be modeled as a respective charge q_A and q_B located at sphere centre; however, at close separations a redistribution of charge occurs. This is modeled with a series of charges q_n, of decreasing magnitude, at increasing separations r_n, from the sphere center.
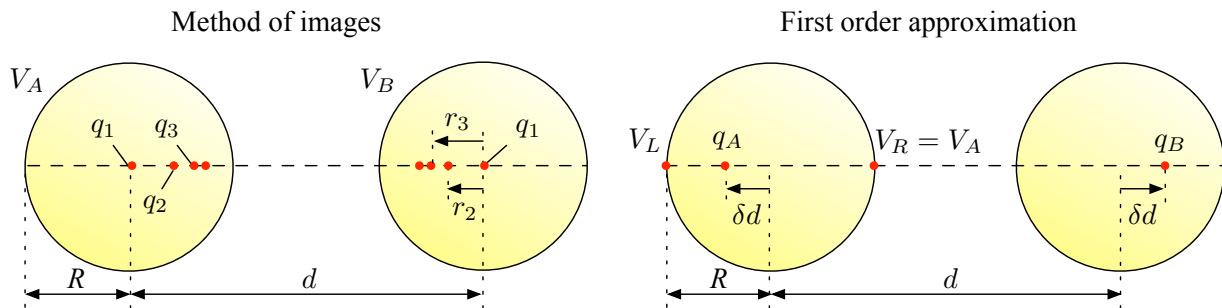
Figure 3.3: Graphical representation of two methods to model uneven charge distribution for close spheres

The values of q_n are computed for spheres of equivalent potential and polarity (repulsive force) using:

$$q_n = -\frac{q_{n-1}}{d/R - r_{n-1}} \tag{3.15}$$

where $n > 1$, $q_1 = q_A$ and $r_1 = 0$ and assumes $R_A = R_B$. The repulsive induced effects result in an overall reduced net Coulomb force. For spheres of equivalent potential but opposite polarity

(attractive force), Equation 3.15 is modified with a positive sign. In this situation, all charges are of the same polarity, increasing the effective Coulomb force. For both repulsive and attractive force model developments it is assumed that the potential magnitude (and consequently charge magnitudes) are equal on each sphere $|V_A| = |V_B|$. The distance of each charge from the sphere center d_i is computed as a value normalized with the radius using:

$$r_n = \frac{1}{d/R - r_{n-1}} \tag{3.16}$$

where $n > 1$ and $r_n = d_n/R$. The ratio of charges, Equation 3.15, and normalized distances, Equation 3.16, are numerically computed for a finite series of M terms. For the geometries and charges used in this dissertation, a series of 20 terms is accurate. Finally, each charge value q_n may require linearly scaling so that the total charge on each sphere is equal to the effective sphere charge

$$\hat{q} = \sum_{n=1}^{M} q_n$$

computed earlier with position dependent capacitance. The normalized distances are converted to absolute distances by multiplying by the sphere radius. The net Coulomb force on the spheres is then computed by summating the force between each individual charge from both spheres based on Equation 3.4:

$$F = k_c \sum_{i=1}^{M} \left[\sum_{j=1}^{M} \frac{q_i q_j}{(d - Rx_i - Rx_j)^2} \right] \tag{3.17}$$

First order approximation.   An alternate model for uneven charge distribution is the first order approximation demonstrated graphically in Figure 3.3. This model shifts the position of each of the original charges from the sphere centre by an offset (δd). The resulting effective separation between the charges accounts for uneven charge distribution. It is shown in Figure 3.3 the setup for spheres of equivalent potential and polarity (repulsive force), however a similar approach is used for the attractive force case. Again, for both repulsive and attractive forces it is assumed that the potential magnitude (and consequently charge magnitudes) are equal on each sphere, $|V_A| = |V_B|$.

The model computes the separation offset for a each sphere by arranging Equation 3.9 given the potential at all positions on each sphere is equal (V_L and V_R) to produce the set of equations:

$$V_L = \frac{k_c q_A}{R_A - \delta d} + \frac{k_c q_B}{d + R + \delta d} \tag{3.18}$$

$$V_A = \frac{k_c q_A}{R_A + \delta d} + \frac{k_c q_B}{d - R + \delta d} \tag{3.19}$$

Combining these two potentials gives the equation:

$$\frac{1}{R - \delta d} + \frac{1}{d + R + \delta d} = \frac{1}{R + \delta d} + \frac{1}{d - R + \delta d} \tag{3.20}$$

which is rearranged to produce a cubic equation in δd that is analytically solved. The solution selected is the positive and real distance solution that is:

$$\delta d_{\text{repulse}} = \text{Real}\left[\frac{1}{12}\left\{ -4R + 8d - \frac{4(-2)^{1/3}(-2R + d)^2}{\Upsilon_r} - 2(-2)^{2/3}\Upsilon_r \right\}\right] \tag{3.21}$$

where

$$\Upsilon_r = \left((2R - d)\left(8R^2 + 19Rd + 2d^2\right) + 3\sqrt{3}\sqrt{Rd(-2R + d)^2\left(16R^2 + 11Rd + 4d^2\right)} \right)^{1/3}$$

Numerically computing this solution over the range of testbed separations produces a small imaginary component (16 orders of magnitude less than distance value) and is omitted. This solution is then added to the original separation to give the effective separation for repulsive forces:

$$\bar{d} = d + 2\delta d_{\text{repulse}} \tag{3.22}$$

Similarly the same procedure is applied to the attractive force case where the spheres have equivalent potential but opposite polarity. The resulting separation offset solution is:

$$\delta d_{\text{attract}} = \text{Real}\left[\frac{1}{12}\left\{ -4(2d + R) + \frac{4(-2)^{1/3}(d + 2R)^2}{\Upsilon_a} - 2((-2)^{(2/3)})\Upsilon_a \right\}\right] \tag{3.23}$$

where

$$\Upsilon_a = \left(-(d + 2R)\left(2d^2 - 19dR + 8R^2\right) + 3\sqrt{3}\sqrt{-dR(d + 2R)^2\left(4d^2 - 11dR + 16R^2\right)} \right)^{1/3}$$

In this situation the charges of each sphere are effectively moved closer together, increasing the effective Coulomb force due to the decreased separation given by:

$$\bar{d} = d - 2\delta d_{\text{attract}} \tag{3.24}$$

To compute the force with induced effects using this method the effective separation is substituted into Equation 3.14 to give:

$$F = k_c \frac{\hat{q}_A \hat{q}_B}{\bar{d}^2} \tag{3.25}$$

This Coulomb force model accounts for both the position dependent capacitance as well as the induced charge effects.

3.2   Vacuum model verification with numerical analysis

With improvements to the model made, it is beneficial to quantify the extent of improvement as well as verify the solutions with numerical simulations. Numerical simulations are performed using the software package Maxwell® 13.0 by ANSYS. Maxwell® provides 3D electromagnetic and electric field simulations using finite elements.[1]

To quantitatively compare the contribution of each model, Figures 3.4 and 3.5 show the Coulomb force of each model along with the point charge force of Equation 3.4. Figure 3.4 shows the increase from the point charge force that occurs for attractive forces, while Figure 3.5 shows the reduction from the point charge force. All forces are computed with parameters based on the testbed. The spheres have a 25 cm diameter, are charged to 30 kV and operate on a range of separations from 30 cm to 80 cm.

The method of images model is computed using 20 charge terms and is adjusted to give an overall charge computed using Equation 3.5 to allow direct comparison to the first order approximation. Higher order terms were also investigated but offered minimal solution improvement. The force with uneven charge effects using the charge images agrees well with the first order approximation solution. Given the ease of implementing the analytic expression of the first order

---

[1] http://www.ansoft.com/products/em/maxwell/, 11/17/11
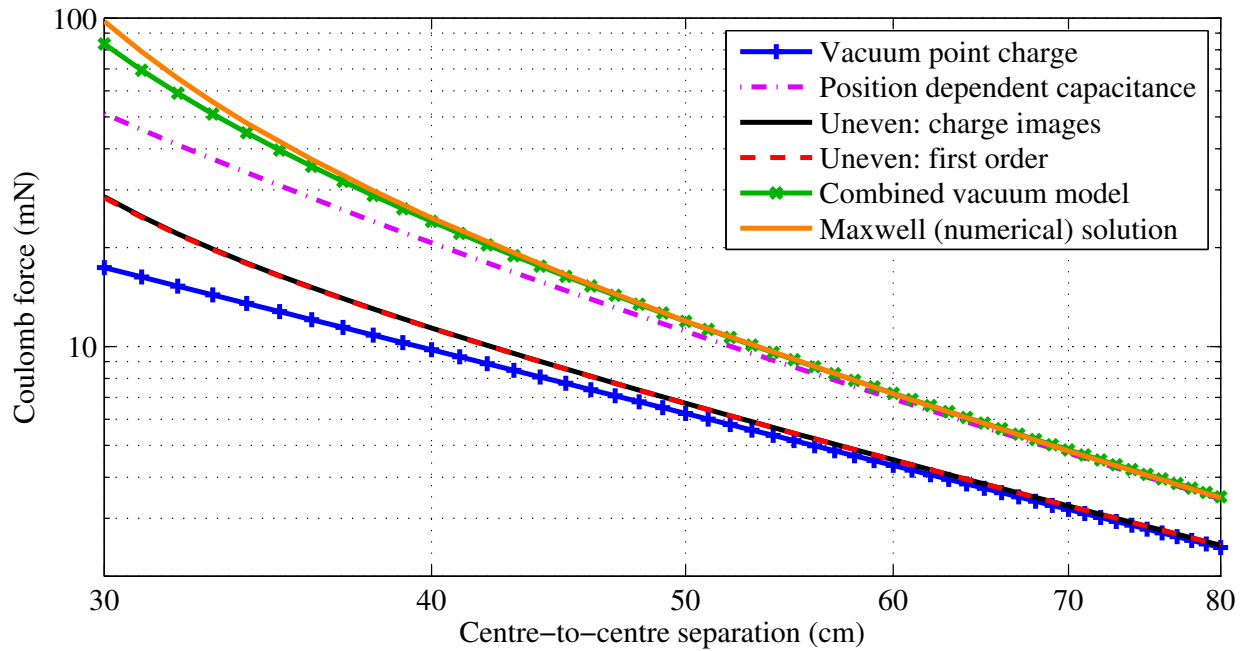
Figure 3.4: Components of attractive vacuum Coulomb force model for spheres at 30 kV, comparing final combined analytic model to numerical solution
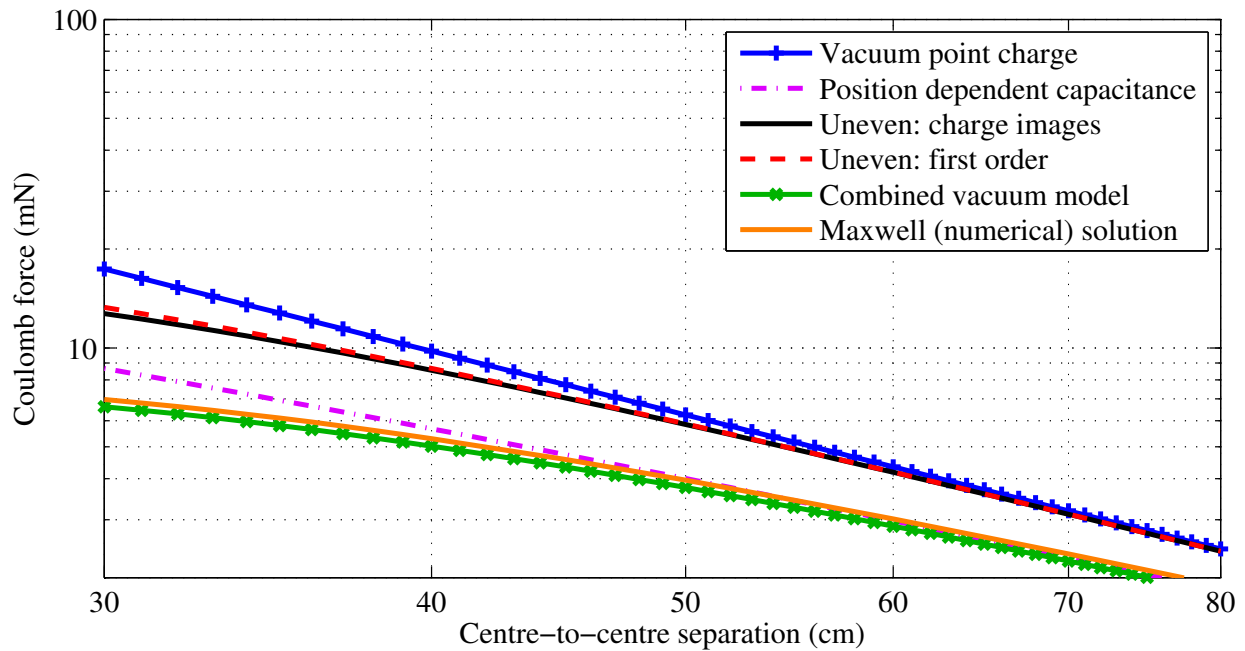
Figure 3.5: Components of repulsive vacuum Coulomb force model for spheres at 30 kV, comparing final combined analytic model to numerical solution

approximation, this model will be used in the remainder of computations that include induced effects.

In the repulsive case, with the inclusion of just the system capacitance and resulting effective charge model the Coulomb force is reduced by 50% from the vacuum point charge model. This comparison is made at the closest separation distance on the testbed. In the attractive case, the force increases the force by 194% from the point charge force at closest separation. Through to separations of 80 cm (6.4 radii) the effects of the close finite spheres and system capacitance is still significant.

The effect of just the induced charge models is also included in this comparison. The results indicate that for very close proximities the effective force with just induced effects decreases the force by 27% for the repulsive case and increases by 64% for the attractive case. The induced charge models also agree well with one another, and beyond a separation distance of 50 cm (4 radii) the net force effects are minimal.

The most important force calculation in this figure is the combination of the finite spheres with position dependent capacitance uneven charge distribution model, denoted the "Combined vacuum model". This accurately captures the true force between two closely separated charged spheres, based on Equation 3.25 using the first order approximation to capture the induced charge influences. This combined model indicates the true repulsive force decreases by 62% from the point charge force and the attractive force increases by 380% calculated at the testbeds closest separation.

Finally, the combined model agrees well with the numerically solved solutions, verifying the suitability of using the analytic Coulomb force model in Equation 3.25 for spheres in close proximity in a vacuum. This combined vacuum force model using the first order approximate solution is used for future force model computations to the vacuum case.

3.3   Simplified analytic Coulomb force modeling in a plasma

A charged body in a plasma will have an altered potential field from the vacuum case. The free-flying charged particles screen the potential field causing it to drop off more rapidly

than vacuum Laplace expression of Equation 3.6. This results in the capacitance of an isolated sphere being altered as well as partially shielding the Coulomb force between charged objects. In this section the characteristics of Coulomb forces in a plasma are developed and a force model is proposed.

3.3.1 Electrostatic field about a charge

Consider a single charge within a homogenous plasma that is at equilibrium. The electrostatic potential and charge motion within the plasma sheath of this charged body is governed by Poisson's second-order differential equation [65]:

$$\nabla^2 \Phi = -\frac{e}{\epsilon_0}(n_i - n_e) = -\frac{en_o}{\epsilon_0}\left[1 - \text{Exp}\left(\frac{eV}{\kappa T_e}\right)\right] \tag{3.26}$$

This is derived with the assumption that at infinity ($\Phi = 0$), the electrons have a Maxwellian velocity distribution. This second order differential equation cannot be solved for an analytic expression of the potential field about the charge in a plasma. Numerical solutions can be computed with finite element solvers and using techniques such as the turning point method [108].

However, assumptions can be made and analytic solutions are proposed. By neglecting the electron density, an approximate solution was found independently by both Child and Langmuir in the early 20th century. This lead to the Child-Langmuir law for a plasma sheath that applies for neutral, planar, and collisionless plasmas that are source-free [65].

Performing a Taylor series expansion on the exponential term in Equation 3.26, keeping only the first-order term, and assuming the body has a low potential compared to the local plasma thermal energy:

$$e_c V \ll \kappa T_e \tag{3.27}$$

produces the reduced linear differential equation [52; 156]:

$$\nabla^2 \Phi = -\frac{e^2 n_o}{\epsilon_0 \kappa T_e} V \tag{3.28}$$

For an isolated charge in an isotropic plasma there exists spherical symmetry so that this equation

is simplified to:

$$\frac{\partial^2}{\partial r^2}(rV) - \frac{e^2 n_o}{\epsilon_0 \kappa T_e}(rV) = 0 \tag{3.29}$$

which has a solution [49]:

$$\Phi(r) = k_c \frac{q_A}{r} e^{-r/\lambda_D} \tag{3.30}$$

This is the Debye-Hückel approximation of the craft potential field about a charge in a plasma. This was developed by Peter Debye and Erich Hückel in the 1920's, originally for electrolytic solutions[34].

The advantage of using this Debye-Hückel potential field is that it provides a simplified analytic solution without the need for numerically solving the full Poisson-Vlasov equations. The consequence of neglecting the higher order terms in the Poisson's partial differential equations is that there is less plasma shielding of the electrostatic fields. The result is that this Debye-Hückel representation is a conservative estimate on the potential function that might actually exist about the charged body in a plasma [97].

Figure 3.6 demonstrates graphically the differences in the potential field from the surface of an isolated 1 m sphere charged to a potential of 50 kV between the vacuum and Debye-Hückel models. The vacuum potential field that corresponds to a vacuum bounds the upper limit of the potential curve, while the Debye-Hückel lower limit is computed for a worst-case, quiet plasma, Debye length $\lambda_D = 4$ m. The true potential field decay will lie in the shaded region between these curves. As the Debye length increases, these lines become closer together.

Given that the E-field and consequently the force is computed from the derivative of the potential field the Coulomb force is also bound within these curves, also shown in Figure 3.6. Due to the gradient of the potential function being larger at very close separations, the E-field for the Debye-Hückel model is actually larger than the Laplace, consequently the force in this region can also be larger. For the CFF concept this is an impractical separation for free-flying craft, except perhaps for deployment conditions. However, this may be advantageous for close proximity Coulomb concepts such as the membrane structure developments. For CFF developments it is

suitable for analytic developments and computations to use the Debye-Hückel force model as it provides a lower limit of force production in a plasma.
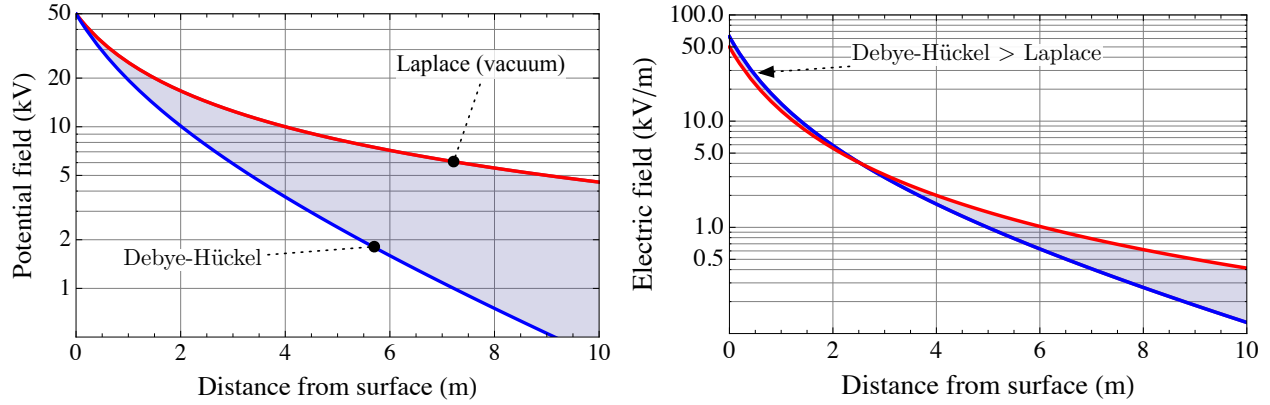
Figure 3.6: Vacuum and Debye-Hückel potential and electric fields from an isolated, 1 m sphere charged to 50 kV in a $\lambda_D = 4$ m plasma

3.3.2 Force between sphere and point charge

For a sphere in a plasma with a fixed surface potential the Debye-Hückel approximation of the craft potential field is modified from Equation 3.30 so that the plasma shielding only commences from the spherical radius [52; 170]:

$$\Phi(r) = \frac{V_A R_A}{r} e^{-(r-R_A)/\lambda_D} \tag{3.31}$$

Taking the gradient of this potential function yields the spherically symmetric E-field for $r \geq R_A$:

$$E(r) = -\nabla_r \Phi(r) = \frac{V_A R_A}{r^2} e^{-(r-R_A)/\lambda_D} \left(1 + \frac{r}{\lambda_D}\right) \tag{3.32}$$

In order to compute the Coulomb force when a point charge is placed in this potential field, an expression for the charge of the sphere which has the desired potential surface potential V_A is obtained. Even for an isolated sphere, the plasma alters its capacitance so that the relationship between charge and potential, of Equation 3.5, no longer holds. Assuming a homogenous surface charge density σ across the sphere (suitable given an isolated sphere and a well-mixed, neutral

plasma), the total charge q residing on the surface is calculated with:

$$E(r = R_A) = \frac{\sigma}{\epsilon_o} = \frac{q}{A\epsilon_o} \tag{3.33}$$

Defining $A = 4\pi R^2$ as the spherical surface area and $k_c = 1/(4\pi\epsilon_0)$ is the Coulomb constant, results in the total charge relationship [170]:

$$q_A = V_A \frac{R_A}{k_c}\left(1 + \frac{R_A}{\lambda_D}\right) \tag{3.34}$$

The resulting capacitance of an isolated sphere in a plasma is [170; 110]:

$$C_S = \frac{R_A}{k_c}\left(1 + \frac{R_A}{\lambda_D}\right) \tag{3.35}$$

This indicates that a craft that maintains a fixed potential will hold a charge that is also influenced by the local plasma. If the plasma Debye length is very small (i.e. LEO regime), the space weather could have a significant impact on the sphere's capacitance, and its effective charge. If this plasma has minimal interaction (large Debye lengths, $R_A \ll \lambda_D$) this charge on the isolated sphere reduces to the classical vacuum formulation of Equation 3.5. If the second charge is an infinitesimal point charge that does not effect the charge of the sphere the resulting Coulomb force is computed based on Equation 3.32 to give:

$$F = \frac{V_A R_A q_B}{d^2} e^{-(d-R_A)/\lambda_D}\left(1 + \frac{d}{\lambda_D}\right) \tag{3.36}$$

There is a slight discrepancy on the force on the sphere to that on the point charge with this computation. The discrepancy arrises from the plasma shielding which is computed for different separations $(r - R_A)$ between the sphere and the point charge in each direction. Direct comparison of these forces is shown in Appendix A. It also shows that if a taylor series expansion of the additional exponential quantity is performed the first order terms are cancelled and if $(R_A \ll \lambda_D)$ then the forces are in fact the same value.

3.3.3   Force between finite spheres

Rearranging Equation 3.34 gives the charge on a sphere due to its potential, including the capacitance from the local plasma. If there are two spheres in close proximity it is also necessary to

include the effects of the second sphere. Combining Equations 3.31 & 3.34 for two spheres separated center-to-center by d, gives the set of equations in matrix form:

$$\begin{bmatrix} V_A \\ V_B \end{bmatrix} = k_c \underbrace{\begin{bmatrix} \dfrac{1}{R_A}\left(\dfrac{\lambda_D}{R_A + \lambda_D}\right) & \dfrac{1}{d}\left(\dfrac{\lambda_D}{R_B + \lambda_D}\right)e^{\frac{-(d-R_B)}{\lambda_D}} \\ \dfrac{1}{d}\left(\dfrac{\lambda_D}{R_A + \lambda_D}\right)e^{\frac{-(d-R_A)}{\lambda_D}} & \dfrac{1}{R_B}\left(\dfrac{\lambda_D}{R_B + \lambda_D}\right) \end{bmatrix}}_{C_{\mathrm{P}}^{-1}} \begin{bmatrix} \bar{q}_A \\ \bar{q}_B \end{bmatrix} \tag{3.37}$$

where C_{P} is the capacitance of the combined charged system including the plasma. For a desired surface potential on each sphere this system of equations are inverted to solve for the effective charges $\bar{q}_i$. These charges are used to compute the resulting Coulomb force between the spheres using:

$$F = k_c \frac{\bar{q}_A \bar{q}_B}{d^2} e^{-(d-R_A)/\lambda_D}\left(1 + \frac{d}{\lambda_D}\right) \tag{3.38}$$

which is obtained from Equation 3.36 by substituting for V_A using the vacuum capacitance relationship of Equation 3.5. The effects of the plasma on the sphere capacitance are still captured when solving for the charge with Equation 3.37. To also capture the effects of uneven charge distribution for spheres operating in extreme close proximity the effective sphere separation can be computed for either repulsive or attractive forces using Equations 3.22 & 3.24 and substituted into Equation 3.38 to give the Coulomb force:

$$F = k_c \frac{\bar{q}_A \bar{q}_B}{\bar{d}^2} e^{-(d-R_A)/\lambda_D}\left(1 + \frac{d}{\lambda_D}\right) \tag{3.39}$$

This is a proposed Coulomb force model between two finite spheres in a plasma. To date numerical solutions have not been used to verify this model. This is not feasible to achieve within the scope of this dissertation given the complexities of implementing and using a full plasma numerical solver. Follow on developments plan to use electrostatic finite element packages for the purposes of verifying this proposed force model in a plasma.

Again, this plasma force model is a conservative estimate of the force between charged bodies in a plasma and is best suited when $e_c V \ll \kappa T_e$. The following section quantifies under what charge conditions violate $e_c V \ll \kappa T_e$ for each plasma. In addition, when this condition is violated a analytic method to more appropriately fit the true force between charges in a plasma is investigated.

3.4 Spacecraft and plasma energies

The Debye-Hückel potential field and resulting Coulomb force model is an analytic expression that is derived by assuming $e_c V \ll \kappa T_e$ holds. Table 3.1 quantifies the spacecraft surface potential required to match the plasma thermal energy, i.e. $e_c V = \kappa T_e$. For all plasma conditions except the rare disturbed environment the potentials required are well below the kilovolt levels that are required for the Coulomb formation flight concept and those that are also used on the testbed. Therefore quickly, the potentials violate the $e_c V \ll \kappa T_e$ assumption and while providing an analytic expression for the Coulomb force between charged bodies it is a conservative estimate.

Table 3.1: Spacecraft potentials required to equal plasma energy $(e_c V = \kappa T_e)$

Plasma Conditions	Debye Length λ_D [m]	Surface Potential V_A [V]
GEO Quiet	4	3
GEO Nominal	200	900
GEO Disturbed	743	10000
LEO Nominal	0.01	0.2

3.5 Effective Debye lengths and Coulomb forces

If a craft potential is potential is much less than plasma energy $(e_c V_{scA} \ll \kappa T_e)$ than the Debye-Hückel potential of Equation 3.31 is a good approximation. If the craft potential is significantly greater than the plasma $(e_c V_{scA} \gg \kappa T_e)$ than the plasma response is closer to the Laplace potential of Equation 3.6. For the Coulomb formation flight application the potentials and plasma properties have similar magnitudes. Consequently the two approximations available give bounds on the range of potential decay from a charged body in a plasma. The resulting Coulomb force that is derived from these potential fields is also bound by these analytic representations.

One method to analytically compute the force within this range is with the an effective Debye length. The effective Debye length, $\hat{\lambda}_D$, is defined by a scaling parameter, α, and the unperturbed

Debye length with the expression:

$$\hat{\lambda}_D = \alpha \lambda_D \tag{3.40}$$

This effective Debye length is larger than the true Debye length and consequently reduces the screening of the potential field. It can then be substituted directly into the Debye-Hückel Coulomb force to more appropriately match the true force. The effective Debye length is numerically computed based on plasma conditions, craft size, and potential. This effective Debye length is computed from numerical solutions in Reference [97] and demonstrated for the 'electrostatic tractor' concept with near Earth objects.

In this NEO application the interplanetary Debye length is 7.4 m, however with potentials up to 20 kV, Murdoch calculates that the effective Debye lengths can be as great as 349 m. This is a scaling increase of approximately 50, and results in significantly less force partial shielding. Preliminary calculations for CFF spacecraft charged to 30 kV indicate α values between 1-20, depending on the local plasma conditions and craft sizes.

The benefit to this is that it allows efficient analytic force computations with improved accuracy. It is also possible that meter level effective Debye lengths can occur around charged bodies at LEO. This improves the Coulomb forces magnitudes and makes them viable for applications such as inflation of membranes or similar at cm level separations.

3.6   Summary

The fundamentals of Coulomb forces between charged bodies is expanded from a vacuum to a plasma. A Coulomb force model that includes plasma and position dependent system capacitance and induced effects is developed and proposed as a suitable, yet conservative, representative force between spheres. Understanding these electrostatic force interactions is integral for further developments. Developed in the next chapter is the space-based estimation problem that uses a force model developed here.

A task of this dissertation is also to determine if there is a suitable Coulomb force model for

the terrestrial testbed. Ultimately the plasma Coulomb force model proposed here is applied to force actuation on the testbed to capture atmospheric electrostatic interactions. The appropriateness of using this plasma equation is determined by fitting an atmospheric "Debye Length" $(\bar{\lambda}_D)$ to testbed experimental results. This provides a means to compare the partial force shielding of a plasma to the atmospheric interactions of the terrestrial environment.

Chapter 4

Space-based Coulomb relative motion estimation

A theoretical foundation of spacecraft plasma interactions and Coulomb force modeling has been developed in previous chapters. A progressive step is to use this knowledge to analyze aspects of the space-based relative motion sensing and estimation capabilities. This chapter demonstrates the complexities involved with accurately sensing a Coulomb actuated spacecraft pair in a space plasma environment.

To perform Coulomb formation flight in space requires the use of relative motion sensing and estimation. Specifically, it is beneficial to understand the capabilities of estimation in space using the relative motion of two charged craft. This incorporates the partial charge shielding from a plasma that inherently changes with time. Using the known relative motion of two charged spacecraft and the plasma Coulomb force model it is shown to what accuracy parameters such as plasma Debye length and craft potential can be estimated. This is only a preliminary estimation study and will ultimately lead to follow on work beyond this dissertation.

To quantify these capabilities a batch algorithm is used with simulated measurements of an idealized system. The analysis also bounds the accuracy requirements on sensors for relative motion and spacecraft charging and includes realistic sensor noise. This estimation work gives an appreciation of the difficulties and requirements of future CFF missions. It also sets the groundwork for future real-time estimation of parameters on the testbed hardware as a precursor to space-based implementation.

4.1   Motivation and setup

The primary goal of this chapter is to bound the capabilities of performing space-based estimation of the plasma force and parameters using charged relative motion. A focus is to independently estimate the plasma Debye length or the potential of one craft and determine what state accuracy is required to obtain these solutions. This requires the use of the plasma force models developed in Chapter 3 and then has follow on applications to estimation on the testbed.

For this estimation application an idealized two craft system operating in deep space is modeled. It incorporates no gravity, differential solar radiation pressure, thrusting or outgassing. The 50 kg craft are spherical with 1 meter radii and an initial separation of 10 m center to center. Maneuvers and variable charge levels are feasible, however for this study a fixed potential of 30 kV is applied to each craft. The resulting Coulomb force that repels the craft is computed for two plasma conditions; nominal ($\lambda_D = 200$ m) and the more extreme shielding from the quiet ($\lambda_D = 4$ m) plasma. The simulated measurements are the relative acceleration between the craft sampled at 5 s time steps for a total data set of 10 mins (120 measurements).

4.2   Batch estimation development

The parameters estimated separately in this study are the plasma Debye length and the potential of one craft using relative motion (acceleration) measurements. These are both interesting and suitable scopes of study for the space based CFF application. If the craft are operating in close proximity they can utilize inter-satellite communication and relative motion sensing for accurate sensing of the local plasma environment without the need for sensors such as Langmuir probes.

The mathematical developments of the batch estimator are shown here. For this case the estimating state vector is the scalar constant:

$$X^* = \lambda_D \tag{4.1}$$

The a priori of the estimate, $\bar{x}_0$, is set to the truth (200 m or 4 m) by default, however is an analyzed parameter and a range of values are studied. The measurement model of this analysis is based on

the Coulomb force that includes the partial force shielding from the plasma as well as the position dependent capacitance of the finite spheres in a plasma. It does not include the uneven charge distribution model, as the separation distance is large enough to omit. This proposed Coulomb model originally derived in Equation 3.38 is repeated again here:

$$F = k_c \frac{\bar{q}_A \bar{q}_B}{d^2} e^{-(d-R)/\lambda_D} \left(1 + \frac{d}{\lambda_D}\right)$$

where $\bar{q}_i$ are computed from inverting the capacitance relationship of Equation 3.37 that includes plasma and close proximity finite sphere effects. The resulting repulsion force between these two craft is computed using Equation 4.2 and graphically displayed for each plasma condition in Figure 4.1(a). This clearly demonstrates the difference in force magnitudes due to plasma shielding. Plotted in Figure 4.1(b) is the resulting separation of the two craft over this 10 min interval.

(a) Coulomb Force

(b) Spacecraft Separation
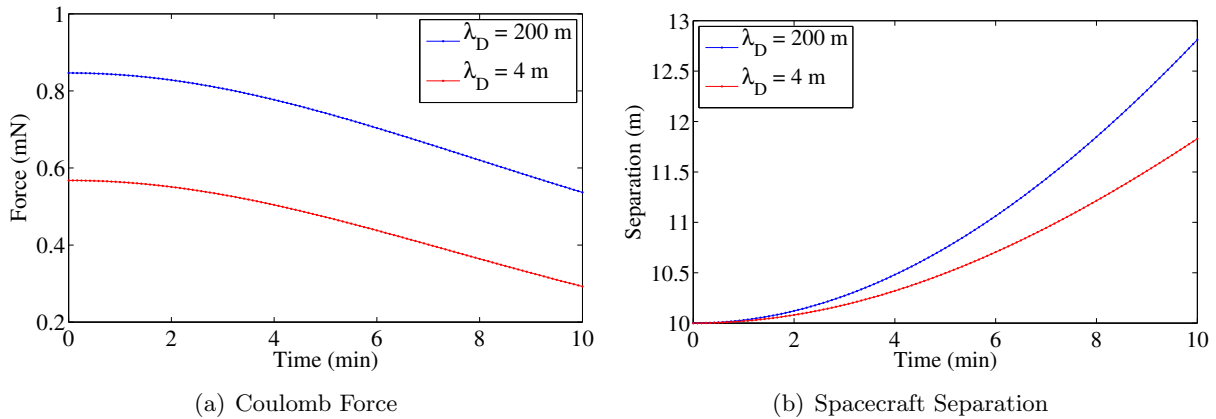
Figure 4.1: Coulomb force and resulting relative distance as a function of time for the two craft in each plasma

With equivalent sphere potentials and radii, the measurement model is:

$$F = \frac{V_A V_B R^2 (d + \lambda_D)(\lambda_D + R)^2 e^{\frac{d+R}{\lambda_D}}}{k_c \lambda_D^3 \left(d e^{d/\lambda_D} + e^{R/\lambda_D} R\right)^2} \tag{4.2}$$

which is arranged to give the equation of motion where the parameter being estimated is the Debye length λ_D:

$$\ddot{d} = \frac{V_A V_B R^2 (d + \lambda_D)(\lambda_D + R)^2 e^{\frac{d+R}{\lambda_D}}}{m k_c \lambda_D^3 \left(d e^{d/\lambda_D} + e^{R/\lambda_D} R\right)^2} \tag{4.3}$$

Here, d is the center to center separation of the spheres and m is the mass of the craft. The simulated measurement at time i is the relative acceleration of the craft, $L_i = \ddot{d}_i$. The measurement sensitivity $\tilde{H}_i$ is computed from the predicted measurements C_i and due to the single state being constant is also mapped back to epoch as the Jacobian [147]:

$$\tilde{H}_i = \frac{\partial C_i}{\partial X^*} = H_i = -\frac{k_c V_A V_B R^2 (\lambda_D + R) e^{\frac{d+R}{\lambda_D}}}{\text{kc}^2 m \lambda_D^5 \left(d e^{d/\lambda_D} + e^{\frac{R}{\lambda_D}} R \right)^3} \Bigg\{ -d^3 e^{d/\lambda_D}(\lambda_D + R) +$$

$$e^{\frac{R}{\lambda_D}} \lambda_D R \left[-2R^2 + r(\lambda_D + R) \right] + d^2 \left(e^{\frac{R}{\lambda_D}} R(\lambda_D + R) + e^{d/\lambda_D}[2\lambda_D R + r(\lambda_D + R)] \right)$$

$$+ d \left(e^{d/\lambda_D} \lambda_D [2\lambda_D R + r(\lambda_D + R)] + e^{\frac{R}{\lambda_D}} R \left[r(\lambda_D + R) + 2 \left(\lambda_D^2 + \lambda_D R - R^2 \right) \right] \right) \Bigg\} \quad (4.4)$$

This example case is observable and a batch processor is used to obtain an estimate of the constant shielding parameter. In order to obtain this estimate, the observation residuals are computed from the difference between simulated and predicted measurements $y_i = L_i - C_i$. Processing through each of the measurements the normal equation is accumulated:

$$(H^T W H)\hat{x}_0 = H^T W \vec{y} \quad (4.5)$$

where W is the measurement weighting matrix at each time and $\hat{x}_0$ is the epoch state deviation vector. For this example application with a single range measurement, W is a scalar that equals the inverse of the measurement noise uncertainty. The measurement is assumed to be Gaussian. The epoch state deviation $\hat{x}_0$, which is the best estimate of state (λ_D), is obtained by solving:

$$\hat{x}_0 = (H^T W H)^{-1} H^T W \vec{y} \quad (4.6)$$

This solution is used to update the reference state at epoch as well as the a priori information $\bar{x}_0$ using:

$$X_0^* = X_0^* + \hat{x}_0 \quad (4.7a)$$

$$\bar{x}_0 = \bar{x}_0 - \hat{x}_0 \quad (4.7b)$$

The entire batch process is reiterated using the same data set to improve the solution estimate until it meets a desired tolerance (1×10^{-4}).

4.3   Estimating plasma Debye length

The first simulation results analyzed are the estimation of the plasma Debye length. To verify the solution convergence using the algorithm, computations are made with unperturbed (noise-free) measurements but initial estimate errors for each plasma. The results of Debye length solution convergence as a function of number of batch iterations is shown in Figure 4.2.

(a) $\lambda_D = 200$ m plasma   (b) $\lambda_D = 4$ m plasma
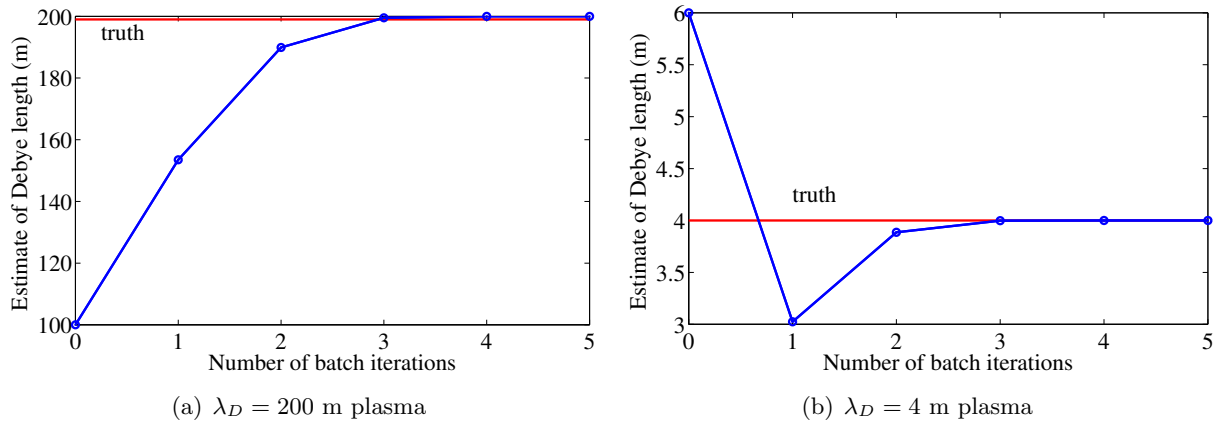
Figure 4.2: Convergence of Debye length estimate solutions for each plasma

For the $\lambda_D = 200$ m plasma the initial estimate is conservative by 50% and converges to the truth within 3 iterations as shown in Figure 4.2(a). Similarly, Figure 4.2(b) demonstrates an initial overestimate of 50% from the $\lambda_D = 4$ m plasma converges within 3 iterations also.

To analyze the robustness of the estimator to initial condition error the plasma Debye length is computed over a sweep of a priori values (1-400 m, an anticipated range of craft potentials). This still uses perfect acceleration measurements. The resulting estimate error as well as the number of iterations necessary to compute each solution are shown for each plasma condition in Figure 4.3. The red solutions indicate the solution is not viable as the estimation diverged or a negative solution found.

The results of this analysis indicate the accuracy requirements of the initial estimate of the plasma Debye length. For the 200 m Debye length an estimate between 20 m to 390 m (10–195%) will converge to the correct solution. For the 4 meter case a correct solution is found with initial

estimates between 1.4 m to 7 m (35–175%). A summary of the range of a priori Debye length values that are required for accurate estimation convergence for each plasma are shown in Table 4.1.

(a) $\lambda_D = 200$ m plasma

(b) $\lambda_D = 4$ m plasma
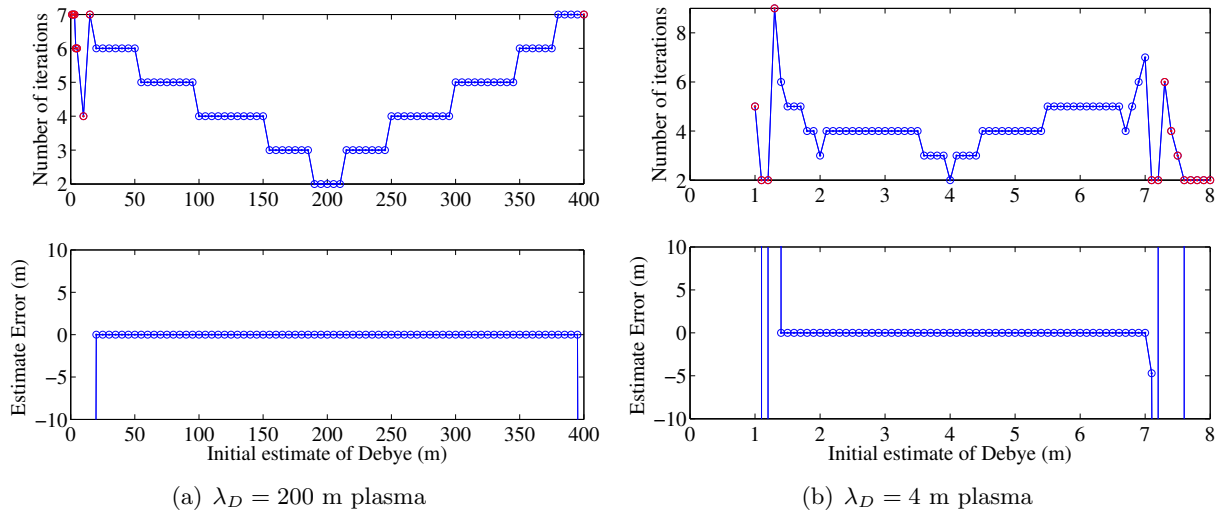
Figure 4.3: Debye length solutions based on a priori value

Perfect measurements are not realistic. Studied here is the effect of measurement noise on solution accuracy. Normally distributed white noise is added to the acceleration measurement. Figure 4.4 displays the acceleration measurement for each plasma, overlaid with noise. Noise with a mean magnitude of 1×10^{-6} ms^{-2} from the perfect acceleration measurement is shown in Figure 4.4(a). This is approximately $1/10^{\text{th}}$ the magnitude of the acceleration signal in this simulation.

Figure 4.4(b) shows the same acceleration with noise of mean magnitude magnitude of 1×10^{-4} ms^{-2} added. This is approximately ten times the acceleration signal of this simulation. To place these values into perspective, the accelerometers onboard the Gravity Recovery And Climate Explorer (GRACE) spacecraft have an accuracy down to 1×10^{-10} ms^{-2} [39].

It is beneficial to see what requirements of accuracy are needed on the acceleration measurement in order to estimate the Debye length. To achieve this, a varying noise value with mean magnitudes ranging from 1×10^{-9} to 1×10^{-3} ms^{-2} are added to the perfect acceleration measurement. The estimation error and number of required iterations for each plasma are shown in

(a) Noise level $(1\sigma) = 1 \times 10^{-6}$ ms^{-2} (b) Noise level $(1\sigma) = 1 \times 10^{-4}$ ms^{-2}
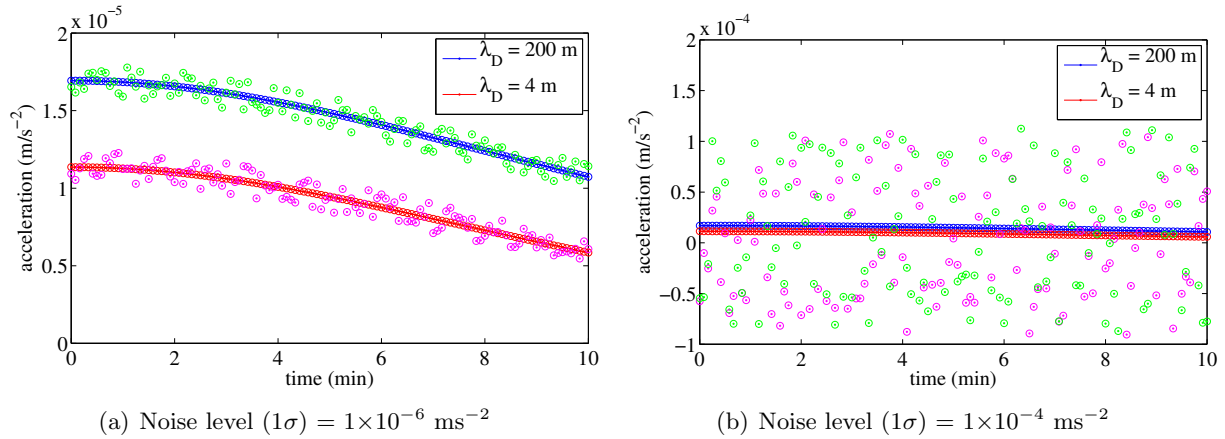
Figure 4.4: Relative acceleration measurements and examples of added noise

Figure 4.5. These solutions assume a perfect initial estimate on the Debye length value for each plasma. The red solutions indicate the solution is not viable as the estimation diverged or gave a negative value.

(a) $\lambda_D = 200$ m plasma   (b) $\lambda_D = 4$ m plasma
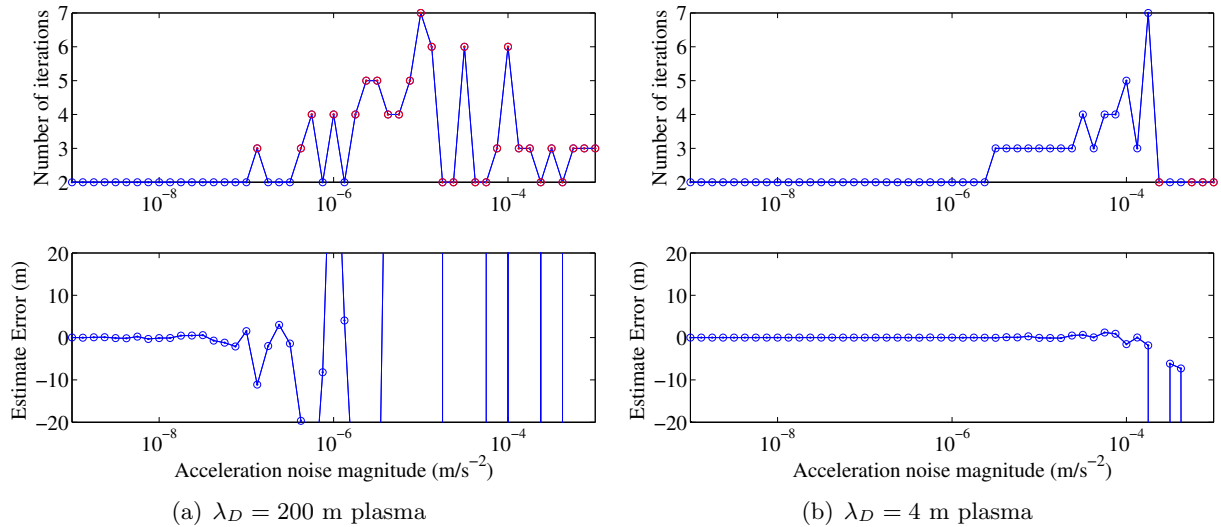
Figure 4.5: Debye length solutions based on noise magnitude

In the 200 m Debye length plasma the estimation accurately computes the Debye length up to noise levels of approximately 3×10^{-7} ms^{-2}. Interestingly, the quiet, 4 m plasma can tolerate noises up to approximately 1×10^{-4} ms^{-2} which is similar magnitude to the measurement value itself. It is found that adding an error to the initial estimate of the Debye does not shift the accuracy

of solution relative to sensor noise, it typically just increases the number of iterations necessary to compute the solution. A summary of the range of measurement noise values for each plasma condition is shown in Table 4.1.

Table 4.1: Range of a priori and measurement noise values required for estimating Debye length

study parameter	λ_D= 200 m	λ_D= 4 m
a priori estimate	$20 - 390$ m	$1.4 - 7$ m
measurement noise	$< 3\times10^{-7}$ ms^{-2}	$< 1\times10^{-4}$ ms^{-2}

4.4   Estimating the potential of one craft

In this simulation case the same two craft system with equivalent properties and dynamics are used. The parameter being estimated in this setup however, is the constant scalar potential of one of the craft:

$$X^* = V_B \tag{4.8}$$

This is computed given the same relative acceleration measurements and with the craft potential V_A known as well as the plasma Debye length λ_D known. This situation is seen as a feasible application corresponding directly to the GEO debris removal concept. In this situation a charged craft that features plasma sensing equipment, such as a Langmuir probe, transfers charge to a uncooperative debris object whose potential is not directly measurable.

The same batch algorithm developed in Section 4.2 is used here, however the modeled equation of motion requires derivation without the equivalent potential assumption $V_A \neq V_B$:

$$\ddot{d} = \frac{e^{\frac{d+R}{\lambda_D}}(d+\lambda_D)R^2(\lambda_D+R)^2 \left(de^{d/\lambda_D}V_B - e^{\frac{R}{\lambda_D}}V_A R\right)\left(de^{d/\lambda_D}V_A - e^{\frac{R}{\lambda_D}}V_B R\right)}{k_c m \lambda_D^3 \left(d^2 e^{\frac{2d}{\lambda_D}} - e^{\frac{2R}{\lambda_D}}R^2\right)^2} \tag{4.9}$$

The new measurement sensitivity is computed as:

$$H_i = \frac{e^{\frac{d+R}{\lambda_D}}(d+\lambda_D)R^2(\lambda_D+R)^2 \left(d^2 e^{\frac{2d}{\lambda_D}}V_A - 2de^{\frac{d+R}{\lambda_D}}V_B R + e^{\frac{2R}{\lambda_D}}V_A R^2\right)}{k_c m \lambda_D^3 \left(d^2 e^{\frac{2d}{\lambda_D}} - e^{\frac{2R}{\lambda_D}}R^2\right)^2} \tag{4.10}$$

Using these equations the batch estimator is first tested with a simple case with no noise but an initial estimate error that is very large relative to the true potential of the craft (30 kV). Figure 4.6 demonstrates the convergence of the algorithm for the 200 m plasma with an a priori of 1 kV and a 4 m plasma with an a priori of 100 kV. For each plasma, the estimator convergences on an accurate solution within 3 iterations.

(a) $\lambda_D = 200$ m plasma

(b) $\lambda_D = 4$ m plasma
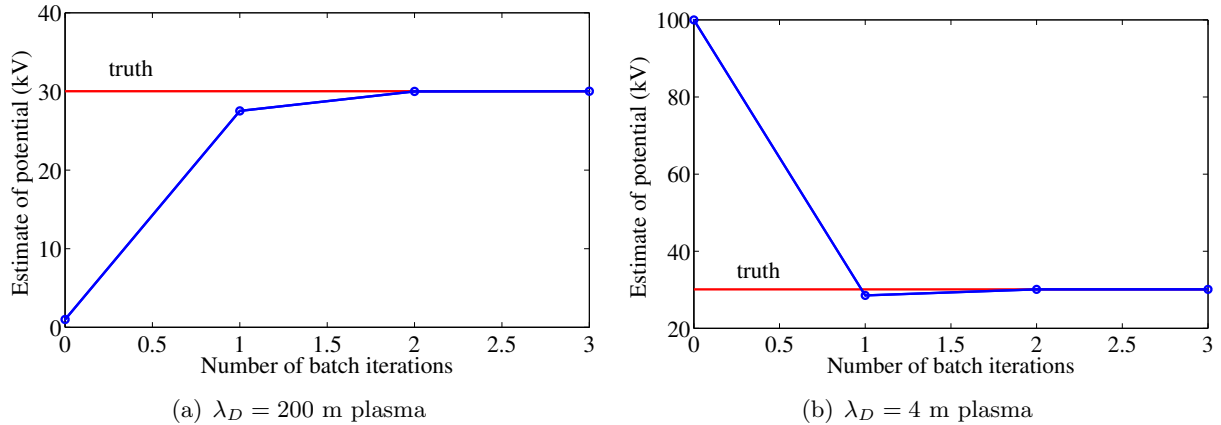
Figure 4.6: Convergence of craft potential estimate solutions for each plasma

To analyze the robustness of the estimator to initial condition error the craft potential is computed over a sweep of a priori values (1 kV to 50 kV, an anticipated range of craft potentials). This still uses perfect acceleration measurements. The resulting estimate error as well as the number of iterations necessary to compute each solution are shown for each plasma condition in Figure 4.7.

The results of this analysis indicate that the accuracy of the initial estimate of the unknown craft potential is not a critical factor. Here all solutions converged within at least 4 iterations across the entire 1-50 kV initial estimates. These results indicate that this scenario of estimating one craft potential is readily observable and robust to a priori values. A summary of the range of spacecraft potential a priori values that are required for accurate estimation convergence for each plasma are shown in Table 4.2.

Again, it is beneficial to see what requirements of acceleration measurement accuracies are needed in order to estimate the craft potential. The equivalent range of noises with mean magnitudes of 1×10^{-9} to 1×10^{-3} ms^{-2} are added to the perfect acceleration measurement. The

(a) $\lambda_D = 200$ m plasma

(b) $\lambda_D = 4$ m plasma
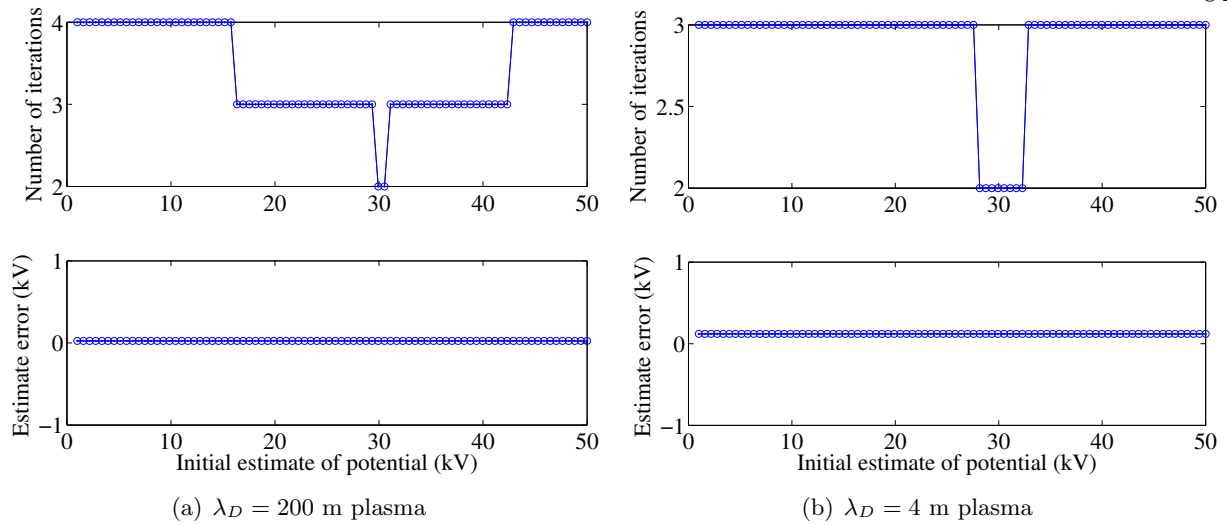
Figure 4.7: Craft potential solutions based on a priori values

estimation error and number of required iterations for each plasma are shown in Figure 4.8. These solutions assume a perfect initial estimate on the craft potential value. The red solutions indicate the solution is not viable as the estimation diverged or gave a negative value.

(a) $\lambda_D = 200$ m plasma

(b) $\lambda_D = 4$ m plasma
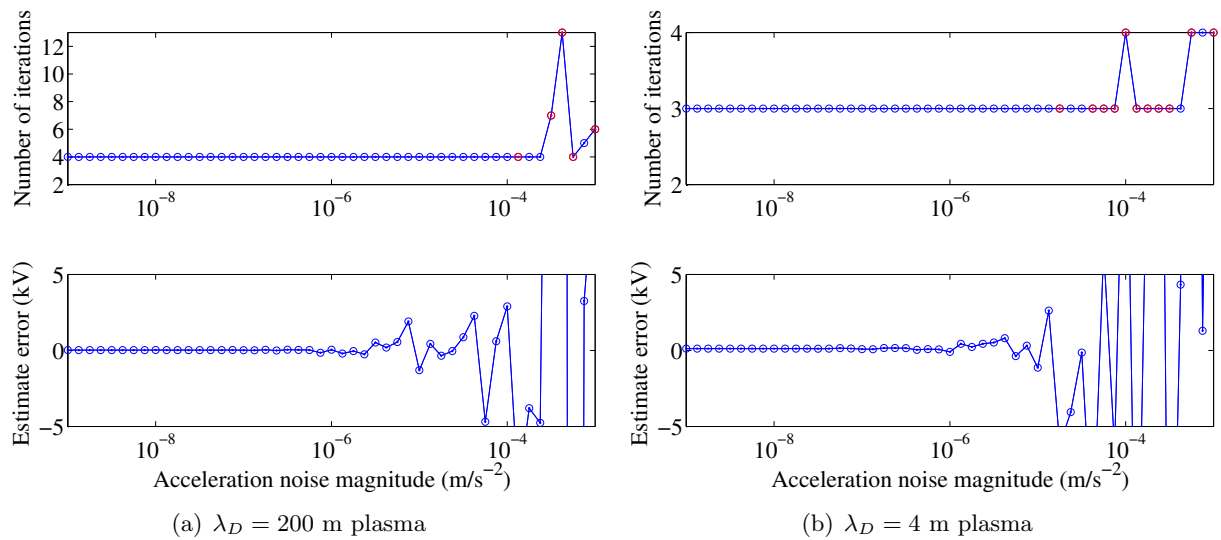
Figure 4.8: Craft potential solutions based on noise magnitude

In this estimation scenario the noise magnitude has a similar effect on both the 200 m and 4 m Debye plasma conditions. The algorithm accurately computes the unknown craft potential up to noise levels of approximately 5×10^{-5} ms^{-2}. This is a good finding that suggests that it is possible

to estimate the potential of a charged craft with relative acceleration measurements with obtainable noise levels. A summary of the range of measurement noise values for each plasma condition is shown in Table 4.2.

Table 4.2: Range of a priori and measurement noise values required for estimating craft potential

study parameter	$\lambda_D = 200$ m	$\lambda_D = 4$ m
a priori estimate	1 kV to 50 kV	1 kV to 50 kV
measurement noise	$< 5 \times 10^{-5}$ ms^{-2}	$< 5 \times 10^{-5}$ ms^{-2}

4.5 Summary

A batch algorithm is developed for two operational scenarios for charged relative motion of two crafts. It is demonstrated that relative motion accelerations measurements can be used to estimate the Debye length using the proposed plasma force model that incorporates combined capacitance of two finite spheres and plasma effects. This is achievable given the potentials of each craft are known. The second scenario involves a craft of unknown potential, however the potential of one craft is known as well as the local plasma Debye length (a feasible situation for the Coulomb GEO debris removal concept).

These analyses feature ideal two craft scenarios but give an indication of the level of initial estimates and sensor measurement noise requirements that are necessary to accurately compute the unknown parameters. The system is robust to unknown craft potential; however the a priori on the Debye length requires higher accuracy due to the more complex observability of this parameter and likely because it is beyond the linear region for filter convergence. For both situations, solutions are obtained with acceleration measurements that feature realistic noise magnitude levels.

This preliminary study gives an appreciation for estimation beyond just space-based applications, with follow-on work to look at implementing the estimation techniques on the testbed. It is envisioned that the cart's relative motion and known voltages can be used to estimate the terrestrial partial force shielding and capture any time dependancies in real-time. This is beyond

the level of scope of this dissertation but is a direct precursor to future space-based estimation techniques.

Chapter 5

The Coulomb testbed

In order to fulfill a preponderance of the research goals listed in Section 1.5, a testbed for electrostatic relative motion control is needed. This chapter gives details on the methodology used to construct and operate the testbed. This includes characterizing the hardware systems and identifying and mitigating disturbances through sensing and motion results.

5.1   Coulomb testbed overview

Section 1.7 listed the unique constraints that make the task of developing a Coulomb testing platform challenging. Considering these challenges and meeting the goals of designing and developing an original and dedicated testbed, a list of specific design requirements are generated for the custom testbed and shown in Table 5.1.

Table 5.1: Testbed design requirements

Independent hover capability of multiple craft
Minimal air flow requirements
Scalable track length
All encompassing safety cage and procedures
Electrostatic charging mechanisms and autonomous control
Accurate position sensing and logging
Charge polarity switching < 1 s
Accelerations > 5 mm/s^2

These requirements stem from the need to design an adaptable testbed platform that accounts for long term use. This allows future expansions to be made enabling experiments to be conducted

beyond the goals of this research. Future efforts may include track extensions, multiple craft relative motion studies, two-dimensional testbed and environment modeling or vacuum operation.

A primary feature of this dissertation research is the design and construction of the one dimensional Coulomb testbed in the Autonomous Vehicle Systems (AVS) Laboratory. The unique testbed is shown in Figure 5.1. It features metallic spheres that are charged with electrostatic power supplies. One sphere sits on a cart and moves along a near-frictionless air bearing track. The vehicle's position is manipulated by controlling the charge of the spheres, which is driven by their respective potential levels. Major hardware components are labelled in Figure 5.1.
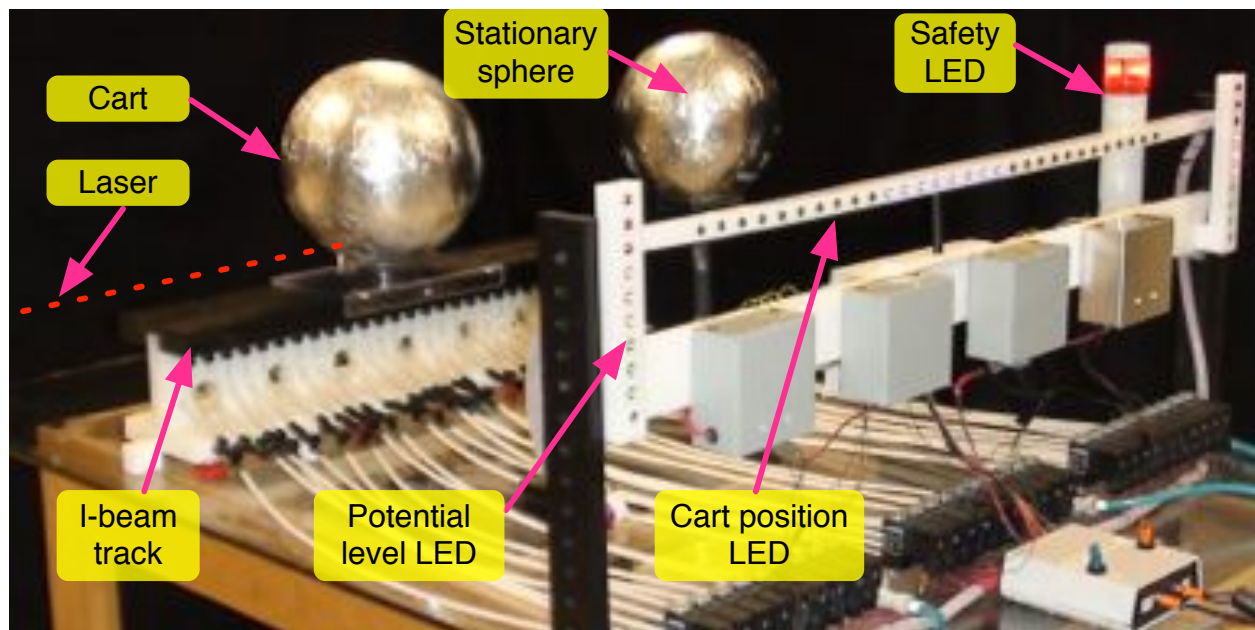
Figure 5.1: Testbed for cart position control with Coulomb forces

In space charge control hardware, based on hollow cathodes or field emission, are used to control the craft potential through charge emission. This is not feasible in an atmospheric environment, so electrostatic power supplies are implemented to charge the spheres to desired potentials.

In order to successfully implement Coulomb control in the laboratory, it is necessary to quantify and mitigate disturbances so Coulomb forces dominate cart motion. For this research the disturbances are broken down into two main categories:

- Mechanical - systematic and random disturbances that can be present at all times

- Electrostatic - disturbances that arise during and as a consequence of electrostatic actuation

The mechanical disturbances include gravity (modeled by track tilt biases and uneven cart mass distributions) and uneven air flow along the track length. Also included here is the system characteristics such as delays in the power supply outputs. Hardware component discrepancies such as these are identified and characterized for terrestrial Coulomb force modeling.

Electrostatic disturbances are interferences which arise during Coulomb actuation as a result of the E-fields. These disturbances also include any residual effects that remain in the apparatus and surrounding atmosphere. Both forms of disturbances are quantified using experimental cart glide test results as well as direct measurements with sensing equipment. The calibrations and findings are discussed in this Chapter.

5.2   Hardware apparatus

Additional pictures of the testbed apparatus is shown in Figure 5.2. This illustrates the aluminum coated styrofoam spheres of 12.5 cm radius. The sphere size is chosen to maximize charge, minimize mass, and allow an adequate range of motion on the track length. Hollow metallic spheres are not feasible at this size as they are too heavy to be actuated on the testbed. Tests conducted with smaller spheres comparing aluminum coated styrofoam and plastic to stainless steel hollow spheres indicated minimal difference between force levels produced.

The non-conducting, air bearing track is constructed of Delrin® is a constructed of poly-oxymethylene, which is commonly known as Delrin®. An advantage with Delrin® is that it is easily machined to the tolerances and surface finishes required for the track and for a single piece of plastic this large it maintains dimensional stability. Alternate track materials such as the glass fiber weave G-10, and the low dielectric constant polyethylene which comes in a anti-static form with added carbon powder were prototyped however did not meet criteria. G-10 is very expensive and difficult to machine, while polyethylene underwent significant warping and deformation over
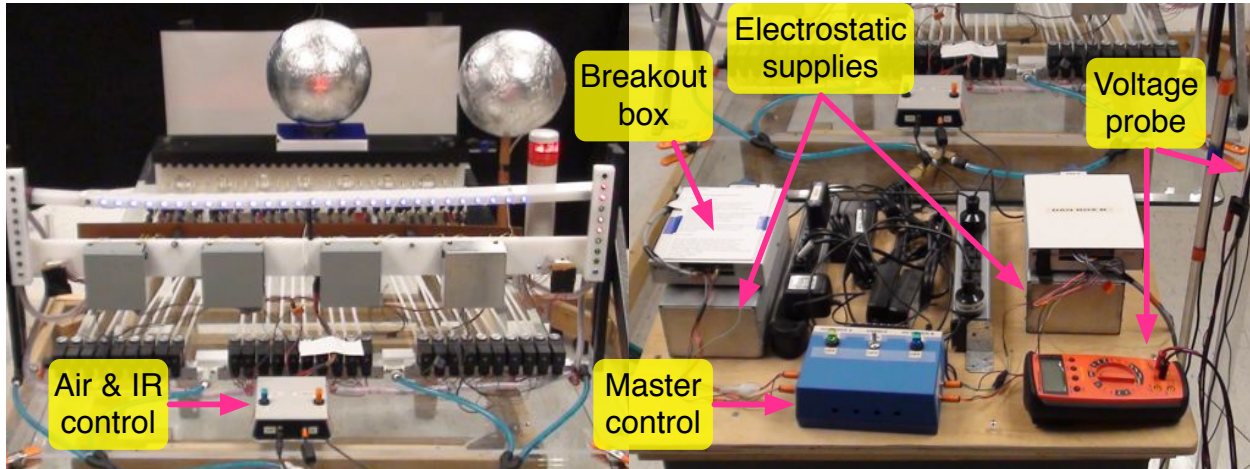
Figure 5.2: Coulomb testbed components

time.

Computer-aided design software is used to visualize components of the track and design integration for drafting and enabling manufacture. The I-beam track and components are shown in Figure 5.3. An I-beam track support made of two pieces of high density polyethylene as it is inexpensive, easy to machine and provides suitable rigidity and support. The I-beam design was selected as it provides good lateral support to the track, does not interfere with track air hole design and allows the air connection hoses to be easily connected on the bottom side of the track. The entire apparatus sits on a glass table, a strong non-conductor, to limit external charge interference. The overall track level can be easily adjusted by screwing the fine pitch thumb screw feet on the I-beam base.

The track has a total length of 76 cm; however experimental cart motion is typically restricted to within 5 cm of each track end. This length allows for interesting electrostatic station-keeping experiments to be performed. The setup is general enough to allow multiple-craft to levitate on the track. At present only one cart is used on the track along with a stationary sphere allowing relative position control experiments to be conducted. Tests with non-zero equilibrium charges are performed by slightly tilting the track to simulate a gravity bias in the relative motion.
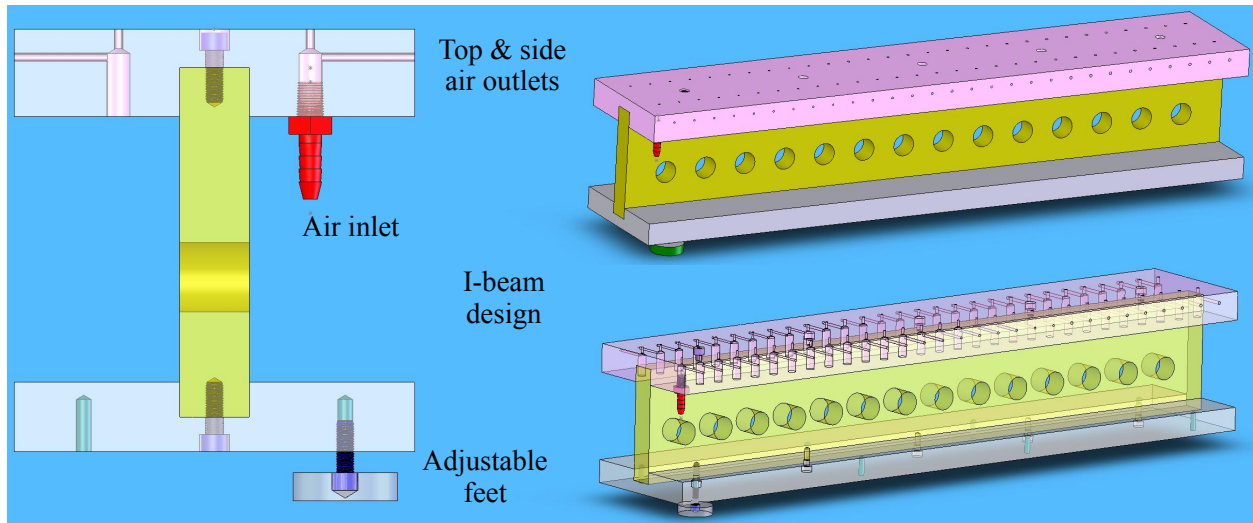
Figure 5.3: Drawing of assembled track components

An air flow system on the track can be operated in manually (all air on) or autonomous modes. For autonomous functionality infrared (IR) sensors are paired to valves through custom electrical logic circuit to control air flow to flow only underneath the cart. This feature reduces possible air flow disturbances and minimizes the air flow requirements, a potential future need. This system has to be completely unobtrusive in a physical and electrostatic sense. It is also desired that it be inexpensive and not require feedback through a central computer, simplifying the system in many ways. This isolates the system away from the track and removes the requirements to have a large array of data acquisition hardware and digitization. The IR sensors are a Sharp GP2Y0A02YK, which have a 20-150 cm range and are not triggered by neighboring cross paths or standard lighting. The valves are a Pneumadyne S8-20-24, two-way solenoid that are connected to a 10 valve manifold. Alternate sensing methods such as inductance and magnetic sensing was discounted as it requires close proximity and metal objects. Figure 5.4 illustrates the IR sensor array and electronics connected to the air valve manifold system. Further details on the IR sensing and analog circuitry is given in Appendix B.

The moveable cart is manufactured from polycarbonate for its smooth surface and dimensional stability. The total cart mass with sphere is 0.328 kg. Cart and track design specifications
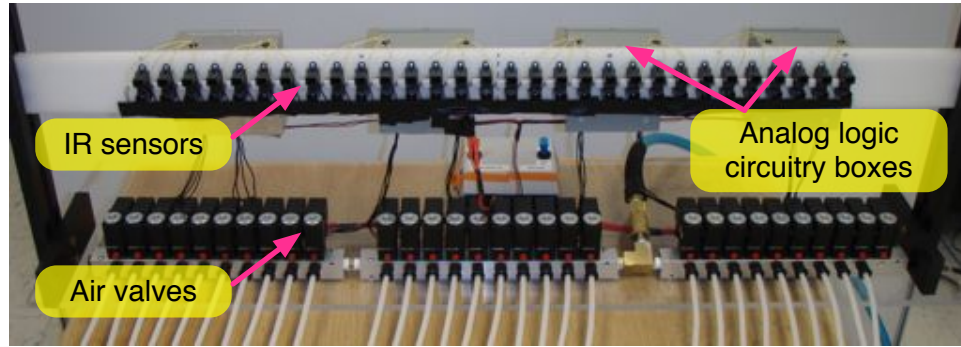
Figure 5.4: Autonomous air flow control system with IR sensors and air valves

are highlighted in Table 5.2. Polarity switching electrostatic power supplies are used to charge the aluminum spheres and control the motion of the cart. Each bench-top unit is capable of supplying ± 30 kV up to 300 μA. This current is more than sufficient for Coulomb testing as the charge needed is a product of high voltage at low current (electrostatics). They are model CZE 2000 manufactured by Spellman High Voltage Electronics Corporation.

With the capability to generate potentials as high as 30 kV and operating at separations of 30-80 cm on the testbed the Coulomb actuation forces that are achievable are estimated using Equation 3.25. This assumes operation in a vacuum with no force shielding but does include combined system position dependent capacitance and induced effects. With these spheres the resulting forces on the testbed at 30 kV are 1 mN to 5.5 mN for repulsion and 2.5 mN to 90 mN for attraction.

A primary goal of the testbed is to use Coulomb forces to induce motion. The verification of cart motion and computation of accelerations is performed with a laser. The class 2 laser, model AccuRange AR1000 manufactured by Acuity Laser Measurement, is positioned along the track length during testing. The position of the cart can be monitored to the sub millimeter level and sampled at up to 50 Hz. This particular setup will only allow for accurate measurement of one cart. Future test beds with multiple craft will have to incorporate additional sensing devices.

Table 5.2: Testbed specifications

Specification	Value
Repulsive force magnitudes	1–5.5 mN
Attractive force magnitudes	2.5–90 mN
Track length	76 cm
Track hole separation	2.54 cm
Track width	14.6 cm
Cart length	21.5 cm
Cart wall thickness	0.4 cm
Cart total mass	0.328 kg

5.3   Testbed operations

The power supplies are externally controlled by the user through a laboratory computer. The connection is made through a National Instruments PXI-6259 data acquisition (DAQ) card and two NI SCB-68 shielded breakout boxes. The DAQ card is a 16-bit, multi-channel card that runs on PCI express architecture. The supplies are monitored and controlled through a custom GUI developed on Cocoa (Mac OS-X native objective C architecture) and is shown in Figure 5.5. Power outputs and fault protections are monitored and the voltage level and polarity of each unit are either controlled manually, with predefined input functions or autonomously with feedback. This external controllability easily allows manual 1-D simulations to be implemented.

5.3.1   Safety

With safety precaution and proper operating practices, the kilovolt level potentials are safely implemented in the AVS laboratory. The Spellman electrostatic power supplies have a low power output, with a maximum of only 9 W. This is a limit on the direct energy available from the power supplies that could lead to unintentional discharge. However, consideration for charge storage, such as that on the testbed spheres, must be made. The energy stored in a capacitor that can be transferred during arcing (spark) is [64]:

$$W = \frac{1}{2}CV^2 \qquad (5.1)$$
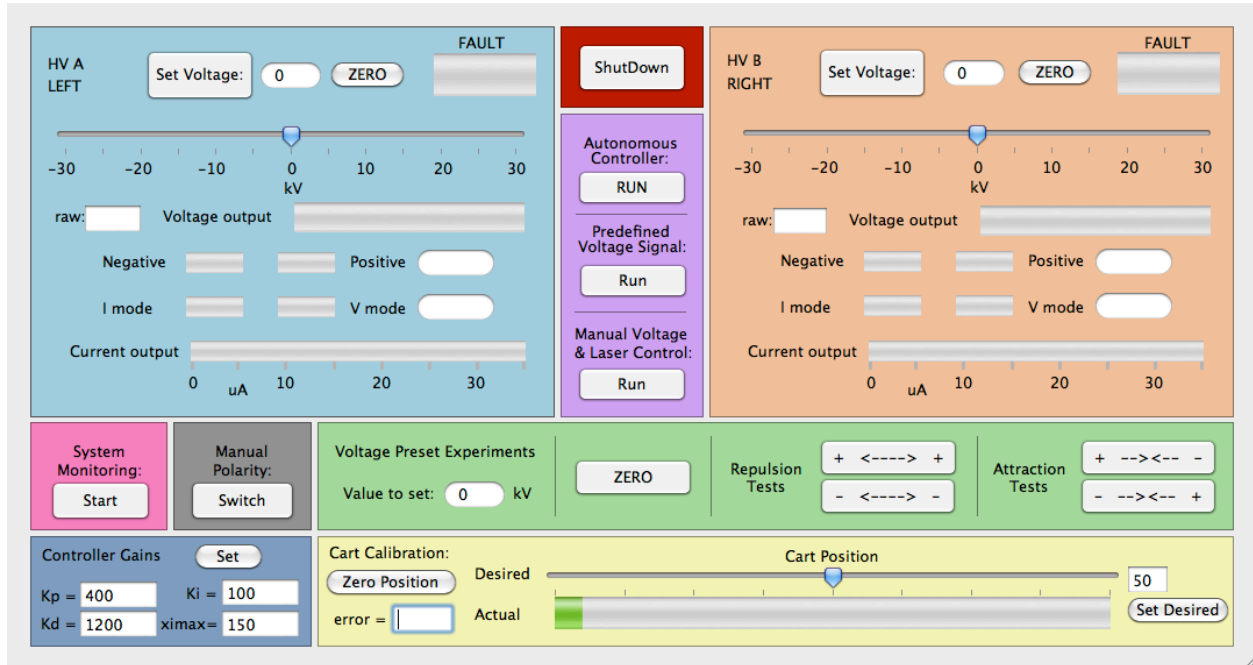
Figure 5.5: Screenshot of the testbed custom graphical user interface

The charged spheres are ultimately storing this open loop charge. With a potential of 30 kV and a capacitance of 13.9 pF the total energy stored is only 0.063 J which is well within typical safe limits, if used with appropriate safety measures.

All tests are performed under stringent safety measures in the AVS lab. All electrostatic and electrical equipment is safely grounded and uses power limiting fuses. Safety and operating procedures are maintained and used during all preparation and testing. The whole testing apparatus is contained within a 6 foot high plastic safety cage that incorporates ground connections and a grounding wand for any necessary discharging. The testbed is only operated with a minimum of two laboratory personnel present.

As well as electrostatic power supply control through the computer GUI there is an additional safety step with external power being provided through manual switches. The laser itself has a visible beam and is safe to use in the lab without eye protection. The testbed also implements LED warning systems indicating if the power supplies have any output potential as well as the voltage

magnitude of each supply.

5.3.2   Autonomous operations

An autonomous feedback control algorithm is implemented with the testbed hardware through the custom C-code application and GUI. The feedback loop operates at 50 Hz and drives the cart to a desired relative position on the track using the electrostatic potentials of the spheres. A schematic of the primary hardware systems and feedback loop for this operation is shown in Figure 5.6.
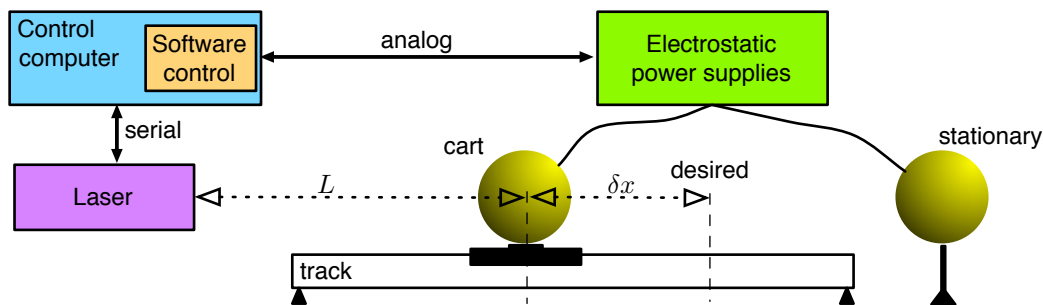
Figure 5.6: Schematic of testbed primary hardware systems and feedback implementation

5.3.3   Experimental maneuver durations

An important consideration with the Coulomb testbed is maneuver durations. For GEO spacecraft clusters, it is anticipated that Coulomb maneuvers last for fractions of days, to multiple days. The differential disturbance forces are 1-2 orders of magnitude smaller than the Coulomb forces [100]. In the laboratory, differential perturbations are a similar order of magnitude to the Coulomb control force. To accommodate this, the electrostatic charges are increased to create millinewton level forces, compared to the more typical micro-Newton levels forces in space. As a result, the maneuver times are reduced for the laboratory experiments to the order of minutes instead of hours.

5.4   Apparatus characteristics

In order to utilize the relative motion of the cart for accurate terrestrial force modeling it is first necessary to understand and characterize the limitations and capabilities of the system. This includes obtaining quantifying apparatus accuracies through statistical measurement of signal noise as well as power supply response characterizations such as output time delays. Both of these aspects are analyzed for the laser and power supplies in this section.

5.4.1   Laser position noise

The laser is the one sensor that is used to ultimately compute the forces acting on the cart during experiments. This is performed by monitoring the position of the cart and differentiating and filtering this measurement to obtain the acceleration and consequently force. The statistically 1σ noise standard deviation in the position measurements of this laser is 0.15 mm. This is inherent to the laser with an approximate 2 Hz error signal. After filtering during the differentiation post processing this corresponds to a standard deviation error on the force estimate of 0.21 mN. This is illustrated in Figure 5.7 that shows the force solution for a 30 second segment of position data for a stationary cart. It also plots the standard deviation bounds. This noise source alone is 20% of the minimum Coulomb actuation force on the testbed.

5.4.2   Power supply response characterization

The electrostatic power supplies have remote voltage monitoring capabilities. This output is used to characterize the true system response as it does not always follow the desired signal. In particular the power supplies indicate a slight reduction in output magnitude and a time delay when switching polarities. This is evident in the comparison of the desired signal to the measured system responses of supplies High Voltage A and B (HVA, HVB) in Figures 5.8, 5.9 and 5.10.

To accurate simulate cart motion the discrepancies between desired and output potential supply response are modeled. The model is developed for each of the power supplies and the
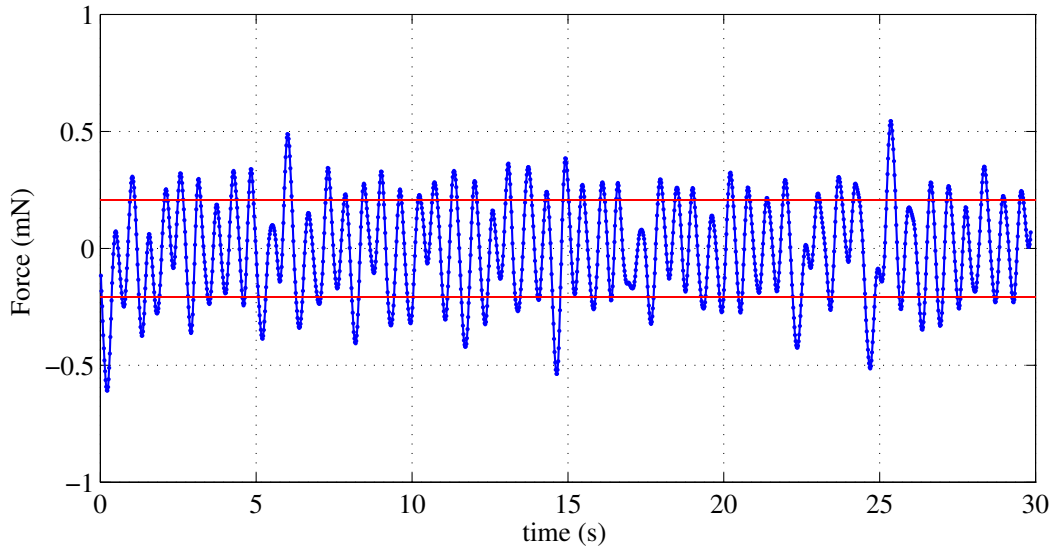
Figure 5.7: Force error magnitude from laser noise, obtained from fixed position measurements
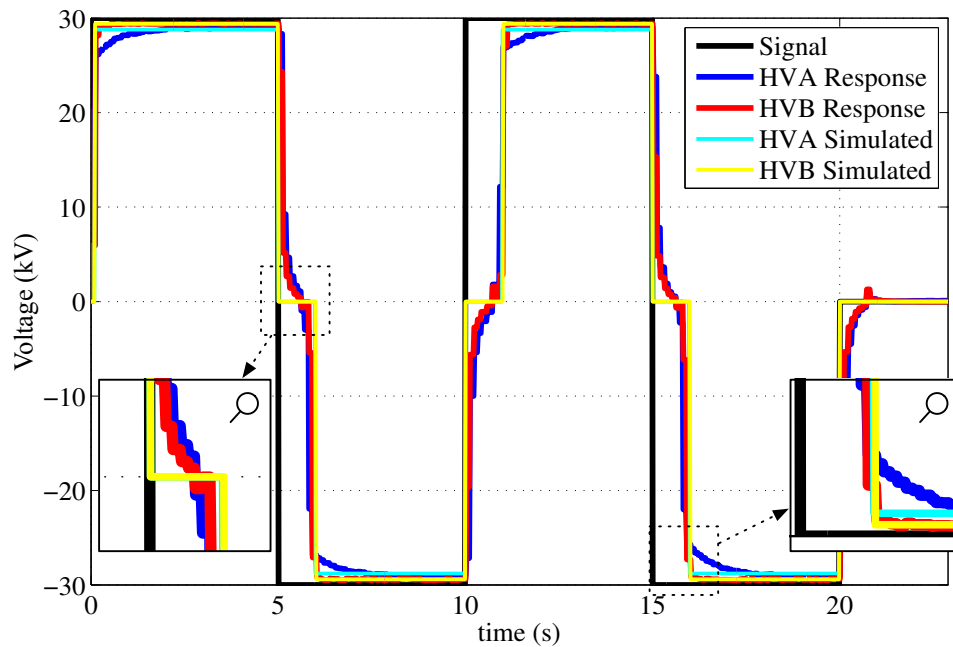
Figure 5.8: Power supply response to input step function and simulate model response

simulated response is shown in each of the Figures 5.8, 5.9 & 5.10. It is evident that with this

model the simulated response matches the measured response more accurately. The parameters
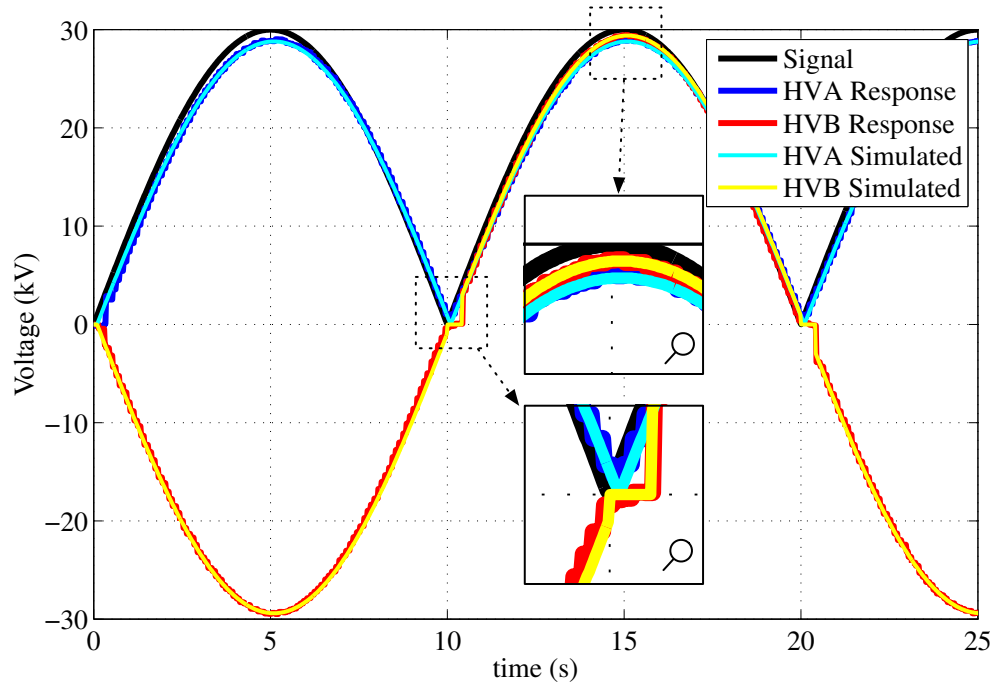
Figure 5.9: Power supply response to input sinusoidal function and simulated model response
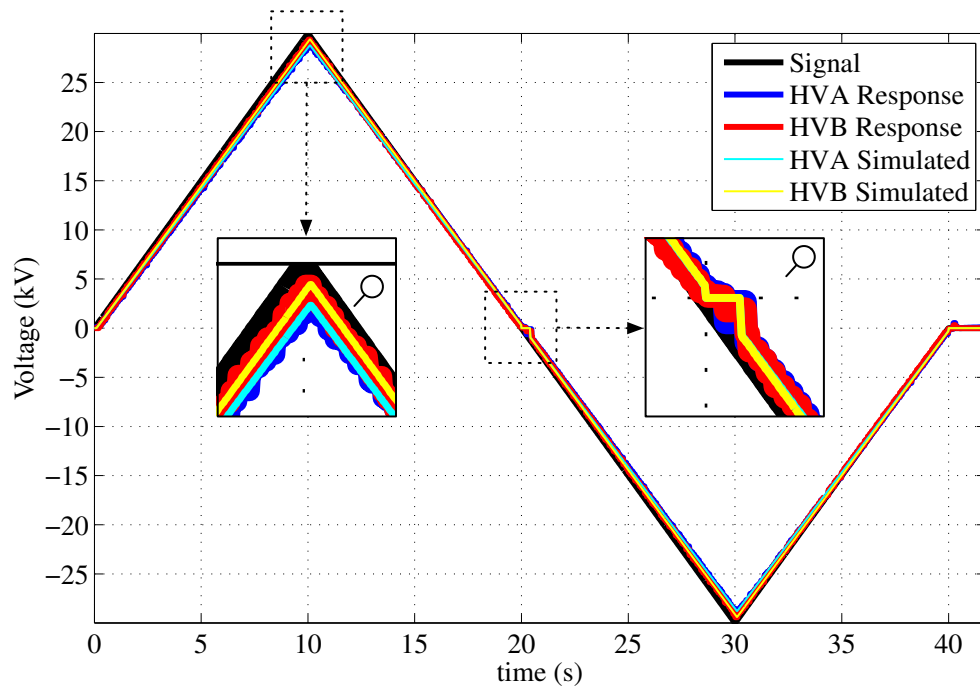
Figure 5.10: Power supply response to input saw function and simulated model response

for this system response model are computed using numerous input signals of varying magnitudes and time and the delays averaged over all data sets. For example, the time delay at the polarity crossing is dependent on the potential magnitude and is as large as one second when switching between ± 30 kV.

5.5   Testbed disturbance identification and mitigation

One of the greatest challenges to overcome with the Coulomb testbed is the mitigation of small disturbances. It is required to reduce disturbances to levels less than the electrostatic forces, allowing the relative motion dynamics to be dominated by Coulomb actuation. To maintain a force signal-to-noise ratio (Coulomb : disturbances) greater than unity and allowing for intentional forces biases, such as track tilt, it is desirable to reduce the summation of all disturbance and noise forces to below 1 mN. This is the estimated minimum actuation force on the testbed, calculated in Section 5.2.

Preliminary experiments demonstrating electrostatic actuation on the track were first presented by Seubert and Schaub at the 19th AAS/AIAA Spaceflight Mechanics Meeting in February 2009 [139]. The disturbances existing in these results were on the order of 10's of mN, which limited early experiments to be performed in sub-sections of the track at close separations where Coulomb forces dominated. Since these results, the sources of these disturbances have been found and methods of reduction are highlighted in this section.

5.5.1   Mechanical disturbances

The numerous mechanical disturbances that can influence motion experiments are investigated here. To measure the extent of the mechanical track disturbances, glide tests are performed prior to all electrostatic experiments. These uncharged glide tests are used to quantify and mitigate small mechanical perturbations acting on the system. This ensures an optimum configuration with a minimum mechanical disturbance state is reached and is used for all Coulomb experiments conducted and presented in this research.

The disturbance forces acting on the cart during example uncharged glide tests are evident in Figure 5.11. Here the cart is given a small impulse at one end of the track and ideally glides with zero force to the other end of the track. The force is plotted for each direction of travel for a number of data sets and a polynomial fit shown overlaid. The forces are also plotted as vector magnitudes as a function of track position with zero at the track end closest to the laser. A positive force is directed away from the laser. The intent of plotting the force profile as a function of track location is to highlight any common disturbances across test cases.

(a) Direction: away from laser   (b) Direction: toward laser
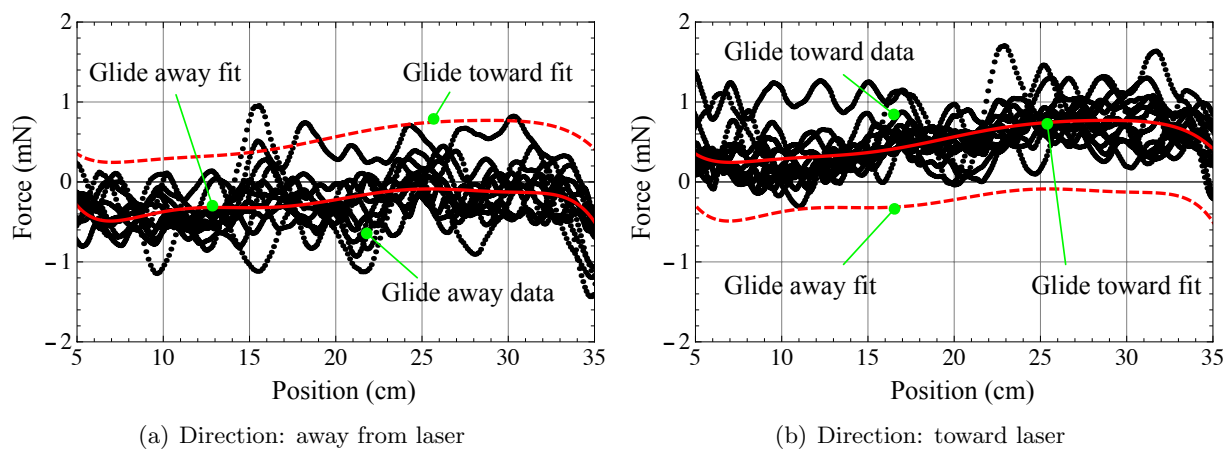
Figure 5.11: Disturbance force levels during uncharged glide tests for each direction, including polynomial fits

The data shown in Figures 5.11(b) and 5.11(a) indicates that the average disturbances for this setup and across all initial speeds tested are within ± 1 mN and consistent between directions of motion as the curves are near identical shape. However, the constant bias between the averages indicates that their is a force that is direction dependent. This trend is observed in all uncharged glide tests and source of this small error is likely the uneven air pocket that forms under the cart as it is traveling.

5.5.1.1   Gravitational disturbances

Glides tests of the cart traveling in both directions, such as though shown in Figure 5.11, are used to identify gravitational disturbances. Gravitational accelerations are reduced through

improved track surface smoothness and leveling as well as even mass distribution on the cart. If the track has a slight gravity bias this is quite evident in glide tests and is removed by adjusting the track tilt.

The first generation of plastic tracks warped as much as $0.1°$, which equates to a disturbance force as large as 8.5 mN for a 0.5 kg cart. A 1 mN gravity disturbance corresponds to a track angled at $0.012°$. Resurfacing of the track in its constructed I-beam design in a unstressed state reduced the total height variation along the track length of 50 cm to below 0.1 mm. The resulting worst case local deviation occurs at only one end of the track which has a maximum angle deflection of $0.02°$ (≈ 1.7 mN), which is close to the desired 1 mN. However, this occurs within 5 cm of one end of the track and is consequently not used for testing.

An additional gravitational disturbance can occur from uneven mass distribution of the cart. Using glide test data, this disturbance force has been detected as great as 3 to 5 mN. The cart mass is precisely distributed through measurements and verified with glide tests prior to Coulomb testing. With the carts floating on a pocket of air they are inherently an unstable, top heavy system. However with even air flow distribution, as described in the next section, the cart remains flat relative to the track and glides smoothly.

5.5.1.2   Air flow disturbances

Uncharged glide data, such as that shown in Figure 5.11 is used to isolate local track discrepancies. Uneven airflow between each row of air holes is one such perturbation that can lead to undesired torques and forces on the cart. There is also a potential disturbance contribution from inaccurate cart position sensing and the air valve switching on and off. These are difficult disturbances to quantify, but they are identifiable and are reduced by accurately monitoring and regulating the air supply at each row of holes and minimizing total air pressure. To study and mitigate the effects of inaccurate cart positioning and the triggering of airflow, numerous glide tests are conducted with the cart. It is also found that the autonomous air flow mode provides low, average air flow disturbances, however the all-air-on mode is very consistent between testing

segments that can span days and weeks. To enable repeatability of glide test air flow disturbances the all-air-on mode is used for the remainder of all experiments used in this dissertation.

5.5.1.3   Charge carrying cable drag

The cart requires a permanent cable attached to drive the spheres potential level during experiments. This cable is a source of disturbances that requires analysis during both uncharged and charged glide tests. Firstly the cable needs to allow the cart to travel along the entire track length uninhibited. This is achieved by suspending the cable from a fixed point above the track center on the laboratory roof.

Another important consideration for the cable selection and implementation is its response when charged. Under potentials as high as |30| kV the cables interact with the E-fields of themselves and the spheres. The result is that the cables can experience stiffening and also undergo vibrations and whipping oscillations that place undesired forces on the cart. It is also necessary to consider the location of the cable attachment point to the sphere as this needs to allow for cart motion. One method for reducing cable disturbances is by utilizing two cables from above so that they mutually repel under charge with a net force perpendicular to the cart direction of travel. Overall, these charge carrying cable disturbances are mitigated to below the 1 mN noise level by analyzing glide tests with a single sphere both uncharged and charged.

After analyzing the disturbances from a number of cables of varying thickness and insulator materials the one chosen with the lowest disturbance levels is a super fine, high-flex, stranded 36 American Wire Gauge (AWG) wire with a Fluorinated ethylene propylene (FEP) insulation layer. This wire was also chosen with consideration for the atmospheric interactions that are investigated in Section 5.5.2.3. The final charge carrying cable implementation that is used on the testbed for all experiments shown in this dissertation is with two of these 36 AWG hi flex wires. Two wires attached lateral to the track length repel from each other canceling any undesired disturbances along the cart range of motion and reduce vibrations.

5.5.1.4   Air drag on cart

Although the speeds on the track are relatively low, the required disturbance levels are very stringent and the drag force from a sphere moving through air must be considered. The speed of the cart on the track has a maximum speed of $v = 0.1$ ms^{-1} during electrostatic actuation. Although applied to high Reynolds number applications, the drag equation is used here to calculate an estimate of typical force levels experienced in air:

$$F_{\text{Drag}} = \frac{1}{2}\rho_{air}v^2 C_d A_s \tag{5.2}$$

where $\rho_{air} = 1.225$ kgm^{-3} is the density of air at standard temperature and pressure, $C_d = 0.47$ is the coefficient of drag for a sphere and A_s is the cross-sectional area. At a maximum speed of 0.1 ms^{-1} the resulting drag force is approximately 0.138 mN, which is a contributing disturbance that is not negligible. No significant changes can be made to the testbed to reduce this disturbance, however, uncharged glide tests of over a vast range of initial speeds (some greater than 0.1 ms^{-1}) do not show any discernible speed dependence in the disturbance forces. Just for perspective, to obtain a 1 mN Drag force a speed of 0.27 ms^{-1} is required.

5.5.2   Electrostatic disturbances

Prior to performing electrostatic measurements uncharged glide tests are conducted to mitigate mechanical disturbances. All disturbances that occur during Coulomb actuation are termed "electrostatic" and are not measurable during these standard glide tests. In this section sources of electrostatic disturbances are discussed. The testbed features apparatus and materials to minimize electrostatic interference and the effects of induced charge. Evaluating the extent of these disturbances is not trivial. Experimental results demonstrate that controlling electrostatic forces can overcome these perturbations; however a goal of the proposed research is to identify, quantify and either mitigate or model these disturbances to better understand Coulomb actuation.

5.5.2.1   Dielectric polarization and antistatic coatings

Dielectric materials such as the Delrin® plastic track have no free electrons to conduct charge. However, due to their molecular composition they can exhibit charged characteristics in the presence of an external electric field. The result is that the molecules align and there is a slight shift in the mean electron position so that the dielectric generates its own electric field [94]. This principle is illustrated in Figure 5.12. Monkman demonstrates the use of polarizable plastics as electroadhesive micro-grippers that can generate up to 200 Nm^{-2} of cohesive pressure with 3 kV potentials [92; 93].
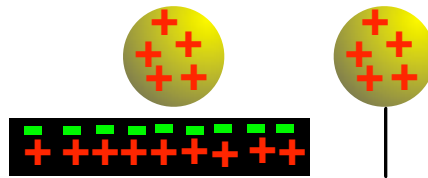
Figure 5.12: Graphical representation of dielectric polarization

This electric field or 'charge memory' also remains after the external field is removed until the dielectric has reached its relaxed, equilibrium state which can take seconds or minutes depending on the electric susceptibility and applied E-field [92]. The electrical susceptibility is a measure of the polarizability of a dielectric and is a function of the relative permittivity (dielectric constant at zero frequency) of the material:

$$\chi_e = \varepsilon_r - 1 \tag{5.3}$$

These polarization potentials and electric fields can be a significant disturbance that the effects are clearly observed on the testbed. In this experiment the cart is left charged at 30 kV at a fixed location on the track (20 cm) for 15 seconds. The cart is then returned to 0 cm and with the 30 kV remaining on is left to glide on its own till it comes to rest. The disturbance force that is accelerating the cart is measured and shown in Figure 5.13 for a number of repeat tests.

At the end of each test the cart comes to rest at its originally fixed location and then with no time for relaxation the test is repeated. This continues for a total of 9 identical tests. The
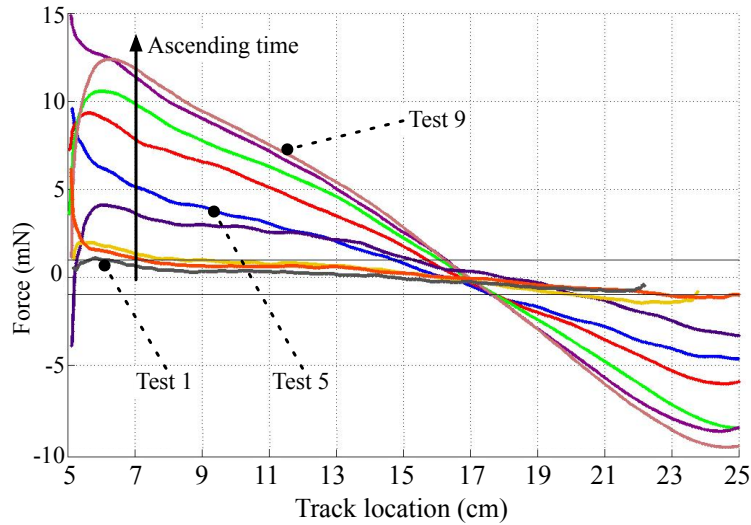
Figure 5.13: Time history of track polarization disturbance force acting on the cart

force level acting on the cart increases after each successive test. This is a result of the dielectric polarization being enhanced each time the cart remains held above the track. The max force reached is approximately 13 mN, which is significantly larger than the desired max disturbance level of 1 mN.

To quantify the extent of polarization and relaxation times, Figure 5.14 shows electrostatic potential measurements made on the testbed track. In these tests a non-contact voltage meter is used to measure the potential field from the track after an external electric field (using the sphere) is held constant for a time of 30 or 60 seconds and then removed. The external E-field is applied by charging the cart sphere to approximately 9 kV and 18 kV respectively, for both positive and negative potentials on top of the track.

Figure 5.14 demonstrates two key parameters. Firstly, the extent of the potential magnitude that is measured on the dielectric track after the charged sphere is removed and the relaxation time of the Delrin® track in this configuration. For initial charges of approximately |9| kV a track potential of |1.5| to |2| kV is measured and for a sphere charged to approximately |18| kV a track potential of |3.5| to |4| kV is measured. This is a significant potential on the track surface and
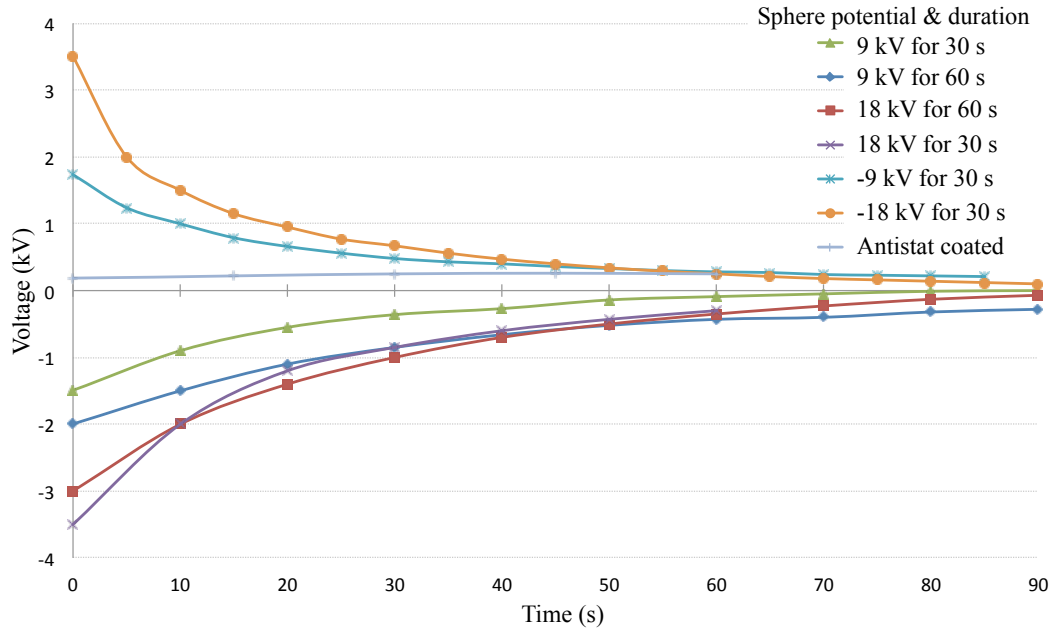
Figure 5.14: Potential measured on the track with non-contact charge sensor after charged sphere held at fixed potentials then removed; demonstrates track polarization relaxation times

explains the large disturbance forces measured. This test also indicates that it takes at least a minute to reduce back to standard noise levels which is much longer than suitable for cart motions that occur on similar time scales.

These polarization forces are extremely difficult to model. The crystal structures of dielectrics are non-homogenous as too are the external E-fields when there are multiple spheres of varying separation [92]. In addition, surface cleanliness is a fundamentally important aspect when using dielectrics and ensuring their properties are upheld. Dirt or moisture on a dielectric surface can cause current leakage under voltage applications [94]. The use of surface coatings however, does provide a solution to polarization disturbances. A antistatic coating on the dielectric track is used to attract moisture, even in low humidity environments to create a thin conductive layer, only a few molecules thick [64]. This layer then essential creates a Faraday cage around the dielectric, shielding it from the external field and preventing polarization or at least equalizing it with a layer of charged particles.

A antistatic coating on the testbed is a proven method to mitigate polarization disturbances. After coating the track, repeats of the tests in Figure 5.13 resulted in no accelerations on the cart. In addition, glide tests after the coating gave results similar to the baselines of Figure 5.11, indicating disturbances are within the required 1 mN noise level. Similarly, the sensing tests of Figure 5.14 show a measurement with antistatic coating. This measurement shows no discernible change in the polarity on the track over time, as it remains at the noise level. One observation with the antistatic coating is that it is necessary to reapply a coat to the testbed track approximately every 2 weeks to mitigate this electrostatic disturbances.

5.5.2.2   Terrestrial atmosphere and humidity interactions

The Coulomb testbed operates in a standard laboratory atmospheric environment. Differences in the results of tests conducted at different times of the year are observed. The laboratory humidity ranges from an average of 10% in winter up to 30% in the summer. The increased water vapor and its susceptibility to holding charge may have a detrimental effect on Coulomb actuation. The effects of humidity on charging is documented in the paper handling and textiles and fabrics industries [92]. In addition, ionized dust particles or the atmospheric air could contribute to reduced effective charge levels. The partial charge shielding may be similar to the charge shielding a spacecraft experiences from its local plasma environment.

In addition, measurements of the true potential fields around spherical charged objects in the laboratory show discrepancies from predicted theory. Measured potentials are always lower than theory, with positive potentials having a slightly larger discrepancy than negative. This may be a result of partial charge shielding and interaction with charged particles in the atmosphere. To further explain these atmospheric interactions a the fundamentals of atmospheric electrostatics is highlighted in the next section.

5.5.2.3   Ionization and corona discharge

A conductive sharp point or wire that is charged concentrates and enhances its electric field strength. The potential and consequently E-field may be large enough at this point that breakdown of the air (ionization) may occur within a few millimeters around the electrode [64]. The maximum field strength in a vacuum for this field emission to occurs is approximately 10^9 Vm^{-1} [64]. In air however, electrical breakdown of the gas occurs at a field strength of around 10^6 Vm^{-1}. This electrical breakdown will produce positive and negative ions and is commonly referred to as corona discharge and can create clouds of charged particles and ion winds. A good indication of corona discharge is the crackling sound of atmospherics [160].

The principle of this ionization in air is that electrons are removed from a oxygen or nitrogen molecule. The remaining positive ion will attract polar molecules, such as water, to itself within a matter of microseconds, creating a positive molecular cluster. The electron may generate further ionization but ultimately attached to an oxygen molecule creating a negative ion and ultimately a negative molecular cluster [64]. These effects may occur on the charged apparatus on the testbed and alter the operating environment and consequently partial force shielding.

A flat plate charge analyzer is used to measure the presence, attraction or creation of ions in the vicinity of the testbed during electrostatic tests. It is found that during tests with charged spheres of a fixed polarity an abundance of oppositely charged particles are present, well beyond steady state measurements in the laboratory. This also occurs when charging the spheres to both polarities. This does not indicate the source of the charged particles but alludes to an explanation of the partial shielding of the potential field measurements and reduced force productions.

To further explore this atmospheric interaction and ion measurements the current loads to the spheres from the electrostatic power supplies is analyzed. This gives a measure of the amount of charge required to obtain and maintain a fixed potential on the spheres during these interactions. The supply current results for a range of potentials from $|0 - 30 - 0|$ kV is shown in Figure 5.15. This figure shows 4 data sets; positive and negative charging of the spheres using 24 AWG cables

with PolyVinyl Chloride (PVC) compared to positive and negative charging using the equivalent polyvinyl 24 American Wire Gauge (AWG) cables that are bare.
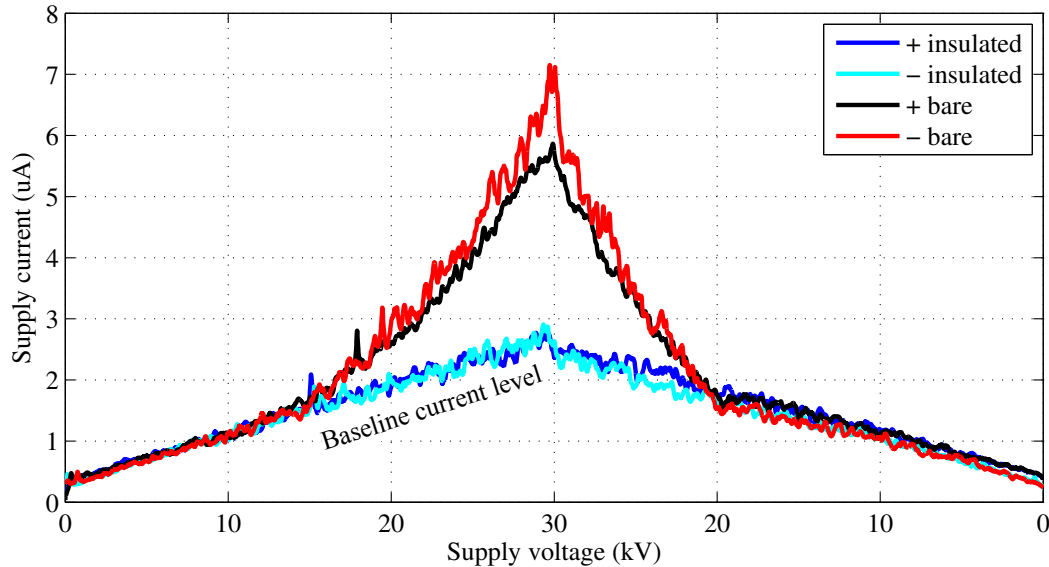
Figure 5.15: Output current supplied to sphere as a function of potential; comparing bare and insulated charge-carrying cable

The results of Figure 5.15 demonstrate a clear discrepancy in the bare and insulated cables. The insulated cable maintains a linear increase in supply current to a maximum of ≈ 3 μA. This is essentially the baseline current that is measured from the electrostatic supplies with no load attached. Indicating that there is minimal loss of charge with this setup. Alternatively, the bare wire current supply shows a similar trend to approximately 15 kV when the current requirements increase to a peak of ≈ 7 μA at 30 kV.

Another observation to make in this data set and similar tests performed is that the negative charging requires slightly more current, which correlates to earlier measurements of the E-fields and cart motions under fixed charged repulsion tests. Additionally, audible crackling is more evident and constant during the bare wire tests and correlates to these higher currents and potentials.

These observations and measurements point to the conclusion that there is interaction between the charged spheres and wires and the atmospheric atmosphere. A fine uninsulated wire

charged to kilovolt potentials will induce air breakdown and generate an ion cloud. This corona discharge is the principal of the electrostatic precipitator that is used in particulate removal and air cleaning, as well as the infamous "ion lifter." Electrostatic precipitators operate at kilovolt-level potentials, equivalent to that on the testbed. It is believed that at high potentials the bare wire generates an ion cloud that envelopes the spheres and increases the partial shielding similar to a space plasma. This is an interesting finding as it could lead to a simple and effective method of mimicking dynamically motions in a space plasma. To mitigate these wire ionization effects the high-flex, stranded 36 AWG wire with FEP insulation is used.

5.6   Summary

This chapter provides details on the design, development and operation of the dedicated Coulomb testbed. Firstly, laser inaccuracies and mechanical disturbances are identified and mitigated below the $\pm$ mN level. This ensure a actuation signal to noise ratio of at least 1. Uncharged and charged glide tests are performed to ensure disturbances below this level are confirmed prior to all Coulomb relative motion tests. As demonstrated through these experimental results and sensing apparatus the testbed is being utilized as a platform to understand the complexities of electrostatic actuation. This includes electrostatic influences of polarization and wire ionization that are successfully mitigated.

However, isolating and mitigating all atmospheric interactions is an extremely difficult task that requires operation in a vacuum, which is beyond the scope of this dissertation. As an alternative approach, analysis of these remaining terrestrial interactions using relative motion experiments is necessary. This can only be achieved with mechanical and electrostatic disturbances significantly reduced to give a baseline disturbance noise level of ± 1 mN, which is demonstrated in this chapter. The next chapter uses this low disturbance test environment to estimate terrestrial partial shielding parameters similar to the space-based plasma modeling.

Chapter 6

Terrestrial Coulomb relative motion experimental results

With the primary testbed disturbances identified and reduced to a baseline noise level below 1 mN it is possible to perform electrostatic actuation. Simple tests using a single cart demonstrate repulsive and attractive relative motion with Coulomb forces. This is a step forward in the progress of CFF implementation as it shows that Coulomb forces can be safely and successfully applied in a laboratory atmospheric environment. This chapter documents the experimental progress of performing repulsion and attraction tests to estimate the atmospheric interactions and force shielding. These parameters are used to propose a terrestrial Coulomb force model for use on the testbed. This is used as a representative model of the terrestrial forces and ultimately allows control algorithm performance verification and expands the future use of the testbed if the produceable forces are accurately known. Comparisons are made between these atmospheric interactions and the space plasma shielding a Coulomb formation would experience. Finally, autonomous position feedback control is implemented and the experimental results are compared to simulations using the developed terrestrial force model.

6.1   Candidate terrestrial force model

The first is a series of simple one-way tests that use a constant sphere potential. Not only does this research document the design and development of the apparatus, it utilizes the resulting testbed to expand the knowledge of atmospheric charge actuation. The objective is to produce electrostatic forces and understand interactions with the apparatus and environment to develop a

model of this terrestrial Coulomb force.

To meet this goal, successful Coulomb actuated relative motion experiments are used to detect and quantify electrostatic interferences. Results of fixed charged, one-way tests where the cart is either repelled or attracted, relative to the stationary sphere, are used. A graphical representation of the testbed setup for Coulomb motion tests is shown in Figure 6.1. The cart's position L is measured with the laser. With the cart initially at rest with a separation distance $x = 30$ cm between sphere centers it is driven under Coulomb repulsion along the track length. Alternatively it is driven with an initial separation of 80 cm toward the stationary sphere under attractive forces. Glide tests prior to actuation tests confirm disturbance forces down to the baseline noise levels.
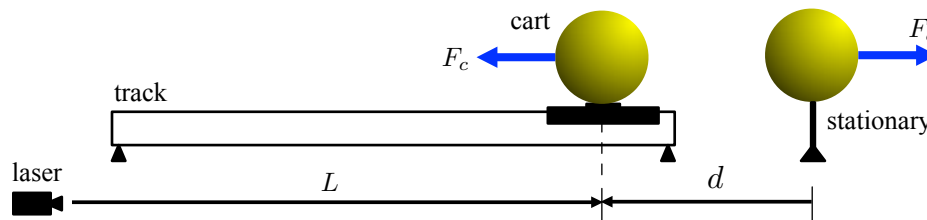
Figure 6.1: Illustration of testbed setup for fixed-potential, Coulomb repulsion tests

Two separate force models for attractive and repulsive forces are developed and applied independently. This is due to different characteristics and force production, as shown in earlier chapters, and allows for more accurate fits to the terrestrial environment forces. Candidate terrestrial Coulomb force models are based on the plasma partial shielded space forces. These plasma nonlinear models are fitted to experimental data by computing an estimate of the plasma-like parameters.

While not a direct comparison between the terrestrial atmosphere and space plasma can be made there are similarities in the force production. The results, presented here highlight correlations between the partial charge shielding experienced in the laboratory atmosphere to the Debye length shielding from a space plasma.

The estimation of the partial shielding model is performed using Coulomb repulsive and

attractive tests and position measurements made with the laser. A nonlinear least-squares batch estimator is used for this study as all data is post-processed. This processor can adopt a variety of proposed shielding models and provide a solution with imperfect initial conditions and noisy data that in this application is generally more accurate than a sequential estimator. Also a batch estimator better utilizes all data measurements in the solution without concern for covariance saturation. In this section the attractive and repulsive force models are presented.

6.1.1   Attractive force model parameters

The proposed plasma partial force shielding model that includes capacitance and induced effects of Equation 3.39 is used as a baseline for the terrestrial attractive force model. The two parameters that are estimated are the shield length, $\bar{\lambda}_D$, and shield radius, $\bar{R}$. The modified space plasma force model used in this estimation analysis is:

$$F_{lab} = k_c \frac{\bar{q}_A \bar{q}_B}{\bar{d}^2} \text{Exp}\left[-\frac{(\bar{d} - \bar{R})}{\bar{\lambda}_D}\right] \left(1 + \frac{(\bar{d} - \bar{R})}{\bar{\lambda}_D}\right) \tag{6.1}$$

where the effective sphere separation, $\bar{d}$, accounts for uneven charge distribution using Equation 3.24, which is computed using the testbed sphere radius R, not the estimated shield radius $\bar{R}$. To compute the effective charge, $\bar{q}$, including the combined capacitance of each charge and the plasma, the following is inverted:

$$\begin{bmatrix} V_A \\ V_B \end{bmatrix} = k_c \begin{bmatrix} \frac{1}{\bar{R}}\left(\frac{\bar{\lambda}_D}{\bar{R} + \bar{\lambda}_D}\right) & \frac{1}{d}\left(\frac{\bar{\lambda}_D}{\bar{R} + \bar{\lambda}_D}\right)\text{Exp}\left[\frac{-(d - \bar{R})}{\bar{\lambda}_D}\right] \\ \frac{1}{d}\left(\frac{\bar{\lambda}_D}{\bar{R} + \bar{\lambda}_D}\right)\text{Exp}\left[\frac{-(d - \bar{R})}{\bar{\lambda}_D}\right] & \frac{1}{\bar{R}}\left(\frac{\bar{\lambda}_D}{\bar{R} + \bar{\lambda}_D}\right) \end{bmatrix} \begin{bmatrix} \bar{q}_A \\ \bar{q}_B \end{bmatrix} \tag{6.2}$$

Based on nonlinear fit results and residual analysis the force model of Equation 6.1 differs slightly from the original space plasma form with an additional -$\bar{R}$ term. This more accurately captures the force over the entire track testing range, while not significantly changing the force model from the base plasma one.

6.1.2 Repulsive force model parameters

For the repulsive force model, Equation 6.1 that is based on the proposed plasma partial force shielding model of Equation 3.39 is also used. The same two parameters ($\bar{\lambda}_D$ and $\bar{R}$) are estimated. The repulsive force parameters are estimated separately as the force magnitudes on the testbed are substantially different than the attractive case. The sphere separation, $\bar{d}$, accounts for uneven charge distribution during repulsive forces using Equation 3.22. A modification here from the attractive force is that the vacuum position dependent capacitance is used to compute the sphere charges ($\hat{q}$) by inverting:

$$
\begin{bmatrix} V_A \\ V_B \end{bmatrix} = k_c \begin{bmatrix} 1/\bar{R} & 1/d \\ 1/d & 1/\bar{R} \end{bmatrix} \begin{bmatrix} \hat{q}_1 \\ \hat{q}_2 \end{bmatrix} \tag{6.3}
$$

This use of the vacuum capacitance model is based on nonlinear fit results and residual analysis to more accurately fit the experimental data.

6.2 Parameter fitting using actuation experiments

The force model is fitted to fixed-potential, one-way repulsion and attraction motion experiments. Numerous tests are conducted over a range of potentials from 10 kV to 30 kV, of both positive and negative polarities. One set of these tests for both attraction and repulsion cases is shown in Figures 6.2(a) and 6.2(b) respectively.

Shown in these figures is the calculated force acting on the cart that is differentiated from the raw position data measured from the laser. This force data is plotted as a function of track location, where 35 cm corresponds to the closest sphere approach. A cart at this location is separated by 30 cm center to center from the stationary sphere. Also shown in each figure is a polynomial fit to the force data in green. This data fit also has any track uncharged glide test biases removed. These track biases are uniquely measured for each day of the test being conducted and are only accepted if below the 1 mN requirement. This is necessary, particularly for the low potential tests and the repulsion tests where the Coulomb actuation signal to noise is very low.

(a) Attraction data

(b) Repulsion data
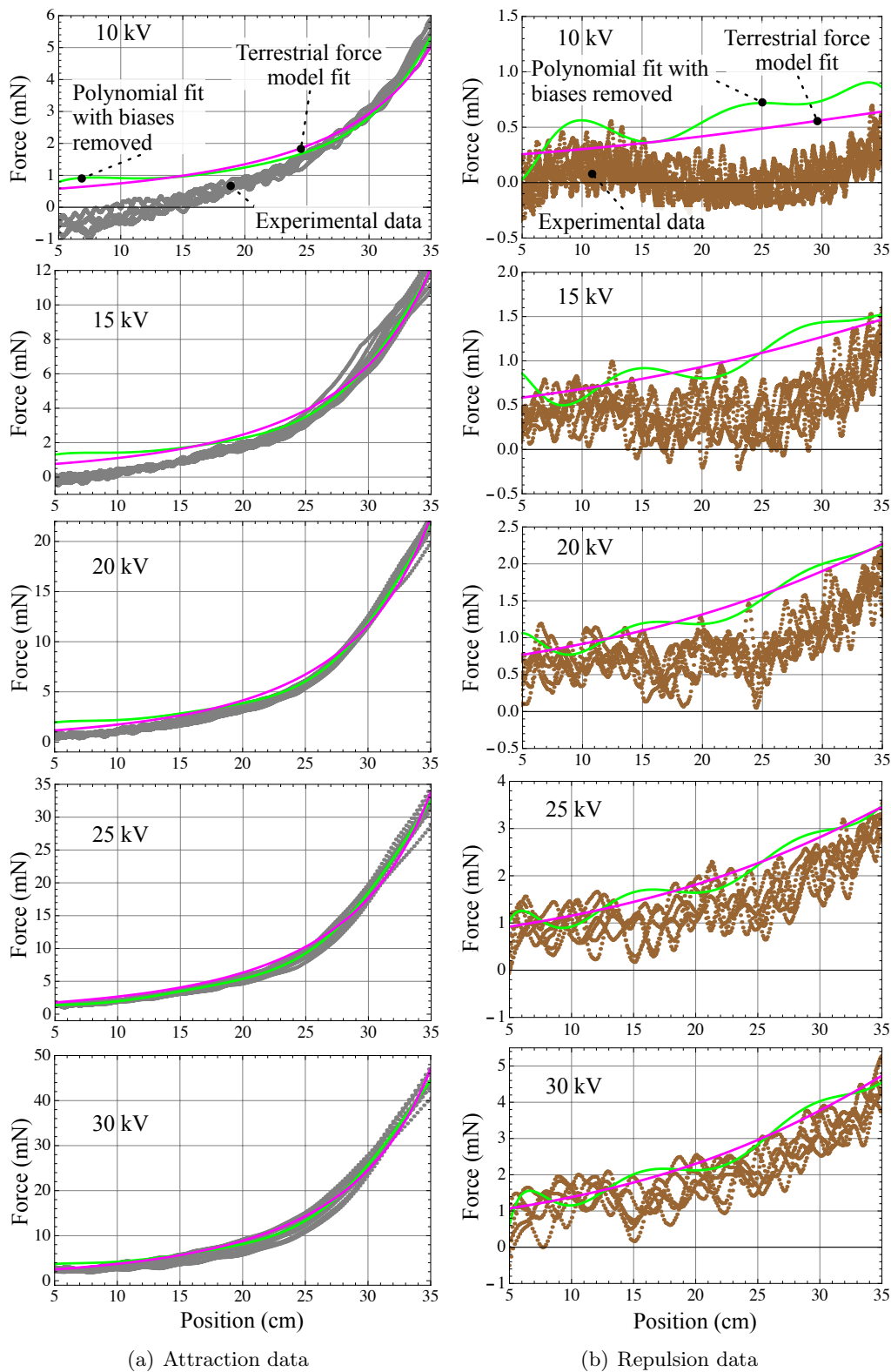
Figure 6.2: Fixed-potential, one-way test data and estimated terrestrial model for each potential

Also shown in Figures 6.2(a) and 6.2(b) is the fit of the proposed plasma-derived force models of Section 6.1. This fitted terrestrial model is shown in each of the figures. Visually, the model fits the data with biases removed well. The solutions of these plasma-like parameters for these fits are shown in Table 6.1. Also shown in this table is the coefficient of determination, $\mathfrak{R}^2$, which gives a statistical measure of fit along with the standard deviation.

Table 6.1: Estimated Coulomb force model parameters and statistical fits for the data shown in Figure 6.2

Tests	Shield length $\bar{\lambda}$ (m)	Shield radius $\bar{R}$ (m)	$\mathfrak{R}^2$	Standard deviation (mN)
Attraction				
10 kV	0.482	0.158	0.994	0.161
15 kV	0.195	0.146	0.996	0.288
20 kV	0.168	0.151	0.997	0.469
25 kV	0.171	0.144	0.998	0.624
30 kV	0.172	0.135	0.997	0.876
Repulsion				
10 kV	1.291	0.462	0.806	0.123
15 kV	1.344	0.452	0.976	0.112
20 kV	0.491	0.277	0.995	0.115
25 kV	0.432	0.137	0.995	0.162
30 kV	0.458	0.054	0.996	0.200

The shield length $\bar{\lambda}$ and shield radius $\bar{R}$ results are also plotted in Figures 6.3 and 6.4 for attraction and repulsion fitting respectively. The results are shown as a function of sphere potential. In addition to the results of the experimental data shown in Figure 6.2 and given in Table 6.1, two repeat sets of data from different days are also provided. While the results are similar, the discrepancies indicate the sensitivity of estimating the parameters with experimental data and the variations that can arise between different testing conditions.

6.2.1 Terrestrial and plasma force shielding parameters

Parameters of space based Coulomb force models are fitted to terrestrial experimental data. This analysis gives a measure of accuracy of these fits and quantifies the effectiveness of the testbed

(a) Debye length $\bar{\lambda}$ solutions

(b) Shielding radius $\bar{R}$ solutions
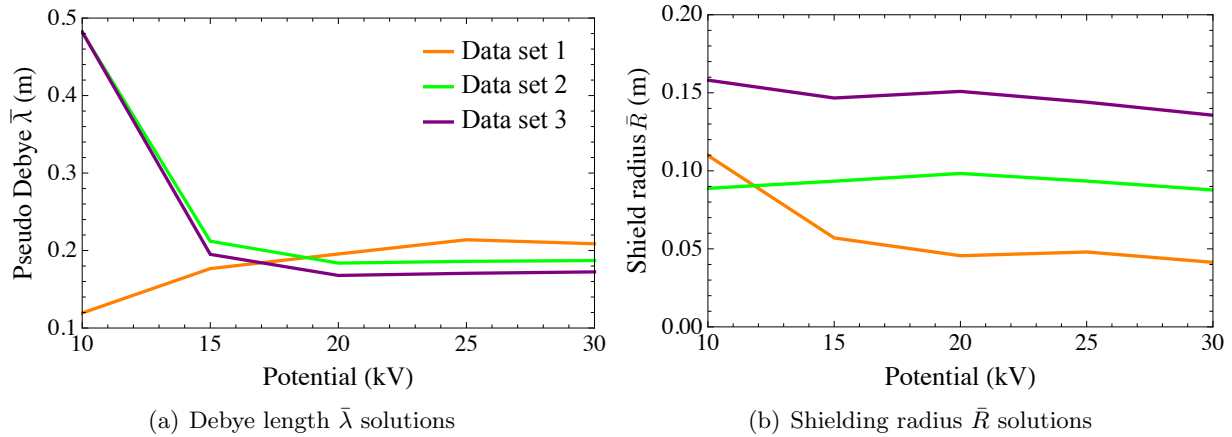
Figure 6.3: Parameter estimation solutions for attraction data sets 1 through 3

(a) Debye length $\bar{\lambda}$ solutions

(b) Shielding radius $\bar{R}$ solutions
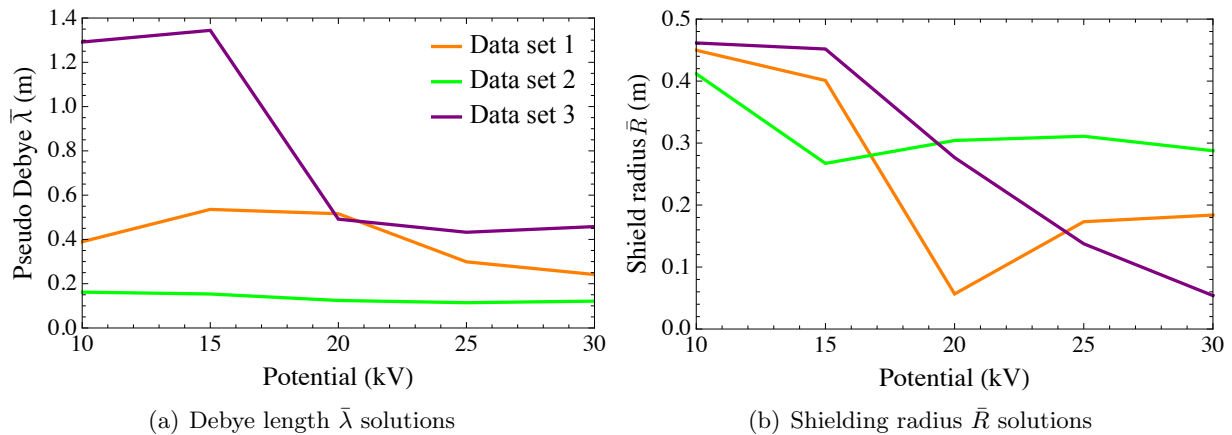
Figure 6.4: Parameter estimation solutions for repulsion data sets sets 1 through 3

apparatus to be used for force estimation. These results indicate that the space-based plasma force models offer a good fit to the terrestrial actuation forces and capture partial shielding characteristics. For the remainder of this dissertation the force model of Equation 6.1 with both repulsive and attractive parameters fitted to experimental data is referred to the "Terrestrial model".

A summary of the solution of each of these parameter values ($\bar{\lambda}$ and $\bar{R}$), averaged using all three data sets is shown in Table 6.2. For this terrestrial model the shield length $\bar{\lambda}$ solutions (at higher potentials) are in the vicinity of 15-25 cm for the attraction cases and in the range of 10 cm to 50 cm for the repulsion tests. The average value for the shield length is approximately 20 cm and 25 cm for the attractive and repulsive cases respectively. While this has no direct correlation to a

plasma Debye length, it quantifies the level of shielding experienced on the testbed, when using the space-based model. This is a distance of approximately 1 sphere diameter, which helps quantify the limits and capabilities of the Coulomb actuation force. This is used solely to give a measure of the partial-shielding-like effects that are observed on the testbed in the terrestrial environment. Regardless, Coulomb actuation is demonstrated along the whole length of the track that is longer than this shield length.

Table 6.2: Average of estimated shielding length and radius

Force model	shield length $\bar{\lambda}_D$ [cm]	shield radius $\bar{R}$ [cm]
Attractive force	20	12
Repulsive force	25	20

The shield radius $\bar{R}$ solutions have a range of values of 5 cm to 15 cm for the attraction tests and 10 cm to 45 cm for the repulsion cases. The average value is approximately 12 cm and 20 cm for the attractive and repulsive cases respectively. Again, this is only an estimated parameter of a model that resembles a space-based Coulomb force model. Interestingly though, the values resemble the true radius of the sphere which is 12.5 cm. This is an important result that gives merit to modeling the terrestrial actuation forces with space-based plasma models and using the partial shielding to account for electrostatic interactions that are being investigated.

6.2.2   Actuation force signal to noise ratios

In analyzing these parameter solutions it is important to consider the actuation force signal to noise ratio during each of these tests. The signal to noise ratio for the testbed spheres charge over the same 10 kV to 30 kV potential range is shown in Figure 6.5 for attraction and repulsion tests. Given that the force is a function of sphere separation, which varies during the course of a test, the figures show contour lines over a range of testbed separation distances. The vacuum model is used to compute this actuation force and includes combined system capacitance and uneven charge distribution effects from Equation 3.25. Although the fitted results predict shielded forces on the

testbed, this vacuum model is used here to give a conservative estimate.

Also highlighted in each figure is the region where the SNR is less than unity. This is a region where we do not expect to obtain satisfactory results from the estimation process as the Coulomb forces do not dominate cart motion. This gives us a measure of the estimation limitations on the testbed with the current apparatus. For the attraction forces, separations larger than 50 cm, center to center separation, and potentials less than 15 kV have an SNR close to unity. For the repulsion case this unity range extends to cover a wider variety of separations and potentials. Potentials less than 20 kV and large separations require caution due to very low SNR. For potentials below 15 kV at any separations on the track the Coulomb actuation forces are down in the noise levels and the estimation results will suffer.

These SNR results of assist in identifying variations in the parameter results identified in Figures 6.3 and 6.4. Two key findings come from analyzing the SNR results of Figure 6.5. Firstly, the large variation in solutions at low potentials (10 and 15 kV) for both repulsion and attraction is contributed to these low SNR values. Similarly, due to repulsive forces being lower magnitude and SNR there is a greater variance in the parameter solutions, across all potentials, compared to the attraction tests.

The results of this section give confidence in accurately modeling the terrestrial Coulomb forces on the testbed. A terrestrial force model that captures partial-shielding characteristics is developed with parameters fitted to fixed-potential, one-direction motion tests. With this terrestrial force model it is possible to look at more advanced applications such as autonomous position control and compare simulations with this model. This is achieved in the following sections.

6.3   Autonomous feedback position control experiments

The next progression of the testbed is enabling autonomous position feedback control with Coulomb forces. This enables testing of control algorithms and mimicking 1-D constrained orbital motions when aligned along the principal orbit frame axes. This dynamical system is replicated by either leveling the test track or adding a small tilt to bias the relative motion in one direction.
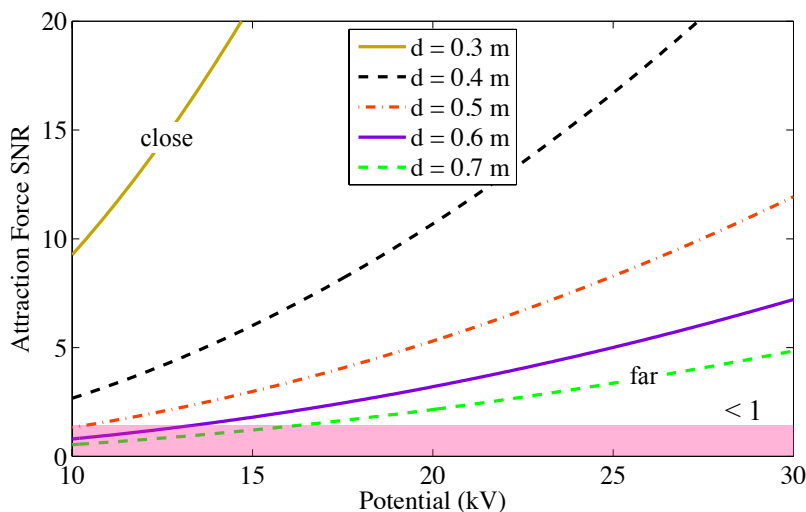
(a) Attraction forces
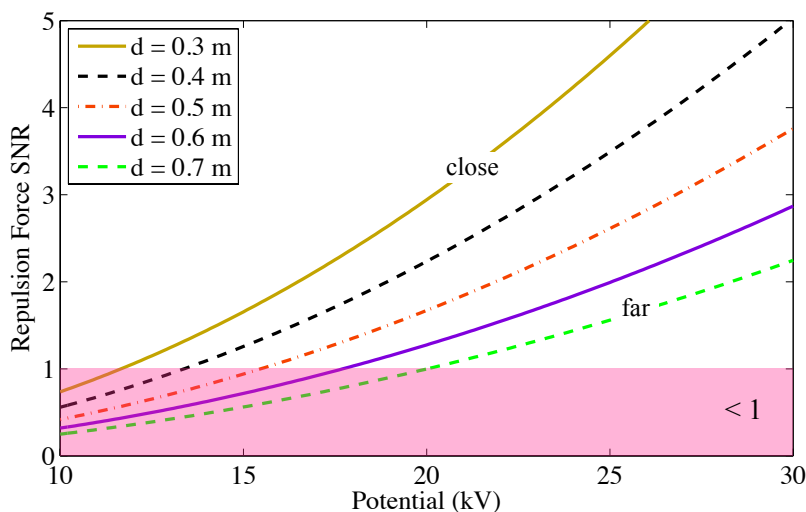
(b) Repulsion forces

Figure 6.5: Force to noise, signal to noise ratio for testbed potentials and sphere separations

The developments of a robust, real-time charge feedback control algorithm is presented and implementations results are presented and compared to simulations using the fitted terrestrial force parameters and system characteristics models.

The terminology used in the testbed control algorithm is defined in Figure 6.6. The desired position of the cart x_r defines the tracking error $\delta x = x - x_r$. The separation variable, x, is used here in instead of d, to signify these are position control developments and experiment results using varying potential levels.
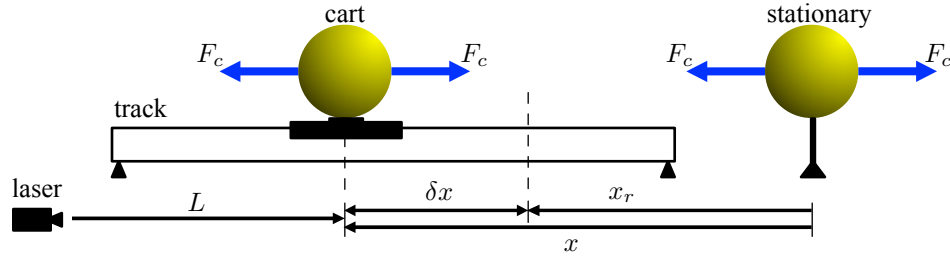
Figure 6.6: Illustration of testbed setup for position control and variable definitions

The generic equation of motion (EOM) for the cart on the track is defined by:

$$\ddot{x} = f(x, u, t) = \frac{1}{m} \left[F_c + f_{\text{system}} + f_{\text{unknown}} \right] \tag{6.4}$$

where m is the cart mass, f_{system} represents known forces acting on the system (such as intentional gravity biases), f_{unknown} are unmodeled disturbance forces and F_c is the Coulomb actuation force. This could be any force model presented earlier, including the partially shielded model based on experimental data. For the interest of simple control development the fundamental vacuum point charge model $F_c = \frac{k_c Q}{x^2}$ is used, where the control parameter is the combined charge product $Q = q_1 q_2$. Although this model does not fit the true dynamics of the cart, the controller is designed in a robust way to allow for generic force models. This is suitable for purposes such as this dissertation research, where models, such as the terrestrial model, are under investigation and performance is being evaluated.

6.3.1 Constrained 1-D charged relative orbit dynamics

The testbed autonomous position control is implemented to mimic restricted 1-D orbital motion. The intent of the testbed and associated control methodology is not to simulate actual relative orbit dynamics. Rather, restricted 1-D relative motions are feasible. In this section the constrained 1-D Coulomb relative orbit equations of motion are generated. These equations are compared to what can be achieved on an inclined track and the resulting Coulomb charge products required for control.

To develop the orbit relative equations of motion the rotating Hill frame $\{\hat{\boldsymbol{o}}_r, \hat{\boldsymbol{o}}_\theta, \hat{\boldsymbol{o}}_h\}$ is used. This frame is fixed at the formation center of mass and has its axes aligned with the orbit radial, along-track and out-of-plane directions. The spacecraft position $\boldsymbol{r}_i$ is expressed in this Hill frame with Cartesian $\{x, y, z\}$ coordinates. Figure 6.7 illustrates the rotating Hill frame, as well as the three possible 2-craft charged relative equilibria configurations aligned with the orbit radial, along-track and out-of-plane axes.
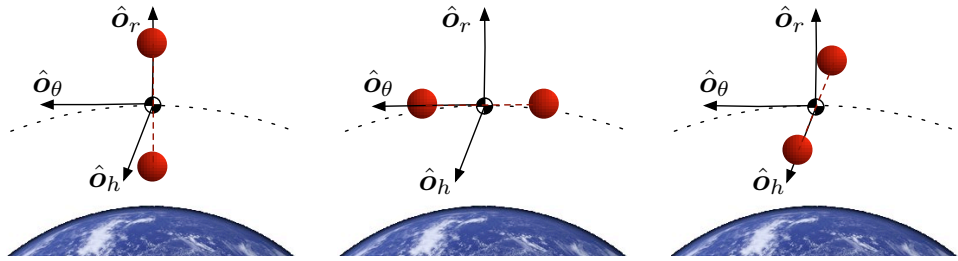
Figure 6.7: Charged, two craft equilibria alignment along the Hill frame principal axes

Equations (6.5) show the linearized Clohessy-Wiltshire-Hill (CWH) equations subject to electrostatic actuation in a plasma environment [100]. The CWH equations define the motion of a satellite relative to the circularly orbiting Hill frame. With a formation of N Coulomb controlled spacecraft the CWH equations of the ith spacecraft relative to the orbit reference is defined by: [100]

$$\ddot{x}_i - 2\Omega\dot{y}_i - 3\Omega^2 x_i = \frac{k_c}{m_i} \sum_{j=1,j\neq i}^{N} \frac{(x_i - x_j)}{|\boldsymbol{r}_i - \boldsymbol{r}_j|^3} q_i q_j e^{-r_{12}/\lambda_d} \left(1 + \frac{r_{12}}{\lambda_d}\right) \tag{6.5a}$$

$$\ddot{y}_i + 2\Omega\dot{x}_i = \frac{k_c}{m_i} \sum_{j=1,j\neq i}^{N} \frac{(y_i - y_j)}{|\boldsymbol{r}_i - \boldsymbol{r}_j|^3} q_i q_j e^{-r_{12}/\lambda_d} \left(1 + \frac{r_{12}}{\lambda_d}\right) \tag{6.5b}$$

$$\ddot{z}_i + \Omega^2 z_i = \frac{k_c}{m_i} \sum_{j=1,j\neq i}^{N} \frac{(z_i - z_j)}{|\boldsymbol{r}_i - \boldsymbol{r}_j|^3} q_i q_j e^{-r_{12}/\lambda_d} \left(1 + \frac{r_{12}}{\lambda_d}\right) \tag{6.5c}$$

where m_i is each spacecraft's mass and the system's center of mass has an orbital rate $\Omega = \sqrt{\mu/R_c^3}$ with R_c being the orbit radius and μ the gravitational constant. These equations are constrained to 1-D motion along the orbit radial, along-track and out-of-plane directions and compared to possible testbed 1-D motions. Given a two craft formation and ignoring any plasma Debye shielding, the

1-D relative equations of motion become:

$$\ddot{x}_i - 3\Omega^2 x_i = \frac{k_c}{m_i}\frac{Q}{(x_i - x_j)^2} \tag{6.6a}$$

$$\ddot{y}_i = \frac{k_c}{m_i}\frac{Q}{(y_i - y_j)^2} \tag{6.6b}$$

$$\ddot{z}_i + \Omega^2 z_i = \frac{k_c}{m_i}\frac{Q}{(z_i - z_j)^2} \tag{6.6c}$$

where $Q = q_i q_j$ is the combined charge product. Equation (6.6a) represents the restricted 1-D orbit radial relative motion. This equation is the form of an unstable oscillator. The result being that the spacecraft will naturally drift apart due to the gravity gradient, expressed by the $(-3\Omega^2 x_i)$ term. However an equilibrium condition is reached (x_i held constant) if an attractive Coulomb force is applied. This is achieved with a heterogeneous charge product solution [7]:

$$Q = -3\Omega^2 x_i(x_i - x_j)^2\frac{m_i}{k_c} < 0 \tag{6.7}$$

This requires each vehicle to have an opposing charge polarity. To mimic this operating scenario on the testbed, the track is intentionally tilted so a gravity bias force naturally repulses the cart from the stationary sphere. Attractive Coulomb control (Q) is used to drive and hold the cart at a desired separation distance.

Similarly, Equation (6.6c) represents the restricted 1-D out-of-plane relative motion, assuming no perturbations. The spacecraft will naturally drift together due to the gravity gradient, expressed by the $(+\Omega^2 z_i)$ term. However an equilibrium condition is reached (z_i held constant) if a repulsive Coulomb force is applied. This is achieved with a homogeneous charge product solution [7];

$$Q = \Omega^2 z_i(z_i - z_j)^2\frac{m_i}{k_c} > 0 \tag{6.8}$$

This requires each vehicle to have an equivalent charge polarity. This configuration is comparable to experiments on the testbed with an intentionally inclined track providing a constant gravity bias force naturally attracting the cart to the stationary sphere. Repulsive Coulomb control (Q) is used to drive and hold the cart at a desired separation distance.

Note that these two inclined track setups do not match the constrained relative orbit motion precisely. The test track has a constant acceleration bias, while the orbit motion is a position

dependent bias. However, both setups result in the nominal charge product Q being nonzero once the craft reaches the desired equilibria state.

Equation (6.6b) represents the restricted 1-D along-track relative motion that is inherently stable without perturbations. To maintain equilibrium (y_i constant) requires no charge, $Q = 0$. This condition is simulated on the testbed with a level track and no bias accelerations. Of these three simulations, the along-track direction is the most challenging to implement because of the need to have a flat and level track. Even small residual disturbances can move the cart once it reaches its desired location. The orbit radial and normal direction simulations are easier to implement since any track un-level biases can be exploited to provide slight gravitational pull or repulsion to simulate this charged axial orbital motion. Here the small disturbances are over-shadowed by the larger intentional gravity bias of the track tilt.

To put these 1-D dynamic analyses into perspective, consider an example two-craft system operating in a radial configuration in GEO. The radial differential gravity force magnitude linearizes to [137]:

$$\delta F_x \approx m \frac{3\mu}{R_c^3} x \tag{6.9}$$

where m is the spacecraft mass and x is the spacecraft separation distance. Consider two craft of 50 kg mass each, aligned in the radial direction with a separation of 20 m. At GEO the craft experience a repulsive gravity gradient force of approximately 16 μN. To overcome this force with Coulomb thrust requires a heterogenous charge of $Q \approx -0.71$ pC calculated using the basic plasma point charge model in Equation (3.36) with a plasma Debye length of 200 m. This corresponds to a required voltage magnitude of approximately 15.2 kV, calculated using the isolated charge relationship of Laplace in Equation (3.5) with a spherical craft of 0.5 m radius. Although only, approximate, it gives an indication of the magnitudes required for this idealized case.

Similarly, consider the same two spacecraft operating in an out-of-plane configuration at GEO. The differential out-of-plane gravitational force magnitude linearizes to [137]:

$$\delta F_z \approx m \frac{\mu}{R_c^3} z \tag{6.10}$$

For this idealized case of point charges in a plasma and a out-of-plane separation of $z = 20$ m the attractive force is approximately 5.3 μN. To overcome this force with Coulomb control requires a charge of $Q \approx 0.24$ pC, corresponding to a spacecraft voltage magnitude of 8.8 kV.

6.3.2   Testbed charge feedback control law

A goal of this research is to demonstrate stable position feedback control actuated with Coulomb forces. A PID controller is implemented to stabilize the cart motion about a desired fixed track location. This robust control law is justified given the complexities of terrestrial close proximity electrostatic interactions and force modeling that is under investigation. This controller accounts for any force model and unknown disturbances as well as introducing system damping which is not inherent to the testbed. A feedback linearizing control solution is chosen of the form:

$$Q = \frac{x^2}{k_c}\Big(- k_D\delta\dot{x} - k_P\delta x - k_I \int_0^t \delta x \mathrm{d}t - f_{\text{system}}\Big) \tag{6.11}$$

where k_P, k_D, and k_I are positive constant controller gains, and $\delta x = x - x_\text{r}$ is the tracking error with respect to constant reference position x_r. This non-linear charge feedback control law Q features feed-forward compensation when known biases f_{system} are acting on the hovering cart. The integral feedback component adds robustness to the steady state system response accounting for discrepancies in the modeling of f_{system} and the electrostatic disturbances. As this research progresses and models of the electrostatic interactions are generated they can be added to this control law. Substituting the control law Q into the equation of motion in Equation (6.4) results in the following closed-loop dynamics:

$$\delta\ddot{x} + k_D\delta\dot{x} + k_P\delta x + k_I \int_0^t \delta x \mathrm{d}t = f_{\text{unknown}} \tag{6.12}$$

With positive control gain values the feedback linearized system response is stable assuming the unmodeled disturbance f_{unknown} is bounded. Note that to implement the charge feedback control Q in Equation (6.11), it is still required to map Q into individual charges q_i and ultimately voltages V_i for the testbed. In the following numerical and experimental simulations the simple solution

of $q_1 = -\sqrt{|Q|}$ and $q_2 = Q/q_1$ is used. This solution is chosen as it is easily implemented on the testbed. For spacecraft the value of q_i can be selected based on a weighting of quantitative parameters such as charge control power usage, charge saturation or equilibrium charge which are functions of the local space plasma and operating conditions.

6.3.3   Sloped-track position control experimental results

The Coulomb control algorithm is implemented on an intentionally inclined track that slopes upward away from the stationary sphere. The testbed dynamics are similar to a 1-D constrained out-of-plane orbit configuration. The experimental results here are directly compared to simulation results that are computed using the vacuum point charge force model of Equation 3.4. This model is chosen solely as a baseline to demonstrate the discrepancies.

System performance and gain selection of the controller is simulated using Equation (6.11) prior to implementation on the testbed. Table 6.3 shows the desired performance parameters for the simulation and experimental results. It also lists the controller gains for the simulation which are selected to give an underdamped response without saturation, an overshoot $< 20\%$ and a 5% settling time of 25 seconds. The simulation has a 2.0 mN bias force added and the track is tilted to give a known mechanical gravity bias of approximately 2 mN. These simulated performances are characteristic only have the vacuum point charge model, and do not give the same response as the testbed cart, but give a target to design within.

Table 6.3: Desired performance and control gains used

Overshoot:		$< 15 \%$	
5% Settling time:		≈ 25 s	
Control gain:	k_D	k_P	k_I
Value:	1800	300	100

The cart is initially at rest at a separation of 30 cm (center-to-center) from the stationary sphere and ascends the track under a repulsive Coulomb force. Figure 6.8 displays both the simu-

lation and experimental results of driving the cart a total of 12 cm up slope to a final separation
of 42 cm.
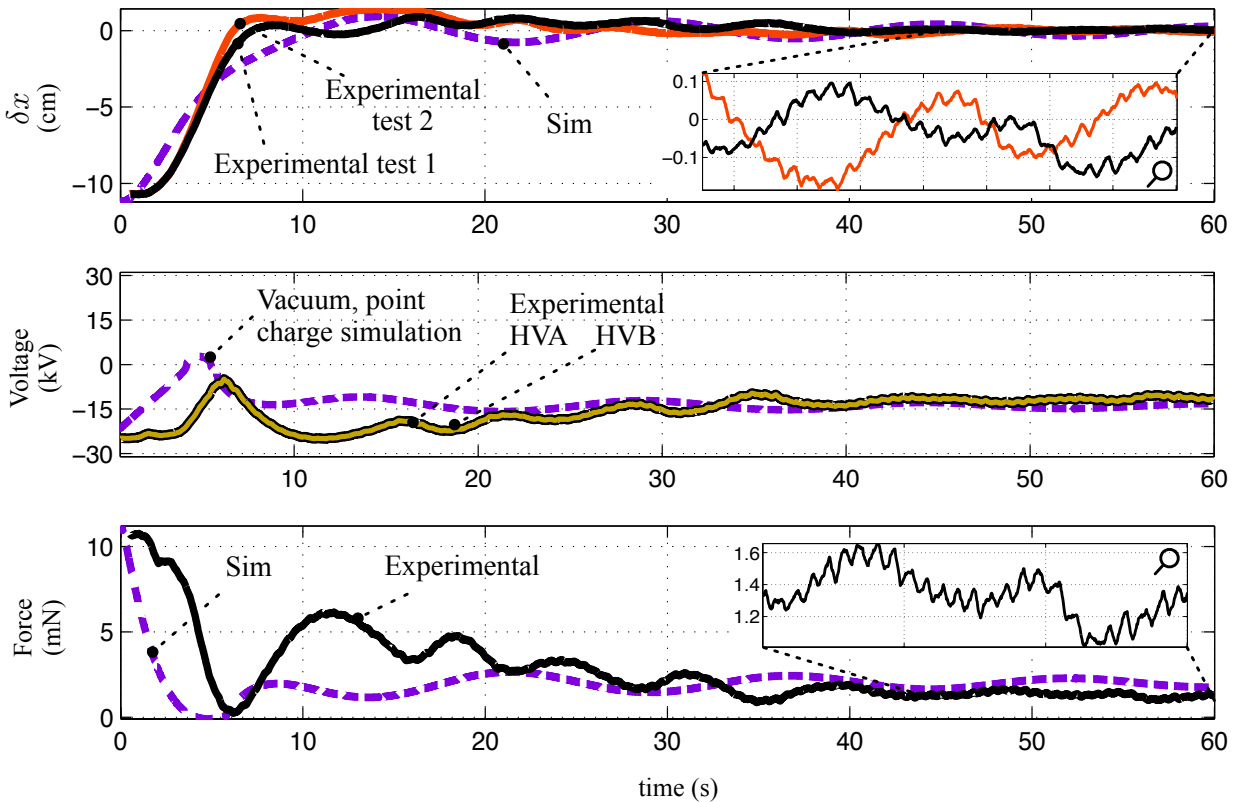
Figure 6.8: Results of experimental cart control on a sloped track that mimics two craft, 1-D
restricted, out-of-plane orbital motion

The cart tracking error δx is shown in Figure 6.8(a) for two identical experimental results and
the simulated response. A magnification showing the settlement of the cart at the desired location
is also shown for each test. Figure 6.8(b) shows the voltage levels that are used to control the cart
during test 1 for both the cart sphere (A) and the stationary sphere (B). By design, the spheres are
driven to negative potentials when repulsive forces are required. Figure 6.8(c) shows the analytic
Coulomb force acting on the cart in test 1 using the basic vacuum point charge relationship defined
in Equation 3.4.

The experimental and simulation results share similar characteristics. The system controlled
experimental response adequately meets the nominal performance parameters outlined in Table 6.3

and the cart settles to $\pm$ 1 mm of the desired location. The charge required to drive the cart this distance and hold the position on the inclined track remains a constant homogeneous charge (repulsive force).

The resulting voltage to maintain the cart at this location is measured to be ≈ -12 kV which equates to a force of ≈ 1.4 mN, calculated using Equation 3.4, whereas the simulation force is 2.0 mN. Using glide test data collected after these out-of-plane experiments (with no electrostatics) it is found that the acceleration acting on the cart at this location equates to ≈ 2 mN. Taking into account the combined system capacitance and induced charge effects, modeled with Equation 3.25 the expected force computed is only 0.76 mN. However, care must be taken in comparing these force values as this is in the separation distances and potential levels where the SNR is close to unity.

Successful experiments demonstrating control on flat and inclined tracks resembling the 1-D constrained motion of orbit-normal and orbit-radial configurations have also been performed. The results of these tests were presented by Seubert and Schaub at the AAS/AIAA Astrodynamics Specialist Conference in August 2009 [138].

An observation made with this feedback experimental results and others is that heterogenous charge solutions (repulsion forces), require reduced sphere separations to allow steady state controllability within desirable timing and consistency. On the contrary, steady state heterogenous charge solutions (attractive forces) are capable of settling smoother and faster as the force production has a much larger SNR.

Also, at steady state there are small amplitude oscillations in both the distance measurement and the voltage settings. These oscillations at ≈ 2 Hz are a direct result of the errors in the laser positioning highlighted in Section 5.2.

While the overall simulation and experimental cart motions are similar there are discrepancies. To really improve the simulated system response it is beneficial to simulate the cart motion using the fitted partial shielded model of the previous section and compare to testbed experimental results as achieved in the next section.

6.4   Comparing experimental results to simulations with terrestrial model

With mechanical disturbances significantly reduced a number of autonomous feedback position control tests are performed to allow comparison to the candidate terrestrial force model fitted to one-way data. For these experiments the track is flat and level with all prior disturbances below the 1 mN noise level. Due to these low baseline disturbances the full range of track motion is used for these experiments. It also allows both initial repulsion (cart starts close) and initial attraction (cart starts far away) tests.

In these series of tests the cart is driven from an initial position far from the stationary sphere (initially attraction forces) to a desired location that is 22 cm away. The position error of 10 identical tests is shown in Figure 6.9. The results demonstrate a smooth over shooting response that settles as desired within approximately 30 seconds. There is good repeatability between each of these tests.
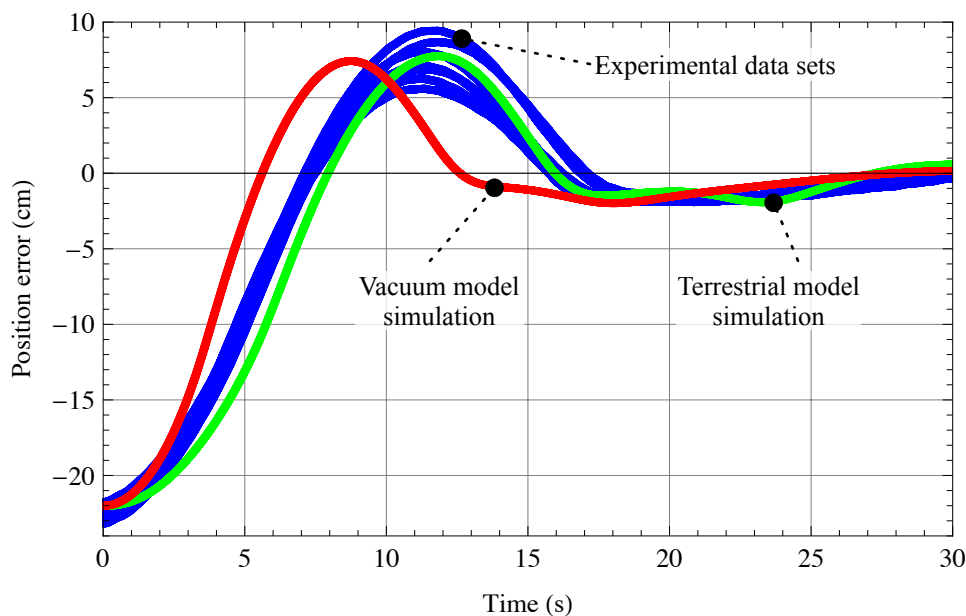
Figure 6.9: Case 1: Comparison of simulated cart position error to measured experimental results

Also shown in this figure is the simulated response using the vacuum force model that does include combined system capacitance and induced effects. As expected, this does not accurately

capture the true motion of the cart as it has no partial shielding. Also shown in this figure is the simulated response using the proposed terrestrial force model with estimated partial shielding parameters. This simulated response matches the experimental data significantly better and appropriately captures the intricate dynamics of the charged cart motion in the atmospheric environment.

A comparison of the experimental voltage supplied during one of the tests is compared to the simulated voltages in Figure 6.10. Again, this indicates the severe discrepancies of the vacuum charge model in capturing the testbed response compared to the terrestrial model that fits the data quite well.
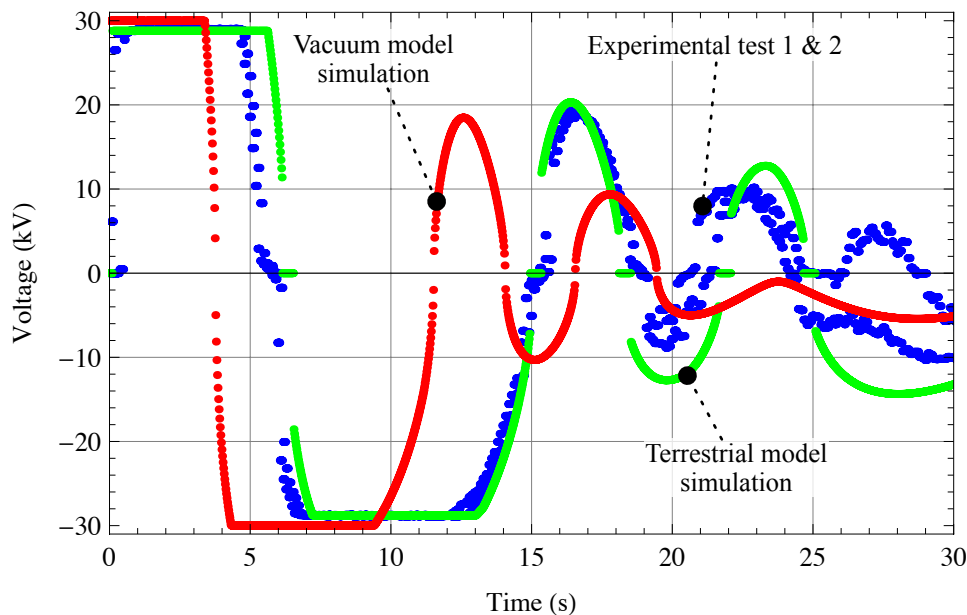
Figure 6.10: Case 1: Comparison of simulated sphere potentials to measured experimental results

In this dissertation, all the developments on disturbance mitigation and modeling are focused on the forces of the testbed. In that regard, it is advantageous to analyze the resulting forces measured on the testbed for comparison. Figure 6.11 shows the computed force from two test results, the vacuum force model as well as the terrestrial model.

Lastly, the residuals between the terrestrial force model and the experimentally determined force response are computed. The residuals are shown in Figure 6.12 for each of the two tests
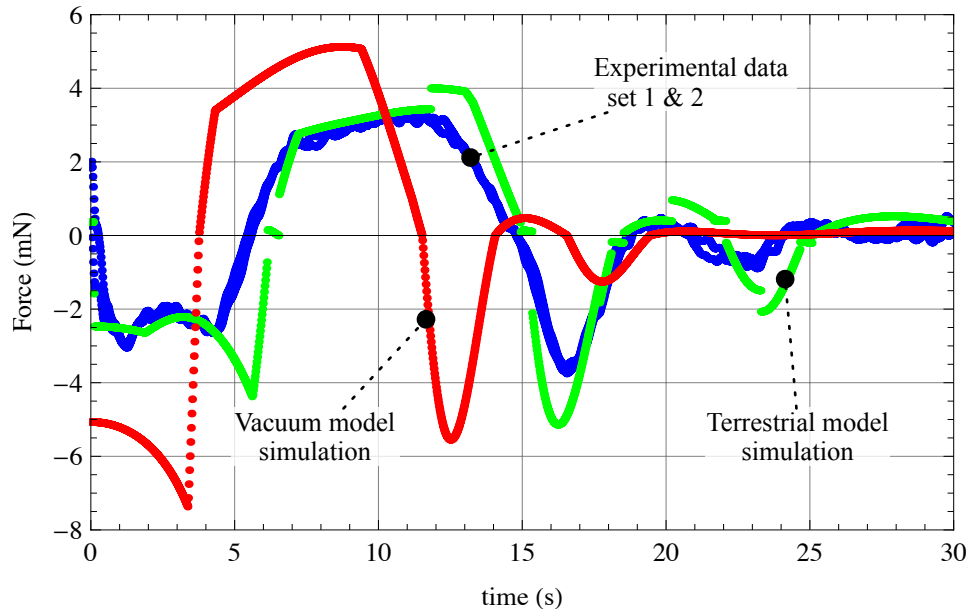
Figure 6.11: Case 1: Comparison of simulated forces and experimental results, obtained by differentiating cart position

analyzed and plotted as a function of time. The mean value of these residuals are 0.1122, 0.0698 mN and have a standard deviations of 1.0289, 1.0429 mN. Looking at these numbers alone, these are good results that indicate that the terrestrial model is fitting the experimental response down to the baseline noise level of 1 mN. However, looking at the figure, it is evident that these residuals are not normally distributed about zero and feature distinct spikes with magnitudes as great as 5 mN. These miscorrelations occur at the voltage zero crossings, (polarity switch).

There are a number of candidate causes for these residual spikes that are proposed. Firstly, in order to compute the force from experimental position data, it undergoes double differentiation and numerical filtering. During this process, smoothing of the true force response occurs. Comparing the force levels in Figure 6.11 it is evident that the simulated response is discontinuous to capture the power supply characteristic response. In contrast, the experimental force data features a continuous response which may be exaggerated or purely a product of the filtering. This is a difficult effect to isolate and determine. Secondly, the modeling of the power supply output response is only an average and may be limited in capturing all response characteristics.
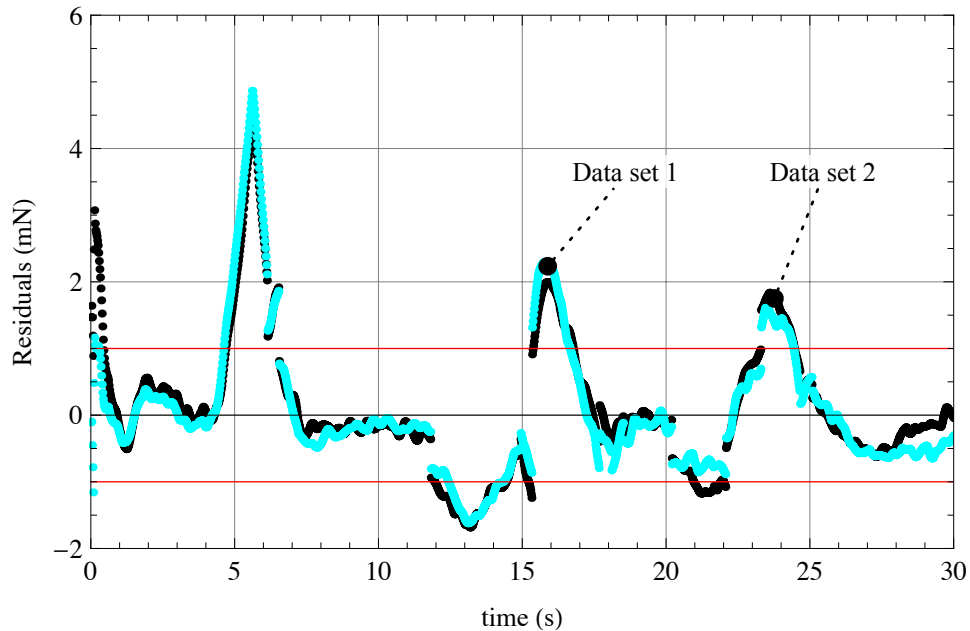
Figure 6.12: Case 1: Force residuals between terrestrial force model and testbed results, obtained by differentiating cart position

Thirdly, the terrestrial model is only a candidate that attempts to capture the partial force shielding in atmosphere. This terrestrial model was developed using fixed potential tests, unlike the dynamic voltage control that is being utilized in these feedback tests. During these potential switches there may be significant changes in the atmospheric interaction that occurs between the spheres and near-instantaneous ion interactions and force discrepancies. Regardless of the cause of this response the terrestrial model fits very well for this series of feedback control tests. These test results may lead to interesting follow-on-work findings at these potential polarity switches.

In these next series of tests the cart is driven from an initial position close to the stationary sphere (initially repulsion forces) to a desired location that is 23 cm away. The position errors of 10 identical tests is shown in Figure 6.13. The results demonstrate a smooth underdamped response that settles as desired within approximately 30 seconds. There is good repeatability between each of these tests.

Also shown in this figure is the simulated response using the vacuum force model. In this
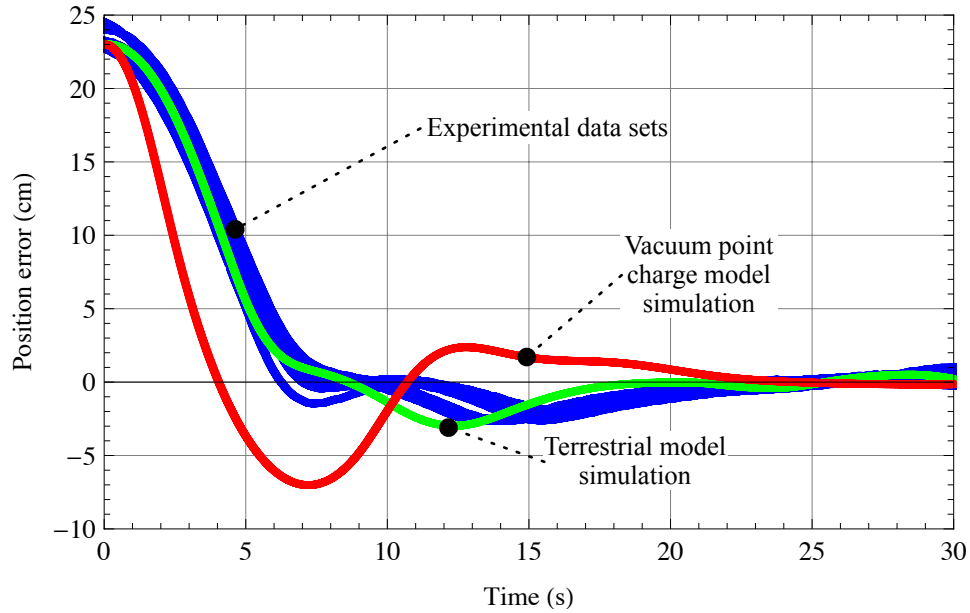
Figure 6.13: Case 2: Comparison of simulated cart position error to measured experimental result

case the original vacuum point charge model that does not include combined system capacitance or induced effects is shown. This provides the greatest contrast between the force models and resulting simulated cart motion that does not capture the true motion of the cart well. Also shown in this figure is the simulated response using the proposed terrestrial force model with estimated partial shielding parameters. This simulated response matches the experimental data significantly better and appropriately captures the intricate dynamics of the charged cart motion in the atmospheric environment.

In the next and final series of tests the cart is again driven from an initial position far from the stationary sphere (initially attraction forces) to a desired location that is 28 cm away. The position errors of 10 identical tests is shown in Figure 6.14. The results demonstrate a smooth underdamped response that settles as desired within approximately 30 seconds. There is good repeatability between each of these tests.

This third test case of Figure 6.14 is important as it demonstrates actuation and controlled motion over the entire length of track. Also shown in this figure is the simulated response using the
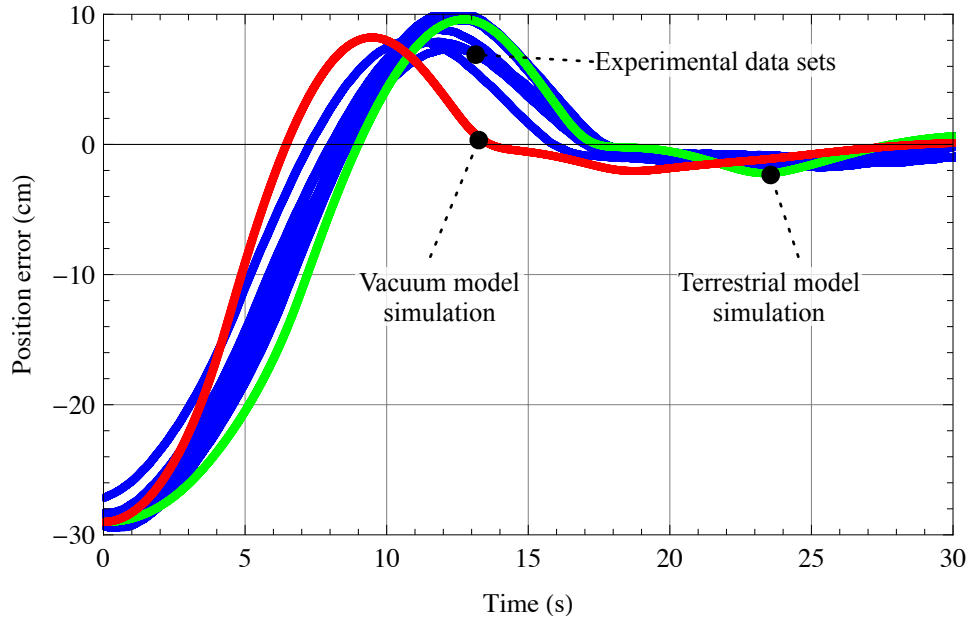
Figure 6.14: Case 3: Comparison of simulated cart position error to measured experimental result

vacuum force model that does include combined system capacitance and induced effects as shown. As expected, this does not capture the true motion of the cart well. Also shown in this figure is the simulated response using the proposed terrestrial force model with estimated partial shielding parameters. This simulated response underestimates the initial attraction forces, however matches the experimental data significantly better and appropriately captures the intricate dynamics of the charged cart motion in the atmospheric environment.

6.5   Summary

Using the knowledge of Coulomb force modeling, this chapter proposes a candidate terrestrial force model with plasma-like parameters to capture shielding from atmospheric electrostatic interactions. This is only achievable because of the low disturbance environment of the testbed and known characteristics of the hardware apparatus. Using experimental one-way data estimates of the model parameters are made and are shown to offer similarities to the plasma properties. Implementing autonomous feedback position control allows the terrestrial force model simulation

to be verified with true data. It is shown that the terrestrial model, that is based on a space plasma model, matches the response of the cart on the track well. However, there are interesting effects that are not captured during polarity switching events that may be a result of instantaneous electrostatic interactions. The terrestrial model that is created based on fixed polarity, one way experiments would not capture this. Developing this terrestrial force model provides understanding of charged body atmospheric interactions and also aids future developments on the testbed by providing a suitable Coulomb force model. As shown in the next chapter, these findings and modeling are also applicable to continuing and expanding theoretical applications that utilize Coulomb formation flight.

Chapter 7

Application: tethered Coulomb structures

To bring the hardware and theoretical developments of this dissertation into context, a final chapter detailing a realistic space-based Coulomb application is presented. The tethered Coulomb structure is a spin-off of the CFF concept. A TCS combines the features of free-flying formations and large space structures. Using Coulomb forces to repel a formation of spacecraft nodes that are connected with fine, low mass tethers can create large quasi-rigid and lightweight space structures. There are numerous uses for a TCS ranging from interferometry and remote sensing to component deployment, local situational awarenes and inflatable structures.

A number of theoretical and analytic studies have been performed by this author. This chapter gives an overview of these studies. Preliminary studies on the TCS concept analyze only relative motions without nodal attitudes and apply a an adjustable tether length control technique to dampen orbital attitude motions [140]. This work was expanded to focus on simplified two-dimensional motions of a two-node TCS system [141]. Linearized analysis in that paper demonstrates the fundamentals of translational and rotational nodal motions and their primary frequencies. A conclusion drawn here is that rotational motions are more challenging to overcome than translational motions. Quantification of the two-dimensional rotational stiffness and angular rate disturbance rejection is shown.

Building on these studies three dimensional analyses with rotations about all axes is conducted in Reference [135]. This looks at maximum nodal rotations based on nodal design parameters such as 1, 2, and 3 tethers as well as inertia, radius and tether connection angles. It

also quantifies the extent of plasma shielding on dynamical response as well as electrical power requirements.

Taking the TCS concept a step further the Mother Child application is introduced in Reference [136]. It is shown that a small tethered Child node can provide situational awareness at GEO at a relatively fixed position and attitude with respect to the Mother craft with minimal sensing, control and propulsion needs. This paper expands upon previous research by simulating two non-identical (size or mass) TCS nodes (Mother and Child) in naturally unstable orbit configurations. It also explores power and propellant mass requirements to maintain kilovolt-level charges in a plasma and quantifies the forces from charge emission. This chapter summarizes the pertinent findings of each of these papers to give insight into realistic applications of a space-based Coulomb technique.

7.1   Tethered Coulomb structure as a GEO sensor platform

Expanding the application of the CFF Concept to a GEO sensing platform has lead to the development of the Tethered Coulomb Structure (TCS) concept first conceived in Reference [137]. The TCS concept offers a number of advantages over the free-flying Coulomb spacecraft cluster concept in that the relative motion is constrained through the tether lengths. The TCS uses discrete spacecraft nodes that are inter-connected with fine, low-mass tethers as illustrated in Figure 7.1. Each node is repelled from the other TCS nodes through the use of electrostatic (Coulomb) forces. The inflationary Coulomb forces provide rigidity and shape control. The TCS size and shape is constrained by the tether lengths which limit how far the nodes can repel from each other.

Similar to the Coulomb formation flying benefits, some key advantages of the TCS system is that it only requires watt-levels of power and very little propellant (low mass ions or electrons). This provides the TCS with long term mission capabilities [137]. The main difference between TCS and Coulomb formation flying scenarios is that the charge control problem is significantly simplified. Instead of requiring precise charge levels to maintain relative positions, as well as complex non-affine control developments, the TCS only requires the charge levels to be maintained above a
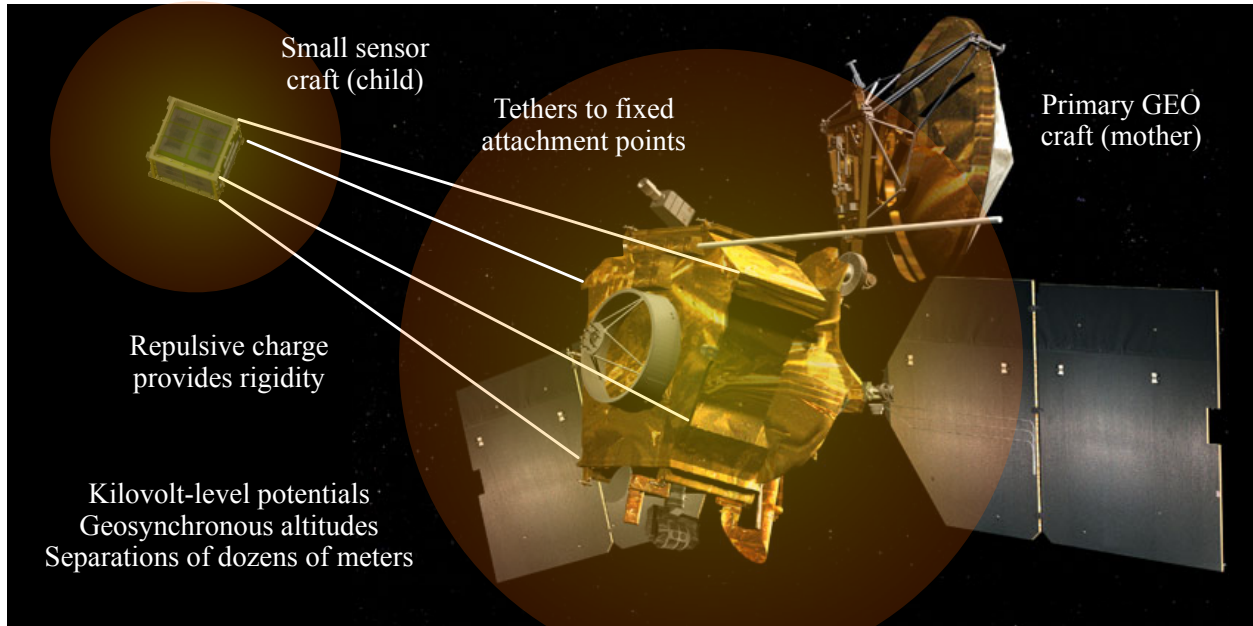
Figure 7.1: Illustration of close proximity sensing with the tethered Coulomb structure concept

certain threshold that guarantees robustness to orbital perturbations. For example, to guarantee tether tension in the presence of differential gravity or solar radiation pressure, the electrostatic inflationary force must simply be larger than these perturbations.

TCS configuration sizes ranging from tens to hundreds of meters are envisioned by connecting strands of charged nodes with tethers. The TCS concept has the advantage of being launched in a compact and stored configuration, that is then inflated or deployed on-orbit. A key feature of TCS is that this Coulomb force inflation provides structural rigidity and an ability to resist deformation and disturbances. With length-adjustable tethers it is possible to change the structures shape and size on-orbit providing an adaptable nodal network to meet variable sensing and mission requirements. The concept can also be used to deploy and hold a small node in a fixed position from a primary spacecraft providing situational awareness or local sensing. An additional advantage of the TCS concept is that tether tensions can be maintained without requiring a particular orbit, equilibrium configuration or spin, like typical tethered systems.

Figure 7.2 shows how the concepts shape change attributes and control requirements compare

to alternate space platform techniques. A large, monolithic space structure such as the Hubble space telescope is essentially launched and deployed as a single unit (except for the deployed solar arrays). This provides good overall rigidity with very little relative motion or flexing control requirements. Larger space structure concepts are considered now. The Air Force Research Laboratory's Innovative Spacebased radar Antenna Technology (ISAT) program for instance, envisions deployable structures that could reach 100 meters in size and larger. This increased shape changing ability results in a very light weight structure that might require active damping and smart materials to dampen out oscillations. Other large spacecraft concepts such as solar sails or gas-inflatable structures achieve even larger shape change capabilities with ever more light-weight structures. On the other end of large space platforms in Figure 7.2 are free-flying formations, such as the CFF concept. Here the space platform shape is free to change subject to thruster propellant and power limitations. However, the relative motion sensing and control requirements are significantly increased in contrast to continuous structures such as iSat or solar sails. The proposed TCS concept falls between the current solar sail and inflatable concepts, and the free-flying spacecraft cluster concepts. While the TCS nodes are interconnected, the millinewton tether tensions are small enough such that the orbital motion must be taking into account when studying TCS dynamics.
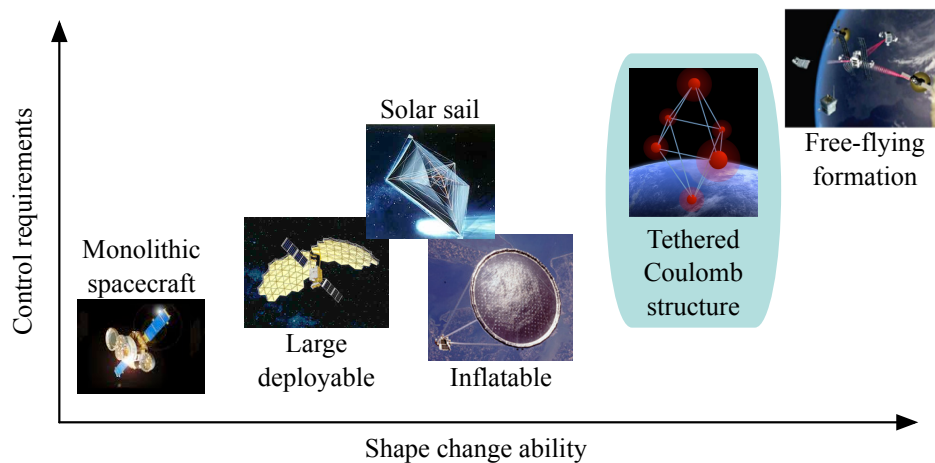
Figure 7.2: TCS concept shape change attributes and control requirements comparison

Similar to the CFF concept, it is necessary to operate a TCS at GEO altitudes or higher where

the plasma is nominally hot and sparse and there is minimal charge screening. Also, kilovolt-levels of charge are considered for the TCS concept using charge control technology previously highlighted. A charge emission device can be used on each of the TCS nodes or on a single node and distributed to other nodes via conducting tethers. The primary benefits and draw backs of either scenario are investigated here.

7.2 Space tethers

The use of tethers in space is a continuing field of aerospace research. Given here is an overview of some of the developments and future projections of space tether mission and materials. This is important as one critical component of the TCS concept is the successful implementation of tethers.

For tethers of any length a significant risk is severance. Micro-meteroid damage is a serious concern for tether damage. The probability of a tether being severed is computed based on the proportion $D^{2.6}/L$ years, where D is tether diameter in mm and L is the tether length in km [12]. For long tethers, the risk of severance is reduced by two orders of magnitude with a two-strand tether [14].

The $Hoytether^{TM}$ is one such multi-braided tether design intended to reduce damage and severance through redundancy as design by Robert P. Hoyt and Robert L. Forward [14]. The $Hoytether^{TM}$ launched on the CubeSat mission Multi-Application Survivable Tether (MAST) in 2007. The 1 km long tether and 3 CubeSats was designed to study electromagnetic tether propulsion, unfortunately the mission failed to be deployed on orbit [172].

Additional space tether missions are briefly introduced here. The Small Expendable Deployer System (SEDS-1) Launched in 1993 with a 26 kg payload on a tether. The tether was cut after 1 orbit to swing payload into a re-entry trajectory [13]. The Plasma Motor Generator (PMG) was launched in June 1993 with a 500 m long, insulated 18 AWG copper wire tether. This tether measured a maximum current of 1/3 A and voltage drops of 25 V [13]. SEDS-2, a follow on mission was launched March 1994 with a 19.7 km long tether. Unfortunately the tethered suffered severance

after only 3.7 days. Until its end of life in May 1994, a 7.2 km length of tether remained attached to the Delta rocket. The tether was a braid of Spectra 1000 fibers with a total diameter of 0.78 mm [13].

The TSS-1R mission onboard STS-75 was a research study for electrodynamic tether development. The 20 km tether deployed to 19.7 km and then failed. The TSS tether featured a Nomex core with ten strands of 34 AWG wire in a 0.305 mm thick Teflon insulation under layers of Kevlar 29 and braided Nomex, giving an overall tether diameter of 2.54 mm [45]. The spun Kevlar provided the load bearing capabilities with a tensile strength of $\approx$3.6 GPa and a relative density of 1.44. Under its nominal load of 65 N, a foreign object penetrated the insulation layer causing failure through arcing and eventual burning [14].

The Tether Physics and Survivability experiment (TiPS) used a nonconductive tether braid of Spectra 1000. With a diameter of 2 mm it had a total length of 4023 m the tether mass was 5.5 kg. The spacecraft mass was 37.7 kg. The tether design featured a 4 strand twisted yarn of Patons Canadiana Acrylic, surrounded by 12 Strands of Spectra 1000 to reduce severance susceptibility [4]. The TiPS tether survived 10 years prior to breaking.[1]

The Advanced Tether Experiment (ATEx), launched in October 1998 is particularly interesting as the tether used had a flat, tape-like, cross-section. The total tether length was 6.5 km, however the mission was aborted after only 22 m was successfully deployed and excessive librations occured. Again Spectra was used to reinforce the low-density polyethylene tether. A fault in this design was the tendency for the tether to adhere to itself and exhibiting mechanical memory effect [14].

Tether materials used and proposed in space include Kevlar, Spectra, Dyneema and M5. A comparison of these tether materials exposed to LEO orbit conditions is conducted in Reference [47]. Another option for a spacecraft tether material is AmberStrand®.[2] AmberStrand® is an electrically conductive hybrid yarn made up of a metal coated polymer that offers a flexible,

---

[1] Naval Ocean Surveillance System Double and Triple Satellite Formations, http://www.satobs.org/noss.html, 10/17/2011

[2] Syscom Advanced Materials, Inc. www.amberstrand.com, 10/17/2011

low-mass and high strength tether. Preliminary strength and application tests have been conducted at the University of Colorado at Boulder on a braid of three twisted Amberstrand® fibers.

Based on these space tether research of these papers generic average parameters are selected for the tethers used in this TCS study. For this work the Young's modulus is $E = 271 \times 10^9$ Pa and the cross sectional area is $A = 5.29 \times 10^{-10}$ m^2. These parameters are representative of the fine, low mass tether materials that are suitable for the short separations of a TCS.

7.3   TCS forces and dynamic modeling

This section develops the fundamental forces acting on a TCS system. The dynamic model considered includes translational and rotational degrees of freedom of each TCS node, Coulomb forces for inflation, and fixed, deployed tether lengths to maintain a constant average size and shape. The TCS shape will undergo small variations due to flexing of the tethers and motion of the nodes. For the studies computed in this dissertation a two node TCS is used as a benchmark. A two-node configuration is chosen because it represents the lower bound of rotational stiffness for a TCS configuration. Furthermore, it allows focused examination of the effects of varying specific system parameters on rotational motions and tether entanglement. A two-node TCS configuration also allows for rotational motion analysis using multiple tethers. Figure 7.3 shows the 3D, two-node configuration with a single-tether connection as well as nodal forces. For this analysis the nodes are modeled as spheres of radius R.
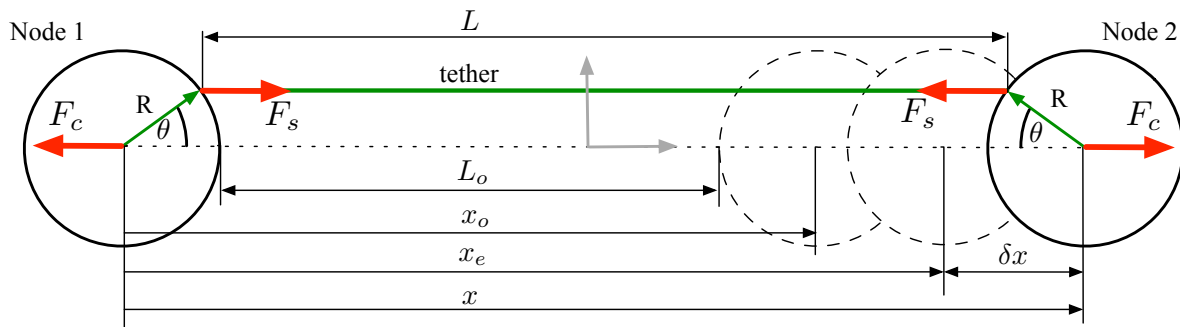
Figure 7.3: Two-node TCS configuration setup with a single tether

This research utilizes a nonlinear numerical simulator that models a general number of spacecraft nodes that are tethered in a selectable configuration. The numerical simulation of this study computes the translational and rotational motion of the two TCS nodes. The only forces assumed to be acting on a TCS at GEO are Coulomb, tensile, gravity, and solar radiation pressure. Lorentz forces for a conducting tether are not considered in this study for a number of reasons. Firstly, the tether lengths are very short and the potentials are ultimately fixed, so there is minimal current in the tether. Additionally, at GEO the tethered craft are in synchronization with the Earth's magnetic field, resulting in zero relative velocity.

Relative motion and attitude simulations are used to determine the conditions that lead to tether entanglement with the TCS nodes, an undesired state. The tethers are modeled as a proportional spring with nonlinear end displacements. This allows for general tether stretching due to arbitrary node translation and/or rotation. The magnitude of the tensile force from a single tether is given by:

$$|\boldsymbol{F}_\mathrm{s}| = \begin{cases} k_\mathrm{s}\delta L & \delta L > 0, \\ 0 & \delta L \leq 0. \end{cases} \tag{7.1}$$

where k_s is the proportional spring constant and δL is the stretch in the tether. The spring constant is computed from the tether properties using the relationship ($k_s = EA/L$).

The Debye-Hückel Coulomb force model with plasma shielding, of Equation 3.36, is used in this TCS analysis. This offers a conservative repulsive force estimate and for simplification does not include combined system position dependent capacitance or uneven charge distribution. Consequently the Laplace relationship of charge to potential for spheres, given in Equation 3.5, is used.

If the TCS system features only a single connecting tether, Eq. 7.1 gives the total tether force on each node. However, the algorithm is capable of simulating multiple tethers between each node. The tether length increase of tether k between nodes i and j is defined by δL_{ijk}. Therefore, the

resulting tensile force acting on node i from the tether(s) connected to node j is:

$$\boldsymbol{T}_{ij} = k_{\mathrm{s}} \sum_{k=1}^{M} \delta L_{ijk} \hat{\tau}_{ijk} \tag{7.2}$$

where M is the number of tethers between nodes i and j and $\boldsymbol{\tau}_{ij}$ is the vector defining the kth tether's connection between node i to j.

A two-body gravity model is simulated for the TCS operating at GEO with a force:

$$|\boldsymbol{F}_g| = \frac{\mu m_i}{|\boldsymbol{r}_i|^2} \hat{r}_i \tag{7.3}$$

where $\mu = 3.986 \times 10^{14}$ m^{3}s^{-2} is the gravitational coefficient for Earth, m_i is the spacecraft node mass and $\boldsymbol{r}_i$ is the inertial position of node i.

The Solar Radiation Pressure (SRP) force at 1 AU is simulated using:

$$\boldsymbol{F}_{SRPi} = P_{SRP} C_r A_s \hat{S}_i \tag{7.4}$$

where P_{SRP}, C_r, and A_s are the solar radiation pressure, surface reflectivity and the cross-sectional area of the spacecraft, respectively and $\hat{S}_i$ is the unit vector from the Sun to node i.

7.3.1   Translational EOM

All four forces simulated at GEO (Coulomb, tensile, gravity and SRP) are included in the translational equations of motion of a TCS node:

$$\ddot{\boldsymbol{r}}_i = -\frac{\mu}{|\boldsymbol{r}_i|^2} \hat{r}_i + P_{SRP} C_r A_s \hat{S}_i + \frac{\boldsymbol{T}_{ij}}{m_i} + \frac{k_c q_i q_j (-\hat{x}_{ij})}{m_i x_{ij}^2} e^{(-(x_{12}-R))/\lambda_D} \left(1 + \frac{x_{ij}}{\lambda_D}\right) , \; i \neq j \tag{7.5}$$

where $\boldsymbol{x}_{ij}$ is the position vector between node i and j and consequently reduce to the separation distance when considering only the two-node case with restricted linear motion.

7.3.2   Rotational EOM

It is assumed that the only torque driving the rotational motion of a TCS node is from the tether forces. Differential gravity and Solar radiation pressure induced torques can be ignored because the spacecraft are spherical and have symmetric mass moments of inertia. With even

charge distribution on the conducting spheres the Coulomb forces act on the center of each node producing no torque. Therefore, the attitude of each spacecraft node is dependent on the torque from each tether:

$$^{\mathcal{B}}\mathbf{\Gamma}_i = \sum_{k=1}^{M} \left({}^{\mathcal{B}}\boldsymbol{p}_{ijk} \times [\mathcal{B}\mathcal{I}]_i {}^{\mathcal{I}}\boldsymbol{T}_{ijk} \right) \quad , \quad i \neq j \tag{7.6}$$

where $\boldsymbol{p}_{ijk}$ is the body fixed vector that defines the location of the kth tether attachment point on node i that connects to node j and $[\mathcal{B}\mathcal{I}]_i$ is the direction cosine matrix of the attitude of node i relative to the inertial frame. The angular acceleration of each node is defined in the body frame with Euler's rotational equations of motion [128]:

$$[I]_i \dot{\boldsymbol{\omega}}_i = -\boldsymbol{\omega}_i \times ([I]_i \boldsymbol{\omega}_i) + \mathbf{\Gamma}_i \tag{7.7}$$

The attitude of each node is represented with the modified rodrigues parameters (MRP) which are integrated using the differential kinematic equation:

$$\dot{\boldsymbol{\sigma}}_i = \frac{1}{4} \left[(1 - \sigma_i^2)[I_{3\times3}]_i + 2[\tilde{\boldsymbol{\sigma}}]_i + 2\boldsymbol{\sigma}_i \boldsymbol{\sigma}_i^T \right] \boldsymbol{\omega}_i \tag{7.8}$$

The MRP set will go singular with a rotation of $\pm360°$. To ensure a non-singular description, the MRP description is switched to the shadow set whenever $|\boldsymbol{\sigma}| > 1$ [128].

7.3.3 Sample force magnitudes

To appreciate the expected force magnitudes a TCS structure will encounter on orbit, consider a two-node tethered system. With nodes of radius 0.5 m, separated by 5 m center to center and charged to a surface potential of 30 kV the expected force levels are shown in Table 7.1. As demonstrated in earlier chapters this is an achievable charge level with current technologies. The solar radiation pressure is computed for one node at 1 Astronomical Unit (AU) from the sun where the solar radiation pressure is 4.56×10^{-6} N/m, and the surface reflectivity is 1. The differential gravity gradient force is computed assuming the nodes are aligned along the nadir line at GEO altitude, each with a mass of 50 kg.

In the absence of external perturbations (such as SRP or gravity gradients) there exists a force equilibrium between the Coulomb and tensile forces. Two nodes at 30 kV potential, with a

desired separation, ($x_o = 5$ m), using Amberstrand® tether material need only stretch 0.75 μm to reach this equilibrium separation, x_e.

Table 7.1: Expected force magnitudes for a two-node TCS separated by 5 m

Force	Value	Units
Coulomb (F_c)	1.0	mN
Tether (F_s)	1.0	mN
SRP (F_{SRP})	3.6	μN
Differential gravity	4.0	μN

7.3.4 Numerical simulation: TCS compression due to external disturbance force

For this example TCS, the force magnitudes of the primary disturbances at GEO, differential SRP and differential gravity, are three orders of magnitude less than the Coulomb control forces. The intent of the following study is to quantify the capabilities of a two-node TCS configuration to resist deformation from an external perturbation, in this case, differential SRP.

Consider two spacecraft nodes connected with a single-tether. The solar radiation pressure is added as a bias force that is compressing the system along the direction of the tether line as shown in Figure 7.4. The SRP force is acting on both nodes, but increasing the size of node 1 produces a differential SRP that attempts to compress the nodes. The concern is whether the Coulomb forces are large enough to maintain tether tension in this setup. The parameters of the study are shown in Table 7.2 and the simulation algorithm used is shown in the Appendix.
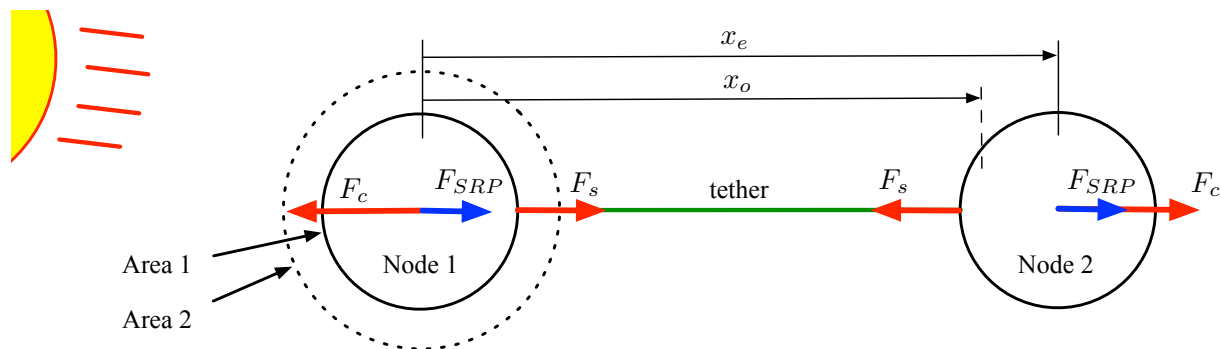
Figure 7.4: Two-node Solar radiation pressure model setup

Table 7.2: Simulation parameters for SRP analysis

Parameter	Value	Units
Spacecraft Area Ratios	1-10	
Spacecraft node radius (R)	0.5	m
Spacecraft separation (x_o)	10	m
Solar pressure (1 AU)	4.56×10^{-6}	Nm^{-2}
Surface reflectivity	1	

The nodes have a desired separation of 10 m. If the Coulomb forces are found to be sufficient to maintain tension for this challenging larger separation distance, then TCS systems of shorter separation distances should not be significantly compressed by differential SRP. The sunlit surface area of node 1 is increased linearly in multiples from one to ten, where one is the nominal surface area corresponding to a 0.5 meter radius circle. An increase in the surface area will cause the homogeneously distributed charge to also increase for a fixed nodal potential. This would further increase the stiffening capabilities of the TCS system. To maintain a worst-case scenario, this model does not incorporate any change in the Coulomb force as the surface area of node 1 is increased. To isolate the differential solar radiation pressure effects, this simulation does not induce attitude rotations and omits gravity forces.

The numerical simulation is set up with the craft initially at their undisturbed equilibrium states. The contour plot of Figure 7.5 shows what the worst-case percentage of the buffer between equilibrium distance and un-stretched distance is compromised by the SRP disturbed relative motion. This value is calculated using:

$$\% = \frac{L_e - \min(L)}{L_e - L_o} 100 \tag{7.9}$$

This percentage value indicates how close the tether length is from becoming slack as a function of both charge and the surface area ratio between the craft. The top left portion of the figure indicates that the crafts relative motion compresses to the point of causing the tether to go slack at times.

As indicated in Figure 7.5 an increase in charge will stiffen the system to resist differential
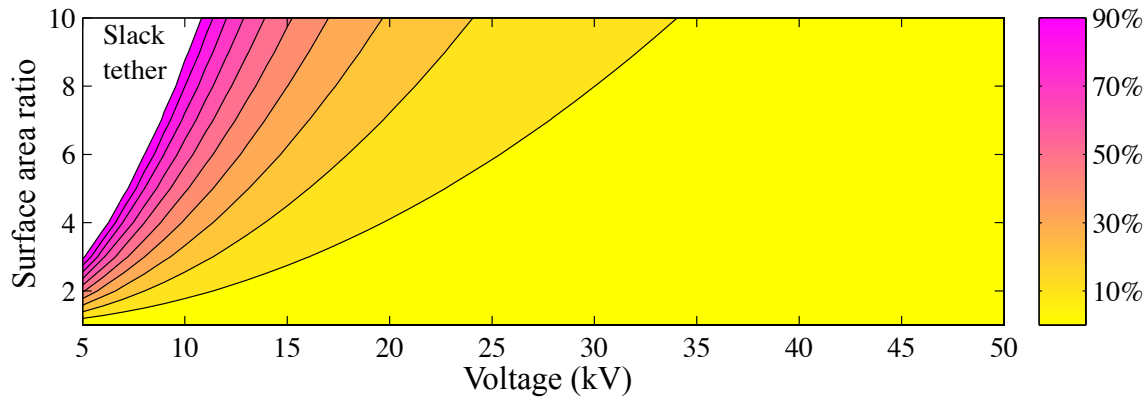
Figure 7.5: Proximity of nodes from generating a slack tether due to SRP compression

perturbations. For shorter separation distances of less than 10 meters the system is further stiffened reducing the voltage requirements to resist the same disturbance force levels. Note that even with a very large TCS node size ratio of 10 and 25 kV potential, the compression due to this worst-case alignment of the differential SRP disturbance would only cause approximately a 20% compression of the equilibrium distance buffer. For TCS separation distances on the meter-level, considering near equal nodal sizes, the differential SRP will have a minimal impact on the TCS shape. Based on the results of this simulation it is appropriate to omit the effects of differential perturbations such as SRP and gravity to analyze short-term dynamical motions and natural frequencies. For long term dynamic studies, the implementation of the full models of Equations 7.5 & 7.6 are used.

7.3.5   Two-node simulation parameters

The intent of this chapter is to provide insight into the dynamics and design parameters of the TCS concept. These studies are based upon the translational and rotational motion of a representative two-node system. Here the response of the two-node system subjected to initial angular rate errors that represent deployment or disturbance torques is investigated.

Simulations are computed with the full three-dimensional equations of motion including attitude dependance. For practical reasons, the simulations are stopped if an attitude reaches a tether

wrap up state (±90 degrees for single-tether). A common set of TCS parameters for each simulation case is shown in Table 7.3. Three un-stretched separations of $x_o = 2.5, 5,$ and 10 m measured from node center to center are used.

Table 7.3: Simulation parameters common for all test cases

Parameter	Value	Units
Spacecraft node mass (m)	50	kg
Spacecraft node radius (R)	0.5	m
Spacecraft potential range (V)	5-50	kV
Spacecraft separations (x_o)	2.5, 5, 10	m
Initial attitude rate errors $\left(\dot{\theta}(0)\right)$	1-120	deg/min

To demonstrate the complex coupling between translational and attitude motions of tethered, charged nodes an example simulation is shown. Figure 7.6 shows the relative motion of a two-node system in deep space. Each node has an initial angular rate of 45 deg/min about different axes. The nodes maintain a fixed potential of 30 kV and there are no gravity or SRP forces acting. The nodes have an un-stretched separation of 5 m, radius of 0.5 m and mass of 50 kg. Figure 7.6 demonstrates the relative oscillatory motion of the two nodes along with the attitude of node 1 and the corresponding tether force levels.

Figure 7.6 indicates the complex dynamics that result from a two-node, single tether TCS system with solely an initial angular rate error. While this numerical simulation can handle general translational and rotational motion of N nodes, the results yield an overwhelming amount of data, making it difficult to gain any insight. This numerical demonstration highlights the need to reduce the complexity of the system. It is beneficial to isolate the motions of the TCS system and appreciate its true capabilities. For this reason, the following section in this paper reduces a generic TCS system to its fundamental translational and rotational motions.

7.4   Translational and rotational stiffness

This section documents the dynamic model of the representative two-node, single-tethered TCS system. This two-node model is reduced to two degrees of freedom (2DOF) and linearized to
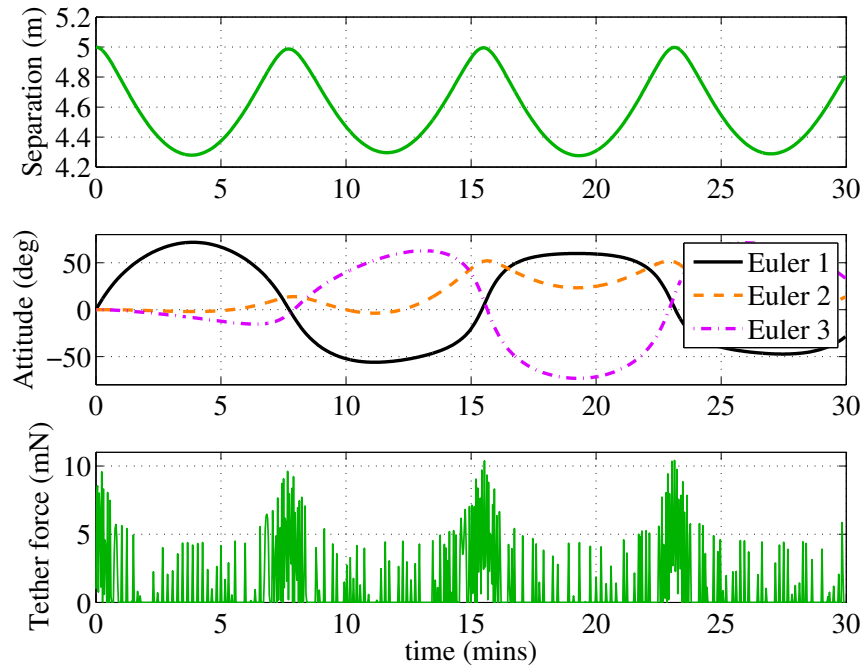
Figure 7.6: Example of two-node, complex 3D relative motion, attitude and single-tether tension (initial angular rates of 45 deg/min)

obtain insight into expected motions about equilibrium. The linearization allows specific analysis of individual translational and rotational motions. The models are developed in this section in the absence of gravitational and SRP perturbations. The two-degree of freedom models developed here also provide verification of the full 3D model and simulation results.

7.4.1   Two degree of freedom model

A simplified 2DOF TCS model is developed to provide insight into how TCS node rotation impacts the charge requirements and related stiffness capabilities. This TCS model features two nodes attached with a single-tether as shown in Figure 7.3.

By constraining the nodes to asymmetrically rotate by an angle θ the tether remains parallel to the line of sight vector resulting in one dimensional translational motion with the Coulomb and Tether forces (F_c & F_s) directly opposing each other. This reduces the model to one rotational degree of freedom and one translational. This motion is desirable as it allows analysis of the

effects of each motion in isolation. Any alternate symmetries cause two dimensional translational motions that are also inherently coupled to rotational motions. The Coulomb force for this model is assumed to have no shielding from the plasma environment due to the very small meter-level separation distances. This is a reasonable assumption given the force magnitude is reduced only 0.03% at a separation of 5 meters in a nominal 200 m Debye length plasma.

The translational equation of motion of this system is:

$$\ddot{x} = \frac{2k_cQ}{mx^2} - \frac{2k_s}{m}\left[x - x_o + 2R(1 - \cos\theta)\right] \tag{7.10}$$

where x_o is the un-stretched node separation and m is the node mass. With the tethers attached at fixed locations on the spherical surfaces any rotation will result in a torque on the node. This is modeled to examine the correlations between translational and rotational motions. The attitude is governed by the rotational equation of motion:

$$\ddot{\theta} = -\frac{Rk_s}{I}\left[x - x_o + 2R(1 - \cos\theta)\right]\sin\theta \tag{7.11}$$

where I is the mass moment of inertia of the node. For this 2DOF model the mass of each node is equal and the mass moment of inertia of a solid disk is used. Future studies can vary these properties to analyze the effect of mass and its distribution on the dynamics of the system.

7.4.2   Single-tether linearized model

To focus on the dynamical motion of the nodes, the 2DOF model is linearized. Equation 7.10 has an equilibrium condition at a separation, $x = x_e$ and an attitude $\theta = 0$. At this equilibrium, the translational equation of motion is reduced to

$$\ddot{x} = 0 = \frac{k_cQ}{x_e^2} - k_s(x_e - x_o) \tag{7.12}$$

which can be arranged to a cubic relationship between the equilibrium distance x_e and the associated charge product Q:

$$k_cQ = k_s(x_e - x_0)x_e^2 \tag{7.13}$$

Of the three x_e solutions only the real solution is practical. At this equilibrium separation distance the Coulomb and tether forces are equal and the nodes remain stationary (with no external disturbances). One interesting consequence of this equilibrium distance is that it is independent of the system mass.

The 2DOF model given in Eqs. 7.10 and 7.11 is linearized about the equilibrium condition to produce a reduced system model to study the dynamic behavior of oscillations about the equilibrium states. Linearizing the translational motion for small departures ($\delta x = x - x_e$) results in:

$$\delta\ddot{x} \approx -\frac{2}{m}\left[\frac{2k_cQ}{x_e^3(Q)} + k_s\right]\delta x \tag{7.14}$$

This approximate translation description is decoupled from the angular rotation and is the form of the stable, undamped harmonic oscillator equation. The natural frequency of this oscillatory translational response is given by:

$$\omega_T = \sqrt{\frac{2}{m}\left[\frac{2k_cQ}{x_e^3(Q)} + k_s\right]} \tag{7.15}$$

The rotational equation of motion is linearized to the form:

$$\ddot{\theta} \approx \frac{-Rk_s}{I}\left[x_e(Q) - x_o\right]\theta \tag{7.16}$$

This linearized rotational equation of motion also decouples and is of the form of the stable undamped harmonic oscillator equation. The natural frequency of this oscillatory rotational response is given by:

$$\omega_R = \sqrt{\frac{Rk_s}{I}\left[x_e(Q) - x_o\right]} \tag{7.17}$$

While these linearized models are only valid for small oscillations, they can be used to offer insight into the response of the system about its equilibrium state.

7.4.3   Linearized model analysis

Using the linearized system model, two case studies are used to analyze motions and sensitivity to the nodal parameters; potential, tether material and separation. Ultimately, it is possible

to gauge the expected stiffness of the TCS, with the linearized models of Equations 7.14 and 7.16 and using the system properties of Table 7.3.

7.4.3.1 Natural frequency response

The natural frequency of the linearized translational and rotational motions of Equations 7.15 and 7.17 gives a measure of the TCS stiffness. Figure 7.7 shows the natural frequency of the linearized translational motion for three separation distances. For the voltage range analyzed, the natural frequency of the response changes less than 0.1%, indicating that it is essentially independent of the spacecraft charge. The translational stiffness is largely determined by the tether material stiffness. As the separation distance between the nodes decreases, the frequency of the system response increases as a result of the shorter (stiffer) tethers and enhanced Coulomb force magnitudes.
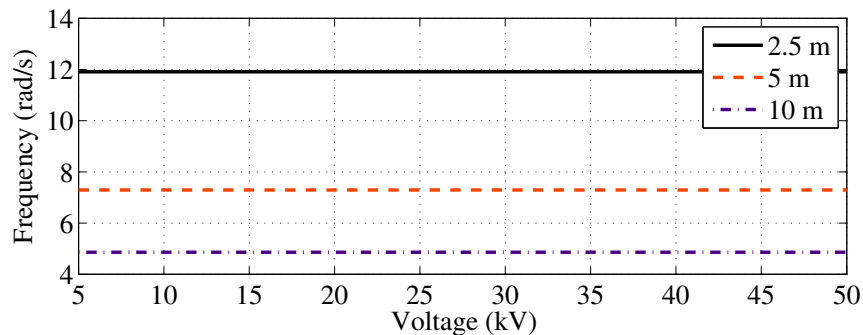
Figure 7.7: Natural frequency of linearized translational motion

Figure 7.8 shows the natural frequency of the linearized rotational motion, Equation 7.17, for three separation distances. In contrast to the translational stiffness which is essentially decoupled from the magnitude of the electrostatic inflation force (assuming AmberStrand®-like materials), the rotational stiffness or natural frequency is directly related to the TCS node potentials. The rotational natural frequency has a near-linear dependance on potential for the range of charges used in this study. In essence, the rotational motion will be stiffened through enhanced charge levels. Only for potentials much larger and unrealistic for spacecraft charging (>2000 kV) does the

response become non-linear.
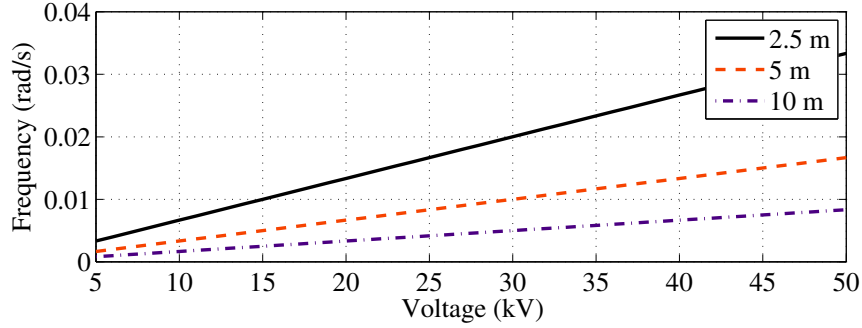
Figure 7.8: Natural frequency of linearized rotational motion

Note that the translational natural frequency is at least two orders of magnitude greater than the corresponding rotational motion. For these uncoupled linearized equations and the system parameters analyzed, this implies that a TCS is naturally superior at constraining translational motion. Based on this outcome, the primary focus of TCS studies in this dissertation is on the nodal rotational responses.

7.4.3.2   Sensitivity of rotational motion to tether material

AmberStrand$^{®}$ is the example tether material used for this study. The use of an alternate tether material would change the material stiffness (spring constant). The linearized model is used to analyze the effect on the resulting rotational node motion by varying this tether material stiffness. Equation 7.16, which is the form of a stable oscillator, has the solution $\theta(t) = A\sin(\omega_R t + \beta)$ where β is the phase offset and the amplitude of the rotational response oscillation, A, is defined as:

$$A = \dot{\theta}(0)\sqrt{\frac{2mR}{5}}\underbrace{\sqrt{\frac{1}{k_s\left(x_e(Q,k_s)-x_o\right)}}}_{\alpha} = \dot{\theta}(0)\sqrt{\frac{2mR}{5}}\alpha \qquad (7.18)$$

Here $\dot{\theta}(0)$ is the initial angular rate and $\theta(0)$ is assumed to be zero. The amplitude A is proportional to α, which is a function of the tether stiffness k_s and node charge product Q. Note that x_e depends on k_s so amplitude is not inversely proportional to the spring constant. For 10 m separated nodes tethered with the nominal AmberStrand$^{®}$ braid the resulting spring constant value

is $k_{s10} = 591$. This spring constant value corresponds to an amplitude factor α_{10}. Investigating the impact of the tether material properties is performed by varying the spring constant value from $k_{s10} \times 10^{-8}$ through $k_{s10} \times 10$. The resulting amplitude multiplication factor α of Equation 7.18 is normalized by the nominal α_{10} value and plotted in Figure 7.9 for a range of node potentials.
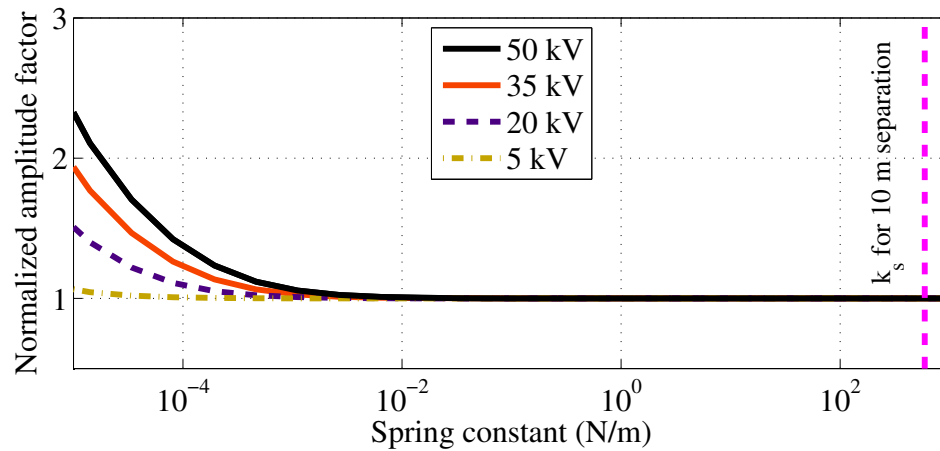
Figure 7.9: Effect of varying tether spring constant on the amplitude of linearized angular oscillations

This study shows that changes in the tether spring constant have a minimal effect on the amplitude of angular rotations compared to the nominal 10 m separation (k_{s10}) response. It requires a spring constant that is reduced by 1×10^{-8} times the value of the 10 m separated case and nodes of 50 kV to increase the maximum angular rotation by only 2.5. Any tether material with a realistic spring constant or anything stiffer than the example tether material will result in the same rotational motion response, an important finding of the linearized analysis.

7.4.3.3   Extent of linearization range

The previous sections use linearized equations to analyze expected motions about equilibrium conditions. Numerical simulations using the 2DOF model are used to quantify the extent of accuracy of these linear approximations. This is achieved by calculating the period of oscillation of the system response to deviations from equilibrium both with the translational and rotational equations of motion.

Figure 7.10 shows the period of oscillation of the two-node system initialized with a transla-
tional offset δx from equilibrium x_e. The period of oscillation is compared to that predicted from
the linearized system of Equation 7.15. The nodes are offset in both the compression and stretch
directions $(x_e \pm \delta r)$ and give different periods of oscillation. This figure indicates that the range of
accuracy of the linearized translational equation is only $\pm 1 \times 10^{-3}$ mm.
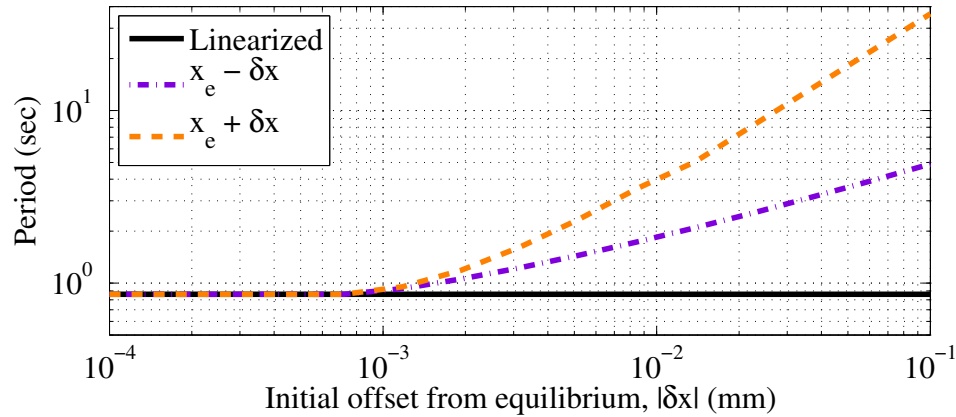
Figure 7.10: Comparison of oscillation periods for linearized translational equation to non-linear
simulation

Similarly, the period of oscillation of the two-node system initialized with a rotational offset
$\delta\theta$ from the equilibrium angle of zero is shown in Figure 7.11. The period of oscillation is compared
to that predicted from the linearized system of Equation 7.17. Due to symmetry, the nodes are offset
only in the positive θ direction. This figure indicates that the range of accuracy of the linearized
rotational equation is $\pm 8 \times 10^{-2}$ degrees. Beyond this linear range the rotational oscillations
abruptly change periods as the tether now becomes marginally slack at times causing the nodes to
to lose their smooth rotations.

The conclusion of this study is that the linearization analysis only holds for very small
departures from the respective equilibriums. The conclusions of the linearized analysis still hold
and give insight into the expected performance of the TCS dynamics; However, the non-linear
nature of the TCS dynamics dominate, leading to the need for numerical simulations for further
analysis.
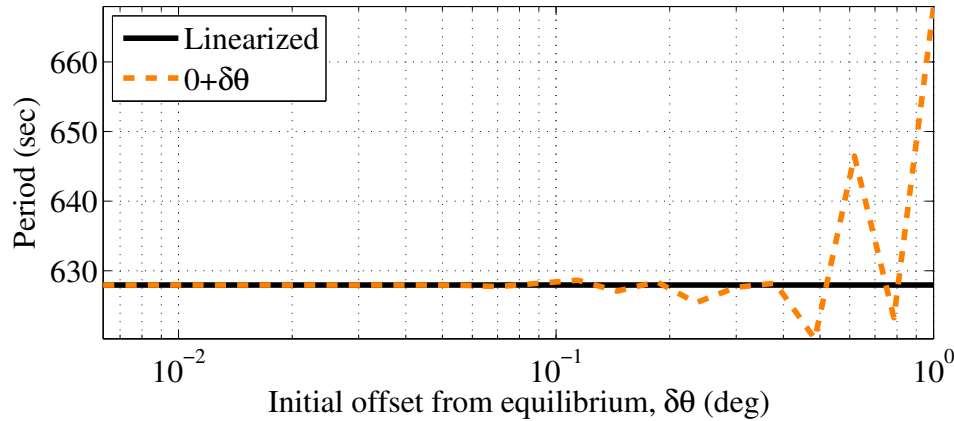
Figure 7.11: Comparison of oscillation periods for linearized rotational equation to non-linear simulation

7.4.4 Numerical simulation: rotational stiffness capabilities

The linearized analysis gave an indication of the translational and rotational motions and their dependence on two key system parameters, craft potential and tether material. Due to the very non-linear nature of TCS dynamics, further analysis of the rotational motion is conducted to demonstrate the TCS stiffening properties and capability to resist angular rate errors.

After deployment, the TCS nodes will not be perfectly at rest with respect to each other. This analysis uses the full 3D non-linear equations of motion to demonstrate the ability of the Coulomb force to stiffen the structure and resist deformation due to this initial angular rate. The two-node, single-tether TCS configuration with three different separation distances are simulated with assymmetric initial angular rotations. Here both nodes perform the same (but opposite) rotation and consequently have one dimensional translational motion, to focus on rotational dynamics.

Figure 7.12 shows the maximum attitude angle that is reached by the nodes for each of the separation distance cases. This is shown as a function of the spacecraft surface potential and each data line corresponds to the initial angular rate error. No material damping is considered in this study as the focus is on the initial rotational response and issues with tethers wrapping up on nodes after a single oscillation. The weak material damping would only impact long-term oscillation amplitudes.
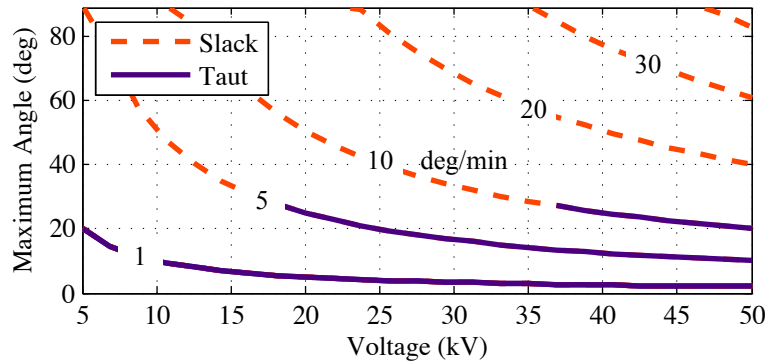
(a) Maximum angle for 10 m separated nodes
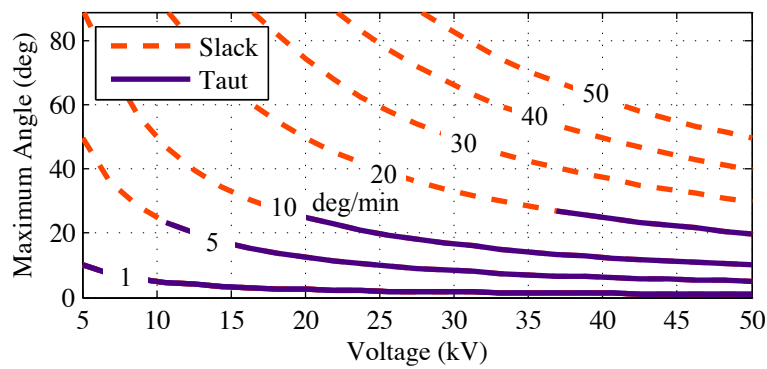
(b) Maximum angle for 5 m separated nodes
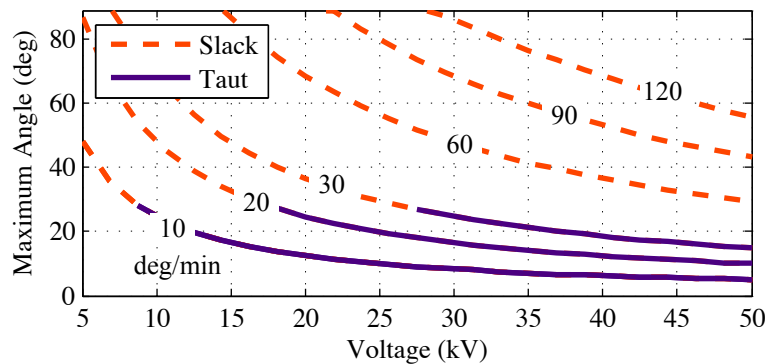
(c) Maximum angle for 2.5 m separated nodes

Figure 7.12: Maximum attitude reached as a function of initial attitude rate error

The solid lines in Figure 7.12 indicate that the tether remains taut for the simulation duration, where as the dashed regions have the tether reach a slack state. For many of these conditions the tether may go slack only a small fraction of the simulation time and is typically much less than

a millimeter from the un-stretched tether length. Given that there are only infrequent times of slight slackness, this is not a significant concern. It is anticipated that passive or active damping be added to the TCS system to assist the transient response to reach a taut tether equilibrium state. Future research investigating the use of active motion damping or passive damping with viscous materials at the tether attachment points is envisioned.

For the three separation cases analyzed the conditions that cause the angle of rotation to go above 27° results in a tether that will periodically go slack. Interestingly this rotation amplitude limit appears to be independent of the initial conditions considered or the node separations. The cause of this correlation is currently under investigation.

A reduction in the spacecraft separation distance results in two key changes on the system as shown in Figure 7.12. Firstly, the tether spring constant increases and secondly the spacecraft will be closer together, increasing the Coulomb force for an equivalent charge level. This increases the stiffening of the rotational motion, as preluded by the earlier linear analysis. This simulation now quantifies the enhanced ability of a stiffened TCS to resist deformation due to an initial angular rate error on the nodes. Figure 7.12(a) shows that a 10 meter nodal separation with 35 kV potentials requires an initial nodal rotation rate less than 10 deg/min, a small value. Otherwise, the tethers will periodically go slack, or the nodes could wrap up with the tethers. In contrast, Figure 7.12(c) shows that reducing the separation to 2.5 m and maintaining a 35 kV potential will constrain a 45 deg/min angular rate. At these separations rates as high as 120 deg/min can be tolerated without nodal wrap up. Shorter separation distances yield significant increases to the rotational stiffness of the TCS nodes.

7.5   Double-tether rotational stiffness capabilities

Having a TCS system that incorporates a redundant set of tethers between the nodes, with the attachment points distributed across the nodes surface, is a method of increasing the rotational TCS node stiffness. The following numerical simulation results quantify by how much the rotational TCS node stiffness can be increased if a double-tether setup is employed.

7.5.1   Two degree of freedom model

The double-tether TCS concept is shown in Figure 7.13 on a two-node system. The intent of the redundant double-tether is to add rigidity and resistance to deformation for the TCS. The system is modeled with asymmetric motions so that it can once again be reduced to two degrees of freedom to gain analytical insight.
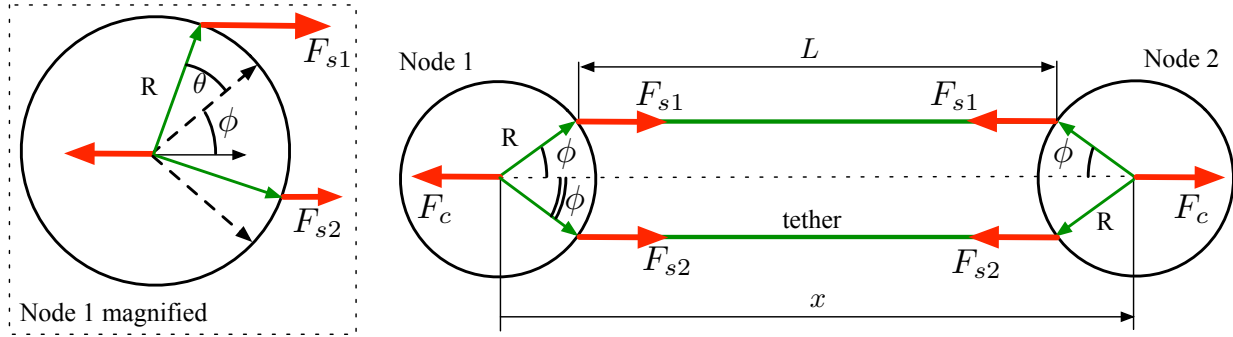
Figure 7.13: Two-node system setup with double-tether

The translational equations of motion of the symmetric double-tether system is:

$$\ddot{x} = \frac{2k_c Q}{mx^2} - \frac{4k_s}{m} \left[x - x_o + 2R\cos\phi(1 - \cos\theta) \right] \tag{7.19}$$

where ϕ is the half angle between the tether attachment points. The rotational equation of motion is given by:

$$\ddot{\theta} = -\frac{2xk_s \sin\theta}{I} \left\{ \cos\phi(x - x_o) + 2x \left[\cos\theta + \cos^2\phi - 2\cos\theta\cos\phi \right] \right\} \tag{7.20}$$

The rotational equation of motion is significantly more complex than the single-tether setup. However, linearizing the double-tether motions about the equilibrium states, still produces a decoupled set of equations. The translational motion for small departures about the equilibrium ($\delta x = x - x_e$) is:

$$\delta\ddot{x} \approx -\frac{4}{m} \left[\frac{k_c Q}{x_e^3(Q)} + k_s \right] \delta x \tag{7.21}$$

This linearized translational motion is of the form of a stable undamped harmonic oscillator. It is also equivalent to the single-tether case of Equation 7.14 with an additional factor of two. This

further increases the natural frequency and stiffness of the translational response. The rotational equation of motion is linearized to the form:

$$\ddot{\theta} \approx \frac{-2Rk_s}{I} \left[(x_e(Q) - x_o) \cos\phi + 2R(1 - \cos^2\phi) \right] \theta \tag{7.22}$$

This linearized rotational equation of motion decouples from the translational motion and is a stable undamped harmonic oscillator equation. Unlike the single-tether rotational motion of Equation 7.16 this linearization features dependance on the tether attachment angle ϕ. Figure 7.14 plots the rotational natural frequency of Equation 7.22 as a function this tether attachment angle and potential. This figure shows how stiffening is significantly increased with the tether angle ϕ. This geometric stiffening is a consequence of the larger moment arm acting on the node. The data in this figure is generated with nodes of 0.5 m radius separated by 2.5 m. It should be noted that with zero tether separation ($\phi = 0$) the double-tether rotational natural frequency is equivalent to the single-tether system shown in Figure 7.8.
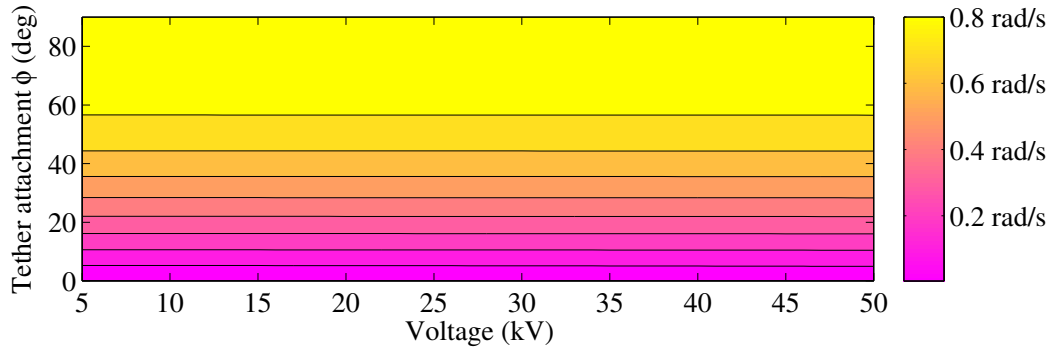
Figure 7.14: Natural frequency of linearized rotational motion of double-tether model

Figure 7.8 showed for the single-tether case that increasing charge increases the natural frequency of the rotational response. This also occurs with the natural frequency of the double-tether shown in Figure 7.14, however has less contribution than the geometric stiffening. Utilizing a double-tether will increase the ability to resist nodal angular rotations.

7.5.2   Double tether system response to angular rate errors

In this simulation case the double-tether response to angular rate errors is compared to that of a single-tether configuration. A two-node configuration with a separation of 2.5 m is analyzed. The simulation is performed using the full 3D and non-linear coupled equations of motion. The parameters of the symmetric simulation are shown in Table 7.4.

Table 7.4: Double tether simulation parameters

Parameter	Value	Units
Initial attitude rate errors $\left(\dot{\theta}(0)\right)$	5,10	deg/min
Spacecraft node radius (R)	0.5	m
Spacecraft separation (x_o)	2.5	m
Tether attachment point angle (ϕ)	20	deg

Using two initial angular rate errors for each tethered system the resulting maximum attitude angle reached is shown in Figure 7.15 on a y-axis log plot. There is a noticeable difference in the systems responses. The double-tethered system performs better at reducing maximum rotation due to initial rate errors. This indicates that the resulting moment arm from the double-tether configuration significantly increases the TCS response to angular rates. While the double-tether system has the advantage of producing a stiffer system, it is also prone to having a tether go slack as shown by the dashed lines in the figure. The tether is only marginally and momentarily slack at times of closest approach between the nodes. Once again, during these times the tether is slack less than 1 mm over its entire length. In contrast, during this simulation case the single-tether system remains taut for any charge above 10 kV, at a cost of reaching higher attitude angles. Another consideration with the double-tether TCS is that the nodes are inherently closer to wrap up due to the tether connection angle. A comparison between the resistance to absolute angular rotation versus the close proximity to wrap up must be considered.

The results of this preliminary double-tether simulation indicate that a TCS system can be significantly stiffened beyond an equivalent single-tether system. An additional advantage is the safety provided by having two tethers between nodes. In case one tether is severed, the remaining
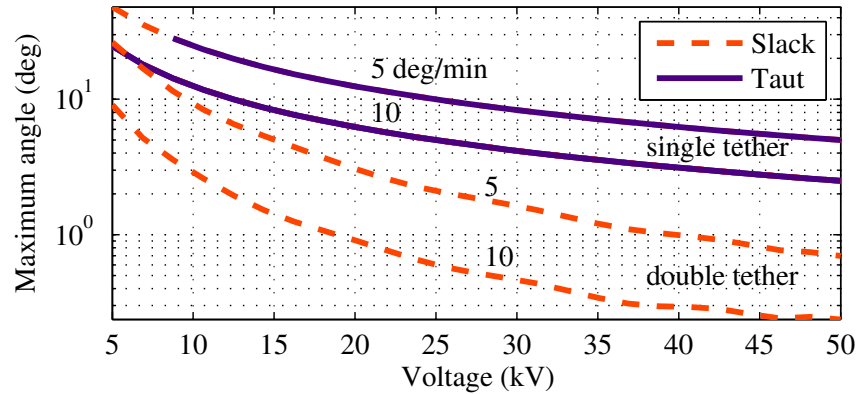
Figure 7.15: Double-tether vs single-tether attitude response to angular rate errors

tether would still maintain the TCS shape, although with reduced accuracy.

Numerical results obtained with the full three dimensional non-linear equations of motion indicate that external perturbations such as SRP or differential gravity have minimal influence on the short-term dynamics. For obtainable kilo-volt level potentials the TCS system will sufficiently inflate and resist deformation from external forces. This is shown firstly through simplified, linearized models, that give an analytical expression for the natural frequency of isolated translation and rotational motions. The natural frequency is an indication of the stiffness of the system and the rotational motions produce lower magnitudes and are therefore the focus of this study. The TCS rotational response to initial angular rate errors is also quantified and shown to significantly improve with the use of an additional tether.

7.5.3   Conceptual node design

Taking into consideration these dynamical results an ideal TCS spacecraft node design may appear similar to the conceptual illustration of Figure 7.16. This design maximizes the spacecraft rotational stiffness, increases nodal wrap-up angles and provides a spherical conductive surface for even Coulomb force generation. The mass moment of inertia is minimized by placing the spacecraft components within a low-mass exterior conducting shell. The tethers are connected to attachment arms that extend beyond the shell increasing the tether moment arms and consequently rotational

stiffness. This attachment arm design also increases the maximum angle before nodal wrap up.
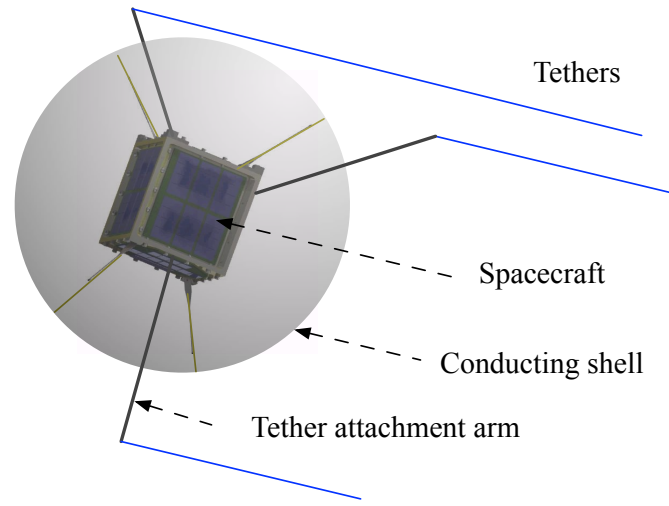
Figure 7.16: Illustration of conceptual TCS spacecraft node design

7.6   Power requirements to maintain a fixed potential in a plasma

The net power required for a charged spacecraft to maintain a fixed potential in a plasma is directly proportional to the spacecraft potential and the net current from the plasma. This is represented with $P = V I_{cc}$, where V is the spacecraft potential relative to the plasma and I_{cc} is the charge control current. It is assumed that the charge control current (I_{cc}) can be either positive or negative charge and equal the net plasma current $I_{net} = I_{cc}$. The net plasma current is developed in Chapter 2 and used here in the form of Equation 2.21. This includes photoelectron current on sun-lit surfaces, as well as secondary and backscattered currents. Only the sun-lit case is examined as this is the typical environment at GEO and also leads to highest power requirements, compared to negative charging in eclipse.

For this power analysis a specific two-node TCS application is used. Here one large spacecraft (the Mother) has a smaller spacecraft (the Child) tethered to it as illustrated in Figure 7.1. While a TCS has many mission potentials this application has the ability to provide a local and small sensor platform to a geosynchronous satellite. This application provides a unique vantage point for on-orbit

inspection of the Mother craft, rendezvous, docking and refueling operations and space environment measurements. This Mother Child (MC) application is analyzed in detail in Reference [136]. Both craft are spherical and feature an outer conducting surface for charge distribution.

The combined power required to equally charge both the 2 m radius Mother and 0.5 m radius Child for each of the plasma conditions is shown in Figure 7.17. The range of spacecraft potentials used in this analysis is -30 kV to 30 kV, based on the earlier plasma current calculations. The total power required of the MC system in a nominal plasma ($\lambda_d = 200$ m) is 8.2 W for -30 kV and 17.2 W for 30 kV. This is a realistic power consumption for a large GEO spacecraft. In the worst-case and rarely experienced quiet plasma ($\lambda_d = 4$ m) the power required by the system to maintain -30 kV is 181 W, and to achieve 30 kV requires 7439 W.
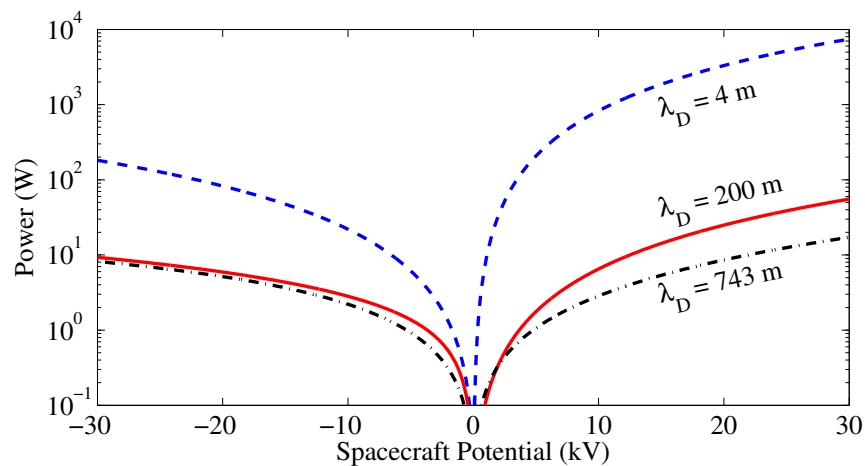
Figure 7.17: Power required in sun light to maintain fixed spacecraft potential for each plasma

These power requirements are independent of the separation distances of the spacecraft. A consideration for the system is whether the Mother features a single charge emission device that charges both itself as well as the Child through a conductive tether. An alternative option is to have a charge emission device on each craft that operate independently. Considering the eclipse operating environment, the craft have an equivalent power requirement during positive charging as this is independent of the photoelectron current. During negative charging, the net plasma current is lower and hence the power requirements are lower than this sun-lit case.

7.7   Positive and negative charging considerations

The previous sections show that increasing charge (Coulomb force) reduces TCS relative motions and that the power requirements are dependent on the polarity and magnitude of the craft potential. An additional consideration for both power consumption and Coulomb force is the size of the spacecraft nodes. Larger nodes generate a greater Coulomb repulsive force (for a given potential level) while also requiring a larger power requirement due to a larger surface area being bombarded by the plasma. Analyzed here is the force generation and power requirements of the baseline MC system in comparison to a equal radii, two sphere system.

The Coulomb force generated between the two spherical TCS nodes of potential V is computed using the force of Eq. 3.36 with shielding from the nominal plasma ($\lambda_d = 200$ m). The total power required is also computed in this nominal plasma in sunlight (photoelectrons included). Both the force and power is shown on a common axis as a function of spacecraft potential in Figure 7.18. The MC power and force is directly compared to a two node system of equal radii of three different values. In this figure the solid lines represent the required power, the dashed lines are the Coulomb force generated. This is computed in a nominal plasma ($\lambda_D = 200$ m) with a center to center separation of 7 m.
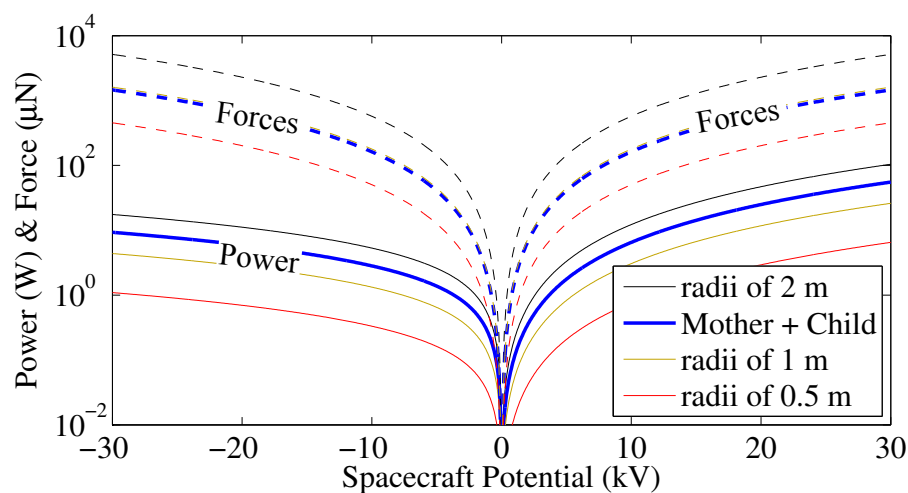
Figure 7.18: Force generated and total power required for two craft in sunlight as a function of sphere potential and showing four radii sizes

Both the force and power are a function of the sphere radius squared, $f(R^2)$, hence at a given potential the proportional increase between each radial line is equivalent. Ultimately, there is no optimal radii, TCS nodal size should be selected based on total power limitations, mass and size constraints or minimum force required for a given potential.

The Coulomb force is a function $F_c = f(V^2)$ which dictates the shape of the curves, and is equivalent magnitude for both positive and negative potentials. The power required during positive charging is also a function $P(V > 0) \approx f(V^2)$ and hence has a similar profile to the force. However during negative charging in this nominal plasma, the dominant current is the constant photoelectrons and the resulting power is a function $P(V < 0) \approx f(V)$. The result is that for negative charging lower power is required to achieve the equivalent force at a given potential.

To demonstrate the relationship between force and power, Figure 7.19 shows the ratio F_c/P for the MC baseline setup. A large ratio value indicates more force is obtained per power required. This figure shows that for positive charging the ratio is constant. Figure 7.19 also shows that it is more advantageous to use negative charge, as an equivalent force can be generated for less power than the same positive charge.
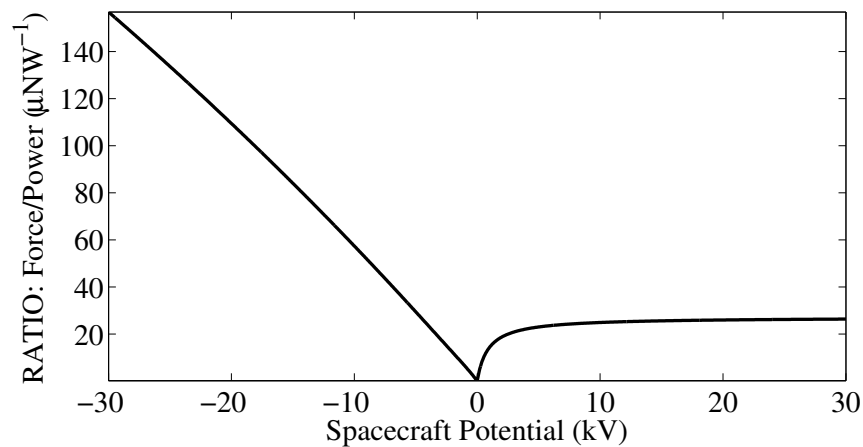
Figure 7.19: Ratio between force generated and power required in sunlight and a nominal plasma

7.8   TCS propellant mass requirements and comparison

Another consideration for implementing a Coulomb repelled tethered Child on a GEO space-craft is the propellant mass requirements. Computed here is the mass required of the charge control device(s) and the associated propellant mass to maintain the desired surface potentials in the three representative plasma conditions (quiet, nominal, disturbed). Similar to the power analysis, the polarity of the spacecraft potentials is a factor in the additional mass required and is addressed here. This is calculated for the baseline MC system with 2 m and 0.5 m radius spheres respectively, operating in sunlit conditions.

7.8.1   Propellant mass flow rates

For a TCS maintaining a fixed potential in a plasma, the required propellant and its mass flow rate is the charge control current emitted to offset the net plasma current. To charge to negative potentials positive ions from an on board propellant source are emitted. For this study the mass flow rate, during negative charging, is computed using Xenon gas ions (Xe^+). For charge control emission it is most advantageous to use the lowest mass particles (ideally protons), however Xenon is used as it is a common hollow cathode propellant and it results in the largest (worst-case) mass flow rate, with a higher ion mass than Indium (a common field emission propellant) [119; 153]. The mass flow rate, during negative charging, is computed using [69]:

$$\dot{m} = \frac{|I_{\text{net}}|m_{\text{ion}}}{e_c} \tag{7.23}$$

where m_{ion} is the mass of the emitted ion species assuming it has a single charge. For positive charging, m_{ion} is replaced with m_{electron}, the mass of an electron, which is 5 orders of magnitude less than Xenon gas ions. An advantage of using electrons is that they are essentially free propellant as they can be obtained on-orbit from solar energy. The instantaneous mass flow rate is directly proportional to the net plasma current and consequently power requirements. The mass flow rate is computed for each plasma and is a scaled version of Figure 7.17. Highlighting, only the fundamental findings of this mass flow rate analysis, Table 7.5 lists the combined MC maximum flow rates for

each of the plasma conditions. The maximum rates correspond to the extremes of the analyzed spacecraft potentials of ± 30 kV.

Table 7.5: Maximum mass flow rate [μgs^{-1}] for each plasma at a given spacecraft potential; computed for the combined Mother and Child configuration

Spacecraft potential	Quiet ($\lambda_D = 4$ m)	Nominal ($\lambda_D = 200$ m)	Disturbed ($\lambda_D = 743$ m)
-30 kV	8.24	0.42	0.37
+30 kV	0.0014	1.0×10^{-5}	3.3×10^{-6}

The maximum required mass flow rate occurs during the worst case, quiet plasma conditions ($\lambda_d = 4$ m) as the net plasma current to the craft is at its highest level then. In a nominal plasma ($\lambda_d = 200$ m) mass flow rates are reduced by at least an order of magnitude. The mass flow rates are orders of magnitudes lower for positive charging as low mass electrons are emitted. The currents here are still higher, so a higher electrical power is required compared to the negative charging.

The highest expected mass flow rate for this combined MC system are below 8 μg/s for all expected plasma conditions. As demonstrated in Section 2.6.3 the current spacecraft charge control technology can produce mass flow rates as high as 0.1 A at 100 μgs^{-1} and 10 A at 200 μgs^{-1} [3; 85], indicating this is an achievable target with current technology. Also, the mass flow rate analysis conducted here does not account for any inefficiencies in the charge control device. In addition, the charge control accuracy for a TCS node system is not important, rather that the overall charge is significant to maintain tether tension and overcome external disturbances. For this reason, a higher mass flow rate increases the nodal charge and ultimately adds stiffness to the MC system.

7.8.2 Total propellant mass comparison

For this mother child TCS application example it is beneficial to estimate the total propellant mass required by the charge control system. The propellant mass is compared to the mass requirements of alternate electric propulsion systems performing an equivalent node repulsive force. The example used is the baseline mother child system with spheres of 2 m and 0.5 m radii. The nodes are operating in an orbit normal configuration at GEO with a desired center to center separation

of 7 m. With a mother mass of 2000 kg and a child mass of 50 kg the differential gravity force compressing the craft has a magnitude of 74.4 μN. In this naturally compressive orbit scenario, the repulsive Coulomb force maintains a taut tether and desired situational awareness separation. To achieve this force in a nominal plasma requires the nodes to be charged to $|12.2|$ kV, using Equation 3.36.

This mother child configuration could also be implemented with free-flying craft that utilize continuous electric propulsion with a thrust opposing the compressive differential gravity. The three electric propulsion methods analyzed are a micro Pulsed Plasma Thruster (PPT), a Colloid thruster, and a Field Emission Electric Propulsion (FEEP) thruster. An important implementation consideration with all of these propulsive methods is that they have possible plume contamination given the close operating proximity of this mother child example, as well as the need for continuos thrust of this application.

For the TCS system the total propellant mass is computed for both negative charging through emission of Xenon ions (Xe^+) and positive charging with electron (e^-) emission using the mass flow rates of Table 7.5. For comparison, the total propellant mass requirements for each electric propulsion system is computed for a single node using the relationship:

$$m_{\text{propellant}} = \frac{t|T_h|}{g\text{I}_{\text{sp}}} \tag{7.24}$$

where t is the duration of propulsive maneuver, g is the gravitational constant and T_h is the desired thrust from a single node, which is equal to the differential gravity force. Table 7.6 gives a representative value of the specific impulse (I_{sp}) of each of the propulsion systems.

The propellant mass is calculated based on the propulsive system applying a continuous thrust to oppose the differential gravity force. This is computed to maintain a 7 m separation for 10 years. The required propellant mass of each of the propulsive methods for this mother child example is also shown in Table 7.6. For the Coulomb system, the propellant mass flow rate is computed for a nominal plasma ($\lambda_D = 200$ m) in sunlit conditions. The propellant mass requirements of each of the propulsion systems is also shown in graphical form in Figure 7.20.

Table 7.6: Comparison of propellant mass requirements to maintain two craft separated by 7 meters in a orbit normal configuration at GEO, for a mission duration of 10 years

Propulsion technology	I_{sp} (s)	Propellant mass (g)
PPT	500	9579
Colloid	1000	4790
FEEP	10000	479.0
Coulomb (Xe^+)	2×10^6	122.4
Coulomb (e^-)	∞	0.0014

As shown in Figure 7.20, the total propellant mass requirements are extremely low for a Coulomb system. If operating in a nominal GEO plasma environment, the TCS system requires 122.4 g of Xenon propellant for positive charging. This propellant mass will increases considering inefficiencies of the system and variable plasma environments, however it is still a significantly low requirement that is very competitive compared to alternate systems.

Another important consideration is the inert mass requirements of the charge control system. The charge control device inert mass is estimated to be low, in the low kg range, which matches well with current charge control technology as shown in the earlier charge control hardware section. As an example, charge control devices for current space missions have masses ranging from 19 kg on ATS-6 [142] through to the more recent Cluster devices weighing only 1.85 kg each [119; 154]. These are devices that could feasible implemented on the mother and child craft.

7.9   Charge emission force considerations

The charge current required to maintain a fixed potential is emitted under electrostatic acceleration. The emission current, while low magnitude, results in a net momentum exchange and consequently a force on the TCS nodes that feature charge control. In earlier studies this force is shown to be negligible for the free-flying charged spacecraft where Debye lengths are assumed to be at least 80 meters or larger [69]. However, these Debye length values are not sufficiently conservative, hence the use of the worst case plasma conditions of this study ($\lambda_d = 4$ m). In addition, if a charge control device is implemented on the low mass Child spacecraft it may experience relatively large
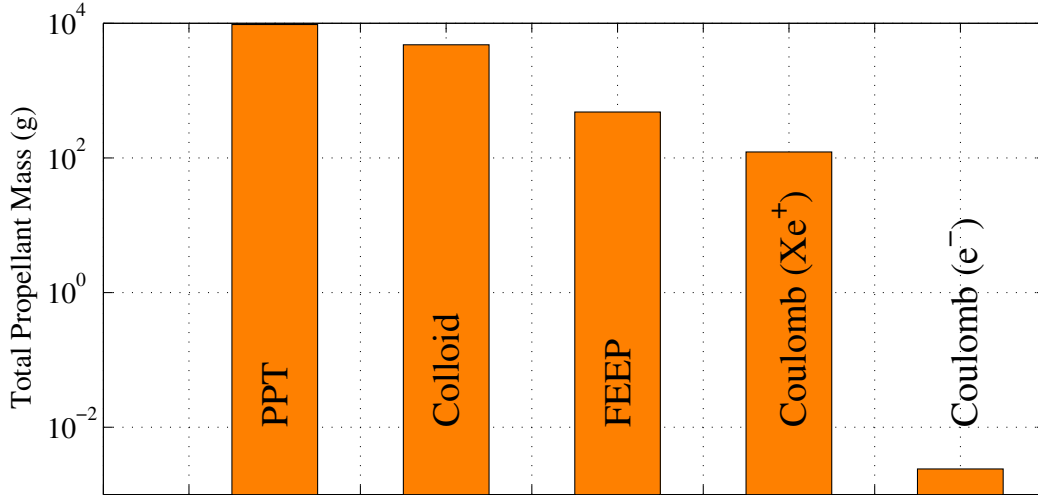
Figure 7.20: Propellant mass estimates for each propellant system to maintain to craft separated by 7 meters in a orbit normal configuration at GEO, for a mission duration of 10 years.

accelerations due to the charge emission force. The charge-thrust force is computed for each of the plasma conditions and compared to the magnitude of the Coulomb force produced for the baseline MC system. The force on a node from the emission current is computed using [48]:

$$F_{cc} = \dot{m} u_{ion} \tag{7.25}$$

where u_{ion} is the emission speed of the ions. During positive charging, low mass electrons are emitted. The mass flow rate is computed using Eq. 7.23 and the emitted ion species is assumed to be Xenon here. The emission speed is proportional to the spacecraft potential V and is calculated using electrostatic repulsion [48]:

$$u_{ion} = \sqrt{\frac{2e_c V}{m_{ion}}} \tag{7.26}$$

Combining Equations 7.23, 7.25 & 7.26 the net charge control force is computed with:

$$F_{cc} = I_{\text{net}} \sqrt{\frac{2m_{ion} V}{e_c}} \tag{7.27}$$

The magnitude of the charge emission force is compared as a ratio of the Coulomb force and shown in Figure 7.21. This total emission force is computed for both the Mother and Child combined in each of the three representative plasmas. The lower shaded region indicates where the charge emission force is greater than the Coulomb force at that potential.
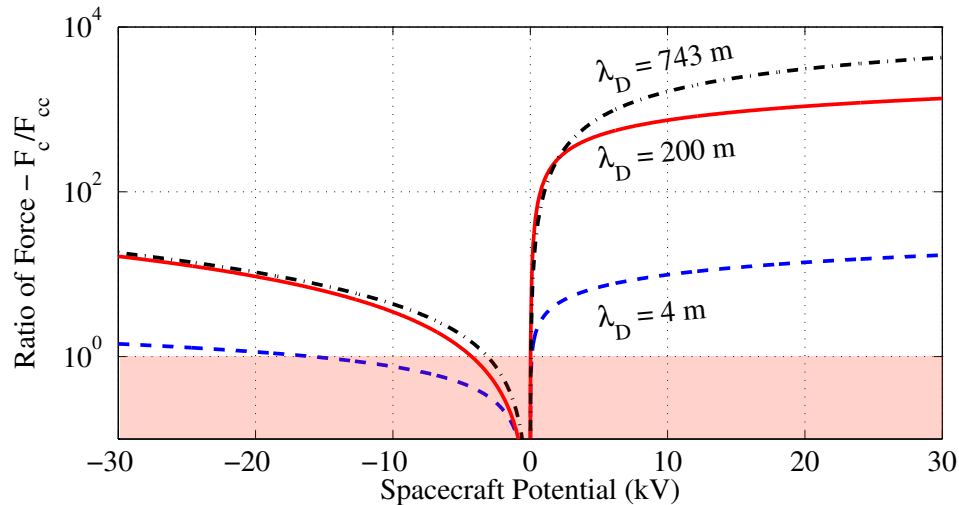
Figure 7.21: Ratio of Coulomb force to charge emission force in each plasma

It is desirable to have a large ratio between these forces given that the Coulomb force is our inflationary actuator and the charge emission force is seen as a potential disturbance on the system. For positive charging the emission of low mass electrons gives a suitably large ratio ($>$ 10 for the worst case plasma). However due to the higher momentum transfer of the Xenon ions during negative charging the ratio between the forces is reduced. In the worst case plasma the forces are very similar magnitude. In the nominal and disturbed plasmas the charge emission force is approximately an order of magnitude less than the minimum Coulomb inflation force.

This study indicates that consideration for the placement and direction of the charge control device on the nodes should be made. If a single charge control device on the Mother is used to charge the system, the emission force can be close or even greater than the Coulomb force magnitudes during negative charging and worst-case plasma conditions. With appropriate placement and the use of multiple emitters the emission force can be directed to create zero net force on the node and not interfere with Coulomb inflation forces. A conceptual example of a charged node with zero net force charge emission plumes is shown in Figure 7.22. In addition, correct placement of the charge device on the Mother or Child could be used as an additional torque source to assist in controlling external perturbations such as gravity gradients.
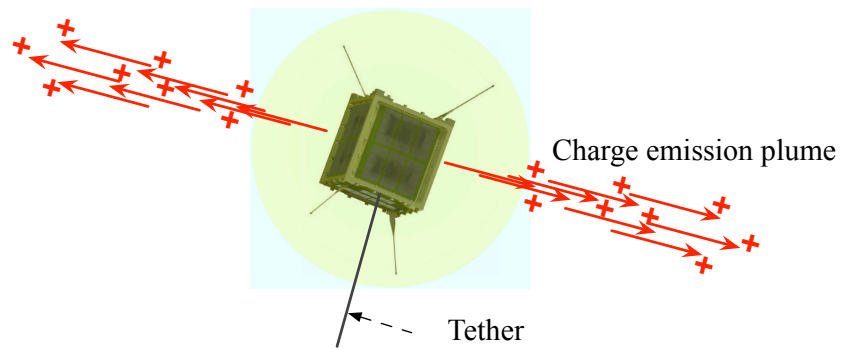
Figure 7.22: Illustration of bi-directional charge emission on a tethered spacecraft node

Chapter 8

Conclusions and future work

This dissertation documents the design and fabrication of the unique Coulomb terrestrial testbed. This testbed provides a platform that is used to explore the intricacies of electrostatic relative motion actuation. The findings of this research support the prospects of the Coulomb spacecraft formation flight concept. Electrostatic power supplies are successfully used to charge spheres and induce one dimensional relative motion in the terrestrial atmosphere of the laboratory. External mechanical and electrostatic disturbances are identified and mitigated to provide an extremely low disturbance environment with perturbations consistently below 1 mN.

Accomplishing a major aim of the testbed, experiments are used to investigate electrostatic force production properties. As documented in this dissertation, this is achieved by using experimental data to estimate parameters of a candidate Coulomb force model. Based on a derived and proposed plasma force model, the terrestrial representation is shown to capture unknown electrostatic interferences. Direct similarities between the space-based plasma shielding and the terrestrial force reductions are shown. This provides a promising opportunity to resemble space-like coulomb actuation on a terrestrial testbed. Further the resulting terrestrial force model is a fundamental component that is required for follow-on testbed verification and implementation purposes.

The implementation of feedback control on the testbed hardware demonstrates the successful repositioning of the cart on the track with Coulomb forces. This feedback control is used to mimic the orbital motion control of two charged craft aligned with the principal orbit axis and achieves non-zero steady state charge solutions. Simulations of these controlled charged motions using

the terrestrial force model accurately predict the true testbed response, which provides bountiful opportunities for future experimental endeavors.

In support of the experimental developments and findings of this dissertation there are fundamental theoretical studies that are also addressed. Shedding light on the future space applications of the CFF concept are two additional research developments. Firstly, a study of relative motion estimation for formations in a plasma is conducted and demonstrates that is feasible to predict local plasma properties using charged relative motion sensing. Finally, a large tethered sensing platform at GEO is proposed and shown to use only watt-levels of power and grams of propellant to maintain its geometry with the use of inflationary Coulomb forces.

Taking a concept from theory and implementing it on hardware opens opportunities to truly explore its details and potential. A wealth of knowledge has already been obtained during the course of this dissertation and is bound to continue with follow-on work involving the testbed. This ultimately is one of its main purposes.

Follow-on work that can carry on from the research of this dissertation includes further analytic applications. A simple and robust controller is used here, however more intricate algorithms can be implemented particularly with the improvements of the terrestrial force model, in this dissertation, to allow more accurate response verification. By using an additional cart on the track control of two free-moving vehicles can be investigated, a dynamical approach more closely resembling free-flying spacecraft. Real-time estimation of parameters such as electrostatic interactions is introduced here, but has a forthcoming implementation on the testbed.

There are also a number of extended experiments and modifications that are envisioned. These include potential environmentally controlled or vacuum operation. Also, a two dimensional testbed would provide an exponential increase in the relative motion maneuvers that could be performed and analyzed. This testbed is a precursor to an abundance of terrestrial experiments that make the prospects of Coulomb formation flight a space-bound reality.

Bibliography

[1] John Adams, Andrew Robertson, Kurt Zimmerman, and Jonathan How. Technologies for spacecraft formation flying. In ION GPS-96; Proceedings of the 9th International Technical Meeting of the Satellite Division of the Institute of Navigation, pages 1321–1330, Kansas City, MO, Sept. 17–20 1996.

[2] B. Amatucci, J. Anderson, S. Arnold, J. Bowen, J. Carroll, S. Coffey, C. Compton, G. Gatling, S. Huynh, P. Jaffe, B. Kelm, S. Koss, J. McGahagan, E. Tejero, and A. Thurn. Ce2: A cubesat electron collector experiment. In AAS/AIAA Spaceflight Mechanics Meeting, Savannah, GA, Feb. 2009.

[3] G. Aston, Aston M. B., and J. D. Williams. Miniature plasma activated systems for tether current generation. In American Institute of Physics, editor, Space Technology and Applications International Forum, 2001.

[4] William Barnds, Shannon Coffey, Mark Davis, Bernard Kelm, and William Purdy. Tips: Results of a tethered satellite experiment. In Proceedings of the AAS/AIAA Astrodynamics Specialist Conference, Sun Valley, ID, Aug. 4–7 1997. Paper AAS 97–600.

[5] Frank H. Bauer, Kate Hartman, Jonathan P. How, John Bristow, David Weidow, and Franz Busse. Enabling spacecraft formation flying through spaceborne gps and enhanced automation technologies. In ION-GPS Conference, Nashville, TN, Sept. 15 2009.

[6] John Berryman and Hanspeter Schaub. Static equilibrium configurations in GEO coulomb spacecraft formations. In AAS/AIAA Spaceflight Mechanics Meeting, Copper Mountain, CO, Jan. 23–27 2005. Paper No. AAS 05–104.

[7] John Berryman and Hanspeter Schaub. Analytical charge analysis for 2- and 3-craft coulomb formations. AIAA Journal of Guidance, Control, and Dynamics, 30(6):1701–1710, Nov.–Dec. 2007.

[8] Gary Blackwood, Curt Henry, Eugene Serabyn, Serge Dubovitsky, MiMi Aung, and Steven M. Gunter. Technology and design of an infrared interferometer for the terrestrial planet finder. In AIAA Space 2003, Long Beach, CA, Sept. 23–25 2003. Paper No. AIAA 2003-6329.

[9] Owen Brown and Paul Eremenko. Fractionated space architectures: A vision for responsive space. In 4th Responsive Space Conference, Los Angeles, CA, April 23–26 2006. Paper No. AIAA-RS-2006-1002.

[10] J. Russell Carpenter, Jesse A. Leitner, David C. Folta, and Richard D. Burns. Benchmark problems for spacecraft formation flying missions. In AIAA Guidance, Navigation and Control Conference, Austin, TX, August 11–14 2003. Paper No. AIAA 2003-5364.

[11] Kenneth G. Carpenter, Carolus J. Schrijver, Margarita Karovska, and SI Mission Concet Development Team. The stellar imager (si) project: A deep space uv/optical interferometer (uvoi) to observe the universe at 0.1 milli-arcsec angular resolution. In Proceedings of the NUVA Conference, El Escorial, Spain, June 2007.

[12] Joseph A. Carroll. Tether applications in space transportation. Acta Astronautica, 13(4):165–174, 1986.

[13] Joseph A. Carroll and John C. Oldson. Tethers for small satellite applications. In AIAA/USU Small Satellite Conference, Logan, Utah, 1995.

[14] M. P. Cartmell and D. J. McKenzie. A review of space tether research. Progress in Aerospace Sciences, 44:1–21, 2008.

[15] Webster Cash. Detection of earth-like planets around nearby stars using a petal-shaped occulter. Nature, 442(6):51–53, July 2006.

[16] Webster Cash, Jeremy Kasdin, Sara Seager, and Jonathon Arenberg. Direct studies of exoplanets with the new worlds observer. In SPIE 5899 - UV/Optical/IR Space Telescopes: Innovative Technologies and Concepts II, San Diego, CA, July 31 2005.

[17] Soon-Jo Chung, Danielle Adams, David W. Miller, Enrico Lorenzini, and David Leisawitz. Spheres tethered formation flight testbed: Advancements in enabling nasa's specs mission. In SPIE – Proceedings of Astronomical Telescopes and Instrumentation Conference, Orlando, FL, 2006. Paper No. 6268-11.

[18] Soon-Jo Chung and David W. Miller. Propellant-free control of tethered formation flight, part 1: Linear control and experimentation. Journal of Guidance, Control and Dynamics, 31(3):571–584, May–June 2008.

[19] Richard G. Cobb, Steven N. Lindemuth, Joseph C. Slater, and Michael R. Maddux. Development and test of a rigidizable inflatable structure experiment. In 45th AIAA/ASME/ASCE/AHS/ASC Structures, Structural Dynamics & Materials Conference, Palm Springs, CA, April 19–22 2004. Paper No. AIAA 2004–1666.

[20] John H. Cover, Wolfgang Knauer, and Hans A. Maurer. Lightweight reflecting structures utilizing electrostatic inflation. US Patent 3,546,706, October 31 1966.

[21] J. Crowley. Simple expressions for force and capacitance for a conductive sphere near a conductive wall. In ESA Annual Meeting on Electrostatics, Minneapolis, MN, June 17–20 2008. Paper D1.

[22] Simone D'Amico, Jean-Sebastien Ardaens, and Sergio Florio. Autonomous formation flying based on gps - prisma flight results. In 6th International Workshop on Satellite Constellation and Formation Flying, Taipei, Taiwan, Nov. 1–3 2010.

[23] V. A. Davis, M. J. Mandell, and Thomsen M. F. Representation of the measured geosynchronous plasma environment in spacecraft charging calculations. Journal of Geophysical Research, 113(A10204), 2008.

[24] V. A. Davis and Duncan L. W. Spacecraft surface charging handbook. Technical Report 92-2232, Air Force Materiel Command, U.S. Air Force, 1992.

[25] S. E. DeForest. Spacecraft charging at synchronous orbit. Journal of Geophysical Research, 77(4):651–659, Feb. 1972.

[26] S. E. DeForest. The plasma environment at geosynchronous orbit. In 1st Spacecraft Charging Technology Conference, pages 37–52, Hanscom AFB, MA, Feb. 24 1977. Air Force Geophysics Laboratory.

[27] W. D. Deininger, G. Aston, and L. C. Pless. Hollow-cathode plasma source for active spacecraft charge control. Review of Scientific Instruments, 58(6):1053–1062, June 1987. -19 kV potential ATS 6.

[28] M. H. Denton, M. F. Thomsen, H. Korth, S. Lynch, J. C. Zhang, and M. W. Liemohn. Bulk plasma properties at geosynchronous orbit. Journal of Geophysical Research, 110(A09215), 2005.

[29] R. E. Denton, J. D. Menietti, J. Goldstein, S. L. Young, and R. R. Anderson. Electron density in the magnetosphere. Journal of Geophysical Research, 109(A09215), 2004.

[30] C. P. Escoubet, M. Fehringer, and M. Goldstein. The cluster mission. Annales Geophysicae, 19(10/12):1197–1200, 2001.

[31] Houfei Fang, Kevin Knarr, Ubaldo Quijano, John Huang, and Mark Thomson. In-space deployable reflectarray antenna: Current and future. In AIAA/ASME/ASCE/AHS/ASC Structures, Structural Dynamics and Materials Conference, Schaumburg, IL, April 7-10 2008. Paper No. AIAA 2008-2209.

[32] J. F. Fennell, H. C. Koons, J. L. Roeder, and J. B. Blake. Spacecraft charging: Observations and relationship to satellite anomalies. In Proceedings of 7th Spacecraft Charging Technology Conference, pages 279–285, Noordwijk, The Netherlands, April 23–27 2001. ESA Spec. Publ.

[33] Dale C. Ferguson and G. Barry Hillard. New nasa see leo spacecraft charging design guidelines - how to survive in leo rather than geo. Technical Report 2003-212737, NASA, Dec. 2003.

[34] Michael E. Fisher and Yan Levin. Criticality in ionic fluids: Debye-hückel theory, bjerrum, and beyond. Physical Review Letters, 71(23):3826–3829, Dec. 1993.

[35] C. R. Francis. Electrostatic charging problems of spacecraft. Journal of Electrostatics, 11:265–280, 1982.

[36] R. E. Freeland, G. D. Bilyeu, , G. R. Veal, and M. M. Mikulas. Inflatable deployable space structures technology summary. In 49th International Astronautical Congress, Melbourne, Australia, Sept. 28 – Oct. 2 1998. International Astronautical Federation. Paper No. IAF-98-I.5.01.

[37] R. E. Freeland, G. D. Bilyeu, and G. R. Veal. Validation of a unique concept for a low-cost, lightweight space-deployable antenna structure. Acta Astronautica, 35(9-11):565–572, 1995.

[38] C. V. M Fridlund. Darwin – the infrared space interferometry mission. Technical report, Space Science Department, ESA Directorate of Scientific Programmes, ESTEC, Noordwjik, The Netherlands, Aug. 2000.

[39] B. Frommknecht, H. Oberndorfer, F. Flechtner, and R. Schmidt. Integrated sensor analysis for grace – development and validation. Advances in Geosciences, 1:57–63, 2003.

[40] Thomas B. Frooninckx. High-latitude spacecraft charging in low-earth polar orbit. Master's thesis, Utah State University, Logan, Utah, 1991.

[41] H. B. Garrett. The charging of spacecraft surfaces. Reviews of Geophysics and Space Physics, 19(4):577–616, Nov. 1981.

[42] H. B. Garrett and S. E. DeForest. An analytical simulation of the geosynchronous plasma environment. Planetary Space Science, 27:1101–1109, 1979.

[43] Henry B. Garrett and Albert C. Whittlesey. Spacecraft charging, an update. IEEE Transactions on Plasma Science, 28(6):2017–2028, Dec. 2000.

[44] Jessica Gersh. Architecting the very-large-aperture flux-pinned space telescope: A scalable, modular obtical array with high agility and passively stable orbital dynamics. In AAS/AIAA Astrodynamics Specialist Conference, Honolulu, Hawaii, Aug. 18–21 2008. Paper No. AIAA 2008-7212.

[45] B. E. Gilchrist, C. Bonifazi, S. G. Bilen, W. J. Raitt, W. J. Burke, N. H. Stone, and J. P. Lebreton. Enhanced electrodynamic tether currents due to electron emission from a neutral gas discharge: Results from the tss–1r mission. Geophysical Research Letters, 25(4):437–440, Feb. 15 1998.

[46] Eberhard Gill, Simone D'Amico, and Oliver Montenbruck. Autonomous formation flying for the prisma mission. AIAA Journal of Spacecraft and Rockets, 44(3):671–681, May–June 2007.

[47] Keith A. Gittemeier, Clark W. Hawk, Miria M. Kinckenor, and Ed Watts. Low earth orbit environmental effects on space tether materials. In 41st AIAA/ASME/SAE/ASEE Joint Propulsion Conference and Exhibit, Tucson, AZ, Jul. 10–13 2005. Paper No. AIAA 2005–4433.

[48] D. M. Goebel and I. Katz. Fundamentals of Electric Propulsion. JPL Space Science and Technology Series. John Wiley and Sons, Hoboken, NJ, 2008.

[49] Tamas I. Gombosi. Physics of the Space Environment. Cambridge University Press, New York, NY, 1998.

[50] R. Grard. Properties of the satellite photoelectron sheath derived from photoemission laboratroy measurements. Journal of Geophysical Research, 78(16):2885–2906, 1973.

[51] R. Grard, K. Knott, and Pedersen. Spacecraft charging effects. Space Science Reviews, 34:289–304, 1983.

[52] D. A Gurnett and Bhattacharjee A. Introduction to Plasma Physics - with Space and Laboratory Applications. Cambridge University Press, New York, NY, 2005. Pages 8–9.

[53] D. E. Hastings. The use of electrostatic noise to control high-voltage differential charging of spacecraft. Journal of Geophysical Research, 91(A5):5719–5724, May 1986.

[54] Daniel E. Hastings and Henry B. Garrett. Spacecraft-Environment Interactions. Cambridge University Press, 1996.

[55] J. L. Herr and M. B. McCollum. Spacecraft environments interactions: Protecting against the effects of spacecraft charging. Reference Publication 1354, NASA Marshall Space Flight Center, Nov. 1994.

[56] Erik Hogan and Hanspeter Schaub. Collinear invariant shapes for three-craft coulomb formations. In AAS/AIAA Astrodynamics Specialist Conference, Toronto, Canada, Aug. 2–5 2010. Paper No. AIAA-2010–7954.

[57] Erik Hogan and Hanspeter Schaub. Linear stability and shape analysis of spinning three-craft coulomb formations. In AAS Spaceflight Mechanics Meeting, New Orleans, LA, Feb. 13–17 2011. Paper AAS 11–225.

[58] J. L. Horwitz and C. R. Chappel. Observations of warm plasma in the dayside plasma trough at geosynchronous orbit. Journal of Geophysical Research, 84(A12):7075–7090, Dec. 1979.

[59] I. H. Hutchinson. Principles of Plasma Diagnostics. Cambridge University Press, 2002.

[60] Roderick Hyde. Eyeglass large aperture, lightweight space optics. Technical Report UCRL-ID-151390, University of California, Lawrence Livermore National Laboratory, Feb. 10 2003.

[61] Roderick Hyde, Shamasundar Dixit, Andrew Weisberg, and Michael Rushford. Eyeglass: A very large aperture diffractive space telescope. SPIE – Highly Innovative Space Telescope Concepts, 4849:28–39, Dec. 18 2002.

[62] Ravi Inampudi and Hanspeter Schaub. Orbit-radial control of a two-craft coulomb formation about circular orbits and libration points. In 4th International Conference on Spacecraft Formation Flying Missions & Technologies, St-Hubert, Québec, May 18–20 2011.

[63] Dario Izzo and Lorenzo Pettazzi. Self-assembly of large structures in space using intersatellite coulomb forces. In 57th International Astronautical Congress, Valencia, Spain, October 2006. Paper IAC-06-C3.4/D3.4.07.

[64] Niels Jonassen. Electrostatics. Kluwer Academic Publishers, second edition, 2002.

[65] Terrence E. Sheridan Jr. and John A. Goree. Analytic expression for the electric potential in the plasma sheath. IEEE Transactions on Plasma Science, 17(6):884–888, Dec. 1989.

[66] I. Katz, G. A. Jongeward, and et. al. Structure of the bipolar plasma sheath generated by spear i. Journal of Geophysical Research, 94(A2):1450–1458, Feb. 1989.

[67] I. Katz, G. A. Jongeward, M. J. Mandell, K. C. Maffei, and J. R. Cooper. Preventing ion bombardment caused breakdown in high voltage space power systems and applications to space power experiments aboard rockets (spear). In IEEE Energy Conversion Engineering Conference, volume 1, pages 447–451. IEEE, Aug. 6–11 1989.

[68] I. Katz, M. J. Mandell, J. C. Roche, and C. K. Purvis. Secondary electron generation, emission and transport: Effects on spacecraft charging and nascap models. Journal of Electrostatics, 20:109–121, 1987.

[69] Lyon B. King, Gordon G. Parker, Satwik Deshmukh, and Jer-Hong Chong. Spacecraft formation-flying using inter-vehicle coulomb forces. Technical report, NASA Institute for Advanced Concepts (NIAC), January 2002.

[70] Lyon B. King, Gordon G. Parker, Satwik Deshmukh, and Jer-Hong Chong. Study of inter-spacecraft coulomb forces and implications for formation flying. AIAA Journal of Propulsion and Power, 19(3):497–505, May–June 2003.

[71] Edmund M. C. Kong, Daniel W. Kwon, Samuel A. Schweighart, Laila M. Elias, Raymond J. Sedwick, and David W. Miller. Electromagnetic formation flight for multisatellite arrays. AIAA Journal of Spacecraft and Rockets, 41(4):659–666, July–Aug. 2004.

[72] H. C. Koons and et. al. The impact of the space environment on space systems. In 6th Spacecraft Charging Control Technology Conference, Hanscom AFB, MA, Sept. 2000.

[73] Daniel W. Kwon, Raymond J. Sedwick, Sang-il Lee, and Jaime L. Ramirez-Riberos. Electromagnetic formation flight testbed using superconducting coils. AIAA Journal of Spacecraft and Rockets, 48(1):124–134, Jan. – Feb. 2011.

[74] J. G. Laframboise, Luo J., and L. W. Parker. High-voltage charging of spacecraft in low polar orbit: A study of physical effects involved. Technical report, Air Force Geophysics Laboratory, Hanscom AFB, MA, April 1988.

[75] S. T. Lai. An overview of electron and ion beam effects in charging and discharging of spacecraft. IEEE Transactions on Nuclear Science, 36(6):2027–2032, Dec. 1989.

[76] S. T. Lai. Spacecraft charging thresholds in single and double maxwellian space environments. IEEE Transactions on Nuclear Science, 38(6):1629–1634, 1991.

[77] S. T. Lai. Theory and observation of triple-root jump in spacecraft charging. Journal of Geophysical Research, 96(A11):19,269–19,281, Nov. 1991.

[78] S. T. Lai. The importance of surface conditions for spacecraft charging. In AIAA Aerospace Sciences Meeting, Orlando, FL, Jan. 5 – 8 2009. Paper AIAA 2009-349.

[79] S. T. Lai and M. Tautz. High-level spacecraft charging at geosynchronous altitudes: A statistical study. In 8th Spacecraft Charging Technology Conference, Huntsville, AL, October 20-24 2003.

[80] Casey Lambert, Alfred Ng, Yosuke Nakamura, and Hiroshi Horiguchi. Intersatellite separation mechanism for the jc2sat formation-flying mission. AIAA Journal of Spacecraft and Rockets, 48(4):654–663, July–Aug. 2011.

[81] Vaios J. Lappas, Chakravarthini Saaj, Dave J. Richie, Mason A. Peck, Brett Streeman, and Hanspeter Schaub. Spacecraft formation flying and reconfiguration with electrostatic forces. In AAS/AIAA Spaceflight Mechanics Meeting, Sedona, AZ, Jan. 28–Feb. 1 2007. Paper AAS 07–113.

[82] Jesse Leitner, Frank Bauer, Jonathan How, Michael Moreau, Russell Carpenter, and David Folta. Formation flight in space: Distributed spacecraft systems develop new gps capabilities. GPS World, 13(2):22–31, February 1 2002.

[83] W. Lennartsson and D. L. Reasoner. Low-energy plasma observations at synchronous orbit. Journal of Geophysical Research, 83(A5):2145 – 2156, 1978.

[84] R. O. Lewis Jr. Viking and stp p78-2 electrostatic charging designs and testing. In Spacecraft Charging and Technology Conference, pages 753–772, 1977.

[85] C. M. Marrese. A review of field emission cathode technologies for electric propulsion systems and instruments. In IEEE Aerospace Conference Proceedings, volume 4, pages 85–98, 2000.

[86] G. Matticari, M. Materassi, G. E. Noci, A. Severi, and J. Sabbagh. Plegpay: A plasma contactor experiment on the international space station. In 27th International Electric Propulsion Conference, Pasadena, CA, Oct. 2001. Paper No. IEPC-01-261.

[87] Shawn B. McCamish, Marcello Romano, Simon Nolet, Christine M. Edwards, and David W. Miller. Ground and space testing of multiple spacecraft control during close proximity operations. In AIAA Guidance, Navigation and Control Conference, Honolulu, Hawaii, Aug. 2008.

[88] D. J. McComas, S. J. Bame, B. L. Barraclough, J. R. Donart, R. C. Elphic, J. T. Gosling, M. B. Moldwin, K. R. Moore, and M. F. Thomsen. Magnetospheric plasma analyzer: Initial three-spacecraft observations from geosynchronousorbit. Journal of Geophysical Research, 98(A8):13,453–13,465, Aug. 1 1993.

[89] D. A. McPherson, D. P. Cauffman, and W. Schober. Spacecraft charging at high altitudes - the scatha satellite program. In AIAA Aerospace Sciences Meeting, Pasadena, CA, Jan. 20–22 1975.

[90] David Miller, A. Saenz-Otero, and J. Wertz et. al. Spheres: A testbed for long duration satellite formation flying in micro-gravity conditions. In Proceedings of the AAS/AIAA Spaceflight Mechanics Meeting, pages 167–179, San Diego, CA, 2000. Univelt.

[91] David W. Miller, , Raymond J. Sedwick, Edmund M. C. Kong, and Samuel Schweighart. Electromagnetic formation flight for sparse aperture telescopes. In IEEE Aerospace Conference Proceedings, volume 2, pages 2–729 – 2–741, Big Sky, Montana, March 9–16 2002.

[92] G. J. Monkman. An analysis of astrictive prehension. The International Journal of Robotics Research, 16(1):1–10, February 1997.

[93] Gareth Monkman. Electroadhesive microgrippers. Industrial Robot: An International Journal, 30(4):326–330, 2003.

[94] A. D. Moore. Electrostatics and its Applications. John Wiley & Sons, Inc., 1973. Corona pp. 17-18,.

[95] E. G. Mullen, M. S. Gussenhoven, D. A Hardy, T. A. Aggson, and B. G. Ledley. Scatha survey of high-voltage spacecraft charging in sunlight. Journal of the Geophysical Sciences, 91(A2):1474–1490, 1986.

[96] E.G. Mullen, A. R. Frederickson, G. P. Murphy, K. P. Ray, E. G. Holeman, D.E. Delorey, R. Robson, and M. Farar. An autonomous charge control system at geosynchronous altitude: Flight results for spacecraft design considerations. IEEE Transactions on Nuclear Science, 44(6):2188 – 2914, December 1997.

[97] Naomi Murdoch, Dario Izzo, Claudio Bombardelli, Ian Carnelli, Alain Hilgers, and David Rodgers. Electrostatic tractor for near earth object deflection. In 59th International Astronautical Congress, Glasgow, Scotland, 2008. Paper IAC-08-A3.I.5.

[98] David J. Naffin and Gaurav S. Sukhatme. A test bed for autonomous formation flying. Technical report, Institute for Robotics and Intelligent Systems, 2002. Paper No. IRIS-02-412.

[99] Tomoko Nakagawa, Takuma Ishii, Koichiro Tsuruda, Hajime Hayakawa, and Toshifumi Mukai. Net current density of photoelectrons emitted from the surface of the geotail spacecraft. Earth Space and Planets, 52:283–292, 2000.

[100] Arun Natarajan and Hanspeter Schaub. Linear dynamics and stability analysis of a coulomb tether formation. AIAA Journal of Guidance, Control, and Dynamics, 29(4):831–839, July–Aug. 2006.

[101] R. C. Olsen. Modification of spacecraft potentials by plasma emission. AIAA Journal of Spacecraft and Rockets, 18(5):462–470, Sept.–Oct. 1981.

[102] R. C. Olsen. Modification of spacecraft potentials by thermal electron emission on ats-5. AIAA Journal of Spacecraft and Rockets, 18(6):527 – 532, Nov. – Dec. 1981.

[103] R. C. Olsen. Experiments in charge control at geosynchronous orbit - ats-5 and ats-6. AIAA Journal of Spacecraft and Rockets, 22(3):254–264, May–June 1985.

[104] R. C. Olsen. Comment on "theory and observation of triple-root jump in spacecraft charging" by shu t. lai. Journal of Geophysical Research, 96(A12):21,411–21,412, Dec. 1991.

[105] R. C. Olsen, T. Van Horn, R. Torbert, and W. J. Raitt. Spear-1 charging behavior. In ESA Space Environment Analysis Workshop, Oct. 9–12 1990.

[106] Committee on the Societal and Economic Impacts of Severe Space Weather Events. Severe space weather events - understanding societal and economic impacts. Report of a workshop, National Academies Press, National Research Council, 2008.

[107] Ad Hoc Committee on the Solar System Radiation Environment. Space radiation hazards and the vision for space exploration. Report of a workshop, National Academies Press, National Research Council, 2006.

[108] M. J. M. Parrot, L. R. O. Storey, L. W. Parker, and J. G. Laframboise. Theory of cylindrical and spherical langmuir probes in the limit of vanishing debye number. Physics of Fluids, 25(12):2388–2400, Dec. 1982.

[109] M. A. Peck, B. Streetman, C. M. Saaj, and V. Lappas. Spacecraft formation flying using lorentz forces. Journal of the British Interplanetary Society, 60:263–267, July 2007.

[110] Mason A. Peck. Prospects and challenges for lorentz-augmented orbits. In AIAA Guidance, Navigation and Control Conference, San Francisco, CA, August 15–18 2005. Paper No. AIAA 2005-5995.

[111] Lorenzo Pettazzi, Dario Izzo, and S. Theil. Swarm navigation and reconfiguration using electrostatic forces. In 7th International Conference on Dynamics and Control of Systems and Structures in Space, pages 257–267, Greenwich, London, England, July 2006.

[112] Lorenzo Pettazzi, Hans Krüger, Stephan Theil, and Dario Izzo. Electrostatic force for swarm navigation and reconfiguration. Acta Futura, 4:80–86, 2008.

[113] Vincent L. Pisacane. The Space Environment and its Effects on Space Systems. AIAA Education Series, Reston, VA, 2008. Pages 208–209.

[114] S. M. L. Prokopenko and J. G. Laframboise. High-voltage differential charging of geostationary spacecraft. Journal of Geophysical Research, 85(A8):4125–4131, Aug. 1980.

[115] Gerd W. Prölss. Physics of the Earth's Space Environment. Springer, 2004.

[116] C. K. Purvis, R. O. Bartlett, and S. E. DeForest. Active control of spacecraft charging on ats-5 and ats-6. In Spacecraft Charging and Technology Conference, pages 107–120, 1977.

[117] C. K. Purvis, H. B. Garrett, A. C. Whittlesey, and Stevens N. J. Design guidelines for assessing and controlling spacecraft charging effects. Technical report, NASA, 1984. Paper 2361.

[118] A. D. Rawlins. Note on the capacitance of two closely separated spheres. IMA Journal of Applied Mathematics, 34:119–120, 1985.

[119] W. Riedler, K. Torkar, F. Rudenauer, M. Fehringer, A. Pedersen, R. Schmidt, R. J. L. Grard, H. Arends, B. T. Narheim, J. Troim, R. Torbert, R. C. Olsen, E. Whipple, R. Goldstein, N. Valavanoglou, and H. Zhao. Active spacecraft potential control. Space Science Reviews, 79:271–302, Jan. 1997.

[120] P. A. Robinson Jr and P. Coakley. Spacecraft charging: Progress in the study of dielectrics and plasmas. IEEE Transactions on Electrical Insulation, 27(5):944–960, October 1992.

[121] P. Rustan, H. Garrett, and MJ Schor. High voltages in space: Innovation in space insulation. IEEE Transactions on Electrical Insulation, 28(5):855–865, Oct. 1993.

[122] C. M. Saaj, V. Lappas, H. Schaub, and D. Izzo. Hybrid propulsion system for formation flying using electrostatic forces. Aerospace Science and Technology, 14(5):348–355, Jul.–Aug. 2010.

[123] C. M. Saaj, Vaios J. Lappas, David J. Richie, Hanspeter Schaub, and Dario Izzo. Hybrid propulsion system for spacecraft swarm aggregation using coulomb force. Journal of British Interplanetary Society, July 2007.

[124] Chakravarthini Saaj, Vaios J. Lappas, Dave J. Richie, Mason A. Peck, Brett J. Streetman, and Hanspeter Schaub. Electrostatic forces for satellite swarm navigation and reconfiguration. Technical Report 19697/06/NL/HE, ESA, 2006.

[125] U. Samir and A. P Willmore. The equilibrium potential of a spacecraft in the ionosphere. Planetary and Space Science, 14:1131–1137, 1966.

[126] Rainer Sandau, Hans-Peter Röser, and Arnoldo Valenzuela (Editors). Small Satellites for Earth Observation: Selected Contributions. Springer, 2008.

[127] Daniel P. Scharf, Fred Y. Hadaegh, Jason A. Keim, Arin C. Morfopoulos, Asif Ahmed, Yan Brenman, Ali Vafaei, Joel F. Shields, Charles F. Bergh, and Peter R. Lawson. Flight-like ground demonstrations of precision maneuvers for spacecraft formations. In AIAA Guidance, Navigation and Control Conference, Honolulu, Hawaii, Aug. 18–21 2008. Paper No. AIAA 2008-6665.

[128] Hanspeter Schaub and John L. Junkins. Analytical Mechanics of Space Systems. AIAA Education Series, Reston, VA, 2nd edition, October 2009.

[129] Hanspeter Schaub and Daniel. F. Moorer. Geosynchronous large debris reorbiter: Challengs and prospects. In AAS Kyle T. Alfriend Astrodynamics Symposium, Monterey, CA, May 17–19 2010.

[130] Hanspeter Schaub, Gordon G. Parker, and Lyon B. King. Challenges and prospects of coulomb formations. Journal of the Astronautical Sciences, 52(1–2):169–193, Jan.–June 2004.

[131] Hanspeter Schaub, Gordon G. Parker, and Lyon B. King. Coulomb thrusting application study. Technical report, Virginia Tech and Aerophysics, Jan. 2006.

[132] Schmidt and et. al. Results from active spacecraft potential control on the geotail spacecraft. Journal of Geophysical Research, 100(A9):253–259, 1995.

[133] H. Schubert and Jonathan How. Space construction: An experimental testbed to develop enabling technologies. In Proceedings of the Conference on Telemanipulator and Telepresence Technologies IV, pages 179–188, Piscataway, NJ, 1997. IEEE.

[134] Jana L. Schwartz, Mason A. Peck, and Christopher D. Hall. Historical review of air-bearing spacecraft simulators. AIAA Journal of Guidance, Control, and Dynamics, 26(4):513–522, 2003.

[135] Carl R. Seubert, Stephan Panosian, and Hanspeter Schaub. Dynamic feasibility study of a tethered coulomb structure. In AAS/AIAA Astrodynamics Specialist Conference, Toronto, Canada, Aug. 2–5 2010. Paper No. AIAA-2010–8131.

[136] Carl R. Seubert, Stephan Panosian, and Hanspeter Schaub. Analysis of a tethered coulomb structure applied to close proximity situational awareness. In AAS/AIAA Spaceflight Mechanics Meeting, Girdwood, AK, July 31 – August 4 2011. Paper AAS 11–632.

[137] Carl R. Seubert and Hanspeter Schaub. Tethered coulomb structures: Prospects and challenges. In AAS F. Landis Markley Astrodynamics Symposium, Cambridge, MA, June 30 – July 2 2008. Paper No. AAS 08–269.

[138] Carl R. Seubert and Hanspeter Schaub. Closed-loop one-dimensional charged relative motion experiments simulating constrained orbital motion. In AAS/AIAA Astrodynamics Specialist Conference, Pittsburgh, PA, Aug. 9–13 2009. Paper No. AAS 09–390.

[139] Carl R. Seubert and Hanspeter Schaub. One-dimensional testbed for coulomb controlled spacecraft. In AAS/AIAA Spaceflight Mechanics Meeting, Savannah, GA, Feb. 8–12 2009. Paper No. AAS 09–015.

[140] Carl R. Seubert and Hanspeter Schaub. Tethered coulomb structures: Prospects and challenges. AAS Journal of the Astronautical Sciences, 57(1–2), 2009.

[141] Carl R. Seubert and Hanspeter Schaub. Rotational stiffness study of two-element tethered coulomb structures. AIAA Journal of Spacecraft and Rockets, 48(3):488–497, May–June 2011.

[142] B. M. Shuman, H. A. Cohn, J. Hyman, R. R. Robson, J. Santoru, and W. S. Willamson. Automatic charge control system for geosynchronous satellites. Journal of Electrostatics, 20:141–154, 1987.

[143] J. Sliško and R.A. Brito-Orta. On approximate formulas for the electrostatic force between two conducting spheres. American Journal of Physics, 66(4):352–355, April 1998.

[144] W. R. Smythe. Static and Dynamic Electricity. McGraw-Hill, 3rd edition, 1968.

[145] Jack A. Soules. Precise calculation of the electrostatic force between charged spheres including induction effects. American Journal of Physics, 58(12):1195–1199, Dec. 1990.

[146] Laura A. Stiles, Hanspeter Schaub, and Kurt K. Maute. Voltage requirements for electrostatic inflation of gossamer space. In AIAA Gossamer Systems Forum, Denver, CO, April 4–7 2011.

[147] Byron D. Tapley, Bob E Schutz, and George H. Born. Statistical Orbit Determination. Academic Press, 1st edition, 2004.

[148] Pablo A. Tarazaga, Daniel J. Inman, and W. Keats Wilkie. Control of a space rigidizable inflatable boom using macro-fiber composite actuators. Journal of Vibration and Control, 13(7):935–950, 2007.

[149] ThalesAleniaSpace. Spacecraft charging active control payload. Information Flyer, Dec. 2006.

[150] M. F. Thomsen, M. H. Denton, B. Lavraud, and M. Bodeau. Statistics of plasma fluxes at geosynchronous orbit over more than a full solar cycle. Space Weather, 5(S03004), 2007.

[151] K. Torkar, H. Arends, Baumjohann W., C. P. Escoubet, A. Fazakerley, M. Fehringer, G. Fremuth, H. Jeszenszky, G. Laky, B. T. Narheim, W. Riedler, F. Rudenauer, W. Steiger, K. Svenes, and H. Zhao. Spacecraft potential control for double star. Annales Geophysicae, 23(8):2813–2823, Aug. 2005.

[152] K. Torkar, A. Fazakerley, and W. Steiger. Active spacecraft potential control: Results from the double star project. IEEE Transactions on Plasma Science, 34(5):2046–2052, Oct. 2006.

[153] K. Torkar, M. Fehringer, H. Arends, R. Goldstein, R. J. L. Grard, B. T. Narheim, R. C. Olsen, A. Pedersen, W. Riedler, F. Rudenauer, R. Schmidt, K. Svenes, E. Whipple, R. Torbert, and H. Zhao. Spacecraft potential control using indium ion source – experience and outlook based on six years of operation in space. In 6th Spacecraft Charging Control Technology Conference, Hanscom AFB, MA, Sept. 2000. AFRL-VS-TR-20001578.

[154] K. Torkar, W. Riedler, C. P. Escoubet, M. Fehringer, R. Schmidt, Grard R. J. L., H. Arends, F. Rudenauer, W. Steiger, B. T. Narheim, K. Svenes, R. Torbert, Andre M., A. Fazakerley, R. Goldstein, R. C. Olsen, A. Pedersen, E. Whipple, and H. Zhao. Active spacecraft potential control for cluster – implementation and first results. Annales Geophysicae, 19(10/12):1289–1302, 2001.

[155] K. Torkar, W. Riedler, F. Rudenauer, C. P. Escoubet, H. Arends, B. T. Narheim, K. Svenes, M. P. McCarthy, G. K. Parks, R. P. Lin, and H. Reme. Spacecraft potential control aboard equator-s as a test for cluster-ii. Annales Geophysicae, 17(12):1582–1591, 1999.

[156] Alan C. Tribble. The Space Environment - Implications for Spacecraft Design. Princton University Press, revised and expanded edition, 2003.

[157] Y. Tsuda, O. Mori, R. Funase, H. Sawada, T. Yamamoto, T. Saiki, T. Endo, and J. Kawaguchi. Flight status of ikaros deep space solar sail demonstrator. Acta Astronautica, 69(9–10):833–840, Nov. – Dec. 2011.

[158] Harsh Vasavada and Hanspeter Schaub. Analytic solutions for equal mass four-craft static coulomb formation. In AAS/AIAA Astrodynamics Specialist Conference, Mackinac Island, MI, Aug. 19–23 2007. Paper No. AAS 07–268.

[159] Sandor M. Veres, Nick K. Lincoln, and Steve B. Gabriel. Testbed for satellite formation flying control system verification. In AIAA Infotech@Aerospace Conference, Rohnert Park, Ca, May 7-10 2007.

[160] Lars Wåhlin. Atmospheric Electrostatics. Research Studies Press, 1986.

[161] Shuquan Wang and Hanspeter Schaub. One-dimensional 3-craft coulomb structure control. In 7th International Conference on Dynamics and Control of Systems and Structures in Space, pages 269–278, Greenwich, London, England, July 16–20 2006.

[162] Shuquan Wang and Hanspeter Schaub. 1-d constrained coulomb structure stabilization with charge saturation. In AAS/AIAA Astrodynamics Specialist Conference, Mackinac Island, MI, Aug. 19–23 2007. Paper No. AAS 07–267.

[163] Shuquan Wang and Hanspeter Schaub. Coulomb control of nonequilibrium fixed shape triangular three-vehicle cluster. AIAA Journal of Guidance, Control, and Dynamics, 34(1):259–270, Feb. 2011.

[164] Shuquan Wang and Hanspeter Schaub. Nonlinear charge control for a collinear fixed shape three-craft equilibrium. AIAA Journal of Guidance, Control, and Dynamics, 34(2):359–366, Mar.–Apr. 2011.

[165] Shuquan Wang and Hanspeter Schaub. Nonlinear feedback control of a spinning two-spacecraft coulomb virtual structure. IEEE Transactions on Aerospace and Electronic Systems, 47(3):2055–2067, July 2011.

[166] C. L. Waters, J. C. Samson, and Donovan E. F. Variation of plasmatrough density derived from magnetospheric field line resonances. Journal of Geophysical Research, 101(A11):24,737 – 24, 745, Nov. 1996.

[167] James R. Wertz. High resolution structureless telescope. Technical Report MC04-1643, NASA/NIAC, April 26 2004.

[168] E. C. Whipple. Observation of photoelectrons and secondary electrons reflected from a potential barrier in the vicinity of ats 6. Journal of Geophysical Research, 81(4):715–719, Feb. 1976.

[169] E. C. Whipple and R. C. Olsen. Importance of differential charging for controlling both natural and induced vehicle potentials on ats-5 and ats-6. In Proceedings of the 3rd Spacecraft Charging Technology Conference, page 887, Nov. 12–14 1980. NASA Conference Publication 2182.

[170] Elden C Whipple. Potentials of surfaces in space. Reports on Progress in Physics, 44(11):1197–1250, 1981.

[171] William R. Wilson and Mason A. Peck. An air-levitated testbed for flux pinning interactions at the nanosatellite scale. In AIAA Guidance, Navigation and Control Conference, Toronto, Canada, Aug. 2–5 2010. Paper AIAA 2010-8221.

[172] Kirk Woellert, Pascale Ehrenfreund, Antonio J. Ricco, and Henry Hertzfeld. Cubesats: Cost-effective science and technology platforms for emerging and developing nations. Advances in Space Research, 47(4):663–684, Feb. 15 2011.

[173] Byoungsam Woo, Kevin M. Ertmer, Victoria L. Coverstone, Rodney L. Burton, Gabriel F. Benavides, and David L. Carroll. Deployment experiment for ultralarge solar sail system (ultrasail). AIAA Journal of Spacecraft and Rockets, 48(5):874–880, Sept.–Oct. 2011.

[174] Douglas Zimpfer, Peter Kachmar, and Tuohy Seamus. Autonomous rendezvous, capture and in-space assembly: Past, present and future. In AIAA 1st Space Exploration Conference: Continuing the Voyage of Discovery, Orlando, FL, Jan. 30–Feb. 1 2005. Paper No. AIAA 2005-2523.

Appendix A

Plasma Coulomb force model discrepancies

A proposed model for the force between a sphere and an infinitesimal point charge in a plasma is developed and shown in Equation 3.36. There is a discrepancy in the confirmation of these force that is explained and discussed in this appendix. The force of Equation 3.36 is derived from computing the E-field about a sphere of finite radius ρ_A, charged to a surface potential V_A, using the conservative Debye-Hückel approximation. This E-field of Equation 3.32 is reproduced here:

$$E_A(r) = -\nabla_r \Phi(r) = \frac{V_A \rho_A}{r^2} e^{-(r-\rho_A)/\lambda_D} \left(1 + \frac{r}{\lambda_D}\right)$$

The Coulomb force on a infinitesimal point charge q_B that is placed in this E-field at a distance d is computed with Equation 3.36:

$$F = \frac{V_A \rho_A q_B}{d^2} e^{-(d-\rho_A)/\lambda_D} \left(1 + \frac{d}{\lambda_D}\right)$$

The capacitance of the sphere and plasma is given by Equation 3.34:

$$q_A = V_A \frac{\rho_A}{k_c} \left(1 + \frac{\rho_A}{\lambda_D}\right)$$

which has no influence from the infinitesimal point charge and can be substituted into the force equation to give:

$$F_{AB} = \frac{k_c q_A q_B}{d^2} \left(\frac{\lambda_D}{\rho_A + \lambda_D}\right) e^{-(d-\rho_A)/\lambda_D} \left(1 + \frac{d}{\lambda_D}\right) \tag{A.1}$$

However, consider now the E-field from the isolated infinitesimal point charge in a plasma given by:

$$E_B(r) = \frac{k_c q_B}{r^2} e^{-r/\lambda_D} \tag{A.2}$$

When the sphere, with a total self capacitance charge of q_B is placed in this field at a distance d the sphere experiences a Coulomb force magnitude:

$$F_{BA} = \frac{k_c q_A q_B}{d^2} \left(1 + \frac{d}{\lambda_D}\right) e^{-d/\lambda_D} \tag{A.3}$$

The force on the point charge is not equivalent to the force on the sphere $F_{AB} \neq F_{BA}$. The discrepancy arrises from the plasma shielding which is computed for different separations between the sphere and the point charge in each direction. The additional terms in F_{AB} are

$$e^{\rho_A/\lambda_D} \left(\frac{\lambda_D}{\rho_A + \lambda_D}\right)$$

If you take the taylor series expansion of the exponent of this additional term it is shown that the first order terms are cancelled and if $(\rho_A \ll \lambda_D)$ then the force does equate to be the same value.

$$\begin{aligned}
\left(\frac{\lambda_D}{\rho_A + \lambda_D}\right) e^{\rho_A/\lambda_D} &= \left(\frac{\lambda_D}{\rho_A + \lambda_D}\right) \left(1 + \frac{\rho_A}{\lambda_D} + \frac{\rho_A^2}{2\lambda_D^2} + ...\right) \\
&= 1 + \left(\frac{\lambda_D}{\rho_A + \lambda_D}\right) \left(\frac{\rho_A^2}{2\lambda_D^2} + ...\right)
\end{aligned} \tag{A.4}$$

Consequently, this is a negligible discrepancy in the computation of the force between a sphere and a point charge in a nominal plasma, $\lambda_D = 200$ m. Even for the small worst case plasma, $\lambda_D = 4$ m, these second order and greater terms have a small effect for meter size craft. The plasma Coulomb force models developed in this dissertation are an analytic estimate and the small discrepancy explored in this Appendix can be safely omitted.

Appendix B

Testbed hardware apparatus details

Additional details on the design and operation of the autonomous air flow system are described here. The infrared sensors are positioned 75 cm from the cart and track in order to not introduce any electrostatic interference. At this range they project a sensing area that is slightly less than 2.54 cm wide (the separation of the holes on the track). There are challenges with the alignment of the IR beams relative to the track to ensure triggering of air occurs with accurate timing. It is necessary to calibrate the alignment and measure the IR beams and valve triggering to reduce additional airflow disturbances.

At this 75 cm range the output voltage signal is in the range 0 to 1V depending on whether there is cart reflection or not. This voltage signal is then used to drive the valve on/off logic through a comparator circuit with a variable threshold setting. The circuit which controls 8 IR and valve combinations also features an analog low pass filter and is encased in shielded boxes directly behind the IR sensors to reduce noise and obtain a clean signal for airflow triggering. The whole position sensing and air flow control is completely analog and self sufficient (not requiring user or computer input). This stand alone architecture can be easily scaled to a track of any length.

The IR sensors are sensitive but can provide a clean signal with a flat reflective surface. During autonomous airflow operation, the cart uses a paper reflective sheet that extends beyond the sphere and is used to directly reflect the IR signal. This reflective sheet is a smaller dimension than the cart length so that the cart overlaps the air holes prior to them being turned on. The sphere on the cart is positioned slightly off center to account for the mass distribution, which is

calibrated prior to each test.

   Tests demonstrated that random erroneous signals from the IR reflecting off the plastic safety cage that surrounds the entire apparatus do occur. To overcome this the safety cage is aligned so that the IR beams reflected at an angle away from their sensing receptors. Similar issues are observed with the cart positioning laser. A small cardboard patch is used to reflect the laser beam. However, if the plastic cage (behind the cart and cardboard patch) is positioned perfectly perpendicular to the laser, the beam can penetrate the cardboard and the plastic acts as the reflection surface. This is easily remedied by giving the plastic cage a slight angle and using a double thickness cardboard patch.